UNIVERSITY OF CALIFORNIA
Los Angeles

Solar-Thermal Production of Hydrogen and Graphitic Carbon via Methane Decomposition

A dissertation submitted in partial satisfaction
of the requirements for the degree
Doctor of Philosophy in Mechanical Engineering

by

Mostafa M. Abuseada

2022

ABSTRACT OF THE DISSERTATION

Solar-Thermal Production of Hydrogen and Graphitic Carbon via Methane Decomposition

by

Mostafa M. Abuseada
Doctor of Philosophy in Mechanical Engineering
University of California, Los Angeles, 2022
Professor Timothy S. Fisher, Chair

Current hydrogen and carbon production technologies emit massive amounts of CO_2 that threaten Earth's climate stability, especially as demands for these materials continue to grow. Compared to alternative clean hydrogen production technologies, solar methane pyrolysis has lower energy requirements, produces carbon materials of commercial interest, and provides higher process efficiencies. In this work, a new solar-thermal methane decomposition process involving flow through a fibrous carbon medium to co-produce hydrogen gas and high-value graphitic carbon product with zero CO_2 emissions is presented and thoroughly investigated. A 10 kW_e custom-designed and built solar simulator is used to instigate the methane decomposition reaction with direct irradiation in a custom solar reactor. In contrast to prior work on solar methane pyrolysis, the present process reaches steady-state thermal and chemical operation from room temperature within the first minute of irradiation due to localized, direct solar heating of fibrous medium. Additionally, the present approach provides enhanced thermal transfer and efficiency, delivers graphitic carbon product in an easy to handle and extract form, and prevents undesired carbon deposition within the reactor that would otherwise lead to process interruption. These aspects are ongoing challenges reported in prior literature. In contrast to similar methane decomposition prior work that reports production of amorphous carbon black, this work produces high-quality graphite with production rates that are order(s) of magnitude higher. Parametric variations of methane inlet flow rate (10-2000 sccm), solar power (0.92-2.49 kW), operating pressure (1.33-40 kPa), and medium thickness (0.36-9.6 mm) are thoroughly presented, with methane conversions as high as 96% and graphite Raman D/G peak ratios as low as 0.06. A pathway to process scale-up for continuous production is presented by implementing a roll-to-roll processing method, which was effective in achieving continuous processing with methane conversion enhancements up to 1.5 times higher. The optical design of the solar reactor was then optimized using a secondary concentrator, by which solar-to-chemical efficiencies increased by up to 62% to reach a maximum demonstrated efficiency of 6.5%. Realizing this process at scale would avoid emissions of 10 kg of CO_2 per kg of H_2 and 5 kg of CO_2 per kg of graphite.

The dissertation of Mostafa M. Abuseada is approved.

R. Mitchell Spearrin

Y. Sungtaek Ju

Yves Rubin

Timothy S. Fisher, Committee Chair

University of California, Los Angeles

2022

Table of Contents

List of Figures **x**

List of Tables **xxiv**

Acknowledgments **xxvi**

Biographical Sketch **xxviii**

1 Introduction **1**

1.1 Motivational background 1

1.2 Methane decomposition literature review 5

1.2.1 Catalytic methane decomposition 5

1.2.2 Solar methane decomposition 7

1.2.3 Solar methane decomposition challenges 11

1.3 Research scope and objectives 15

1.4 Document outline 16

2 High Flux Solar Simulator **19**

2.1 Introduction 19

2.2 Experimental setup and procedure 24

2.2.1 High flux solar simulator 24

2.2.2 Radiometer and temperature measurements 25

2.2.3 Spectral characteristics 26

2.2.4 Direct heat flux mapping 27

2.3 Heat flux methodology 30

2.3.1 Monte Carlo ray tracing 31
2.3.2 Inverse method 32
2.4 Results and discussion 39
2.4.1 Heat flux gauge 39
2.4.2 Monte Carlo ray tracing simulations 40
2.4.3 Inverse method 41
2.5 Additional considerations 47
2.5.1 Treatment of surrounding surfaces 47
2.5.2 Sensitivity analysis 50
2.5.3 Quartz thermal effects 52
2.6 Conclusions 54

3 Methane Decomposition Setup and Auxiliaries 57
3.1 Methane pyrolysis experimental setup 58
3.1.1 Small-scale solar reactor 58
3.1.2 Reactor auxiliaries 59
3.1.3 Process and control automation 61
3.2 Product stream monitoring setup 62
3.2.1 Laser absorption spectroscopy 62
3.2.2 RGA monitoring and calibration 66
3.3 Carbon product analysis tools 71
3.3.1 Raman spectroscopy 71
3.3.2 Scanning electron microscopy 75
3.3.3 BET characterization 75
3.3.4 X-ray diffraction 76
3.4 Local heat flux distribution 77

3.5 Conclusions . . . 79

4 Methane Decomposition Initial Study 80

4.1 Theory and methodology . . . 81
  4.1.1 Carbon felt composition and pretreatment . . . 81
  4.1.2 Temperature measurements . . . 83
  4.1.3 Chemical kinetics analysis . . . 85
  4.1.4 Efficiency quantification . . . 88
  4.1.5 Residence time and permeability . . . 89
4.2 Overall process performance . . . 90
4.3 Chemical kinetics and pyrolysis performance . . . 93
4.4 Solid carbon characterization . . . 96
  4.4.1 Deposition rates and morphology . . . 96
  4.4.2 Product quality . . . 101
4.5 Other process characteristics . . . 103
  4.5.1 Process transient performance . . . 103
  4.5.2 Effect of process substrate . . . 105
4.6 Conclusions . . . 106

5 Parametric Study of Methane Decomposition 108

5.1 Methodology . . . 108
5.2 Thermal treatment . . . 109
5.3 Representative carbon product characteristics . . . 112
5.4 Effect of flow rate . . . 116
5.5 Effect of solar power . . . 121
5.6 Effect of pressure . . . 125
5.7 Effect of reaction zone size . . . 132

5.8 X-ray diffraction 136
5.9 Transient performance and carbon capture 137
  5.9.1 Transient performance 137
  5.9.2 Carbon capture 140
5.10 Conclusions 141

6 Process Scale-Up by Continuous Processing 144
6.1 Introduction 144
6.2 Experimental setup and methodology 147
  6.2.1 Large-scale solar reactor 147
  6.2.2 Solar simulator and auxiliaries 149
  6.2.3 Roll-to-roll mechanism 150
  6.2.4 Materials and characterization techniques 151
6.3 Transient process performance 152
  6.3.1 Methane conversion and product yields 152
  6.3.2 Solid carbon product characterization 156
6.4 Parametric study 158
  6.4.1 Process performance 158
  6.4.2 Carbon product quality 164
6.5 Conclusions 167

7 Optical Optimization of the Solar Reactor 169
7.1 Introduction 169
7.2 Setup and secondary concentrator 172
7.3 Theory and methodology 174
  7.3.1 Monte Carlo ray tracing 174
  7.3.2 Geometry constraints and optimization 179

7.3.3 Materials and methods 179
7.4 Results and discussion 180
7.4.1 Simulations and optimization 180
7.4.2 Secondary concentrator design 183
7.4.3 Thermal measurements 184
7.4.4 Methane pyrolysis 186
7.4.5 Carbon product quality 188
7.5 Conclusions 189

8 Closure 191

8.1 Photocatalytic contribution 191
8.1.1 Temperature-dependent deposition rates 192
8.1.2 Direct and indirect solar irradiation 196
8.1.3 Thermal conductivity 200
8.2 Alternative starting materials 202
8.3 Opportunities for future work 205

Appendices 208

A Methane decomposition process schematics 208
B LAS chemical kinetics methodology 212
C Methane pyrolysis results summary 214

References 216

List of Figures

2.1 (a) Overview of the solar simulator and its main components. (b) Experimental setup used in characterizing the solar simulator, where the figure inset shows front view of vacuum chamber with target. . . 25

2.2 Spectral distribution output measured from the HFSS at different powers (supply currents) and normalized by area under the curves. . 27

2.3 Experimental setup for characterizing the HFSS using a HFG for validation of the inverse heat flux mapping method. 28

2.4 Transient nature of the heat flux output from the HFSS. 30

2.5 (a) Photograph of the radiometer developed and used in this study, and (b) schematic illustration of the control volume considered. . . . 34

2.6 Variation of peak heat flux values with HFSS current supply as measured by the HFG. 40

2.7 Validation of the in-house MCRT model with respect to measurements from the HFG outside the vacuum chamber showing (a) heat flux distribution at the focal plane and 160 A HFSS supply current, and (b) peak heat flux values at different focal distances and at 120 A HFSS supply current. 41

2.8 Mesh independence study for the heat transfer numerical model. . . . 42

2.9 (a) Time-averaged temperature profile of the graphite sample back surface obtained using the IR camera for a test at HFSS supply current of 100 A (centered black rings with $r = 5$, 10, 15, and 20 mm illustrate distribution and angular uniformity). (b) IR camera radially averaged temperature distribution and predictions from the inverse heat transfer model for front and back sample surfaces. 43

2.10 (a) Results of the inverse heat transfer (HT) model at HFSS supply current of 100 A showing heat flux distribution inside the vacuum chamber of five repeated experimental runs and their average compared to corrected measurements from HFG. (b) Final averaged results of the inverse heat transfer model at HFSS supply current of 140 A showing the heat flux distribution inside the vacuum chamber compared to corrected measurements from HFG. Gray shaded regions represent the uncertainty bounds of the inverse model heat flux results. 44

2.11 Illustration of the radiosity model considered for the numerical heat transfer model, showing the vacuum chamber with different surfaces treated (left) and the constructed electrical network analogy (right). . 48

2.12 Sensitivity analysis of model parameters for the inverse heat transfer mapping technique. 51

2.13 Vacuum chamber's quartz window temperature distribution for a test at HFSS supply current of 140 A. 53

2.14 Heat flux distribution measured using the HFG at the focal plane with 160 A supplied current along with fitted Lorentzian distribution. . . . 56

3.1 A schematic of the small-scale solar reactor overall process and configuration. 59
3.2 Photographs of the solar reactor's (a) upstream auxiliaries and (b) exhaust line. 60
3.3 Photographs of the solar reactor's (a) automation components and (b) data acquisition and controls system. 61
3.4 Laser absorption spectroscopy experimental configuration, monitoring CH_4, C_2H_4, and C_2H_6 in product stream. 63
3.5 Example absorbance spectra and spectral fits of the (a) CH_4 and C_2H_4, and (b) C_2H_6 transitions. 65
3.6 CH_4 calibration test runs for the LAS system at different gas compositions and pressures. 66
3.7 Schematic illustrating the MS configuration and sampling from the reactor's main product stream. 67
3.8 Calibration and validation runs of the MS at different gas compositions. 69
3.9 Photographs of the Raman spectrometer configuration. 71
3.10 Raman spectra of (a) crystalline silicon and (b) POCO graphite measured during the validation steps of the built Raman spectrometer. 73
3.11 Heat flux distribution from the HFSS (a) normalized mean and uncertainty bounds for different inverse characterization tests, and (b) locally within the reactor in contrast to the gross distribution outside the reactor at the focal plane and a supply current of 160 A. . 79

4.1 Photographs of the solar methane decomposition small-scale reactor from different views: (left) perspective, (middle) side, and (right) front. 81

4.2 Thermogravimetric analysis performed on original C100 carbon felt for a temperature up to 1300 K. 83

4.3 Schematic illustration of experimental setup used to measure front surface temperatures, with the front temperature contour (distorted due to 45° view angle) shown on right. 85

4.4 Maximum front and back temperatures measured during methane pyrolysis at solar power of 1.86 kW, methane inlet flow rate of 100 sccm, pressure of 3.33 kPa, and reaction zone thickness of 3.2 mm. . . 86

4.5 (a) Temperature profile of the carbon felt's back surface during CH_4 decomposition obtained using the IR camera (centered black rings with $r = 5$, 10, 15, and 20 mm illustrate distribution and angular uniformity), and (b) photograph of carbon felt with carbon deposition. CH_4 decomposition at 100 sccm flow rate, 3.33 kPa pressure, 1.86 kW net radiant power, and 20 min reaction period. 91

4.6 Methane pyrolysis at flow rate of 100 sccm, pressure of 3.33 kPa, solar power of 1.86 kW, and medium thickness of 3.2 mm showing (a) product mole fractions as a function of time as measured by LAS, and (b) maximum and average temperatures of the fibrous medium. . . . 92

4.7 Methane product mole fraction as a function of time under HFSS solar irradiation cycling in an on/off manner at flow rate of 100 sccm, pressure of 3.33 kPa, solar power of 1.86 kW, and medium thickness of 3.2 mm. 93

4.8 Real-time monitoring results from the calibrated mass spectrometer showing (a) mole fractions in the product stream, and (b) methane conversion and product yields for CH_4 decomposition through carbon felt at 100 sccm flow rate, 3.33 kPa pressure, 1.86 kW solar power, and 20 min reaction period. 94

4.9 SEM images of the carbon felt after methane decomposition and carbon deposition at 100 sccm flow rate, 3.33 kPa pressure, 1.86 kW solar power, and 20 min reaction period for radial distances of (a) 0, (b) 2.5, (c) 5, (d) 7.5, (e) 10, and (f) 12.5 mm from the center and under the same magnification. 97

4.10 Morphology analysis on carbon felt product showing (a) fiber diameter as a function of radial distance from the center as compared to the original carbon felt diameter, and (b) SEM image at the center of the carbon felt demonstrating the nature and amount of carbon deposition. CH_4 decomposition at 100 sccm flow rate, 3.33 kPa pressure, 1.86 kW solar power, and 20 min reaction period. . . . 98

4.11 BET results for the (a) carbon product from 0-5 mm radius and (b) original carbon felt for CH_4 decomposition at 100 sccm flow rate, 3.33 kPa pressure, 1.86 kW solar power, and 20 min reaction period. . . . 99

4.12 Structural analysis on carbon felt product showing (a) Raman spectra of the carbon product at the center and 5 mm radial distance as compared to the original carbon felt, and (b) XRD spectra of the carbon product at the central region as compared to the original carbon felt. CH_4 decomposition at 100 sccm flow rate, 3.33 kPa pressure, 1.86 kW solar power. 103

4.13 Real-time monitoring results from the calibrated mass spectrometer showing (a) mole fractions in the product stream, and (b) methane conversion and product yields for CH_4 decomposition through carbon felt at 100 sccm flow rate, 3.33 kPa pressure, 1.86 kW solar power, and 120 min reaction period. 104

4.14 SEM image of the carbon felt's central region after CH_4 decomposition and carbon deposition at 100 sccm flow rate, 3.33 kPa pressure, 1.86 kW solar power, and 120 min reaction period. 105

4.15 Real-time monitoring results from the calibrated mass spectrometer showing (a) mole fractions in the product stream, and (b) methane conversion and product yields for CH_4 decomposition through ceramic felt at 100 sccm flow rate, 3.33 kPa pressure, 1.86 kW solar power, and 20 min reaction period. 106

5.1 Methane conversion, hydrogen yield, and carbon yield for methane pyrolysis at flow rate of 100 sccm, solar power of 1.86 kW, pressure of 3.33 kPa, and medium thickness of 3.2 mm with thermal pretreatment (red) and without thermal pretreatment (black). 110

5.2 (a) Raman, (b) XRD, and (c) EDS spectra of original fibrous carbon material and thermally-treated material under vacuum at a solar power of 1.86 kW for a duration of 20 min. 111

5.3 (a) Raman and XRD spectra of representative conditions of 1.86 kW solar power, 3.33 kPa pressure, 100 sccm CH_4 inlet flow rate, and 3.2 mm fibrous medium thickness. (b,c) SEM images of (b) original fibrous material and (c) representative cross-sectional cut of fibrous medium with carbon deposition. 113

5.4 Methane decomposition at a pressure of 3.33 kPa, solar power of 1.86 kW, and medium thickness of 3.2 mm. Effect of methane inlet flow rate on (a) methane conversion, hydrogen yield, and carbon yield, and (b) acetylene byproduct concentration and hydrogen production rate. 117
5.5 Methane pyrolysis at solar power of 1.86 kW, pressure of 3.33 kPa, and reaction zone thickness of 3.2 mm. (a) Raman spectra of carbon product at different methane inlet flow rates. (b,c) SEM images in the central region of the fibrous medium at (b) 25 sccm after 80 min and (c) 2000 sccm after 3 min. 119
5.6 Methane conversion in addition to carbon and hydrogen production rates at various methane inlet flow rates for methane pyrolysis at solar power of 1.86 kW, pressure of 3.33 kPa, and reaction zone thickness of 3.2 mm. 121
5.7 Effect of solar power (and maximum operating temperature) on methane conversion, hydrogen yield, and carbon yield at operating pressure of 3.33 kPa, methane inlet flow rate of 100 sccm, and medium thickness of 3.2 mm. 122
5.8 Methane pyrolysis at inlet flow rate of 100 sccm, pressure of 3.33 kPa, and reaction zone thickness of 3.2 mm. (a) Raman spectra of carbon product at different solar powers and maximum temperatures. (b,c) SEM images in the central region of the fibrous medium at (b) 2.49 kW after 20 min and (c) 0.92 kW after 30 min. 124
5.9 Effect of operating pressure on methane conversion, hydrogen yield, and carbon yield at methane inlet flow rate of 100 sccm, solar power of 1.86 kW, and medium thickness of 3.2 mm. 126

5.10 Methane pyrolysis at solar power of 1.86 kW, inlet flow rate of 100 sccm, and reaction zone thickness of 3.2 mm. (a) Raman spectra of carbon product at different operating pressures. (b,c) SEM images in the central region of the fibrous medium after 20 min at (b) 1.33 kPa and (c) 40 kPa. (d,e) SEM images of amorphous CB produced in lower temperature regions of the fibrous medium at 40 kPa. 128
5.11 Comparison of methane conversion, hydrogen yield, and carbon yield at varying flow rates for two operating pressures (3.33 kPa and 13.3 kPa), solar power of 1.86 kW, and medium thickness of 3.2 mm. . . . 129
5.12 Methane pyrolysis at solar power of 1.86 kW, pressure of 13.3 kPa, and reaction zone thickness of 3.2 mm. (a) Raman spectra of carbon product at different methane inlet flow rates and a relatively elevated pressure. (b,c) SEM images of the fibrous medium at 800 sccm after 5 min. 131
5.13 Effect of reaction zone size thickness on methane conversion, hydrogen yield, and carbon yield at operating pressure of 3.33 kPa, solar power of 1.86 kW, and methane inlet flow rate of 100 sccm. 133
5.14 Methane pyrolysis at solar power of 1.86 kW, pressure of 3.33 kPa, and inlet flow rate of 100 sccm. (a) Raman spectra of carbon product with different reaction zone thicknesses. (b) SEM image in the central region of the fibrous medium with zone thickness of 0.36 mm after 20 min of CH_4 decomposition. 135
5.15 XRD spectra of the central region of carbon product generated at various process operating conditions of solar power (Q), flow rate (FR), and pressure (P), all with a reaction zone thickness of 3.2 mm. 137

5.16 (a) Transient carbon yields at solar power of 1.86 kW and pressure of 3.33 kPa with (i) Run 1: $\dot{m}_{\mathrm{CH_4}}$ of 100 sccm and reaction zone thickness of 3.2 mm, (ii) Run 2: $\dot{m}_{\mathrm{CH_4}}$ of 100 sccm and reaction zone thickness of 0.36 mm, and (iii) Run 3: $\dot{m}_{\mathrm{CH_4}}$ of 1750 sccm and reaction zone thickness of 6.35 mm. (b) Theoretically and experimentally measured carbon deposition rates at different inlet flow rates, solar power of 1.86 kW, pressure of 3.33 kPa, and reaction zone thickness of 3.2 mm. . . 139

6.1 (a) Process overview of the roll-to-roll solar-thermal methane pyrolysis experimental setup. Figure inset in the top right shows photographs of the roll-to-roll mechanism and radiation shield. (b) Photograph of the roll-to-roll experimental setup. 148

6.2 Photographs of the (a) large-scale roll-to-roll solar reactor used for continuous processing and (b) roll-to-roll auxiliaries and motion feedthroughs. 149

6.3 CAD model of the roll-to-roll mechanism. 151

6.4 Experimental testing of roll-to-roll solar-thermal methane pyrolysis demonstrating effective operation at four operating conditions as quantified via conversion and yields. Testing at operating pressure of 3.33 kPa and (a) power of 1.86 kW and thickness of 0.89 mm (b) power of 1.86 kW and thickness of 6.35 mm (c) flow rate of 200 sccm, power of 2.34 kW, and thickness of 0.89 mm, (d) flow rate of 200 sccm, power of 2.26 kW, and thickness of 1.78 mm. 153

6.5 Characterization results of solid carbon product of the four different experimental roll-to-roll initial tests. SEM images for: (a) original carbon cloth/roll, (b) Roll 1, (c) Roll 3, (d) Roll 4, and (e) cross-section of Roll 2. (f) Raman and (g) XRD spectra of the roll-to-roll original carbon cloth and carbon products of different tests. 157

6.6 Roll-to-roll methane pyrolysis at a pressure of 3.33 kPa and solar power of 2.34 kW. (a,c) Effect of methane inlet flow flow rate on methane conversion and product yields with (a) 0.89 mm and (c) 1.78 mm thick rolls. (b,d) Effect of inlet flow rate on acetylene secondary byproduct and hydrogen and carbon production rates for (b) 0.89 mm and (d) 1.78 mm thick rolls. 160

6.7 Effect of solar power on methane conversion and product yields for roll-to-roll methane decomposition at methane inlet flow rate of 100 sccm and pressure of 3.33 kPa, with (a) 0.89 mm and (b) 1.78 mm thick rolls. 163

6.8 Effect of pressure on methane conversion and product yields for roll-to-roll methane pyrolysis at methane inlet flow rate of 100 sccm and solar power of 2.34 kW, with 0.89 mm thick roll. 164

6.9 Raman spectra of carbon product at (a) different solar powers at pressure of 3.33 kPa and inlet flow rate of 100 sccm with 0.89 mm thick roll; (b) different pressures at solar power of 2.34 kW and flow rate of 100 sccm with 0.89 mm thick roll; (c) different solar powers at pressure of 3.33 kPa and inlet flow rate of 100 sccm with 1.78 mm thick roll; (d) different flow rates at solar power of 2.34 kW and pressure of 3.33 kPa with 1.78 mm thick roll. 166

7.1 Schematic illustration of the large-scale solar methane pyrolysis experimental setup with secondary concentrator. 173
7.2 Geometry and surfaces modeled within the MCRT simulation for the secondary concentrator. 175
7.3 Flowchart illustration of the MCRT algorithm. Sections highlighted in orange correspond directly to the solar simulator and its modeling. 176
7.4 MCRT simulation results of relative power enhancement with secondary concentrator geometry showing (a) a contour map of relative power with respect to concentrator's length and radius, and (b) 2D plots of relative power variation with concentrator's length at different radii. 181
7.5 (a) Output power distribution from the solar simulator for the cases with and without a secondary concentrator. (b) 2D radially-averaged normalized heat flux distributions at the focal plane with and without secondary concentrator. 182
7.6 CAD model of the conical secondary concentrator and configuration. Figure inset on the left shows a photograph of the secondary concentrator system placed within the solar reactor. 184
7.7 (a) Maximum temperatures with and without secondary concentrator as a function of solar simulator's current, and (b) representative temperature contour with secondary concentrator at 170 A as measured using the IR camera. 185
7.8 Methane conversion and product yields with and without secondary concentrator for methane pyrolysis at a flow rate of 100 sccm, solar power of 1.86 kW, pressure of 3.33 kPa, and fibrous medium thickness of 3.2 mm. 187

7.9 (a) Raman spectra and (b,c) SEM images of graphitic carbon product of Exp 1 (b) without and (c) with the secondary concentrator. 189

8.1 (a) IR camera temperature measurements of a representative test for methane pyrolysis at solar power of 1.86 kW, pressure of 3.33 kPa, methane inlet flow rate of 100 sccm, and fibrous medium thickness of 3.2 mm (centered black rings with $r = 5$, 10, 15, and 20 mm illustrate distribution and angular uniformity). (b) Fiber diameter measurements of a representative test using SEM images of the carbon medium after methane pyrolysis for 20 min. 194

8.2 (a) Arrhenius plot of reaction kinetics raw measurements, with negative slopes of the blue and black linear fits being 41.9 and 15.9 $\times 10^3$ K, respectively. (b) Heat flux distribution along the fibrous medium's surface at a solar power of 1.86 kW. (c) Adjusted Arrhenius plot, accounting for 300 K temperature increase from solar irradiation absorbed by PAHs. 195

8.3 (a) Experimental setup of solar methane pyrolysis testing with direct and indirect irradiation. (b) Photograph of light shield used for direct and indirect solar irradiation. (c) Contour of IR camera temperature measurements for testing with a light shield, where black lines indicate the area covered by the light shield. 197

8.4 (a) Fiber diameters after methane pyrolysis with light shield for 25 min at solar power of 2.41 kW, methane inlet flow rate of 100 sccm, and pressure of 3.33 kPa. (b-d) SEM images of the carbon product demonstrating the significant fiber growths at regions receiving direct solar irradiation, showing (b) fibers at edge of the light shield, (c) a 2 mm long single fiber at the transition between indirect and direct irradiation, and (d) fibers across two light shield's ligaments. 199

8.5 (a,b) SEM surface images and (c) Raman spectrum of the graphite product used for thermal diffusivity measurements. (d) Photograph of the experimental setup for thermal diffusivity measurements using a modified Ångström's method. (e,f) Amplitude ratio and phase shift measurements along tested graphite sample at a heating frequency of 0.1 Hz. 201

8.6 (a) Raman spectra of carbon product obtained with different starting materials after methane decomposition at a solar power of 1.86 kW, methane inlet flow rate of 100 sccm, and pressure of 3.33 kPa. (b,c) XRD spectra of starting material and solid product for (b) zirconia and (c) silica substrates. (d) SEM image and (e-g) EDS maps of the solid product with a silica substrate representing constituent (e) carbon, (f) silicon, and (g) oxygen elements. 204

8.7 Schematic illustration of a roll-to-roll solar-thermal methane decomposition process for solar field implementation with a parabolic dish system. 207

A.1 An overall P&ID schematic illustration of the small-scale methane decomposition experimental setup and auxiliaries. 209

A.2 LabVIEW front panel screenshot of VI created for controlling and monitoring the small-scale methane decomposition experiments. . . . 210

A.3 LabVIEW block diagram screenshot of VI created for controlling and monitoring the methane decomposition experiments. 211

List of Tables

1.1 Summary of solar methane decomposition in prior literature. 9

3.1 Summary of inverse heat flux distribution local results for methane decomposition experiments. 78

4.1 Comparison of LAS and MS measurements of species concentration for methane decomposition through carbon felt at 100 sccm flow rate, 3.33 kPa pressure, and 1.86 kW solar power. 96

4.2 Summary of BET results at different radial regions of the carbon felt for CH_4 decomposition at 100 sccm flow rate, 3.33 kPa pressure, 1.86 kW solar power, and 20 min reaction period. 98

7.1 Methane pyrolysis process conversions, product yields, and solar-to-chemical efficiencies with and without the secondary concentrator at four operating conditions. Exp 1: 1.86 kW power, 100 sccm flow rate, 3.33 kPa pressure, and 3.2 mm thick medium; Exp 2: 2.26 kW, 100 sccm, 3.33 kPa, and 6.4 mm thick; Exp 3: 2.26 kW, 400 sccm, 0.67 kPa, and 6.4 mm thick; Exp 4: 2.26 kW, 2000 sccm, 3.33 kPa, and 6.4 mm thick. 188

8.1 Results of different materials tested for solar methane pyrolysis. . . . 203

C.1 Results summary of the small-scale reactor parametric study. Methane pyrolysis operating conditions, chemical conversions and yields, solar-to-chemical efficiencies, carbon product deposition rates, and Raman quality. Reported values are based on initial steady-state measurements observed prior to slight reduction in performance due to significant flow constriction. 214

Acknowledgments

I would like to express my appreciation and gratitude to my advisor, Prof. Timothy S. Fisher, for his great mentorship, invaluable discussions, continuous support, and funding. His support and guidance at different stages of this work contributed significantly to my research progress and development, and it provided me with countless opportunities for collaboration with other scholars on work beyond the scope of this dissertation.

I would also like to sincerely thank Prof. R. Mitchell Spearrin, Prof. Yves Rubin, and Prof. Y. Sungtaek Ju for their research collaborations, helpful discussions, valuable feedback, and for serving on my PhD committee.

Additionally, I would like to thank members of the Nanoscale Transport Research Group (NTRG) for their collaborations and support, especially Yuan Hu and Akshay Bharadwaj Krishna. More specifically, I greatly appreciate and acknowledge the contributions of Abdalla Alghfeli in co-designing and building the solar simulator (presented in Chapter 2), laboratory general instrumentation and in-house Raman spectrometer (presented in Chapter 3), and the vertical solar reactor and roll-to-roll system (presented in Chapter 6). Furthermore, Abdalla contributed to the inverse problem methodology presented in Chapter 2 by providing insights on the determination of thermal and optical properties used for accurate thermal modeling.

Moreover, I would like to express my gratitude to other scholars for their assistance and research collaborations that also extended beyond the scope of this dissertation. I would like to thank Chuyu Wei and Barathan Jeevaretanam for their contributions in providing the laser absorption spectroscopy equipment and methodology presented in Chapter 3. For work extending beyond this dissertation, I would like to thank Prof. Bruce Dunn and Jacky Yu for their collaboration in testing the solid carbon product of the present work for battery applications, Yijun Ge for her collaboration in studying photocatalytic effects through first principle modeling, and Julia Chang for her collaboration in developing chemical precursors to enhance process conversions and yields.

Financial support of this work was provided by the Noble Family Innovation Fund of the California NanoSystems Institute (CNSI) at University of California, Los Angeles (UCLA). I am sincerely grateful for receiving this support, which was a direct outcome of preliminary work and results obtained in the early stages of my research. I am also grateful for receiving various support from UCLA, including a fellowship award by the Graduate Division office in my first year as a PhD student.

I also appreciate the support received from all staff of the Mechanical and Aerospace Engineering department at UCLA, and for any other people and entities who have contributed to this work and were left unnamed.

Sections of this dissertation that were previously published will be clearly indicated and acknowledged by a footnote at the beginning of each chapter. The entirety of materials included in this document were solely prepared by myself, not by other co-authors, unless otherwise noted.

Finally, I would like to thank my parents, Mohamed Osama and Mona, and my brother, Mahmoud, for their continuous guidance, encouragement, and care. Their unconditional love and support plays an integral role in my development, both as a research scholar and as a person. This academic work is dedicated to them.

Biographical Sketch

a. Professional Preparation

Texas A&M University at Qatar	Mechanical Engineering	B.S., 2015
University of Minnesota Duluth	Mechanical Engineering	M.S., 2019

b. Journal Publications

A. Alghfeli, M. Abuseada, T. S. Fisher, Solar-thermal cold-wall chemical vapor deposition reactor design and characterization for graphene synthesis, Journal of Vacuum System & Technology B 40 (2022) 064205.

M. Abuseada, A. Alghfeli, T. S. Fisher, Graphitic surface layer formation on organic substrates for electronics using a concentrated solar simulator, MRS Advances 7 (2022), 641-648.

M. Abuseada, A. Alghfeli, T. S. Fisher, Indirect inverse flux mapping of a concentrated solar source using infrared imaging, Review of Scientific Instruments 93 (2022), 073101.

C. Wei, M. Abuseada, B. Jeevaretanam, T. S. Fisher, R. M. Spearrin, Concentrated solar-thermal methane pyrolysis in a porous substrate: Yield analysis via infrared laser absorption, Proceedings of the Combustion Institute (2022).

N. Ozalp, H. Abedini, M. Abuseada, R. Davis, J. Rutten, J. Verschoren, C. Ophoff, D. Moens, An overview of direct carbon fuel cells and their promising potential on coupling with solar thermochemical carbon production, Renewable and Sustainable Energy Reviews 162 (2022), 112427.

M. Abuseada, C. Wei, R. M. Spearrin, T. S. Fisher, Solar-thermal production of graphitic carbon and hydrogen via methane decomposition, Energy & Fuels 36 (2022), 3920-3928.

Y. Hu, M. Abuseada, A. Alghfeli, S. Holdheim, T. S. Fisher, High-temperature thermal diffusivity measurements using a modified Ångström's method with transient infrared thermography, Journal of Heat Transfer 144 (2022), 023502.

M. Abuseada, N. Ozalp, Experimental and numerical study on heat transfer driven dynamics and control of transient variations in a solar receiver, Solar Energy 211 (2020), 700-711.

C. Ophoff, M. Abuseada, N. Ozalp, D. Moens, Systematic approach for design optimization of a 3 kW solar cavity receiver via multiphysics analysis, Solar Energy 206 (2020), 420-435.

M. Abuseada, N. Ozalp, Experimental and numerical study on a novel energy efficient variable aperture mechanism for a solar receiver, Solar Energy 197 (2020), 396-410.

M. Abuseada, N. Ozalp, Numerical characterization of a high flux solar simulator using forward and inverse methods, Journal of Heat Transfer 142 (2020), 022105.

M. Abuseada, C. Ophoff, N. Ozalp, Characterization of a new 10 kWe high flux solar simulator via indirect radiation mapping technique, Journal of Solar Energy Engineering 141 (2019), 021005.

M. Abuseada, N. Ozalp, C. Ophoff, Numerical and experimental investigation of heat transfer in a solar receiver with a variable aperture, International Journal of Heat and Mass Transfer 128 (2019), 125-135.

A. Rajan, M. Abouseada, P. Manghaipathy, N. Ozalp, F. Abdul Majid, A. Srinivasa, An experimental and analytical study on the feasibility of SMA spring driven actuation of an iris mechanism, Applied Thermal Engineering 105 (2016), 849-861.

A. Rajan, M. Abouseada, P. Manghaipathy, A. Srinivasa, N. Ozalp, Feasibility of using shape memory alloy (SMA) spring to facilitate actuation of an iris coupled to a solar reactor, Chemical Engineering Transactions 45 (2015), 841-846.

Chapter 1:

Introduction[1,2]

1.1 Motivational background

Current industrial processes for power, fuel, and commodity production are responsible for massive, ongoing carbon dioxide (CO_2) emissions into the atmosphere that adversely affect the Earth's climate stability with potentially disastrous consequences [1]. These emissions result from the use of limited fossil fuel resources in such processes. For example, the main sources of electricity production consist of 67% non-renewable and CO_2 emitting combustible fuels [2]. With the increasing global production and energy demand (yearly electricity production increase of 3.9%), the need for clean and renewable energy sources as substitutes is highly stressed. Furthermore, 50% of the global energy consumption is dedicated to the heating market, out of which 80% derives from fossil fuel and massively contribute to approximately 40% of the globally emitted CO_2 [3]. A significant fraction of this heat is used for the production of hydrogen (H_2) and

---

[1] All or some portions of this chapter contributed to paper by M. Abuseada, C. Wei, R. M. Spearrin, and T. S. Fisher, titled Solar-thermal production of graphitic carbon and hydrogen via methane decomposition, published in Energy & Fuels 36 (2022), 3920-3928.

[2] All or some portions of this chapter contributed to paper by N. Ozalp, H. Abedini, M. Abuseada, R. Davis, J. Rutten, J. Verschoren, C. Ophoff, and D. Moens, titled An overview of direct carbon fuel cells and their promising potential on coupling with solar thermochemical carbon production, published in Renewable and Sustainable Energy Reviews 162 (2022), 112427.

carbon (C) products with virtually no utilization of the bountiful 75,000 terawatts of solar power reaching the Earth's surface [4]. The advantages of replacing the 36.6% and 29.5% of the natural gas consumption in industrial and residential activities are fruitful [5]. Therefore, increased interest exists in incorporating the use of clean and renewable energy sources, mainly solar power, in energy conversion processes [6], which include the production of hydrogen [7], syngas [8], carbon [9], and other commodities [10].

Current global warming concerns create a high interest in more sustainable energy sources, where hydrogen has been perceived as a desirable, clean fuel [11, 12]. Hydrogen is a storable and light fuel with high energy density and emits no direct pollutants upon combustion. Thus, the demand for hydrogen is continuing to rise significantly, where its demand has grown more than three-fold since 1975 and almost 20% since 2010 to a total value of 73.9 megaton in 2018. Hydrogen is also seen as a promising replacement of fossil fuels in the production of industrial chemicals such as methanol and ammonia [13]. Unfortunately, the present hydrogen demand is almost completely met by fossil fuels through unsustainable production technologies that lead to emissions of approximately 830 megaton of CO_2 annually. The leading source of hydrogen production with around 75% contribution is natural gas, which consists mainly of methane (CH_4) [14].

The main industrial pathway for hydrogen production is currently a process known as steam methane reforming (SMR) [15, 16], while partial oxidation and autothermal reforming of CH_4 (or other hydrocarbons) are less economical alternatives [17]. If hydrogen is the desired final product rather than syngas, the highly endothermic SMR reaction is coupled with the water-gas shift reaction as:

$$\mathrm{CH_4 + H_2O \rightarrow CO + 3H_2} \quad (\Delta H^o = 206.2\ \mathrm{kJ/mol}) \tag{1.1}$$

$$CO + H_2O \rightarrow CO_2 + H_2 \quad (\Delta H^o = -41.2 \text{ kJ/mol}) \tag{1.2}$$

where ΔH^o represents the standard molar enthalpy of the reaction [18]. It is estimated that emissions from the SMR reaction are approximately 8.9 kg CO_2/kg H_2 [19], and can reach up to 11.85 kg-equivalent CO_2/kg H_2 for a large-scale SMR plant [20]. Despite the SMR's status as a mature technology with low hydrogen production costs, the process raises concerns due to its inherent emission of greenhouse gases.

A prior study that used solar heating for SMR required the use of specialized catalysts to achieve "fuel conversion at reasonable rates"[21]. However, the resulting catalyst and support introduce additional costs, complexity, and durability limits related to sintering and catalyst deactivation. SMR does offer an intrinsic advantage in producing one more mole of hydrogen per reactant mole of methane molecule than pyrolysis, but this benefit comes with the cost of higher heat input, $\Delta H^o_{\mathrm{SMR}} = 206$ kJ/mol [22]. Using hydrogen's lower heat value of -242 kJ/mol, at least 54% of the additional hydrogen from SMR would be recycled for process reaction heat.

SMR is the most cost-effective current hydrogen production process. Water electrolysis driven by solar energy is an emerging alternative [23], with potentially 30% solar-to-hydrogen efficiency but significantly higher production costs at present [24]. Similar challenges exist for alternative solar-driven processes such as CO_2/H_2O dissociation [25]. Moreover, alternatives such as dry reforming of methane with CO_2 have attracted recent attention [26], but related emissions benefits are projected to be small [27]. In efforts to eliminate CO and CO_2 emissions from such reactions and reduce hydrogen production cost, research work has been shifting towards the direct decomposition of CH_4 as a more sustainable alternative [28]. Compared to alternative clean hydrogen production methods, solar methane pyrolysis has lower energy requirement [29], produces solid product of commercial interest [9], and potentially provides higher process efficiency [30].

The direct thermal decomposition of CH_4, also known as methane cracking, dissociation, or pyrolysis, is an endothermic reaction that breaks down CH_4 into solid carbon and H_2 gas in the following global dissociation reaction:

$$\mathrm{CH_4} \rightarrow \mathrm{C} + 2\mathrm{H_2} \quad (\Delta H^o = 75.6\ \mathrm{kJ/mol}) \tag{1.3}$$

This reaction proceeds at temperatures in excess of 1000 K and follows a more complex stepwise mechanism that includes several light hydrocarbons mainly acetylene (C_2H_2), ethylene (C_2H_4), and ethane (C_2H_6) as intermediaries [31]. A simplified stepwise dehydrogenation mechanism can be expressed by Eq. 1.4, where each step indicates the loss of H_2 [32].

$$2\mathrm{CH_4} \xrightarrow{-\mathrm{H_2}} \mathrm{C_2H_6} \xrightarrow{-\mathrm{H_2}} \mathrm{C_2H_4} \xrightarrow{-\mathrm{H_2}} \mathrm{C_2H_2} \xrightarrow{-\mathrm{H_2}} 2\mathrm{C} \tag{1.4}$$

The decomposition reaction requires temperatures in excess of 1300 K for satisfactory conversion rates, which improves by reductions in pressure per Le Chatelier's principle. Methane decomposition can be achieved using purely thermal means and additionally can be enhanced by the use of catalysts to increase reaction rates and decrease required process temperatures [33, 34]. Although methane pyrolysis has been extensively studied at atmospheric pressure, few experimental studies have considered the effect of vacuum-aided decomposition [35].

One of the key features of the direct decomposition of CH_4 is its potential for producing commercial grade carbon black (CB), carbon nanotubes (CNTs), and carbon nanofibers (CNFs) in addition to the hydrogen co-product [36]. These added value products are both a challenge and a key to making this process more economically feasible. For example, the cost of hydrogen production in the United States through SMR in 2018 is estimated to be \$1 per kg of H_2 with no carbon capture, utilization, and storage (CCUS) [14]. This cost can increase by more than 20% if CCUS is applied to reduce the carbon footprint of the process. For CH_4 decomposition however, the production cost of H_2 can be as high as twice of that obtained from SMR when hydrogen is the only sellable product considered [12]. If valuable commercial grade CB, CNTs, and CNFs were to be produced and sold, the cost of hydrogen will reduce to become more competitive than that obtained through SMR. This could additionally lead to CH_4 decomposition substituting for conventional carbon production processes, where the avoided greenhouse gas emissions are estimated to be 13.9 kg-equivalent CO_2/kg H_2 from both SMR and the furnace black process for producing CB [37]. This emission estimation assumes that the CH_4 decomposition process is entirely driven by a clean energy source, such as solar energy, and it is projected to be larger with the production of higher quality ordered nanocarbons that demand higher energy compared to CB.

1.2 Methane decomposition literature review

1.2.1 Catalytic methane decomposition

Catalytic thermal methane pyrolysis has been investigated in many prior studies to enhance process conversions and yields [38]. Catalysts can be generally classified as (i) carbonaceous or (ii) metal-based. Carbon catalysts are often preferred due to: (1) lower cost, (2) higher resistance to high temperatures, (3) higher tolerance to impurities normally present in natural gas feedstock, (4) absence of generated metal carbides, and (5) simpler separation to obtain a marketable solid carbon product

[39]. Muradov [40] and many others [38, 41, 42] have extensively studied the catalytic activities of different carbonaceous catalysts, including activated carbon (AC), CB, CNT, mesoporous carbon (MC), and graphite. Prior studies generally conclude that initial catalytic activity strongly correlates with specific surface area, and disordered carbons are generally more catalytic compared to ordered ones as a result of defects that potentially provide active sites for CH_4 decomposition [42]. In general, AC has the highest initial catalytic activity but rapidly deactivates due to pore blockage [43], while MC provides high catalytic activity but is significantly more stable to deactivation as a result of larger mesopores that accommodate more carbon deposition. In contrast, CB and graphite have lower and significantly lower initial activity, respectively, but are less prone to deactivation [38, 40].

However, carbonaceous catalysts generally produce amorphous carbon with different morphologies, exhibit much poorer catalytic activity compared to metal-based catalysts, and are susceptible to catalyst deactivation [44, 45]. To obtain higher value-added products (nano-structured carbons such as CNT and CNF) in addition to reducing operating temperatures, many studies have focused on metal-based catalysts, including Fe, Ni, Cu, Co, and noble metals [33, 46]. Despite significantly enhancing CH_4 pyrolysis kinetics and products, metal-based catalysts suffer from sintering, dissolution, rapid deactivation due to carbon deposition, and the need to separate the deposited carbon to obtain a metal-free product [38, 39]. The rapid deactivation issue inspired other promising techniques, such as reactors utilizing molten metal alloy catalysts [47, 48]. The molten forms reduce catalytic deactivation but the solid carbon product may suffer from significant metal impurities, which is estimated to be 8% in a prior study [47].

1.2.2 Solar methane decomposition

The advantages of using solar energy to drive methane decomposition are many. First, a direct solar reactor has the potential of using photo-thermal catalytic effects, thus improving chemical conversion in addition to product yields and qualities [49, 50]. Additionally, solar energy can be readily concentrated to achieve localized heating via optics to reduce high overall reactor operating temperatures that lead to significant thermal losses [51]. Furthermore, utilizing solar energy to drive the endothermic reaction to produce solid carbon and hydrogen gas avoids significant amounts of greenhouse gas emissions [37].

In solar methane pyrolysis, or more generally concentrated solar power application, reactors are classified under two types: (a) direct and (b) indirect solar reactors. In direct solar reactors, the reactant(s) flow is directly subjected to solar irradiance, and so an aperture with a transparent window is essential. In indirect solar reactors however, a cavity or tube is directly heated by solar irradiation and re-radiation, where it then exchanges thermal energy with the reactant(s) flow [52]. The latter type usually has a transparent window to allow solar irradiation input while keeping the cavity at an inert atmosphere to avoid its degradation at high temperatures. However, such a configuration is less efficient from a heat transfer perspective as it suffers from high radiative losses and depends on re-radiation and conduction/convection to heat the flow and primary reaction chamber [39, 53]. In contrast, indirect solar reactors for methane decomposition eliminate issues relating to the integrity of the transparent window mainly due to carbon deposition on its surface, which could potentially lead to local heating and failure [39]. In reactors with an aperture, the aperture size is designed to increase thermal efficiency based on a compromise between the amount of solar irradiation captured and re-radiation lost [51]. Since the methane decomposition process generally requires solar heating between 1200-2000 °C [54], the determination of an optimum aperture size can be of great importance.

Prior work on non-catalyzed solar methane pyrolysis requires relatively high operating temperatures (T) of 1600-2100 K for satisfactory methane conversions ($X_{\mathrm{CH_4}}$), as summarized in Table 1.1. The work by Dahl et al. [37] considers an indirect solar graphite tubular reactor for CH_4 decomposition at operating temperatures varying from 1500-2000 K in a solar furnace. With solar power varying from 2-9 kW, the authors obtained methane conversions in the range of 0.05-0.7 and concluded that complete dissociation, although expected, was not achieved due to heat transfer limitations. Importantly, their graphite reaction tube was porous to allow recycled H_2 to flow radially through the pores, mitigating carbon deposition along the tube walls that could lead to tube clogging. Another work by Rodat et al. [55] presents a pilot-scale indirect 50 kW solar reactor that consists of seven graphite tubular reaction zones. Testing was performed for a temperature range of 1608-1928 K and at pressures of 42-46 kPa with different inlet CH_4 mole fractions and flow rates. The most significant gas species present in the product stream were H_2, CH_4, C_2H_2, C_2H_4, and C_2H_6. However, C_2H_2 was much more abundant than the latter two, which were assumed to be negligible. For the gas composition, the study concluded that the amount of C_2H_2 decreased with increasing residence times (t_{res}). Despite methane conversions ranging from 0.71-1 [55], hydrogen and carbon yields only ranged from 0.57-0.88 and 0.41-0.63 due to significant C_2H_2 formation as a byproduct. In another study [32], a 10 kW indirect solar graphite tubular reactor was tested in a facility capable of delivering up to 9000 suns. Methane decomposition was tested at operating temperatures in the range of 1740-2073 K with residence times of 11-70 ms, leading to methane conversions in the range of 0.62-1 with high C_2H_2 molar concentrations. The work above does not utilize any catalysts, and hence requires high temperature operating conditions to achieve relatively high methane conversions.

Table 1.1: Summary of solar methane decomposition in prior literature.

Reactor	Catalyst	Solar Input	T [K]	t_{res} [ms]	X_{CH_4}	Ref.
Indirect	None[a]	2-9 kW	1500-2000	60-120	0.05-0.7	[37]
Indirect	None[a]	50 kW	1608-1928	37-71	0.72-1	[55]
Indirect	None[a]	$<$ 10 kW	1740-2073	11-70	0.62-1	[32]
Direct	CB[b]	$<$ 4.9 kW	1300-1600	1100-2400	0.4-0.99	[56]
Indirect	CB[c]	1 $\mathrm{kW_{abs}}$	1273-1473	120	0.58-0.98	[57]
Indirect	CB[b]	1 kW	1423-1673	38-140	0.08-0.9	[53]
Direct	CB & metal[d]	$<$ 3000 $\mathrm{kW/m^2}$	923-1223	-	0.43-0.67	[36]

[a]Graphite reactor; [b]Entrained/Flow-seeded; [c]Packed-bed; [d]Rotary-bed; abs: absorbed

Other solar methane pyrolysis studies have considered the potential of thermo-catalytic processes to decrease operating temperatures to 923-1600 K (see Table 1.1). In a study by Maag et al. [56], a 5 kW carbon-seeded particle-flow direct solar steel alloy reactor was presented for CH_4 decomposition using µm-sized carbon particles in a solar furnace with concentrations up to 1720 suns. The use of carbon-seeded flow was primarily to enhance the absorption and thermal efficiencies of the reactor (as CH_4 is transparent) and increase the CH_4 catalytic decomposition nucleation sites. In an effort to eliminate carbon deposition on the window and reactor walls, the authors used argon flow directed at the window and radial flow inlet nozzles with a conical axial outlet. Methane conversions in the range of 0.4-0.99 were obtained under operating temperatures of 1300-1600 K with residence times of 1.2-2.4 s. Another work by Abanades et al. [57] presented an indirect solar thermo-catalytic process using carbon black powder catalysts in a graphite cavity receiver with packed-bed alumina tubular reactor operating within a temperature range of 1273-1473 K. The reactor operates in a semi-continuous mode due to the need for catalyst replacement and is tested in a solar furnace facility capable of delivering a maximum solar irradiance of 16 MW/m^2. With a significantly longer residence time of 120 ms, as compared to the work by Rodat et al. [55], and the use of carbon catalysts, reported methane conversions ranged from 0.58-0.98 with most of the outlet feed being hydrogen and minimal C_2H_2 as their main secondary byproduct. The authors reported prompt catalyst deactivation after approximately 1500 s, after which the deactivated catalyst was combusted and replaced with fresh carbon catalyst for further experimentation. In another study by Abanades et al. [53], a 1 kW indirect solar entrained-flow tubular alumina reactor with carbon black nanoparticles and a particle feeding system was presented. Methane conversions and hydrogen yields in the range of 0.08-0.9 and 0-0.8 were obtained with C_2H_2 as a significant byproduct for operating temperatures of 1423-1673 K with residence times varying within 38-140 ms. The authors concluded that the CB entrained-flow did not lead to noticeable enhancement to the reactor's overall heat transfer and methane conversion results, which was primarily due to catalytic and surface area enhancements as a result of the added catalyst not outweighing the additional thermal load of catalyst heating under their configuration and operating conditions.

A different work by Pinilla et al. [36] investigated the solar thermo-catalytic decomposition of CH_4 using metal-based and carbon-based catalysts, namely: (a) Ni-AL_2O_3 , (b) Fe-AL_2O_3, and (c) carbon black (Cabot BP2000). The authors used a direct solar rotary kiln/bed reactor which was heated using a solar furnace with a concentration factor of 3000 suns and a 20 cm diameter beam. Good methane conversions were achieved with moderate temperatures using their configuration, with maximum methane conversions of: (a) 0.55 for Ni-AL_2O_3 at 923 K, (b) 0.67 for Fe-AL_2O_3 at 1073 K, and (c) 0.43 for carbon black at 1223 K. Additionally, methane conversion occurred with no or minimal byproducts (such as C_2H_2) under unknown residence times. The authors noted however that metallic catalysts suffer from catalyst sintering and deactivation as a result of encapsulation [36].

Two of the major challenges for all solar methane decomposition work summarized earlier are: (a) significant carbon deposition in reactors that leads to clogging and process interruptions, and (b) the carbon product is always carbon black and thus is of relatively low economic value when compared to its counterparts (e.g., CNFs). The only exception was with the use of metal-based catalysts [36], where CNFs and multi-walled CNTs were produced. These challenges are further discussed in the following sections.

1.2.3 Solar methane decomposition challenges

Several challenges exist for applications utilizing concentrated solar power, such as those pertaining to the sun's transient nature [58]. In this section, some of these challenges are briefly discussed with a primary focus on solar methane pyrolysis.

Value of carbon product

The structure and quality of the carbon product obtained through methane decomposition contributes significantly towards the process economics and competitiveness compared to SMR [22, 54]. It can even lead to hydrogen production at "zero cost" with a high quality carbon product [12, 39]. The product obtained in all the previous solar CH_4 decomposition (non-catalyzed or carbon-catalyzed) processes is always carbon black and hence amorphous in structure with relatively low economic value. For example, the carbon product in the work by Rodat et al. [55, 59] had a high D/G Raman peak ratios of 1.6 (the lower the ratio, the better the carbon quality) with the absence of a 2D peak, which indicates that the carbon product is of relatively low quality. The primary particle sizes were inconsistent, but the fractal structure of the product was similar to commercial conductive grade carbon black powders. Additionally, the carbon product obtained by Pinilla et al. [36] with their carbon catalyst showed no distinct X-ray diffraction (XRD) peaks, which is a direct indication to its amorphous structure. Although high-quality carbon product with distinct XRD peaks was obtained for their metal-based catalysts [36], the drawbacks of sintering and fast deactivation in addition to the need to separate the carbon product from the catalyst to obtain a metal-free product create a major challenge. The deterioration of the carbon product quality upon separation is unknown. Although no quantitative product characteristics were provided in other literature [32, 37, 53, 56, 57], the carbon product was determined to be amorphous carbon black. Therefore, research should focus on effectively producing higher-quality solid carbon forms to drive process economics in favor of methane pyrolysis.

Handling of carbon product and deposition

In CH_4 decomposition processes, the carbon product is the key to hydrogen production at very competitive costs, as discussed above, but yet it creates a major difficulty. This difficulty is due to challenges of: (a) unconfined carbon deposition and reactor clogging, and (b) ineffective separation and collection of the carbon product. Unconfined carbon deposition can lead to significant process interruptions, where the process may need to be terminated an hour into processing as a result of progressive tube clogging [55]. In the work by Abanades et al. [60], tubes were completely blocked during their testing. Therefore, the pressure in the product stream should be carefully monitored to detect tube blocking as a result of thermophoretic carbon deposition as also reported by Rodat et al. [32], where 34% of their carbon content in the methane inlet flow deposited in the reactor tubes. Additionally, window carbon deposition requires extra elimination measures [56, 61], as previously discussed.

The separation of the solid carbon product from a non-carbon catalyst for collection and upon catalyst deactivation is also a major challenge with an unknown penalty on the degradation of the carbon quality upon separation [36]. An inefficient approach to overcome this issue is by combusting the carbon product for regenerating the catalyst, producing CO_2 upon combustion [36, 55, 62]. A different possible approach is to use the carbon product in gasification with water vapour to produce more hydrogen [12, 63, 64]. However, in attempts to overcome the aforementioned challenges, research on CH_4 decomposition and conversion has been investigated using other approaches. An innovative approach to separating the carbon product is through the use of molten metal reactor systems [47, 48]. For example, Upham et al. [47] have used a CH_4 metal catalyst (Ni) dissolved in a relatively low melting temperature inactive metal (Bi) in a 1.1 meter bubble column reactor. The motivations behind using a molten metal alloy catalyst were to: (a) avoid deactivation of the metal catalyst due to carbon deposition, (b) enhance heat transfer to the CH_4 gas medium, and (c) obtain a relatively effective carbon removal method. The solid carbon product has a lower density and thus floats to the surface of the molten metal, where it can then be swept and collected [47]. The authors achieved a methane conversion of 95% at an operating temperature of 1338 K. However, the carbon content in their product was only approximately 92%, with metal impurities present.

Others researchers have used a different path for methane conversion by confining or avoiding any carbon product. For example, a recent work by Kimura et al. [65] proposed solar CH_4 decomposition via a two-step conversion process to address some of the challenges identified in other literature, namely carbon deposition and soot formation on reactor walls and windows. A totally different non-solar approach was presented by Guo et al. [66], where the complete dehydrogenation of CH_4 was avoided by using a lattice-confined single iron sites catalyst that only activates the first C-H bond in CH_4, thus producing hydrogen, ethylene, and aromatics (benzene and naphthalene) with no solid carbon product. The motivation behind their work was to avoid the formation and deposition of solid carbon along with its challenges and the lower value of coke (the author's assumption of the carbon product form). Though their process temperatures varied from 1223-1363 K, the catalyst production process involved an energy intensive process requiring temperatures as high as 2000 K [66]. Despite effectiveness of such methods in eliminating challenges related to solid carbon production and deposition, these approaches neglect a key product in driving the cost of clean hydrogen production down.

Heat transfer and efficiency

One of the technical challenges in solar methane pyrolysis is obtaining sufficiently high process conversions and production rates with high yields that provide high-purity products [29]. This challenge is due to methane gas being transparent to solar irradiation, which places a higher burden on reactor design considerations. As previously discussed, several approaches aimed at increasing the surface area available for methane pyrolysis using carbon particles were investigated. Approaches that introduce fresh particles with the flow (entrained/flow-seeded reactors) [53, 56] suffer from additional thermal loads of particles introduced into the reactor at room temperature, which often do not compensate for the added benefits due to increased reaction surface areas. From this perspective, packed-bed solar reactors [36, 57] are usually more efficient, as carbon particles remain within the reaction zone during methane pyrolysis.

Another important considerations are the thermal and optical designs of solar reactors. A prior work has shown that approximately 60% of the power input into a solar receiver was lost through reradiation [51]. In a different study on solar catalytic methane dry reforming through a catalytic bed [67], the authors estimated process efficiencies to be less than 1% when accounting for total irradiation intercepted by the solar reactor. Process efficiencies significantly increased to almost 25% when only accounting for irradiation intercepted by the reactor bed. These two examples emphasize the importance of optimized solar reactor designs in overcoming challenges pertaining to poor heat transfer and process efficiency.

1.3 Research scope and objectives

The main objectives of this research include developing, testing, characterizing, optimizing, and scaling-up a novel solar-thermal methane decomposition process in a laboratory setting. In addition to developing and studying the process, work includes designing and building necessary equipment and capabilities that allow obtaining complete, reproducible results that well characterize the developed solar decomposition process, which comprises designing and building a solar simulator, solar reactor, product monitoring systems, and other auxiliaries from scratch. The CH_4 pyrolysis process should provide a viable and desirable alternative to current hydrogen and/or solid carbon production methods, such as SMR. The process should additionally be driven by a clean energy source, more specifically concentrated solar power, with net-zero CO_2 emissions. Furthermore, the developed CH_4 decomposition process should mitigate issues and challenges reported in prior methane decomposition processes, which include reactor clogging, low product yields/rates, and production of relatively low-quality carbon. Finally, the process should be readily amenable to scale-up, as should be demonstrated by this work.

1.4 Document outline

This document is divided into eight chapters, including this introductory chapter. Each chapter is dedicated to presenting certain information, concepts, or studies that act as building blocks for understanding the underlying process and achieving the main objectives of this research work. The dissertation outline is as follows:

- **Chapter 2**: In this chapter, an in-house custom-designed and built high flux solar simulator is presented. The solar simulator provides a controllable source of irradiation that closely resembles the solar spectrum to allow for accurate laboratory-scale testing of technologies. The solar simulator is characterized using a well established direct measurement technique in addition to a simple and novel inverse characterization method, which has been experimentally validated. Characterization of the solar simulator's output provides key measures for quantifying process efficiencies, and for providing guidance on scaling-up the process under actual solar irradiation.
- **Chapter 3**: In this chapter, the experimental setup and auxiliaries custom-designed and built for this work are introduced and thoroughly presented. Process monitoring and characterization systems, whether developed in this work or were readily available, utilized in subsequent chapters are further introduced and discussed along with adequate

background of technical information and calibrations, whenever applicable. This chapter aims to develop a solid basis and reference for following chapters regarding details related to methodology and experimental equipment used.

- **Chapter 4**: In this chapter, an initial investigation of solar-thermal methane pyrolysis through a fibrous carbon medium in a small-scale reactor is performed and presented. Methane decomposition occurs locally within a porous substrate placed at the solar simulator's focal plane, which provides efficient and effective decomposition of the methane feed into hydrogen-rich gas and high-quality graphitic product without any unconfined carbon deposition issues. This chapter focuses on defining and quantifying process and product characterization metrics that are used to critically evaluate the process prior to conducting a parametric study.

- **Chapter 5**: In this chapter, the solar-thermal methane decomposition process through fibrous carbon media is tested under different operating conditions to thoroughly characterize the process performance and products quality. The different operating conditions considered include various methane inlet flow rates, solar concentrations and powers, pressures, and fibrous medium thicknesses. Process conversions, yields, efficiencies, and product qualities are reported and discussed.

- **Chapter 6**: In this chapter, a scalable route to continuous solar-thermal methane pyrolysis is investigated in a large-scale solar reactor. The route employs a continuous roll-to-roll mode of operation to supply fresh fibrous medium after significant carbon deposition and to mitigate process performance decline with time. The efficacy of the roll-to-roll approach for methane decomposition is evaluated, and a parametric variation of operating conditions is presented.

- **Chapter 7**: In this chapter, an in-house developed and validated ray tracing code is used to optimize the optical design of the large-scale solar reactor and roll-to-roll solar-thermal methane decomposition process. The optical optimization is achieved by using a conical secondary concentrator that further increases solar concentration ratios attained within the fibrous reaction zone, allowing for more effective radiative heat transfer. Dimensions of the secondary concentrator were optimized based on numerical simulations, and the enhancement in resulting solar concentrations and process performance are experimentally evaluated through a series of tests.

- **Chapter 8**: In this chapter, initial observations and results of photocatalytic contributions to the present solar-thermal methane decomposition process are presented and briefly discussed. This discussion aims to initially explain the high graphite deposition rates observed in this work, and guide future work investigating the presence of photocatalytic effects. Additionally, initial results obtained using alternative starting materials to produce various carbon composites are briefly presented. The chapter then concludes this dissertation with a brief discussion on opportunities for future work.

Chapter 2:
High Flux Solar Simulator[1]

In this chapter, a custom-designed and built high flux solar simulator is presented and its irradiation output is thoroughly characterized [68]. The solar simulator provides a mean to experimentally simulate concentrated solar irradiation in a laboratory setting to allow testing the solar-thermal methane decomposition process introduced in Chapter 4. Proper characterization of the solar simulator's output provides key measures for quantifying process efficiencies, and for providing guidance on scaling-up the process under actual concentrated solar irradiation.

2.1 Introduction

High flux solar simulators (HFSSs) provide highly controllable and adjustable radiation that mimics the sun's spectral irradiance [69]. They provide a platform to conduct a wide range of experiments, which include producing solar fuels and commodities [9, 70], testing photovoltaic devices [71], processing materials under high irradiation fluxes [72], and characterizing thermal properties at high temperatures [73]. A HFSS consists of a single or multiple high-power lamps as the

---

[1] All or some portions of this chapter contributed to paper by M. Abuseada, A. Alghfeli, and T. S. Fisher, titled Indirect inverse flux mapping of a concentrated solar source using infrared imaging, published in Review of Scientific Instruments 93 (2022), 073101.

radiative source, where each is placed within its own truncated reflector, usually ellipsoidal, to concentrate radiation onto a single focal plane or target. The most common type of lamp used in prior work is the xenon short arc, while metal halide and argon lamps are alternatives [74]. By varying the current input to the lamps, their arrangement, and focus, the output power and distribution from a HFSS can be tailored to fit a variety of experimental needs.

As interest in using HFSSs for research grows, developing simple, accurate, and inexpensive strategies to characterize their output irradiation is warranted. This characterization not only indicates the thermal performance of the HFSS, but also provides thermal input parameters required for energy balance and efficiency calculations [75]. The current state-of-the-art method used for characterizing HFSSs involves an indirect grayscale heat flux mapping approach with minor variations in the experimental methodology and equipment incorporated [76–79]. Briefly, a heat flux gauge (HFG) [76, 80, 81] or equivalent [78] is used to calibrate a CCD or CMOS grayscale camera correlated to images of a water-cooled Lambertian (diffusely reflecting) target's illuminated front face with heat flux measurements. Once the grayscale camera is calibrated, the light source can be aligned, optimized, and characterized across different planes using a two or three-dimensional sliding stage. In the usual manner, the HFG measurements and grayscale images are obtained using two different setups. However, slight misalignment can occur during the transition between setups and can lead to changes in the peak heat flux values as high as 6% [82].

To eliminate the setup transition and to reduce characterization time, a smaller uncooled 3 mm thick movable Lambertian target can be used to cover the HFG mounted at the center of a Lambertian target [83]. However, the uncooled target is subject to deterioration under high irradiation, which can significantly alter the grayscale camera correlation. Alternatively, the target can be moved away from its center to capture a smaller, but large enough, uninterrupted continuous area, and post-processing tools can be used to create a larger flux map by superposition [76]. The linear relationship between heat flux and grayscale values in addition to the inverse grayscale method's accuracy in instantly mapping the heat flux distribution makes it the most common in literature. However, any indirect grayscale mapping method suffers from high cost due to requiring a separately dedicated experimental configuration and additional expensive and uncommon thermal equipment (e.g., water-cooled Lambertian target and grayscale camera) to characterize and regularly monitor HFSS performance.

Apart from indirect grayscale heat flux mapping, researchers have attempted to characterize HFSSs using other techniques. For example, sources have been characterized directly using a thermogage [84] or a thermopile flux sensor [85] to measure heat flux values at discrete points in a plane using sliding stages that scan the area of interest to generate a heat flux map. This approach potentially provides measurements with a higher accuracy than the indirect grayscale mapping technique because it avoids calibration errors associated with additional equipment (mainly the grayscale camera), such as perspective shape distortion errors [76, 78]. However, the direct method is time-consuming, especially for properly aligning the HFSS, and it provides a low map resolution as a result of the discrete captured locations.

A comparison among three different HFSS characterization techniques was performed by Garrido et al. [86]: a radiometer based on a thermopile sensor, a large flat-plate calorimeter to obtain total power, and the indirect grayscale heat flux mapping method. Through uncertainty analysis, the authors concluded that the indirect grayscale mapping method was not appropriate for characterizing the output from their Fresnel lens-based HFSS, and that the approach of coupling radiometer and calorimeter measurements improves characterization accuracy. Alternatively, a HFSS was characterized with an inexpensive experimental setup by obtaining transient temperature maps of a target placed in the plane of interest to determine the corresponding heat flux map via an inverse method [87]. Temperatures of the 0.8 mm thick stainless steel target were recorded using an infrared (IR) camera placed off the target's optical axis and facing its black painted front (illuminated) or back side, depending on the heat flux magnitudes (due to method limitations). Validation of the transient inverse method was presented away from the focal plane with relatively low heat flux values (up to 7 kW/m^2) to avoid deterioration of the front side's black paint. To map higher heat flux distributions at the focal plane, transient temperatures of the target's rear side were monitored up to 300 °C with a peak flux of 1.3 MW/m^2. However, solving an inverse transient problem that additionally includes an unaccounted temperature gradient between the front and back surfaces can induce significant errors.

The determination of heat flux, thermal properties, and volumetric heat generation can be realized by solving an inverse problem with different minimization algorithms. An iterative minimization solver based on the Broyden–Fletcher–Goldfarb–Shanno (BFGS) algorithm with a simple step method was used to compute temperature-dependent thermal conductivity and specific heat from thermocouple measurements [88]. Others used methods of steepest descent and conjugate gradients to characterize heat transfer parameters such as surface/boundary heat flux [89, 90], convection coefficient [90], body surface temperature [90], and volumetric heat generation [91]. Non-iterative approaches were also introduced to determine thermal properties either by employing an integral method [92, 93], or by transforming the heat transfer differential governing equations into a linear matrix [94]. For solar systems, the heat flux distribution has been mapped by solving an inverse problem with a sensitivity matrix methodology [95, 96], golden section search method [87], and Levenberg-Marquardt algorithm [97] from IR camera temperature measurements. Although, generally, in-house numerical models have been developed for inverse problems, the incorporation of commercial software such as ANSYS is also possible [96, 97].

Using any of the aforementioned techniques, the heat flux distribution can be characterized at the focal plane but, due to practical considerations, the flux cannot be determined under the actual conditions of intended experimentation. Such example includes irradiation of a substrate in a reactor/vacuum chamber, which is the case of the present work as introduced in Chapter 3 [9]. Although numerical models such as Monte Carlo ray tracing (MCRT) can be fitted to experimental measurements of the HFSS and used to compensate for additional components, such as quartz windows and reactor cavity [51, 98], significant errors may arise. Therefore, in this chapter, the heat flux from a 10 kW_e xenon short arc lamp HFSS is characterized inside a vacuum chamber using an inverse mapping technique with IR thermography. A readily obtainable sample of known properties is placed inside the vacuum chamber and used as a radiometer to measure the irradiation distribution on a target under similar conditions. In contrast to prior literature, the camera is placed normal to the target to avoid errors associated with off-axis placement, and steady-state temperature measurements are used to increase the robustness of the inverse methodology. Additionally, the methodology targets characterizing solar sources with moderate to high heat flux distributions as compared to limited irradiation concentration in prior work [87], and with the potential of facile in-house and routine calibration (without requiring a sample of well-known properties) [73]. The accuracy of results obtained by this inverse technique is evaluated, and results are compared to two other independent methods: measurements recorded using a HFG and simulation results from a validated MCRT in-house code.

2.2 Experimental setup and procedure

2.2.1 High flux solar simulator

The custom-designed and built HFSS assembly shown in Fig. 2.1 encompasses a 10 kW_e xenon short arc lamp (Superior Quartz, SQP-SX100003) aligned at the first focal point of a truncated ellipsoidal reflector (Optiforms, E1023F). The aluminum reflector has two focal points at 7.49 and 102.3 cm from the ellipsoid's vertex and is coated with silver to enhance its reflective properties. The reflector is truncated at a diameter of 10.0 cm to allow for lamp placement at the first focal point without interference, and the reflector ends at a diameter of 38.7 cm. The HFSS is also equipped with a variable power supply to control the output power of the lamp by varying its supply current over the range of 100-200 A. The assembly is equipped with intake and exhaust fans to maintain proper cooling of the lamp. An IR temperature sensor (OMEGA, OS151-HT-K) is used to monitor the cathode's end seal temperature and to ensure that it remains below 200 °C. Finally, the HFSS is equipped with a motorized douser to provide an additional degree of control over its output (e.g., cyclic or attenuated solar irradiation), and the solar simulator's operation is fully automated via LabVIEW. An overview of the solar simulator and its main components in the horizontal orientation is shown in Fig. 2.1a; the HFSS can also be rotated to a beam-down configuration, as presented in Chapter 6.

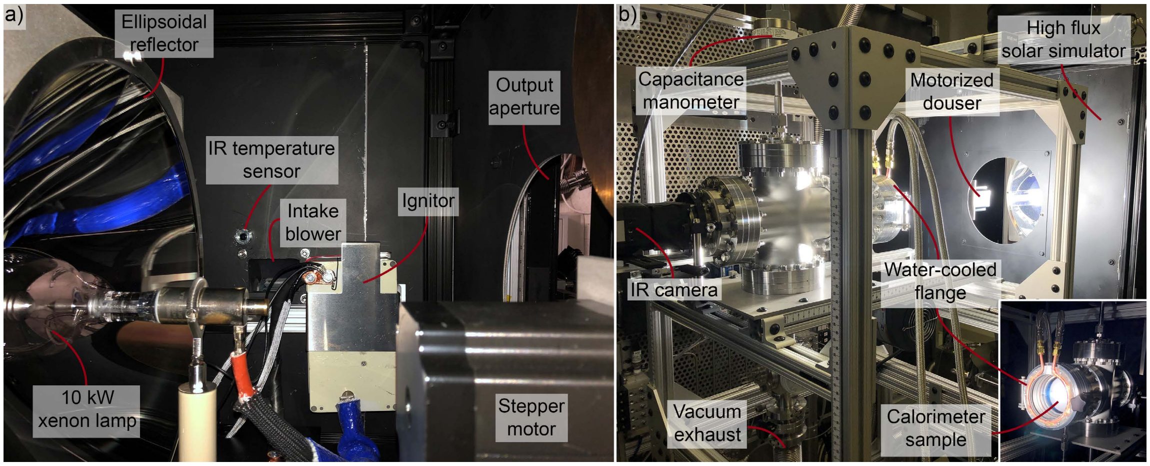

Figure 2.1: (a) Overview of the solar simulator and its main components. (b) Experimental setup used in characterizing the solar simulator, where the figure inset shows front view of vacuum chamber with target.

2.2.2 Radiometer and temperature measurements

The experimental setup, shown in Fig. 2.1b, consists of a stainless steel cylindrical vacuum chamber with an inner diameter of 9.7 cm (6” CF flange) and a 10.2 cm aperture with a fused quartz window. An additional water-cooled flange was added to maintain the window and vacuum chamber at relatively low temperatures. A titanium mount and thin graphite disk target for inverse characterization of the HFSS at different powers (supply currents) are placed into the vacuum chamber at the HFSS’s focal plane (7 cm from chamber’s front flange). A 0.8 mm thick isotropic graphite disk (Entegris/Poco Graphite, TM-grade) that is 8.9 cm in diameter was used as the target for characterization and is hereafter referred to as the ‘radiometer’. The vacuum chamber has a capacitance manometer port to monitor the chamber’s vacuum pressure and a zinc selenide (ZnSe) viewport for monitoring the radiometer’s back side temperature using IR thermography. A high-resolution science-grade longwave infrared camera (FLIR, A655sc) monitors and measures the temperature of the radiometer. The camera has a resolution of

640 x 480 pixels, 16-bit dynamic range, accuracy of ± 2% over its full scale, spectral range of 7.5-14.0 µm, and can measure temperatures up to 2000 °C. During camera calibration to account for the ZnSe window's transmissivity (τ_{IR}), a flat transmissivity value of 0.72 from 7.5 to 10 µm was measured and validated across a reference temperature transducer to be appropriate for IR temperature monitoring.

2.2.3 Spectral characteristics

The spectral distribution output from a xenon short arc lamp has been measured in many prior studies, and it best simulates the air mass 1.5 solar standard spectrum [71, 99]. Here, the spectral distribution of the HFSS is also presented but with a focus on its variation in relation to output power (controlled by varying the supplied current from 100 to 200 A) since such measurements have not been reported elsewhere. This characterization was performed using an imaging spectrometer (Horiba, iHR 550) with a SynapsePlus CCD camera sensor and a blazed holographic grating of 1200 gr/mm to obtain measurements between 0.4-1 µm. The CCD camera is thermoelectrically cooled to -95 °C and has an active spectral range of 0.2-1.1 µm. The normalized spectral distribution output from the HFSS is shown in Fig. 2.2 at different supply currents, illustrating the variation of the spectral output under different operating conditions. As shown in Fig. 2.2, as the power output of the xenon short arc decreases from its maximum, the spectral output deviates in excess of 5% within the range of 450-800 nm, and all spectral line peaks become more pronounced; uncertainty from the imaging spectrometer contributes negligibly to measurement deviations, but temporal spectral variations in the lamp's output provide normalized spectra repetitiveness within 2%. Such spectral features are not expected to be significant in most applications but might be important to consider in testing spectrally sensitive photovoltaic or photocatalytic systems.

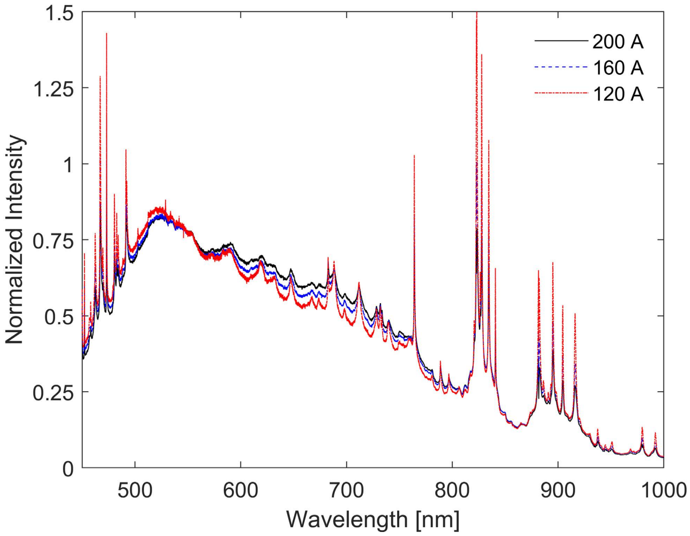

Figure 2.2: Spectral distribution output measured from the HFSS at different powers (supply currents) and normalized by area under the curves.

2.2.4 Direct heat flux mapping

The heat flux distribution from the HFSS was characterized directly using a HFG in the experimental setup shown in Fig. 2.3. Measurements were obtained at discrete points on the focal plane outside the vacuum chamber, without a quartz window, and at different operating lamp powers (supply currents). The water-cooled Gardon type gauge (Vatell Corporation, TG1000-0) is calibrated as-received and has an active gauge area with 1 mm diameter. The HFG is coated with colloidal graphite and can measure heat flux values up to approximately 5 MW/m^2 with a linear output voltage of 0-10 mV and an accuracy of ±3%, as reported by the manufacturer. This type of HFG has been employed in several prior studies [77, 80, 81] and its measurements are used here to validate the present inverse characterization method. The HFG was mounted on and insulated from a water-cooled alumina-coated (white) aluminum target that supports the gauge and intercepts the concentrated radiation from the HFSS. The target's water-cooling and alumina coating to diffusely reflect most of the intercepted irradiation prevent heating of the target to ensure that minimal heat transfer occurs between the target and insulated housing of the HFG. The target is then mounted on a three-dimensional linear stage to obtain heat flux measurements at various discrete points.

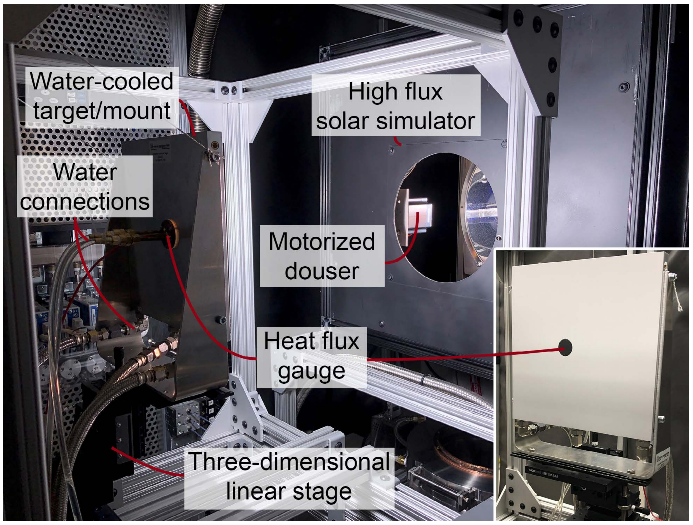

Figure 2.3: Experimental setup for characterizing the HFSS using a HFG for validation of the inverse heat flux mapping method.

Prior work has shown that the manufacturer's calibration for the type of HFG used in the present study may overestimate heat flux measurements by up to 30% due to a mismatch between the solar spectrum and that of the blackbody radiation used for calibration when the blackbody temperature is 1123 K (corresponding heat flux of 92 kW/m^2), as the spectral absorptivity of the HFG's colloidal graphite coating changes significantly with wavelength [79, 100]. In contrast, the present HFG has been factory-calibrated with incident heat flux values up to 2 MW/m^2 (corresponding maximum temperature of 2440 K), where the factory-calibrated sensor emissivity/absorptivity is reported as 0.82. By using spectral absorptance measurements of the colloidal graphite coating presented in prior work [100], the corresponding total absorptivity is estimated to be 0.66 for irradiation from a blackbody at 1123 K, 0.75 for a blackbody at 2440 K, and 0.84 for solar irradiation (blackbody at 5800 K). The preceding results indeed match well with prior conclusions indicating that a calibration temperature of 1123 K would overestimate solar irradiation (blackbody at 5800 K) by approximately 30% [79, 100]; from total absorptivity results indicated here, the overestimation is determined to be $(0.84/0.66 - 1) = 27\%$. In contrast, a calibration temperature of 2440 K leads to an overestimation of only $(0.84/0.75 - 1) = 12\%$. Based on the foregoing discussion and acknowledging possible variations in spectral emissivity among different surface conditions, the highest spectral absorptivity value of 0.88 at approximately 0.5 µm [100] instead of the estimated solar total absorptivity value of 0.84 is used to estimate an additional conservative uncertainty contribution towards measurements obtained by the HFG. Hence, the mismatch between the maximum spectral absorptivity and that of the sensor calibration induces an additional uncertainty in the heat flux measurements of $\pm 7\%$.

Prior literature has shown that xenon arc lamps undergo an initial transient period before reaching a long-term temporal quasi-steady state. This transient period is 10-20 minutes for lamps of different sizes [76, 77, 98] and is characterized here in Fig. 2.4 for the initial 20 minutes. Instantaneous flux measurements were normalized by their average steady-state values 60 minutes after lamp ignition. As shown in Fig. 2.4, the HFSS requires approximately 15 minutes to reach 98% of its steady-state heat flux distribution. As such, all experimental work presented in this research was conducted after this initial transient period. The HFG was then used to map the heat flux distribution at the focal plane in discrete radial increments of 1 mm along the main axes starting from the center and up to a total distance of 27 mm at different supplied currents to the lamp (100-200 A). For data acquisition and processing, the HFG was connected to a National Instruments PXI system (PXIe-1092) and its thermocouple module (PXIe-4353). Accounting for the manufacturer's calibration uncertainty of $\pm 3\%$, sensor absorptivity uncertainty of $\pm 7\%$, and variations in time and radially averaged measurements uncertainty of $\pm 2.5\%$, an overall uncertainty of approximately $\pm 8\%$ is estimated for the heat flux measurements. This overall uncertainty is consistent with recent work [77].

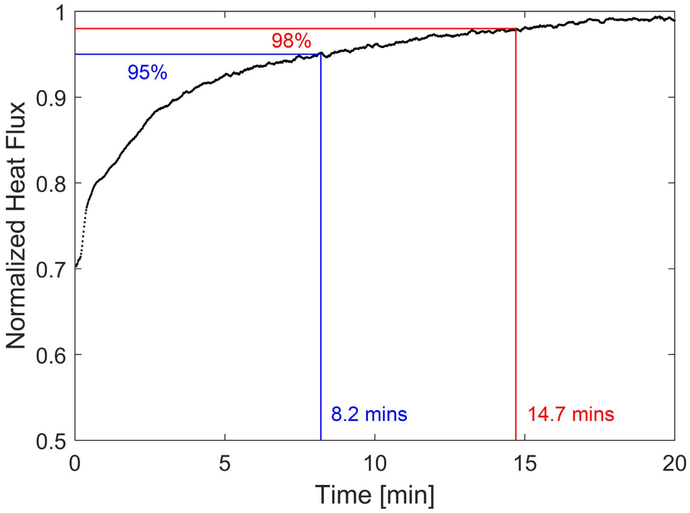

Figure 2.4: Transient nature of the heat flux output from the HFSS.

2.3 Heat flux methodology

The heat flux distribution from the HFSS is determined by solving an inverse problem that uses steady-state spatial temperature measurements from an IR camera. Because of symmetry in the heat flux output of a properly aligned HFSS and vacuum chamber, experimental temperature measurements are radially averaged to provide 1D radial temperatures along the graphite radiometer; this averaging significantly reduces measurement noise. Then, parameters of a predefined heat flux function are estimated by implementing a minimization algorithm (Nelder-Mead) to a 2D numerical heat transfer model. The Nelder-Mead algorithm is a direct search method to solve unconstrained optimization problems without requiring a function gradient, where a simplex shape structure with $(n+1)$ vertices is used to minimize the objective function of n input dimensions [101]. The shape structure points are evaluated, and a selection rule is used to move these points relative to their outputs based on any of the following operations: reflection, expansion, contraction, and shrinkage [102]. Thus, the minimization algorithm is solved iteratively until convergence is achieved.

To assess the accuracy of the inverse technique in determining the heat flux inside the vacuum chamber, its results are compared to measurements obtained directly using the HFG outside the chamber and by utilizing a validated MCRT model, where both methods are completely independent from the inverse mapping method. The MCRT model is used to further verify measurements from the HFG and to draw conclusions on possible deviations between heat flux distributions inside and outside of the vacuum chamber. Importantly for validation of the inverse mapping technique, heat flux results obtained outside the vacuum chamber using the HFG were multiplied by a factor of 0.92 to compensate for the quartz window's solar transmissivity ($\tau_{\mathrm{qrt}} = 0.92 \pm 0.02$).

2.3.1 Monte Carlo ray tracing

MCRT is an accurate method for modeling radiative heat transfer and, more generally, optical systems [103, 104]. An experimentally validated in-house MCRT model of a HFSS was previously developed and presented in prior work [82, 105]. The model's methodology is thoroughly outlined in prior work [82], and hence it is not be described here for brevity. In this work, the 3D MCRT model is used to predict the heat flux distribution, with minor modifications reflecting differences in the HFSS configuration, to further verify the accuracy of HFG measurements. The MCRT model assumes the xenon arc lamp to be an isotropic emitting composite volume that consists of a hemisphere attached to a cylinder. Both the hemisphere and cylinder have diameters of 2 mm and emit power at a ratio of 0.23:0.77, the cylinder is 10 mm long, and the composite shape is positioned within the truncated reflector (reflectivity assumed to be 0.9) with the hemisphere's center coinciding with the reflector's theoretical focal point [105].

Although peak flux values obtained from the original model were consistent with experimentally measured heat flux values using the HFG, the general distribution was slightly changed due to differences in the HFSS configuration. To account for such differences, the electrical power conversion efficiency (η_{el}) and the surface specular error (θ_{sp}), which is a deviating zenith angle with a Gaussian distribution around zero, were treated as free parameters to allow for better fits to the experimental HFG measurements at the focal plane. These two parameters were chosen, as they do not change the inherent physics of the validated MCRT model, but rather provide fitting of parameters that could vary between different HFSSs; η_{el} depends on system connections and condition of the lamp, while θ_{sp} depends on manufacturing tolerances associated with the ellipsoidal reflector geometry and its surface condition. Upon fitting these parameters to the heat flux distribution obtained by the HFG at the focal plane, η_{el} and θ_{sp} changed from 50% and 5 mrad to 59% and 6.75 mrad.

2.3.2 Inverse method

Inverse problems are generally ill-posed and lack unique solutions, unlike forward well-posed problems [106]. They are usually subject to issues such as solution existence, uniqueness, and instability to small noises or perturbations [107] that become more severe with respect to the ratio between the number of solution unknowns and known measurements. Therefore, an effective approach in characterizing the HFSS is to adopt an inverse problem and reduce the number of solution unknowns by transforming the problem into a parameter estimation problem to yield a stable, well-conditioned problem. This approach is performed here by applying constraints on the heat flux distribution based on expected trends from the HFSS.

Expected trends from the HFSS

Due to the shape of the HFSS's ellipsoidal reflector, the heat flux distribution output at the focal plane strongly resembles a Gaussian or Lorentzian distribution [76, 108, 109]. The nature of the distribution being Lorentzian versus Gaussian depends on the optical alignment of the system, any optical distorters such as a quartz window, and potentially the lamp power. To encompass the nature of both profiles, the heat flux distribution (q''_{sol}) is represented using a weighted summation of both profiles as:

$$q''_{\mathrm{sol}}(r) = A_{\mathrm{sol}} \left[\frac{(1-\alpha_{\mathrm{Lor}})}{\sigma_{\mathrm{Gau}}\sqrt{2\pi}} \exp\left(\frac{-r^2}{2\sigma_{\mathrm{Gau}}^2} \right) + \frac{\alpha_{\mathrm{Lor}}}{\pi} \left(\frac{\sigma_{\mathrm{Lor}}}{r^2 + \sigma_{\mathrm{Lor}}^2} \right) \right] \tag{2.1}$$

where α_{Lor} is the weighing parameter and ranges from 0 to 1, σ_{Lor} is the half width at half maximum of the Lorentzian distribution, σ_{Gau} is the standard deviation of the Gaussian distribution, A_{sol} is the amplitude parameter adjusting both profiles, and r is the radial distance from the center. The assumed profile can be valid under different conditions, such as with a quartz window or away from the focal plane. Additionally, another trend incorporated in the inverse problem solution here is the linear relationship that exists between the heat flux distribution and HFSS current supply [76, 110].

Numerical modeling

A steady-state heat transfer model was developed to estimate the fitting parameters of the heat flux distribution (Eq. 2.1) by solving an inverse problem using the IR camera temperature measurements. Because the system and radiation source considered here are both symmetric in cylindrical coordinates, the model can be treated as 2D without loss of accuracy. A photograph of the radiometer and an illustration of the control volume considered later for the heat transfer model are shown in Fig. 2.5. Additionally, the outer edge of the graphite radiometer is assumed to be perfectly insulated from conduction heat transfer as a result of using alumina washers with a low thermal conductivity and small contact area with the radiometer (see Fig. 2.5a). The radiometer is only tested under vacuum conditions, and hence convection heat transfer can be neglected. Therefore, the steady-state energy conservation governing equation reduces to:

$$\nabla \cdot (k \; \nabla T) = \frac{1}{r}\frac{\partial}{\partial r}\left(k \; r \; \frac{\partial T}{\partial r}\right) + \frac{\partial}{\partial z}\left(k \; \frac{\partial T}{\partial z}\right) = 0 \tag{2.2}$$

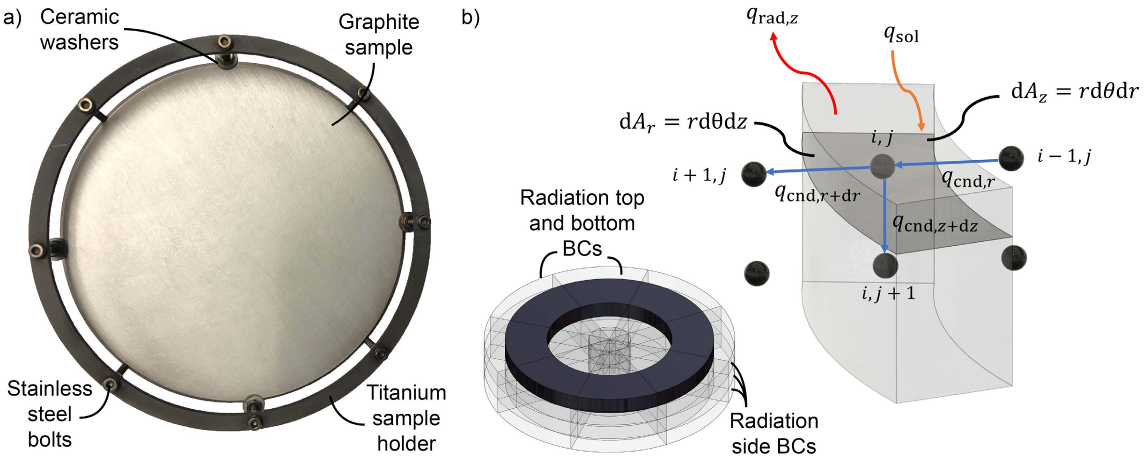

Figure 2.5: (a) Photograph of the radiometer developed and used in this study, and (b) schematic illustration of the control volume considered.

where T is temperature and k is a temperature-dependent thermal conductivity. The boundary condition at the center of the graphite radiometer is $\partial T/\partial r|_{r=0} = 0$ due to symmetry. The other boundary conditions encompass radiation thermal losses in addition to solar irradiation from the HFSS where applicable. For radiation thermal exchange, the surrounding surfaces are assumed to have a uniform temperature and emit like a blackbody in order to reduce the complexity of the numerical model without significantly affecting its results. Justification of the aforementioned assumptions is not discussed here for brevity, but is addressed through experimental measurements and a detailed radiosity model in Section 2.5.

Based on the foregoing discussion, the boundary conditions at the radiometer's outer radial edge ($r = R$), back surface facing IR camera ($z = t$), and front surface facing the HFSS ($z = 0$) are:

$$-k(T)\,\frac{\partial T}{\partial r}\bigg|_{r=R} \quad \text{and} \quad -k(T)\,\frac{\partial T}{\partial z}\bigg|_{z=t} = \left[\varepsilon(T)\sigma T^4 - \alpha(T_{\text{sur}})\sigma T_{\text{sur}}^4\right] \tag{2.3}$$

$$-k(T)\,\frac{\partial T}{\partial z}\bigg|_{z=0} = \alpha_{\text{sol}} q''_{\text{sol}} - \left[\varepsilon(T)\sigma T^4 - \alpha(T_{\text{sur}})\sigma T_{\text{sur}}^4\right] \tag{2.4}$$

where t is the radiometer's thickness, ε is emissivity, and α is absorptivity. Due to the temperature dependence of thermal conductivity when evaluating the governing equation, the term $\partial k/\partial r$ is substituted as $(\partial k/\partial T)(\partial T/\partial r)$. A similar approach applies to the z component. Upon evaluating the governing equation for interior nodes and surface nodes based on the boundary conditions, the finite difference (central difference when applicable) approximation is used to solve the partial differential equations.

Following the foregoing methodology, the discretized form of the governing equation for the inner front surface nodes (facing HFSS at $z = 0$ and $0 < r < R$, see Fig. 2.5b) is:

$$
\begin{aligned}
T_{i,j}\left(\frac{2k}{\Delta r^2}+\frac{2k}{\Delta z^2}\right) &= T_{i+1,j}\left(\frac{k}{\Delta r^2}+\frac{k}{2r_i\Delta r}\right)+T_{i-1,j}\left(\frac{k}{\Delta r^2}-\frac{k}{2r_i\Delta r}\right)\\
&+T_{i,j+1}\left(\frac{2k}{\Delta z^2}\right)+\frac{1}{4\Delta r^2}\left(\frac{\partial k}{\partial T}\right)\left(T_{i+1,j}-T_{i-1,j}\right)^2-T_{i,j}^4\left(\frac{2\varepsilon(T_{i,j})\sigma}{\Delta z}\right)\\
&+T_{\text{sur}}^4\left(\frac{2\varepsilon(T_{\text{sur}})\sigma}{\Delta z}\right)+\left(\frac{2\alpha_{\text{sol}}}{\Delta z}\right)q''_{\text{sol}}(r_i)
\end{aligned}
\tag{2.5}
$$

With a similar methodology to that of Eq. 2.5 above, eight additional discrete equations can be obtained for all remaining nodes.

Determination of thermal and optical properties

The proper evaluation of thermal (k) and optical (α, ε) properties for the steady heat transfer model used in the inverse problem is crucial for accurate heat flux characterization. Starting with the thermal conductivity and based on solid state theory, its total value can be determined via lattice and electronic contributions to thermal transport [111]. By assuming that these heat transfer modes are independent, the total thermal conductivity can be defined as: $k_{\text{tot}} = k_{\text{lat}} + k_{\text{el}}$ [112]. The electronic contribution to k_{tot} can be determined following the Wiedemann-Franz law [113] as: $k_{\text{el}} = N_L\sigma_{\text{el}}(T)T = N_L T/\gamma_{\text{el}}(T)$, where N_L is the Lorenz number, σ_{el} is the electrical conductivity, and γ_{el} is the electrical resistivity, which for isotropic graphite varies linearly with temperature above 1000 K [112, 114]. The graphite's electronic contribution to k_{tot} is reported to be less than 5% for temperatures up to 1000 K [112].

The lattice contribution to k_{tot} includes various scattering mechanisms, of which the significant ones are phonon-phonon and grain boundaries (phonon-electron and impurity scattering rates are many orders of magnitude smaller) [114]. Based on a grain/particle size of 10 µm for the graphite sample [115], scattering due to grain boundaries can be further ignored. Therefore, the dominant scattering in lattice thermal conductivity is the three-phonon scattering process, of which only Umklapp scattering directly impedes thermal transport [111] with a T^{-1} variation in thermal conductivity [114]. Here, the total thermal conductivity function is taken as $k_{\mathrm{tot}} = 1/(A+BT)$, where such a model describes graphite's thermal conductivity accurately from room temperature up to $\sim$ 2000 K [112]. By fitting the model for k_{tot} to the graphite manufacturer's thermal conductivity data to reduce measurement errors and uncertainty, the following parameters are obtained: $A = 5.69\times10^{-3}$ m K/W and $B = 9.62\times10^{-6}$ m/W.

For optical properties, an approximate three-level semi-gray model is constructed using literature data. The semi-gray model is based on the spectral ranges 0-2 µm, 2-7.5 µm, and $>$ 7.5 µm as these three ranges can be represented by constant values that remain within approximately ±3% of reported spectral emissivity measurements. Normal spectral emissivity ($\varepsilon_{\lambda,\mathrm{n}}$) measurements of a mechanically polished isotropic graphite (similar to the one used in this study) were reported by Autio and Scala at wavelengths greater than 2 µm and at temperatures near 1450 K [116]. The reported values of $\varepsilon_{\lambda,\mathrm{n}}$ were observed to be temperature-independent across a wide temperature range (as large as 500-1800 K), as also observed in other studies [117, 118], and averaged 0.60 ± 0.02 within the wavelength interval of 7.5-14 µm, which is the same spectral range as the IR camera used in this work. Hence, this value was used for the sample's emissivity ($\varepsilon_{\mathrm{IR}}$) in IR camera temperature measurements, which agrees well with calibration measurements using a type K thermocouple taken at temperatures up to approximately 700 K. For the wavelength interval of 2-7.5 µm, normal spectral emissivity measurements [116] averaged around 0.72 ± 0.02, which was further incorporated into the semi-gray model developed here. In other studies [117, 119], an average value of approximately 0.78 ± 0.02 was reported for the normal spectral emissivity at wavelengths less than 2 µm, and this value has been adopted in the semi-gray model to represent the spectral range of 0-2 µm:

$$\varepsilon_\mathrm{n}(T) = (0.78)F_{0\to 2\ \mu\mathrm{m}}(T) + (0.72)F_{2\to 7.5\ \mu\mathrm{m}}(T) + (0.6)\left(1 - F_{0\to 7.5\ \mu\mathrm{m}}(T)\right) \tag{2.6}$$

where $F_{\lambda_1\to\lambda_2}$ represents the fraction of total blackbody emission at temperature T in the wavelength interval between λ_1 and λ_2.

To determine the overall absorptivity of the graphite target (radiometer), the model presented in Eq. 2.6 is used for absorptivity based on Kirchhoff's law for opaque materials: $\varepsilon_{\lambda,\theta} = \alpha_{\lambda,\theta} = 1 - \varrho_{\lambda,\theta}$. The irradiance from the HFSS onto the sample is close to the normal direction and well represents the solar spectrum with equivalent blackbody radiation at 5800 K. Therefore, Eq. 2.6 is used to quantify α_n(5800 K), which is equivalent to α_sol, and produces a value of 0.776 ± 0.02. A blackbody radiation spectrum at 5800 K is used to determine α_sol rather than that measured in-house, as measurements presented in Fig. 2.2 only encompass approximately 70% of the solar simulator's total output power.

As for graphite's emissivity, its normal emissivity can be correlated to hemispherical emissivity either through experimental measurements [118, 120] or by using electromagnetic wave theory [121]. Prior studies have indicated that optical properties of polished graphite behave similarly to metals [117]. As such, when electromagnetic waves impinge on the surface of a conducting medium with a complex index of refraction ($m = n - ik$) at an angle from normal, Fresnel's relations can predict the parallel and perpendicular reflectivity for polarized light [121]. Under the assumption of unpolarized light, $\varrho = 0.5(\varrho_\parallel + \varrho_\perp)$ in the infrared region and by utilizing Kirchhoff's law, the ratios of hemispherical to normal spectral emissivity ($\varepsilon_\lambda/\varepsilon_{\lambda,\mathrm{n}}$) are derived [121] and available in terms of n and k/n.

The complex indices of refraction for graphite have been measured in prior work [122, 123], where n and k/n vary from 4.0 to 8.0 and 0.75 to 1.0 for the wavelength region from 2 to 10 µm, respectively. Therefore, the variation in complex indices of refraction within the infrared region leads to $\varepsilon_\lambda/\varepsilon_{\lambda,\mathrm{n}}$ varying from 1.05 to 1.13. Additionally, experimental measurements have been reported for graphite's normal and hemispherical emissivity at a wavelength shorter than 2 µm [118], more specifically at 0.65 µm, where $\varepsilon_\lambda/\varepsilon_{\lambda,\mathrm{n}}$ varies between 1.06 and 1.10 within the temperature range from 1273 to 2173 K. Based on the foregoing discussion and results, the ratio of hemispherical to normal emissivity was estimated to be $\varepsilon/\varepsilon_\mathrm{n} = 1.1 \pm 0.05$. Therefore, the hemispherical emissivity of the graphite sample for the heat transfer model is obtained at different temperatures using: $\varepsilon(T) = (\varepsilon/\varepsilon_\mathrm{n})\varepsilon_\mathrm{n}(T) = 1.1\varepsilon_\mathrm{n}(T)$.

2.4 Results and discussion

2.4.1 Heat flux gauge

The heat flux distribution was directly characterized outside the vacuum chamber using the HFG at the focal plane and various powers (supply currents), as well as at different focal planes. Results from the HFG for flux distribution are presented in the following sections; here the variation of peak flux with respect to current supply is presented. Measurements were obtained from different experimental runs, and the current supply was both increased and decreased to account for any hysteresis effects (if present). Based on the results in Fig. 2.6, a linear relationship exists for the variation of peak flux and total power with current (I) in the range of 100-200 A, giving $CF = 0.0066I - 0.32$, where CF is a correlation factor normalized by the peak value of 4.54 MW/m^2 at maximum current (200 A). This factor is used in determining the supply current dependence of HFSS output.

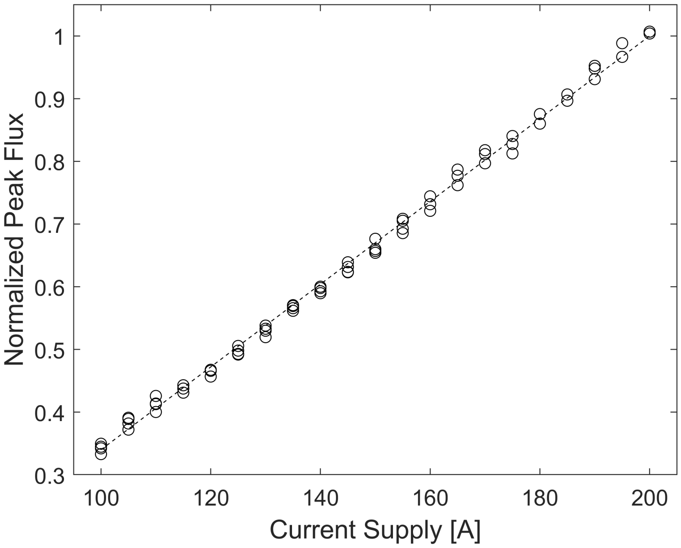

Figure 2.6: Variation of peak heat flux values with HFSS current supply as measured by the HFG.

2.4.2 Monte Carlo ray tracing simulations

The MCRT model with its two free parameters were fitted to heat flux distribution results obtained using the HFG at the focal plane and at different supply currents, where CF was used to correlate the model results at different supply currents. Results from the MCRT model for the heat flux distribution outside the vacuum chamber and at a supply current of 160 A are shown in Fig. 2.7a, where good agreement exists between model results and HFG measurements. The MCRT heat flux distribution at the focal plane falls within the uncertainty of all HFG measurements by additionally accounting for the uncertainty in radial position of ± 0.2 mm (not shown). Because the validated MCRT model only used system specific variables (η_{el} and θ_{sp}) in fitting the experimental results as discussed earlier, the accuracy of HFG measurements can be further assessed from results of the peak flux variation with respect to distance from the focal plane as shown in Fig. 2.7b. Both results from the HFG and MCRT follow the same declining trend, and results predicted by the MCRT simulation fall within the uncertainty of the HFG, which is estimated to be approximately ± 8%.

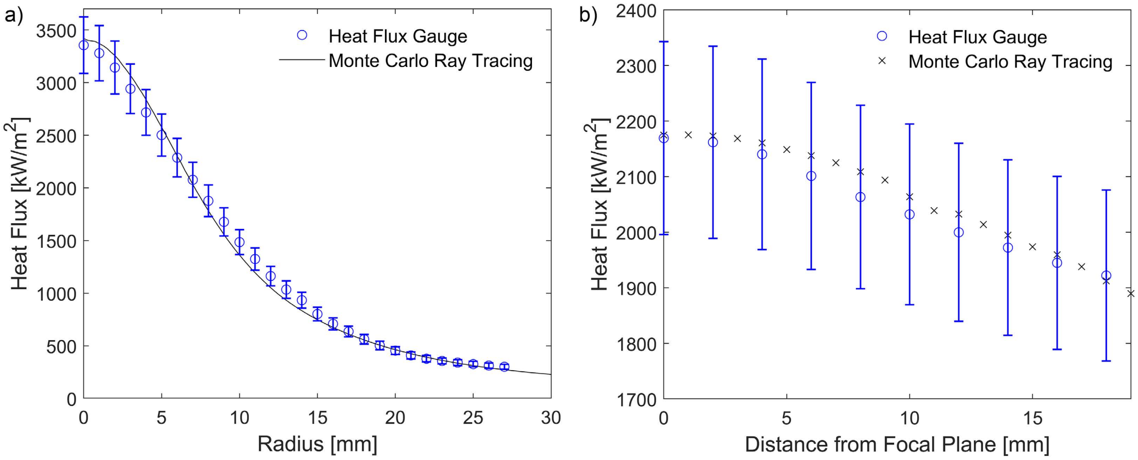

Figure 2.7: Validation of the in-house MCRT model with respect to measurements from the HFG outside the vacuum chamber showing (a) heat flux distribution at the focal plane and 160 A HFSS supply current, and (b) peak heat flux values at different focal distances and at 120 A HFSS supply current.

2.4.3 Inverse method

The inverse heat transfer problem was solved using the python scipy.optimize package that implements the Nelder-Mead algorithm to minimize residual error between the IR camera temperature measurements and those of the sample's modeled back surface. In this minimization problem, the fitting parameters that determine the heat flux distribution in the vacuum chamber are α_{Lor}, σ_{Gau}, σ_{Lor}, and A_{sol}, as introduced in Eq. 2.1. Prior to solving the inverse problem, a mesh independence study was conducted to evaluate the optimum mesh size to use and to verify the accuracy of the model, where numerical convergence was achieved around $\Delta r \sim 10^{-3}$ m. The value of Δz had an insignificant effect due to the thin graphite disk, and its value was set to 1×10^{-3} m. Results of the mesh independence study are shown in Fig. 2.8 for the relative peak temperature error (at the center) of the front and back surfaces with respect to a very fine mesh. The convergence criteria for the iterative numerical heat transfer model presented here was set to a maximum temperature error of 1×10^{-9}.

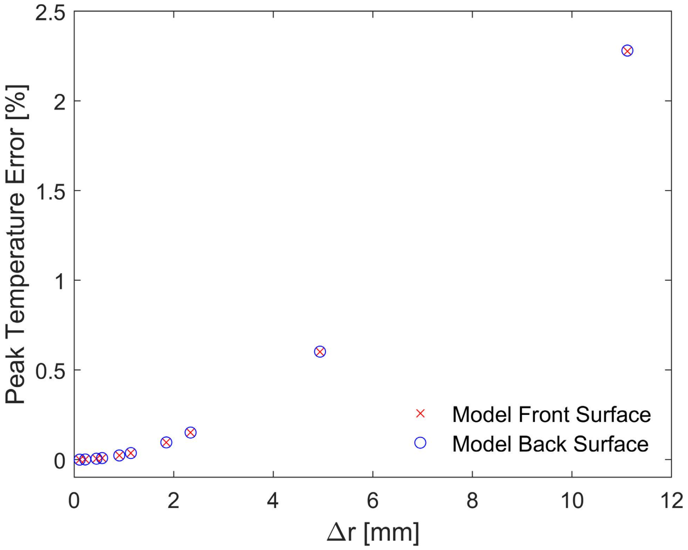

Figure 2.8: Mesh independence study for the heat transfer numerical model.

The time-averaged temperature contour of the sample's back surface as measured by the IR camera with a high resolution of 0.26 mm/pixel is shown in Fig. 2.9a. The contour distinctly exhibits the expected radially symmetric temperature distribution consistent with the heat flux input, and further supports the implementation of radial temperature averaging to reduce measurement noise and inverse model computational load. Additionally, Fig. 2.9b shows the time and radially averaged temperature profile of the graphite radiometer as measured by the IR camera compared to its front (facing HFSS) and back (facing IR camera) surfaces as predicted by the heat transfer model. The IR camera temperature radial variation in Fig. 2.9b remains within 2.5% over the entire surface of the radiometer. Three observations are paramount: (1) radially averaged IR camera temperature measurements represent a smooth distribution consistent with the heat flux profile assumption implemented here; (2) the experimental temperature profile's gradient nearly decays to zero at the outer radius of the radiometer, consistent with the radial outer boundary condition of no conduction heat transfer; and (3) a very small difference is observed between the front and back surfaces of the graphite radiometer as a result of its thickness. The latter observation suggests that the heat transfer model can be potentially reduced further from 2D to 1D and still provide acceptable heat flux characterization. However, because computational time was not of concern here, the 2D model was employed.

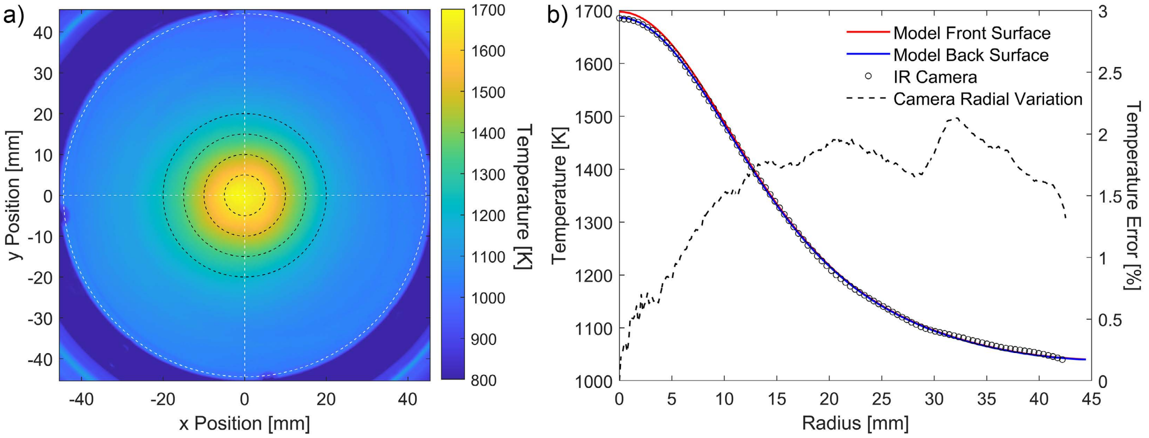

Figure 2.9: (a) Time-averaged temperature profile of the graphite sample back surface obtained using the IR camera for a test at HFSS supply current of 100 A (centered black rings with $r = 5$, 10, 15, and 20 mm illustrate distribution and angular uniformity). (b) IR camera radially averaged temperature distribution and predictions from the inverse heat transfer model for front and back sample surfaces.

The solution of the heat flux distribution inside the vacuum chamber was obtained for HFSS supply currents in the range of 100-140 A with an increment of 10 A, and five experimental tests were performed at each current value. This approach allows evaluation of parameters such as the measurement uncertainty of the inverse heat flux characterization technique in addition to a unified heat flux distribution profile that varies linearly with the HFSS supply current, per expectation [76]. Fig. 2.10a shows the inverse heat transfer model results at a supply current of 100 A, where the individual heat flux radial profiles determined from the five repeated tests are indicated and can be readily converted into symmetric heat flux contour maps. The five profile sets were used to construct a mean heat flux distribution with an uncertainty interval (based on the standard deviation) shown in Fig. 2.10a that was then compared to the measurements obtained using the HFG outside of the vacuum chamber. Because HFG measurements were not obtained with the window in place, they are corrected in Fig. 2.10 to compensate for the quartz window's solar transmissivity ($\tau_{\mathrm{qrt}} = 0.92$).

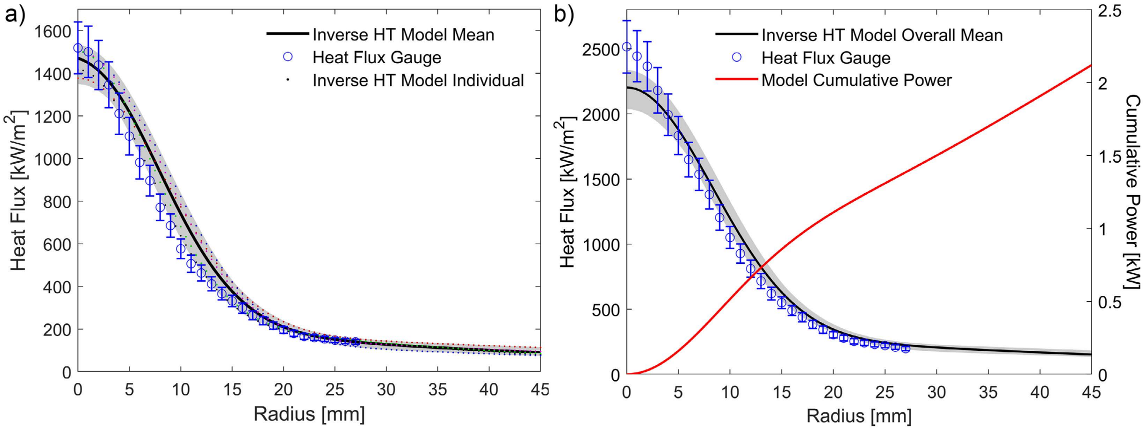

Figure 2.10: (a) Results of the inverse heat transfer (HT) model at HFSS supply current of 100 A showing heat flux distribution inside the vacuum chamber of five repeated experimental runs and their average compared to corrected measurements from HFG. (b) Final averaged results of the inverse heat transfer model at HFSS supply current of 140 A showing the heat flux distribution inside the vacuum chamber compared to corrected measurements from HFG. Gray shaded regions represent the uncertainty bounds of the inverse model heat flux results.

As shown in Fig. 2.10a, the inverse heat transfer model results and uncertainties fall within the uncertainty range of HFG measurements but with a slightly broader heat flux distribution. To determine the effect of inverse model parameter uncertainties on the obtained heat flux profile, a sensitivity analysis was performed as presented and discussed further in Section 2.5. The sensitivity analysis demonstrates that the inverse model results are most sensitive to the radiometer's optical properties, particularly those pertaining to the IR camera measurements, and that the radiometer's thermal conductivity significantly affects the determined peak heat flux with no changes to the determined total power. Although the uncertainty of inverse model parameters can contribute to the slight discrepancy between the two general profiles in Fig. 2.10a, such deviation is also potentially due to refraction from the quartz window and/or annular beam truncation by the vacuum chamber. However, the effects of additional components on the heat flux distribution at the radiometer's position were determined to be minimal based on results from the MCRT model when applying Snell's law and room temperature optical properties for the quartz window (apart from linear attenuation due to τ_{qrt}).

The results in Fig. 2.10a suggest that thermal effects due to temperature-dependent optical properties of the quartz window as a result of a non-uniform temperature profile could potentially contribute to such a difference, similar to the work presented by Gurwich and Spector [124]. Such a detailed investigation is outside the scope of this study, but the temperature gradient on the quartz window was recorded and is presented in Section 2.5 with a discussion on the relatively large temperature gradient observed. Additionally, the discrepancy between HFG measurements and the inverse technique results can be due to misalignment of both experimental setups, where a misalignment as small as 4 mm can lead to reduction in the peak heat flux values as high as 6% with insignificant reduction in the total power [82]. Comparing total powers at 100 A from the inverse model's average flux profile and Lorentzian fit from the HFG measurements, the total powers on the radiometer (integrals of heat flux over a circular area with a diameter of 8.9 cm) were estimated to be 1.31 ± 0.07 kW and 1.23 ± 0.1 kW, respectively. Therefore, based on the foregoing discussion in addition to good agreement in heat flux and total power values, the presented inverse technique for heat flux characterization and monitoring can be considered validated.

A similar procedure was performed at different HFSS supply currents, where the entire heat flux profile sets were normalized to obtain the composite Lorentzian/Gaussian distribution parameters, which are independent of current supply, and the magnitude parameter A_{sol}, which is assumed to depend linearly on current. The current-dependent values of the heat flux distribution presented in Eq. 2.1 are $A_{\text{sol}} = 0.740I - 20.5$ kW/m, $\sigma_{\text{Lor}} = 0.0492$ m, $\sigma_{\text{Gau}} = 0.00829$ m, and $\alpha_{\text{Lor}} = 0.519$. These final averaged parameters were then used to plot the final inverse heat transfer model results compared to those obtained using the HFG and corrected for a HFSS supply current of 140 A as shown in Fig. 2.10b.

Testing was not continued beyond HFSS supply currents of 140 A because the radiometer began to deteriorate at its center, which produced changes in graphite's thermal and optical properties. Therefore, the inverse radiometer presented here is limited to peak solar irradiation up to approximately 2400 kW/m^2. Despite this limitation, the current-dependent relationship presented earlier can be used to extrapolate to higher HFSS supply currents and thus HFSS irradiation. Using the foregoing parameters of the heat flux distribution, the total powers obtained from the inverse model at supply currents of 160, 180, and 200 A were estimated to be 2.50 ± 0.13 kW, 2.88 ± 0.14 kW, and 3.26 ± 0.16 kW. These compare well to 2.43 ± 0.19 kW, 2.86 ± 0.23 kW, and 3.29 ± 0.26 kW from the corrected HFG measurements. Therefore, despite some deviation of peak heat flux at higher HFSS power as a result of the different heat flux profiles, the cumulative power results are consistent. This outcome further validates the inverse model results and its extrapolation.

2.5 Additional considerations

2.5.1 Treatment of surrounding surfaces

As noted in the methodology section, the surrounding surfaces are assumed to have a uniform temperature of T_{sur}. Values for T_{sur} have been estimated based on IR camera temperature measurements of the vacuum chamber's inner walls from recorded regions outside of the radiometer's area in addition to the quartz window's external surface. Both temperature measurements were of similar magnitude and were further consistent with measurements recorded using a temperature transducer located on the outer surface of the cylindrical vacuum chamber after accounting for the expected temperature drop due to conduction across the stainless steel wall. Estimated values for T_{sur} averaged around 550 K. Additionally, the sensitivity of the numerical model towards T_{sur} is presented below, where results indicate a very weak sensitivity to the value of T_{sur}. Therefore, this insensitivity justifies the treatment of the surrounding temperature as uniform.

To investigate the effects of different surfaces within the vacuum chamber on radiation thermal exchange of the numerical model, a radiosity model was constructed and evaluated as shown in Fig. 2.11. The radiosity model divides the vacuum chamber into two enclosures, where each enclosure is comprised of three surfaces; two surfaces represent the graphite radiometer, two surfaces represent the stainless steel cylindrical chamber, one surface represents the quartz window, and the last surface represents an imaginary blackbody surface. All surfaces within the model are assumed to be gray and at uniform temperatures. For the graphite radiometer, the surface is assumed to be at the average temperature of 1400 K with its corresponding hemispherical emissivity determined based on Eq. 2.6 at 1400 K.

The assumption of a gray surface with the prescribed emissivity is justifiable by the minor contribution of thermal radiation from surrounding surfaces compared to that of the graphite. Additionally, the difference between $\varepsilon(T)$ and $\varepsilon(T_{\mathrm{sur}})$ is too small to induce a non-negligible difference. As for the imaginary surface (surface 6 - see Fig. 2.11), it is treated as a blackbody as a result of the adjacent larger cavity and is assumed to have a uniform temperature of 350 K; the rear portion of the vacuum chamber is at a significantly lower temperature than surfaces closer to the graphite radiometer.

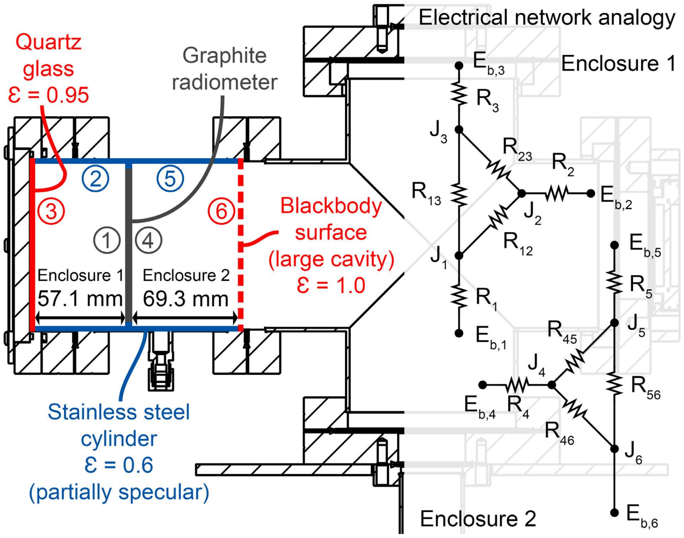

Figure 2.11: Illustration of the radiosity model considered for the numerical heat transfer model, showing the vacuum chamber with different surfaces treated (left) and the constructed electrical network analogy (right).

Regarding the stainless steel cylindrical chamber, its two surfaces are assumed to have uniform temperatures of 550 K with gray emissivity of 0.6 [51, 121]. As all clean metals are known to demonstrate strong specular reflection especially for thermal radiation [121], the stainless steel surface needs to be treated as a partially specular surface. Therefore, the radiosity model considers the surface to reflect 25% as a diffuse surface and 75% as specular, which is consistent with prior observations

[125, 126]. This treatment provides diffuse (ϱ^d) and specular (ϱ^s) components of the stainless steel reflectance equivalent to 0.1 and 0.3. Finally for the quartz window, its surface is assumed to be opaque with an emissivity of 0.95 and a uniform temperature of 550 K. The assumption of an opaque surface is appropriate based on the scope of the radiosity model [121] and the relatively constant values for the combined emissivity and transmissivity of quartz [127, 128]. As transmitted radiation through the quartz window to the room does not affect the radiosity model's results of interest, and transmitted radiation has a negligible fraction of being redirected back into the vacuum chamber, such an assumption is valid.

The model consists of a system of equations that are solved simultaneously to determine the radiosity (J_i) and heat transfer rate (q_i) of each surface i. The results of interest here are the heat transfer rates of the graphite radiometer's two surfaces (i.e., q_1 and q_4). The combined transfer rate is then compared to that assuming black, uniform temperature surrounding surfaces to determine the associated error of such an assumption. To develop the radiosity model, equations for the heat transfer rate are constructed using [121]:

$$q_i = \frac{E_{b,i} - J_i/(1-\varrho_i^s)}{\varrho_i^d/\left[(1-\varrho_i^s)\varepsilon_i A_i\right]} = \sum_{j=1}^{N} \left[\frac{J_i}{1-\varrho_i^s} - \frac{J_j}{1-\varrho_j^s}\right](1-\varrho_i^s)(1-\varrho_j^s)A_i F_{ij}^s \tag{2.7}$$

where $E_{b,i}$ is blackbody emissive power (σT_i^4), A_i is surface area, and F_{ij}^s is the specular view factor from surface i to surface j (i.e., fraction of thermal radiation leaving surface i that intercepts surface j via direct diffuse emission or specular reflection). All diffuse view factors are obtained based on tabulated relations [121] for the view factor from a disk to another parallel coaxial disk of unequal radius, in addition to the view factor's summation and reciprocity relations. The specular view factors are then determined based on the crossed-strings method, and the corresponding summation relation is modified to be consistent with the new treatment of partially specular surfaces [121] to yield $\sum_{j=1}^{N}(1-\varrho_j^s)F_{ij}^s = 1$.

Based on the foregoing methodology and discussion, the radiosity model was solved to yield a combined heat transfer rate out of the graphite radiometer (q_1 and q_4) of 2085 W. In contrast, assuming a uniform black surrounding with a temperature T_{sur} of 550 K would yield a heat transfer rate out of $2\varepsilon\sigma A_1(T_1^4 - T_{\mathrm{sur}}^4)$, which corresponds to 2112 W. This provides a relative percentage error of 1.28%, which is insignificant compared to other uncertainty estimates within the inverse model. Therefore, the assumption of the surrounding surfaces emitting like a blackbody can be implemented to reduce the complexity of the inverse model with no significant effect on the accuracy of its results. Finally, the estimated relative error is negligibly sensitive to the assumed radiometer's surface temperature ($T_1 = T_4 = 1400$ K), which further justifies the applicability of the comparison performed here to that of the actual temperature gradient observed.

2.5.2 Sensitivity analysis

A sensitivity analysis was conducted to determine the effect of different model parameters on the inverse heat flux distribution, as quantified by sensitivity coefficients, S_i, for the different parameters, i, involved in the inverse model. The sensitivity coefficients for peak heat flux ($S_{q'',i}$) and total power ($S_{Q,i}$) were determined through 5% perturbation above and below the nominal parameter values and by employing a central difference scheme using:

$$S_{q'',i} = \frac{\partial q''}{\partial \beta}\frac{\beta_0}{q''_0} = \frac{q''(\beta_0+\Delta\beta) - q''(\beta_0-\Delta\beta)}{2\Delta\beta}\frac{\beta_0}{q''_0} \tag{2.8}$$

where β is the investigated parameter, $\Delta\beta$ is the parameter's associated uncertainty/perturbation, and the subscript '0' denotes values at nominal conditions (no perturbation). A similar equation is formulated for evaluating $S_{Q,i}$. Results of the sensitivity analysis are shown in Fig. 2.12, where absolute values of the sensitivity coefficients are plotted and labeled as being positive or negative. A positive value indicates that a perturbation in the parameter value reflects a change in the determined quantity in the same direction (i.e., an increase in parameter value leads to an increase in the determined quantity).

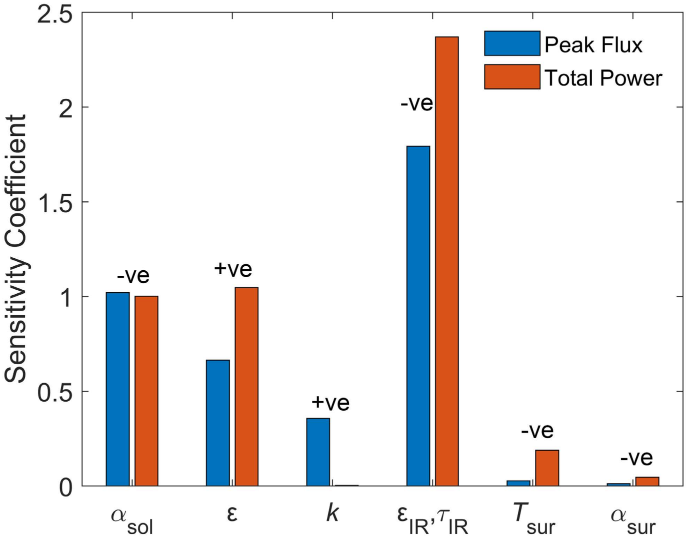

Figure 2.12: Sensitivity analysis of model parameters for the inverse heat transfer mapping technique.

Based on results in Fig. 2.12, both the peak flux and total power are most sensitive to the optical properties used by the IR camera to quantify temperatures of the radiometer, consisting of the calibrated graphite emissivity ($\varepsilon_{\mathrm{IR}}$) and transmissivity of the ZnSe viewport (τ_{IR}). Therefore, care must be taken in evaluating these two parameters from spectral measurements either performed in-house or found in literature, and the parameters were further confirmed to be appropriate against temperature transducers. Therefore, the uncertainties in these two parameters are relatively low, especially given that graphite's emissivity in the far IR region is significantly less sensitive to surface conditions [116, 117]. The next two parameters with relatively high sensitivity coefficients are α_{sol} and ε. The uncertainties in these two parameters, especially that of ε, are more sensitive to surface conditions and are expected to contribute noticeably to the overall uncertainty in the determined heat flux distribution. However, as measurements were performed and averaged over five different trials for each operating condition, errors due to slight variations of surface condition are expected to be significantly reduced.

The radiometer's thermal conductivity follows next, but only the peak flux is sensitive to k. As shown in Fig. 2.12, the total power determined by the inverse model is almost entirely unaffected by errors in thermal conductivity. With regards to the two final parameters that involve heat transfer to/from the surrounding (i.e., T_{sur} and α_{sur}), Fig. 2.12 shows a very weak sensitivity towards these two parameters, making the assumption pertaining to a uniform and constant surrounding temperature justifiable.

2.5.3 Quartz thermal effects

The temperature of the quartz window was recorded using the IR camera positioned at the front side of the vacuum chamber and aligned off-axis at an approximate angle of 45°. The temperature contour of one of the measurements at a HFSS supply current of 140 A is shown in Fig. 2.13, where the quartz window's assumed IR camera emissivity is 0.90. The assumed value is consistent with spectral emissivity measurements provided by the manufacturer (Technical Glass Products) within the IR camera's spectral range. As shown in Fig. 2.13, the quartz window reaches relatively elevated temperatures and, more importantly, a large temperature gradient is observed on the window with temperatures varying from approximately 450 K to 700 K primarily as a result of variation in heat flux from the HFSS on the window (see Eq. 2.1). Such a temperature gradient can potentially cause a difference between the heat flux distribution measured using the HFG and that determined from the inverse mapping technique (i.e., heat flux distribution inside and outside the vacuum chamber), as shown in Fig. 2.10 and demonstrated in other work [124]. Since the MCRT model does not consider temperature-dependent quartz optical properties or account for the effect of a large temperature gradient, the aforementioned difference was not captured by MCRT simulation results.

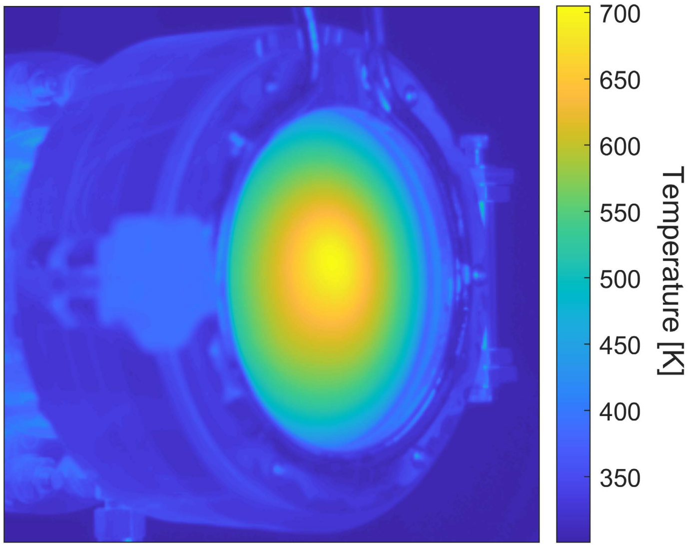

Figure 2.13: Vacuum chamber's quartz window temperature distribution for a test at HFSS supply current of 140 A.

A detailed investigation regarding effects of the quartz window on the heat flux distribution inside the vacuum chamber is outside the scope of this work. However, a brief discussion is presented on the methodology of accounting for the window's optical properties variation with temperature. Such a variation in properties can be implemented into the MCRT simulation either by simply mapping the IR camera temperature measurements onto a corresponding plane that represents the quartz window in the ray tracing model, or by fitting a heat transfer numerical model that includes the quartz window, HFSS, cylindrical walls of chamber, and the radiometer. In the former approach, the MCRT model and the radiometer's inverse heat transfer model are completely independent. IR camera temperature measurements are used to estimate temperature-dependent spatial optical properties of the quartz window within the MCRT simulation, which include varying window transmissivity and index of refraction. In contrast, for the latter approach, the heat transfer model of the quartz window is coupled to that of the radiometer and MCRT, where thermal properties of relevance can be additionally tuned to fit the IR camera measurements. Once the temperature distribution along the quartz window has been modeled, the distribution becomes an input to the MCRT simulation. The foregoing discussion provides the basis for a detailed investigation on the quartz window effects for high-flux systems in possible future work.

2.6 Conclusions

In this chapter, a custom-designed and built HFSS with a peak heat flux that can be controlled within the range of 1.5-4.5 MW/m^2 is introduced and thoroughly characterized. First, its transient response to reaching a steady-state operation was determined, with the conclusion that the HFSS requires 15 min to stabilize prior to conducting experiments. Additionally, the spectral distribution of its output with respect to current supply was measured. The heat flux distribution output from the HFSS was then characterized using a heat flux gauge to determine the gross solar irradiance output and to validate the presented inverse characterization technique. The latter provides a simpler, inexpensive, and accurate characterization method for determining the heat flux output using IR temperature measurements of a graphite sample (radiometer) in a vacuum chamber. Additionally, the present inverse technique provides a much faster approach to monitoring the HFSS's performance over time, instead of using a separate, dedicated system for characterization; the radiometer can be placed directly into a solar reactor to determine changes in the heat flux distribution, as performed and presented in Chapter 3. However, this inverse technique was determined to be limited to solar irradiation up to 2400 $\mathrm{kW/m^2}$, and higher peak fluxes were determined by extrapolating the parameters. For a HFSS employing multiple lamps that provide a higher combined solar irradiation, lamp outputs can be individually characterized to provide the effective combined irradiation by superposition. Although peak flux values from the inverse technique at higher HFSS supply currents ($\gtrsim$ 140 A) start to deviate from those obtained using the HFG due to quartz window thermal effects, the total powers obtained using both methods were consistent. Finally, a MCRT model was developed and further tuned to represent the irradiation from the HFSS to further verify heat flux measurements, and to provide a powerful tool in modeling radiation heat transfer throughout this work.

Based on heat flux measurements from the HFG, a general heat flux distribution can be obtained to represent the gross solar irradiance in following chapters. Measurements were fitted using a Lorentzian distribution instead of the composite distribution used in the inverse characterization since a value of $\alpha_{\mathrm{Lor}} = 1$ was obtained (see Fig. 2.14). Therefore, the radiative heat flux distribution at a given supply current can then be estimated using:

$$q''_{\mathrm{sol}}(r, I) = \frac{A_{\mathrm{sol}}(I)}{\pi} \frac{\sigma_{\mathrm{sol}}}{\sigma_{\mathrm{sol}}^2 + r^2} \tag{2.9}$$

with $\sigma_{\text{sol}} = 0.00864$ m and $A_{\text{sol}} = 0.8189I - 38.88$ kW/m. At an operating current of 160 A, the value of A_{sol} is 92.1 kW/m. Regardless of the current supplied and peak heat flux, the full width at half maximum (FWHM) represents the most concentrated region and equals $2\sigma_{\text{sol}}$ (1.7 cm).

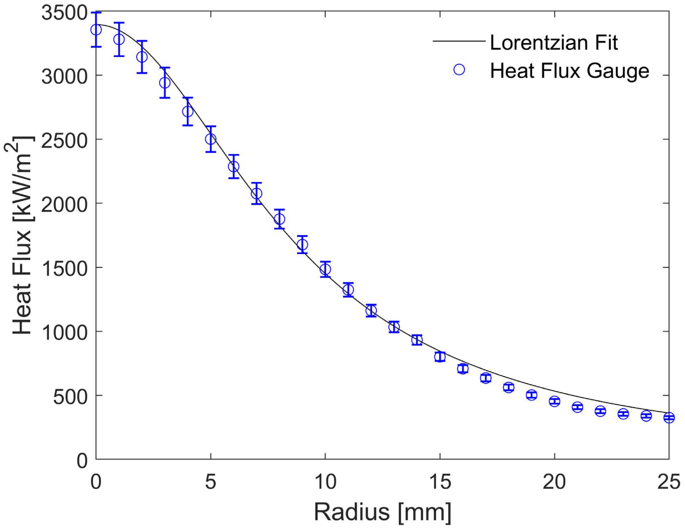

Figure 2.14: Heat flux distribution measured using the HFG at the focal plane with 160 A supplied current along with fitted Lorentzian distribution.

Chapter 3:

Methane Decomposition Setup and Auxiliaries[1,2]

In this chapter, the experimental setup and auxiliaries custom-designed and built for this research work are introduced and thoroughly presented. Additionally, process monitoring and characterization systems, whether developed in this work or were readily available, that will be utilized in subsequent chapters are further introduced and discussed along with adequate background of technical information and calibrations, whenever applicable. This chapter aims to develop a solid basis and reference for the next few chapters with regards to details related to methodology and experimental equipment used.

---

[1] All or some portions of this chapter contributed to paper by M. Abuseada, C. Wei, R. M. Spearrin, and T. S. Fisher, titled Solar-thermal production of graphitic carbon and hydrogen via methane decomposition, published in Energy & Fuels 36 (2022), 3920-3928.

[2] All or some portions of this chapter contributed to paper by C. Wei, M. Abuseada, B. Jeevaretanam, T. S. Fisher, and R. M. Spearrin, titled Concentrated solar-thermal methane pyrolysis in a porous substrate: Yield analysis via infrared laser absorption, published in Proceedings of the Combustion Institute (2022).

3.1 Methane pyrolysis experimental setup

3.1.1 Small-scale solar reactor

A small-scale custom-built solar reactor (Fig. 3.1) is used for the experimental study of solar-thermal methane pyrolysis presented in this work. Flow enters the reactor from the front side facing the HFSS and into a 9.7 cm inner diameter cylindrical section, where the feed then flows through a carbon porous substrate that is attached to a reducing flange with a flow diameter of 6.9 cm. The reactor is sealed via a 10.2 cm quartz window that allows direct irradiation from the HFSS to reach the carbon substrate, which is placed 14.0 cm from the front side of the cylindrical reactor and aligned at the solar simulator's focal plane. The flange supporting the quartz window is being water-cooled via a chiller with a 1.4 kW cooling capacity (Thermo Fisher Scientific, TF14BA) to prevent undesired heating of the quartz, which otherwise could lead to unwanted carbon deposition on the glass. The quartz window and front section of the reactor are additionally being cooled via two small blowers. A schematic illustrating the process and solar reactor is shown in Fig. 3.1.

The methane decomposition reaction will take place locally within the porous substrate, depositing solid carbon product and leaving primarily hydrogen gas and any unconverted methane in the product gas stream. To monitor and control the process, a capacitance manometer (MKS, 727A) is connected downstream of the carbon felt to actively monitor the operating pressure, and a high-resolution science-grade longwave IR camera (FLIR, A655sc) is used to measure the temperature distribution of the substrate's back surface. The reactor is also supplemented with additional auxiliary and product monitoring components, which are discussed further in the following sections.

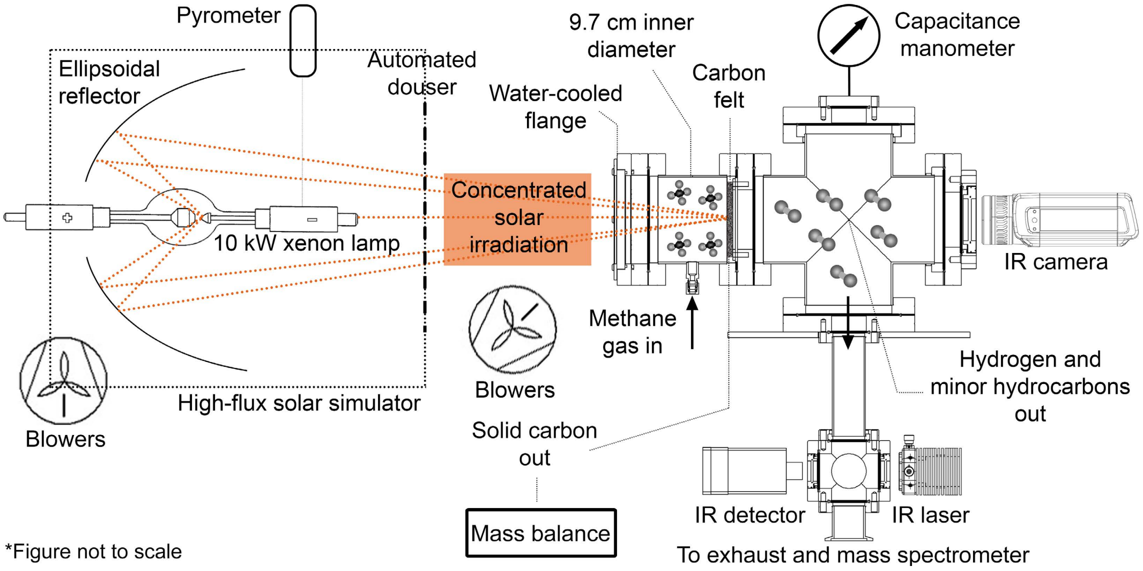

Figure 3.1: A schematic of the small-scale solar reactor overall process and configuration.

3.1.2 Reactor auxiliaries

The solar reactor is equipped with many upstream and downstream auxiliaries to support accurate and reproducible experimental testing. Upstream of the reactor, four different re-programmable mass flow controllers (MKS, GM50A) connect to a stainless steel 316 gas manifold (Burger and Brown Engineering, custom). The four mass flow controllers have full ranges of: (1) 2000 sccm of CH_4, (2) 100 sccm of CH_4, (3) 1000 sccm of H_2, and (4) 100 sccm of N_2. For added safety and full automation of the system, pneumatic shutoff valves (Swagelok, SS-4BK-1C) are installed upstream of the mass flow controllers and downstream of the gas manifold. Additional pneumatic valves are also installed elsewhere in the system. The pneumatic valves are controlled via dedicated solenoid valves (Parker, P2LAX) with access to a compressed air line. Additionally, a pressure transducer with a range of 100 psia (MKS, AA07) is connected to the gas manifold to monitor the reactor's upstream pressure and provide an indication of a pressure buildup or clogging due to carbon deposition (if applicable). All connections (NPT, VCR, etc.) and tubing were made of stainless steel 316 and primarily supplied by Swagelok. The reactor's upstream auxiliaries are shown in Fig. 3.2a.

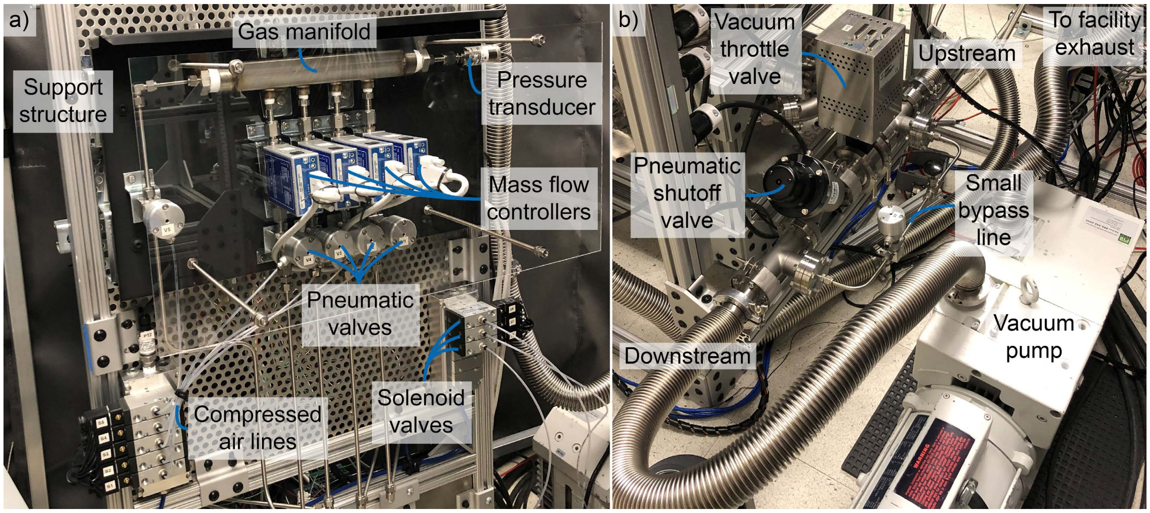

Figure 3.2: Photographs of the solar reactor's (a) upstream auxiliaries and (b) exhaust line.

Downstream of the reactor, several auxiliary components ensure safe and steady operation of the solar reactor. A rotary vane vacuum pump (Leybold, D65BCS) connects the 2.75 inch diameter exhaust line of the reactor to that of the facility. The main exhaust line includes a vacuum high-speed throttle valve (MKS, T3B) to control the vacuum suction rate from the pump and to maintain steady operating pressures through variable positioning. The main line is further equipped with a pneumatic vacuum shutoff valve (MKS, 162) for added safety and sealing. For slower vacuum suction rates from atmospheric pressures, a small bypass line with a manual needle valve (Swagelok) and pneumatic valve is installed with a fixed suction rate. The exhaust line is shown in Fig. 3.2b, while a full overall schematic of the small-scale methane decomposition experimental setup and auxiliaries can be found in Appendix A.

3.1.3 Process and control automation

To allow for automating the methane decomposition process and controls, further electrical auxiliaries are installed. These include: (1) a contactor for the three phase vacuum pump, (2) AC relays for the chiller, blowers, and AC powered auxiliaries, and (3) DC relays for the exhaust throttle valve, HFSS douser motor, and DC powered instrumentation. The 24 VDC power supply (Siemens, SITOP PSU6200) of the auxiliaries is further equipped with an eight-channel selectivity module (Siemens, SITOP SEL1200) to protect major auxiliaries against current overloads. Additionally, a vacuum system controller (MKS, 946) is used to interface with and control MKS mass flow controllers, vacuum throttle valve, and the reactor's capacitance manometer. Components used in the reactor's process automation are shown in Fig. 3.3a.

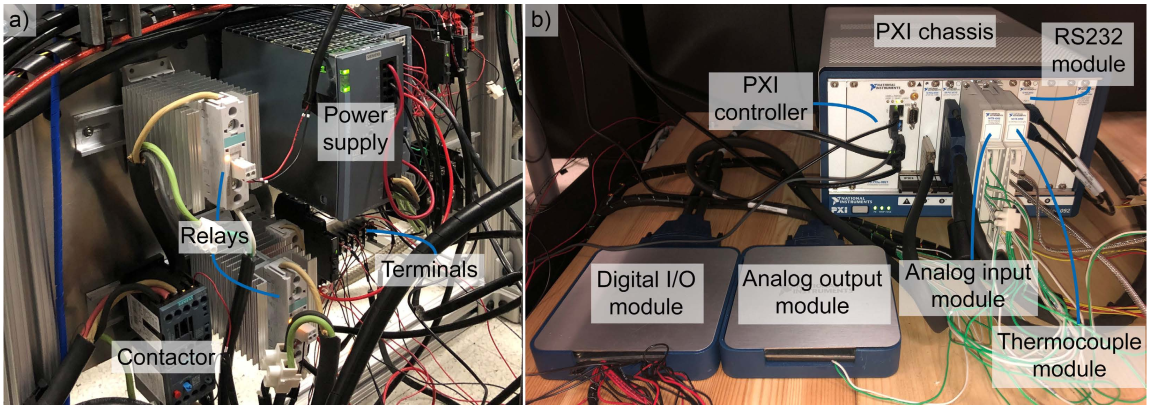

Figure 3.3: Photographs of the solar reactor's (a) automation components and (b) data acquisition and controls system.

The process automation is developed using LabVIEW and National Instrument's (NI) PXI platform (Fig. 3.3b). A PXI system chassis (NI, PXIe-1092) with eight slots is used with the following modules: (1) PXI controller (PXIe-8821) for standalone automation with labVIEW Real-Time, (2) digital I/O module

(PXI-6515) to control pneumatic solenoid valves, contactors, relays, and motors, (3) analog output module (PXIe-6738) to control the HFSS's power supply via 0-10 V signal, which in turn adjusts the current supplied to the xenon lamp, (4) analog input module (PXIe-4302) for pressure transducers, (5) thermocouple input module (PXIe-4353) for thermocouples and HFSS lamp temperature monitoring sensor, and finally (6) RS232 serial interface (PXI-8430) to communicate with and control the water chiller and vacuum controller. The entire process and equipment control is then achieved via a LabVIEW virtual instrument (VI), where the front panel and block diagram of the developed VI code can be found in Appendix A. The developed VI allows for intuitive process monitoring and controls (via PID controllers when automated, such as for operating pressure), and it implements various safety interlocks and trip points to prevent human errors and pressure build up as a result of reactor clogging.

3.2 Product stream monitoring setup

3.2.1 Laser absorption spectroscopy

A laser absorption spectroscopy (LAS) setup was designed, built, and installed downstream of the reaction zone (see Fig. 3.1) to enable real-time analysis of methane conversion and chemical kinetics. By exploiting recent advances in mid-wave IR photonics that enable spectral coverage of the fundamental C-H stretch vibrational bands near 3 µm with compact, room-temperature semi-conductor lasers [129, 130], various hydrocarbon species such as CH_4 and C_2H_4 can be monitored. This approach allows for direct continuous monitoring of involved species (i.e., with no fluid sampling required as with mass spectrometry) and can be used to monitor trace products (e.g., C_2H_6) that were not possible to quantify in other CH_4 decomposition studies due to their low concentrations [57]. The time-resolved nature of the spectroscopic measurements provides direct information on the chemical evolution of the decomposition process and allows for rapid comparison and optimization of process conditions (temperature, pressure, etc.). The LAS experimental setup directly monitoring CH_4, C_2H_4, and C_2H_6 is shown in Fig. 3.4.

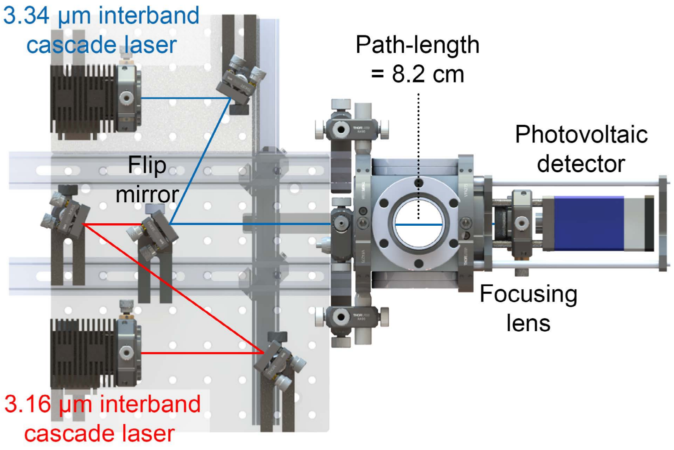

Figure 3.4: Laser absorption spectroscopy experimental configuration, monitoring CH_4, C_2H_4, and C_2H_6 in product stream.

LAS is an optical diagnostic technique well-suited for time-resolved and quantitative measurement of species and temperature. LAS is well detailed in prior literature [131], and therefore only a brief overview is presented here. Molecular absorption through a uniform gas medium is governed by the Beer-Lambert law:

$$\alpha_v = -\ln\left(\frac{I_t}{I_0}\right)_\nu = \sum_i P x_{\text{abs}} S_i(T) \varphi_i\left(\nu, T, P, x_{\text{abs}}\right) L \tag{3.1}$$

where I_t/I_o is the ratio of experimentally measured transmitted and incident laser intensities at frequency ν [cm^{-1}], α_ν is the spectral absorbance at that frequency, P [atm] is the total pressure, $S_i(T)$ [cm^{-2}/atm] is the temperature-dependent linestrength of transition i at temperature T [K], x_{abs} is the mole fraction of the absorbing molecule, L [cm] is the path-length of the absorbing medium, and φ_i [cm] is the spectral lineshape of transition i. For well-isolated transitions, the integrated absorbance area can be calculated by integrating over the spectral domain:

$$A_i = \int_{-\infty}^{\infty} \alpha_v d\nu = PS_i(T)x_{\text{abs}}L \tag{3.2}$$

which eliminates the dependence on the lineshape function φ_i. The integration can be achieved in practice by fitting an assumed lineshape function to the measured spectrum, or through direct numerical integration. Assuming independent knowledge of pressure and temperature from direct measurements and with the path-length known and fixed (Fig. 3.4), the absorbing species mole fractions x_{abs} can be accurately determined.

A mid-infrared LAS system was developed for online monitoring of various hydrocarbon species (CH_4, C_2H_4, and C_2H_6) present in the conversion process, as shown in Fig. 3.4. Two continuous-wave distributed feedback interband cascade lasers (nanoplus Nanosystems and Technologies GmbH) were used to access the R(15) manifold of the ν_3 band of CH_4 as well as one R(14) transition of the ν_9 band of C_2H_4 near 3166 cm^{-1} and the $^{R}Q_3$ line cluster of C_2H_6 at 2997 cm^{-1}, respectively. The two laser beams were aligned concentrically using flat mirrors and a flip mirror as shown in Fig. 3.4. The manually flipped mirror alternates the laser beams that are focused onto the PV detector (VIGO System, PVI-4TE-5) for one second of data collection every 15 seconds (or 6 seconds during the first 2 minutes to better resolve the initial transient period), yielding an overall 30-seconds time resolution for each species. The lasers are current-modulated to scan over wavelength at 1 kHz to resolve the lineshapes of the spectral transitions and to minimize noise from mechanical vibrations of the solar reactor system. The raw signals were averaged over the one-second collection period, where examples of measured spectra of the target species are shown in Fig. 3.5.

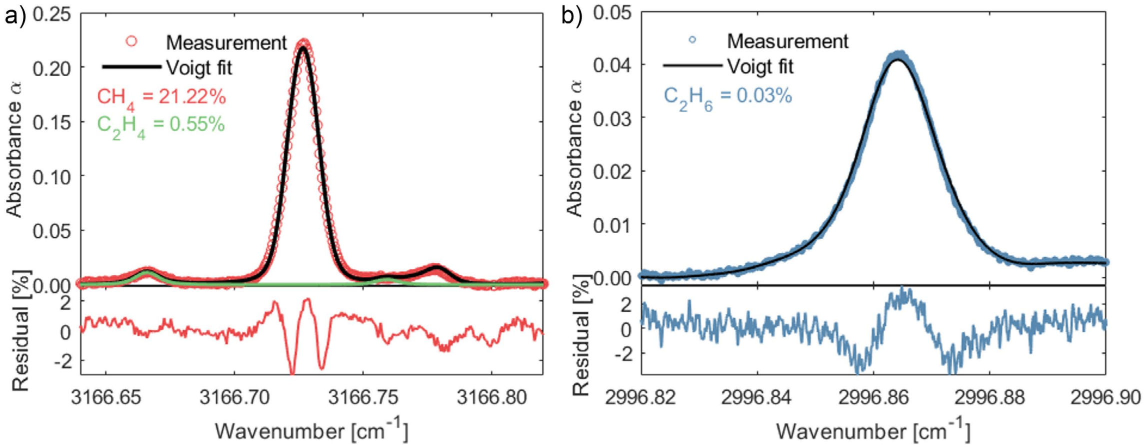

Figure 3.5: Example absorbance spectra and spectral fits of the (a) CH_4 and C_2H_4, and (b) C_2H_6 transitions.

For CH_4 and C_2H_4 measurements, relatively isolated transitions are resolved as shown in Fig. 3.5a. The measured absorbance spectra were least-squares fitted assuming two Voigt lineshapes for CH_4 and C_2H_4. Absorbance areas A_i and collisional width ν_c were free parameters in the fitting process, and the Doppler width ν_d was calculated using temperatures from thermocouple measurements. Mole fractions of each species were then determined from Eq. 3.2. However, for C_2H_6 measurements, rovibrational transitions are numerous and blended such that spectra appear as a continuum rather than discrete transitions. For this case, measured spectra were least-squares fitted with mole fraction x_{abs} directly as the free parameters using spectra parameters provided in literature [132] to model these blended features. The final fractional residual (residual/maximum absorbance) from the Voigt fits of each line cluster was typically less than 2% for all transitions, confirming the general accuracy of the spectral models used.

To further validate and assess the accuracy of LAS measurements, a set of calibration runs for CH_4 monitoring were conducted using known gas stream compositions consisting of the three most prominent product species of the methane decomposition process (CH_4, H_2, and C_2H_2). The gas stream composition was controlled using a calibrated mass flow controller for each species at varying pressures. Results are shown in Fig. 3.6, where all CH_4 measurements agree with an average error of 1.35%.

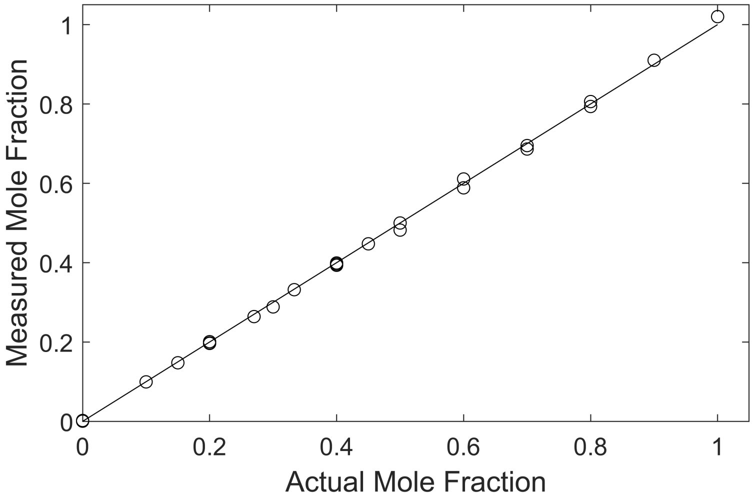

Figure 3.6: CH_4 calibration test runs for the LAS system at different gas compositions and pressures.

3.2.2 RGA monitoring and calibration

A compact, high-resolution residual gas analyzer (RGA) was installed and used as an in situ mass spectrometer (MS) for identification and quantification of the product stream composition. The RGA (INFICON, TSPTT200) consists of an ionizer, a quadrupole mass filter, and 0-200 AMU Faraday cup detector with an electron multiplier that provides enhanced peak amplitude and position stability. Since the RGA needs to operate below pressures of $\sim 1 \times 10^{-3}$ Pa, a suitable configuration was developed to enable continuous sampling from significantly higher pressures while ensuring that pressure within the RGA chamber remains below the maximum acceptable limit. To achieve this, an adjustable leak valve (Kurt Lesker, VZMD9538) was attached to the reactor's outlet stream, while the RGA compartment was coupled to a turbomolecular pump (BOC Edwards, EXT255H/100CF) and a backing rotary vane pump (Edwards, RV3). This configuration allows maintaining a pressure of around 1×10^{-5} Pa within the MS chamber. The leak valve can then be adjusted to control sampling from the reactor's product stream and ensure that MS pressure is maintained within the desired operating range. Such an arrangement can be seen in Fig. 3.7, which provides a response time to changes in the main outlet feed as fast as few seconds.

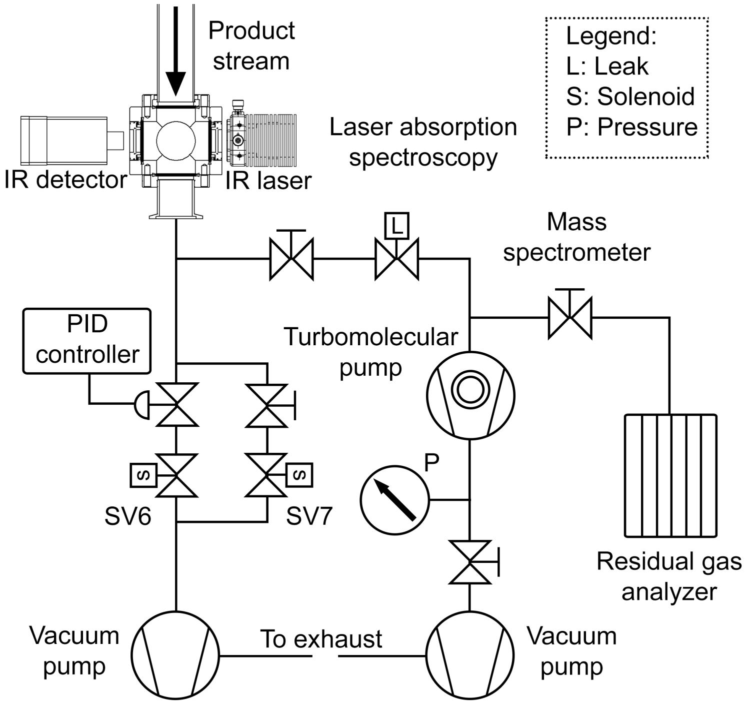

Figure 3.7: Schematic illustrating the MS configuration and sampling from the reactor's main product stream.

Although a MS is a very powerful tool used in qualitative chemical analyses, its sole use for a full quantitative analysis is challenging, and is subject to errors [133]. MS methods usually perform poorer compared to the well-established alternatives (optical spectroscopy, flame ionization detector (FID), etc.) [134]. This results from the MS signal suffering from species signal interference, variation in different ions detection efficiencies, and non-linear calibration curves for broad ranges [135, 136]. Therefore, quantitative analyses using MS are preferably conducted using hyphenated techniques, such as using gas chromatography (GC/MS) and FID. However, with the enhancement of new generation MS and when the analysis is performed on a gas sample with relatively known/expected composition, the MS can be properly calibrated at similar conditions to that experimentally anticipated to provide relatively accurate quantitative results [134, 136]. Acknowledging and mitigating challenges in MS quantification techniques including: (1) species interference, (2) non-linear dynamic response (especially for a wide dynamic range), (3) variable sensitivity for each mass/charge ratio (m/z), and (4) possible calibration changes over time, a MS can be used as an accurate quantification tool for determining the composition of a gaseous stream.

The MS was calibrated to provide relative quantitative results (mole fractions) using known gas stream compositions consisting of the three most expected and prominent product species of the methane decomposition process. Under the investigated process conditions, these are CH_4, H_2, and C_2H_2. The gas stream composition was controlled using a calibrated mass flow controller for each species and at conditions similar to that anticipated experimentally. Such a procedure also accounts for possible variation of species diffusion through the leak valve and into the RGA compartment. The MS calibration runs are plotted in Fig. 3.8, which shows the actual stream composition with respect to that measured upon calibration. These runs were conducted at three different dates to average errors within MS intensity signal variability. For all calibration runs and MS monitoring tests, the pressure in the RGA chamber was maintained at around 1 x 10^{-5} Pa to reduce sensitivity errors.

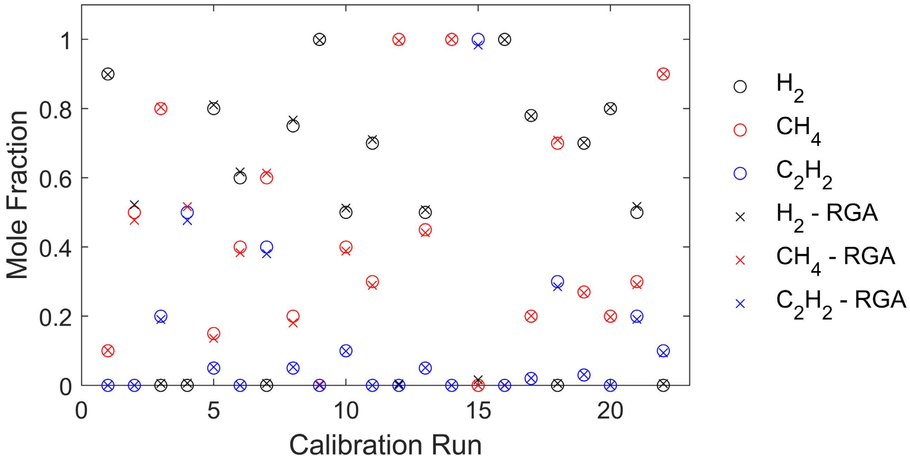

Figure 3.8: Calibration and validation runs of the MS at different gas compositions.

Linear calibration relationships can be obtained especially when a relatively narrow dynamic range is desired [136]. In other cases, a non-linear calibration relationship might be necessary. For MS calibration presented here, a first-order model was used for H_2 and C_2H_2, while a second-order model was used for CH_4. The methodology implemented here consists of first identifying each species fragmentation pattern (mass spectrum) under the RGA optimized configuration (emission current, electron voltage, etc.). The fragmentation patterns obtained for the three prominent species are in good agreement with those available on the NIST database [137]. For example, the fragmentation fractions of H_2 obtained from the MS are 2.12% and 97.88% at 1 and 2 AMU, as compared to 2.06% and 97.94% from the NIST database. Following identification of the fragmentation pattern, the most prominent AMU peak with the lowest interference from the three most prominent species (and other expected species such as C_2H_4 and C_2H_6) was chosen to be representative of the specific species. For H_2, CH_4, and C_2H_2, these are 2, 16, and 26 AMU. By taking into account the fragmentation factor at these masses for each of the representative species, a sensitivity factor was then fitted into the calibration runs to obtain the calibration factor. The calibration factor is then multiplied by the RGA raw current to provide an adjusted intensity current, which along with other intensity currents provide the mole fraction of the specific species.

The calibration factors for H_2 (2 AMU), CH_4 (16 AMU), C_2H_2 (26 AMU), C_2H_4 (28 AMU), and C_2H_6 (30 AMU) are 1.08, $0.88(x_{\mathrm{CH_4}}) + 1.39$, 1.01, 0.91 and 2.08. The latter two calibration factors were obtained using the NIST database fragmentation factors [137] along with the sensitivity factors obtained from fitting MS results to LAS results. This should provide satisfactory quantitative results, since mole fractions of C_2H_4 and C_2H_6 do not exceed 0.5% under various process conditions. Additionally, in the presence of any species that have significant overlapping fragmentation patters (e.g., intensity at 26 AMU is a contribution from C_2H_2, C_2H_4, and C_2H_6), the adjusted intensity accounts for such an overlap using fragmentation factor data and other adjusted intensities. For the example of 26 AMU for C_2H_2, the intensity signal at 26 AMU will be subtracted by the fragmentation factors multiplied by the adjusted intensities of C_2H_4 and C_2H_6 at 26 AMU to obtain the adjusted intensity corresponding to C_2H_2.

Using the calibrated RGA, errors during calibration verification and comparison to LAS results were 1.5, 2.7, 4.2, 28, and 35% for H_2, CH_4, C_2H_2, C_2H_4, and C_2H_6. The relatively large errors in the latter two species are due to their very low concentrations within the product stream and resulting low signal-to-noise ratios. Although the calibration of a MS remains constant for a relatively long time duration, it is vital to check the calibration regularly to avoid any quantification errors [136]. Throughout the work of this research, the calibration factors did not require any further adjustments.

3.3 Carbon product analysis tools

A variety of tools and approaches are used to characterize the quality of the carbon product. The main equipment used and any relevant methodologies are identified in the following sections.

3.3.1 Raman spectroscopy

An in-house custom-built Raman spectrometer was used for obtaining all Raman spectra reported in this work. The instrument's configuration is based on a Horiba iHR 550 imaging spectrometer having a focal length of 550 mm and three different blazed holographic gratings (1200, 1800, and 2400 gr/mm). The Raman spectrometer configuration is shown in Fig. 3.9.

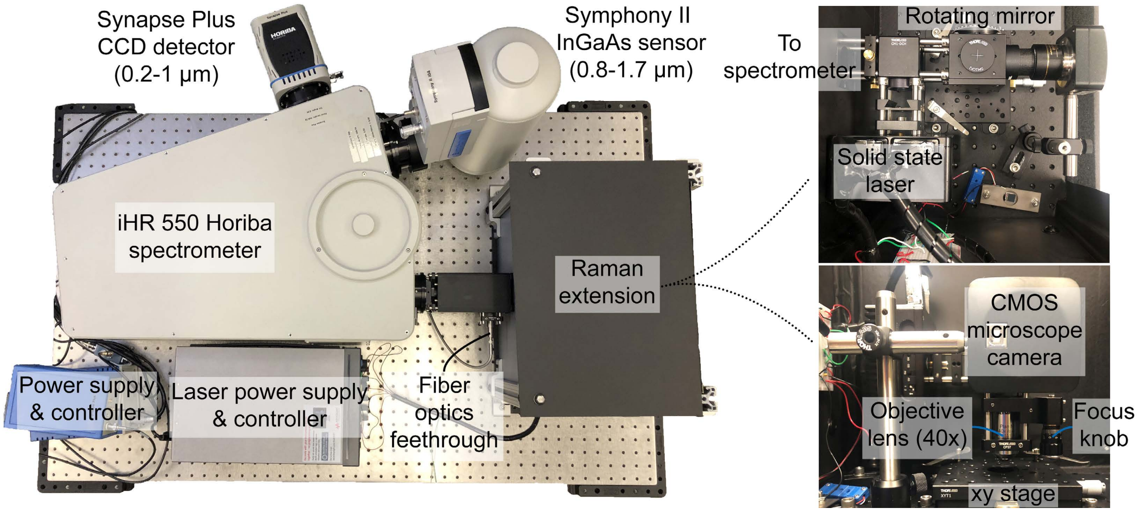

Figure 3.9: Photographs of the Raman spectrometer configuration.

The in-house built Raman extension uses a 532 nm diode-pumped solid state laser with a thermoelectric cooled mount (Thorlabs, DJ532-40 and LDM56), for which the laser's temperature is maintained at 22.5 °C via a PID controller to achieve stable laser emission wavelength. The PID controller is implemented using an external power supply and the PXI system with a custom LabVIEW VI. To further enhance the laser's output, a collimating aspheric lens is installed in front of the laser, where the output is then guided to the sample using a dichroic mirror (cut-off frequency of 550 nm), protected silver mirror on a rotating stage, and a 40× achromatic objective lens (see Fig. 3.9). The choice of the dichroic mirror (reflects $<$ 550 nm and transmits $>$ 550 nm) was mainly to enhance the signal-to-noise ratio (SNR), in contrast to using a beam splitter for instance. To properly place and focus the analyzed sample, a CMOS microscope camera (AmScope, MU1000) is used with the silver mirror turned by 90° to allow for focusing using a z-axis mount for the objective lens. On the scattered light's way back from the sample, the light passes through a notch filter (533 nm with FWHM of 17 nm) to avoid sensor overexposure to the laser's signal. Finally, additional lenses were installed for optimum focusing of the output light through the spectrometer entrance slit to allow for small openings and further improve the SNR. All optical components are optimized to operate within the desired wavelengths through anti-reflective coatings within the range of 350-700 nm. To control the laser's output power, depending on the sample to be analyzed, various neutral density filters are used. In general, 10 mW of output laser power is used to avoid damaging the analyzed samples. It is finally noted that with such a configuration, Raman shifts below $\sim$ 600 cm^{-1} are subject to varying attenuation. However, such an attenuation is not critical for the objectives of the study reported here.

To validate the accuracy of the Raman configuration, three different materials were tested: (a) crystalline silicon (c-Si), (b) acetone, and (c) POCO graphite (used for the study in Chapter 2). The spectra obtained for both silicon and graphite are shown in Fig. 3.10, where the c-Si peak at ≈ 520 cm^{-1} agrees well to that in literature [138]. Same validation applies to the graphite D, G, and 2D peaks at $\approx$ 1350, 1580, and 2700 cm^{-1} [139]. Therefore, accuracy of the custom built Raman spectrometer is validated, and its results can be treated as reliable for the scope of this work.

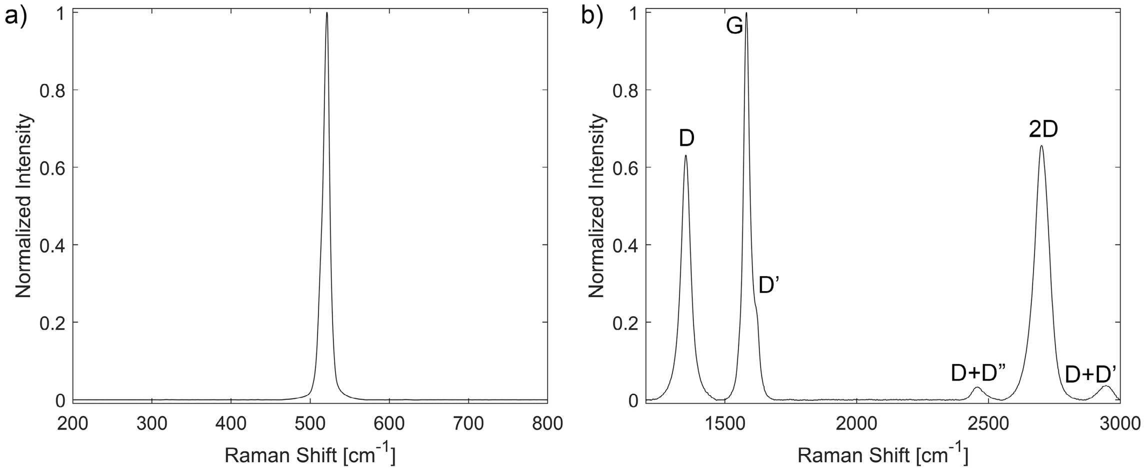

Figure 3.10: Raman spectra of (a) crystalline silicon and (b) POCO graphite measured during the validation steps of the built Raman spectrometer.

Raman scattering (inelastic scattering of photons as opposed to elastic scattering - Rayleigh scattering) can provide great information on the structure of carbonaceous materials in a non-destructive approach [139]. The positions, relative intensities, and shapes of the main Raman peaks (D, G, and 2D) change with the quality of the carbon material, and understanding these changes can significantly aid in characterizing the quality of carbon product of the CH_4 decomposition process studied here [140]. As previously mentioned, the Raman D peak is located at $\approx$ 1350 cm^{-1} and derives its name from “Disorder”, whereas the Raman G peak is located at $\approx$ 1580 cm^{-1} and derives its name from “Graphite” [141]. The changes in these two primary peaks (which can be further decomposed into further peaks in certain cases) provide information on the nature and quality of the carbon material, in addition to the 2D peak located at $\approx 2700\ \mathrm{cm}^{-1}$ [142]. These Raman peaks along with other prominent ones for graphite are shown in Fig. 3.10b.

The aim of this section is to briefly summarize literature observations that are used in characterizing graphitic and amorphous carbon materials. First, observations of moving from a defect-free graphite to a nanocrystalline graphite with a deterioration in quality includes the following: (a) appearance of a D peak and the increase of the D/G peaks intensity ratio ($I_\mathrm{D}/I_\mathrm{G}$), (b) appearance of D' peak at $\approx 1620\ \mathrm{cm}^{-1}$, (c) significant broadening of D, G, and 2D peaks (hence increase in their full widths at half maximum, FWHM), and (d) appearance of the D+D' and D+D" peaks at ≈ 2950 and $2450\ \mathrm{cm}^{-1}$ [139]. Additionally, the intensity ratio $I_\mathrm{D}/I_\mathrm{G}$ varies inversely with the crystallite size (L_a), meaning that the lower the ratio the better the graphite quality [143]. Second, observation of moving from a nanocrystalline graphite to an amorphous carbon with a deterioration in quality includes the following: (a) further increase in FWHM of all peaks, (b) disappearance of distinct D and G peaks as they start to merge (in addition to appearance of other peaks), (c) significant reduction in the 2D peak until disappearance, and (d) generally reduction of the position of the G peak [144, 145]. Thus, the FWHMs of Raman peaks generally increase with the level of disorder [146]. Finally, a laser dependent relationship to estimate the average inter-defect distance, $L_\mathrm{D,Ram}$, is [139]:

$$L^2_\mathrm{D,Ram}\ (\mathrm{nm}^2) = \frac{4.3\times 10^3}{E^4_\mathrm{Las}\ (\mathrm{eV}^4)}\left[\frac{I_\mathrm{D}}{I_\mathrm{G}}\right]^{-1} \tag{3.3}$$

where the laser excitation energy is $E_\mathrm{Las} = \hbar\omega_\mathrm{Las}$ and the relationship is valid for $L_\mathrm{D,Ram} \gtrsim 3$ nm. Based on the laser used throughout this study with a wavelength of 532 nm, the corresponding E_Las is 2.33 eV.

3.3.2 Scanning electron microscopy

A ZEISS Supra 40VP field emission scanning electron microscope (SEM) with a high efficiency In-lens, secondary electrons (SE), and backscattered electrons (BSE) detectors was used to obtain SEM images. The SEM instrument also has a high performance variable pressure mode (VPSE detector) and an integrated energy dispersive (EDS) system for elemental analysis. All carbon samples used and analyzed were of satisfactory conductivity to allow for capturing SEM images using the SE detector without any prior sample preparation steps (e.g., coating). To obtain quantifiable results from SEM images, primarily carbon thickness measurements to quantify growth rates, post processing techniques were applied on resulting images at various different locations (approximately five). Final results are then reported with an uncertainty margin that is twice the measurements' standard deviation.

3.3.3 BET characterization

Surface area measurements were obtained using a high-performance adsorption surface characterization analyzer (Micromeritics, 3Flex). Samples analyzed were all pretreated and outgassed at 250 °C to remove volatile impurities that might affect surface area measurements. Then, by monitoring nitrogen gas adsorption at 77 K, surface areas of different samples were quantified using the adsorption isotherm plots and Brunauer-Emmett-Teller (BET) method [147]. The BET method is an extension of Langmuir adsorption model to multiple layers, with the BET isotherm equation being [147]:

$$\frac{1}{v_a[(p_0/p)-1]} = \frac{c-1}{v_m c}(\frac{p}{p_0}) + \frac{1}{v_m c} \tag{3.4}$$

where v_a is the volume of gas adsorbed, p_0 is the gas saturation pressure, v_m is the monolayer volume of gas adsorbed, and c is the BET constant. By using the intercept (c_{BET}) and gradient (m_{BET}) of the linear region of the isotherm (usually in the range p/p_0 of 0.05-0.3), both v_m and c can be determined using:

$$c = 1 + \frac{m_{\mathrm{BET}}}{c_{\mathrm{BET}}} \tag{3.5}$$

$$v_m = \frac{1}{m_{\mathrm{BET}} - c_{\mathrm{BET}}} \tag{3.6}$$

The total surface area, S_{total}, can then be determined using:

$$S_{\mathrm{total}} = \frac{v_m N_A s_{\mathrm{ad}}}{V_{\mathrm{ad}}} \tag{3.7}$$

where N_A is Avogadro's constant, s_{ad} is the adsorbate molecular cross-sectional area, and V_{ad} is the molar volume of the adsorbate gas.

3.3.4 X-ray diffraction

XRD measurements were obtained using a Panalytical X'Pert Pro X-ray powder diffractometer that is equipped with a Cu Kα source ($\lambda_{\mathrm{XRD}} = 1.54$ Å) operating at 45 kV and 40 mA. The XRD scan ranges from 2θ of 5 to 100°, with a step size of 0.017°. Running at a continuous scanning mode with a computer-controlled divergence slit size, the scan time was set to 11°/min. Structural quantitative parameters of the carbon material can then be determined using XRD spectra. The average interplanar distance between the carbon layers, d_{002}, is determined from the (002) reflection position, θ_{002}, using Bragg's law [142]:

$$d_{002} = \frac{\lambda_{\mathrm{XRD}}}{2 \sin \theta_{002}} \tag{3.8}$$

Additionally, using the full width at half maximum (FWHM) of the (002) reflection in radians, β_{002}, the average crystallite size along the c-axis, $L_{\mathrm{c,XRD}}$, is determined using the Scherrer equation:

$$L_{\mathrm{c,XRD}} = \frac{0.9\lambda_{\mathrm{XRD}}}{\beta_{002}\cos\theta_{002}} \tag{3.9}$$

3.4 Local heat flux distribution

The local heat flux distribution on the porous medium at the solar simulator's focal plane is expected to be less than that determined and presented in Chapter 2. This deviation is due to the following reasons: (a) the quartz window attenuates (absorption) and deforms (refracts) the Lorentzian distribution of the HFSS, (b) the cylindrical reactor's front surface intercepts some irradiation due to displacement of the porous substrate 14.0 cm into the reactor, and (c) reflection and re-radiation from the reactor's walls slightly change the irradiation profile. Therefore, the heat flux distribution was further characterized using the validated inverse mapping method presented in Chapter 2 with the radiometer at the location and conditions of the porous medium. From such characterization, the actual heat flux distribution on the substrate can be determined, and it is expected to have a distribution that combines Lorentzian and Gaussian profiles (see Eq. 2.1).

The heat flux distribution was mapped inversely at different HFSS supply currents ranging from 100-140 A due to method limitations indicated in Chapter 2. Table 3.1 summarizes the parameters' results (per Eq. 2.1) at different supply currents. From Table 3.1, parameters affecting the general distribution of the irradiance (σ_{Lor}, σ_{Gau}, and α_{Lor}) are observed to be relatively constant. This observation is consistent with earlier conclusions of supply current linearly affecting the heat flux distribution, and is further confirmed by Fig. 3.11a, which shows the normalized mean heat flux distribution along with the distribution's upper and lower bounds. All results at different supply currents lie within these two bounds, which represent the uncertainty range. The final heat flux distribution parameters at different supply currents (I) are: $A_{\text{sol}} = 0.683I - 28.52$ kW/m, $\sigma_{\text{Lor}} = 0.0222$ m, $\sigma_{\text{Gau}} = 0.00684$ m, and $\alpha_{\text{Lor}} = 0.595$. Fig. 3.11b shows the local heat flux and cumulative power distributions as a function of radial distance from the center at a HFSS supply current of 160 A. A significant difference is observed between the irradiance distribution on the porous medium presented in Fig. 3.11a (local) and that measured outside the reactor by the HFG in Chapter 2 (gross).

Table 3.1: Summary of inverse heat flux distribution local results for methane decomposition experiments.

Current [A]	A_{sol} [kW/m]	σ_{Lor} [m]	σ_{Gau} [m]	α_{Lor}
100	39.41	0.0172	0.00636	0.627
100	40.97	0.0198	0.00658	0.614
110	45.77	0.0200	0.00663	0.600
110	46.99	0.0224	0.00687	0.597
120	52.14	0.0218	0.00682	0.588
120	53.46	0.0242	0.00707	0.581
130	59.86	0.0234	0.00696	0.583
130	61.55	0.0265	0.00726	0.579
140	67.25	0.0245	0.00704	0.583

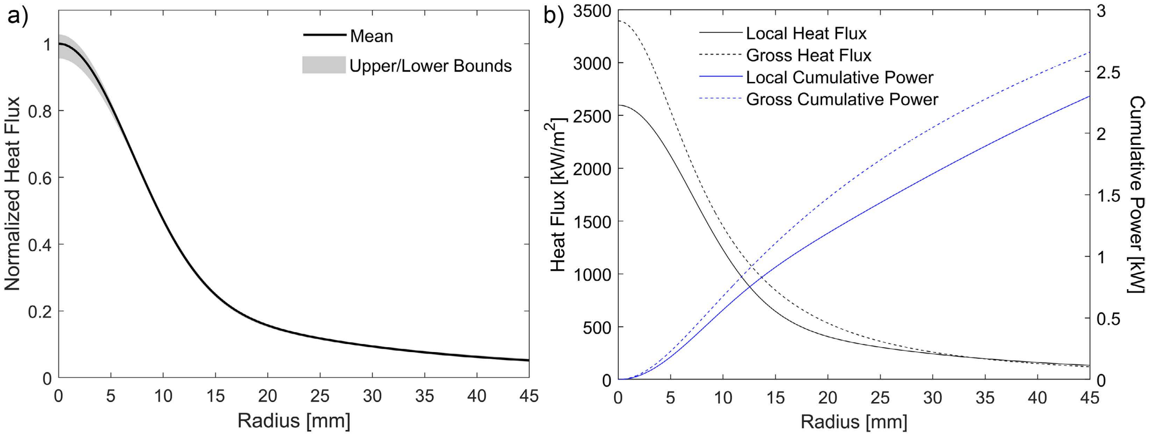

Figure 3.11: Heat flux distribution from the HFSS (a) normalized mean and uncertainty bounds for different inverse characterization tests, and (b) locally within the reactor in contrast to the gross distribution outside the reactor at the focal plane and a supply current of 160 A.

3.5 Conclusions

In this chapter, the solar-thermal methane pyrolysis experimental setup and auxiliaries were thoroughly presented. Process monitoring and characterization tools were also introduced and discussed, which include: (a) LAS, (b) on-line MS, (c) Raman spectrometer, (d) SEM, (e) surface characterization analyzer, and (f) XRD. In the last section of this chapter, the local heat flux distribution on the porous medium at the focal plane was determined. Based on presented results, gross and local total powers at a HFSS current of 160 A and on an area with a diameter of 68.6 mm (size of the porous substrate) were determined to be 2.24 and 1.86 kW. Similar values can be determined at different HFSS supply currents, and are used in upcoming work for numerical modeling and efficiency quantification.

Chapter 4: Methane Decomposition Initial Study[1,2]

In this chapter, an initial investigation of solar-thermal methane pyrolysis through a fibrous carbon medium is thoroughly performed and presented [9]. The solar reactor and auxiliaries were introduced earlier in Chapter 3, in which a porous medium is placed at the HFSS's focal plane and is directly irradiated with simulated solar power. This chapter focuses on defining and quantifying process and product characterization metrics that are used to critically evaluate the potential of the process prior to conducting a parametric study, which is presented in Chapter 5. Photographs of the assembled experimental setup and reactor auxiliaries used for the initial investigation and parametric study (Chapter 5) are shown in Fig. 4.1.

---

[1] All or some portions of this chapter contributed to paper by M. Abuseada, C. Wei, R. M. Spearrin, and T. S. Fisher, titled Solar-thermal production of graphitic carbon and hydrogen via methane decomposition, published in Energy & Fuels 36 (2022), 3920-3928.

[2] All or some portions of this chapter contributed to paper by C. Wei, M. Abuseada, B. Jeevaretanam, T. S. Fisher, and R. M. Spearrin, titled Concentrated solar-thermal methane pyrolysis in a porous substrate: Yield analysis via infrared laser absorption, published in Proceedings of the Combustion Institute (2022).

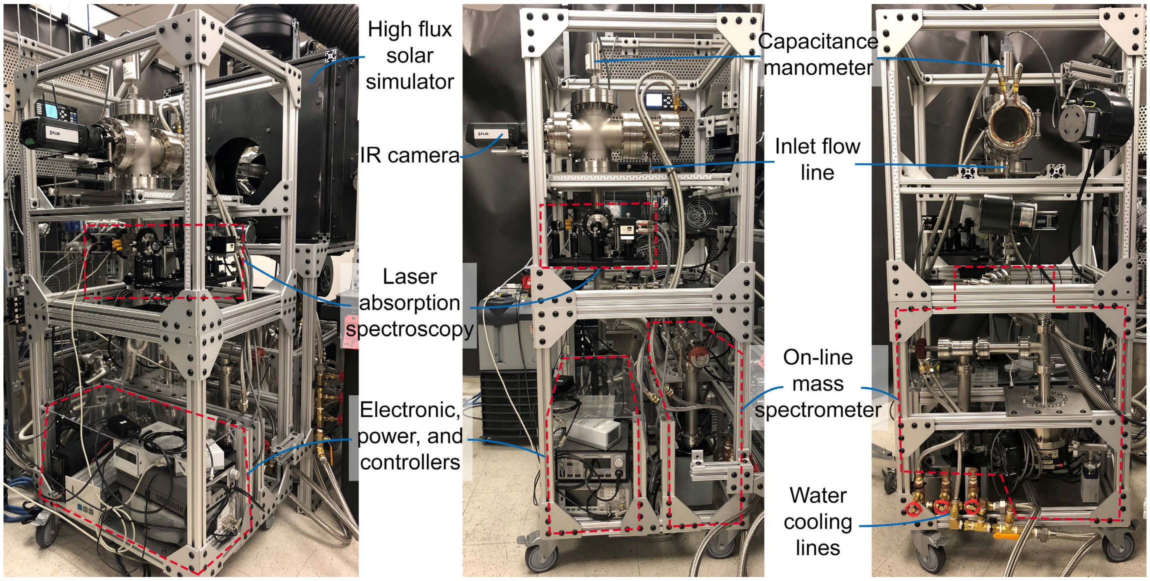

Figure 4.1: Photographs of the solar methane decomposition small-scale reactor from different views: (left) perspective, (middle) side, and (right) front.

4.1 Theory and methodology

4.1.1 Carbon felt composition and pretreatment

The carbon felt used in the present investigation (FuelCellEarth, C100) can be approximated as a regular array of carbon fibers. Fiber diameters in the C100 carbon felt are approximately $D_{\text{fib}} = 9.6$ µm, and its effective density is calculated from the manufacturer's specifications for areal density of 285 g/m^2 and thickness of 3.2 mm:

$$\rho_{\text{C100}} = \frac{\text{Areal Weight}}{\text{Thickness}} = \frac{285}{0.0032}\ \text{g/m}^3 = 89\ \text{kg/m}^3 \tag{4.1}$$

The C100 felt is made from PAN (polyacrylonitrile) fibers, whose solid density falls in the range of 1.75 to 1.93 g/cm^3 [148]. Here, the average value of 1.84 g/cm^3 (1840 kg/m^3) is adopted. Moreover, the conformal pyrolysis growth product is initially assumed to maintain this solid density. Given the foregoing metrics and assumptions, the solid volume fraction of the C100 felt is:

$$\Phi_{\text{C100}} = \frac{89\ \text{kg/m}^3}{1840\ \text{kg/m}^3} = 0.0484 \tag{4.2}$$

This volume fraction provides a basis for calculating the average fiber pitch (P) in the C100 felt:

$$P^2 = \frac{1}{0.0484}\frac{\pi D^2}{4} \rightarrow P = 4.03D = 38.7\ \mu\text{m} \tag{4.3}$$

At this average pitch, the number of rows of fibers through the thickness of the felt is $N = 83$.

Prior to methane decomposition, the carbon felt is thermally-treated under the same power and distribution from the HFSS, and for a duration of approximately 20 min in a vacuum environment. The main motivation for the thermal pretreatment is to purify the felt from volatiles and trapped air to obtain more accurate mass measurements of the felt before and after processing to determine the total mass of carbon produced and captured. After the thermal pretreatment, the carbon felt loses approximately 3% of its total original mass.

To investigate the thermal stability of the carbon felt further and confirm prior experimental observations, a thermogravimetric analysis (TGA) was performed on the original C100 carbon felt using a Pyris Diamond TG/DTA (PerkinElmer). A carbon felt with a starting mass of 17.4 mg was placed in an alumina crucible and heated to approximately 1300 K at a rate of 20 K/min in an argon inert atmosphere, after which the temperature was maintained for additional 40 min. The sample temperature and percent weight with respect to time are shown in Fig. 4.2.

The TGA results in Fig. 4.2 indicate a bake-off of approximately 1% starting near 400 K that is likely related to moisture. A plateau then occurs until 1200 K. Thereafter, as the sample temperature approaches and persists at the instrument's

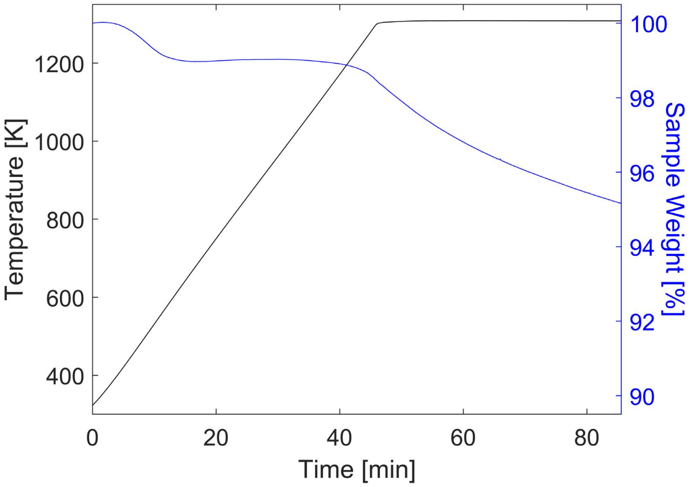

Figure 4.2: Thermogravimetric analysis performed on original C100 carbon felt for a temperature up to 1300 K.

limit (1300 K), a steady, moderate mass loss is apparent that is likely related to mild pyrolysis of the pre-carbonized fibers. The TGA results thus indicate that the starting carbon felt substrate is relatively thermally stable, consistent with prior observations of low mass loss during thermal pretreatment.

4.1.2 Temperature measurements

Spatial temperature measurements of the fibrous medium are recorded using a high-resolution science-grade longwave IR camera that is factory-calibrated to a maximum temperature of 2000 °C with a manufacturer's estimated uncertainty of ± 2%. The IR camera has been calibrated in-house to the fibrous material and optics used in this work with a reference temperature transducer, producing a calibration emissivity of 0.9 and a temperature uncertainty estimate of ± 30 K. As shown in Fig. 3.1 and Fig. 4.1, the IR camera primarily monitors temperatures of the fibrous medium's back (unilluminated) side, which can potentially be significantly lower than front (illuminated) side temperatures due to limited thermal conductivity of the original felt prior to carbon deposition.

Due to the nature of the porous medium and carbon deposition, the temperature distribution of the medium changes during methane decomposition experiments. As carbon deposits onto the fibrous medium, its thermal conductivity significantly increases, resulting in more effective thermal transport along and through the medium. This phenomenon changes operating temperatures slightly under otherwise constant conditions. As illustrated in Fig. 3.1, temperature measurements of the rear, unilluminated side of the fibrous medium are recorded, with no access to front surface temperatures. Therefore, duplicate testing was performed using a different experimental configuration shown in Fig 4.3 that allows measurements of front surface temperatures from a 45° viewport, while still validating rear surface temperatures measured in the usual setting (Fig. 3.1). This angled perspective does not change the fibrous material's effective emissivity [149], but it results in a slightly distorted image (see Fig. 4.3). Measured temperatures from the configuration shown in Fig. 4.3 are used to determine the relationship between front and backside temperatures, while the usual configuration shown in Fig. 4.1 is primarily used in testing as it is more compact and faster responding.

As a result of enhancement in radial and axial thermal conductivity upon methane pyrolysis and carbon deposition, front temperatures of the fibrous medium decrease over time, while rear temperatures increase. Fig. 4.4 shows the maximum front and back temperatures measured on a 3.2 mm thick fibrous medium during methane pyrolysis at solar power of 1.86 kW, methane inlet flow rate of 100 sccm, and pressure of 3.33 kPa, which constitute the experimental conditions of the present initial study. The temporal temperature change reaches an approximate steady-state with sufficient carbon deposition, such that both front and rear surface temperatures remain relatively unchanged but with a radial temperature gradient due to the solar irradiation profile (Eq. 2.1). Front temperatures decrease by

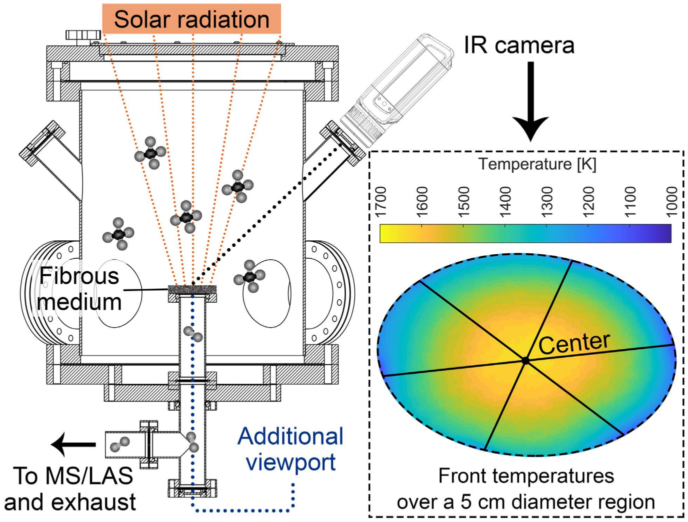

Figure 4.3: Schematic illustration of experimental setup used to measure front surface temperatures, with the front temperature contour (distorted due to 45° view angle) shown on right.

approximately 50-180 K, depending on operating conditions and medium thickness, and rear temperatures increase by approximately 20-100 K, giving a temperature gradient between front and rear surfaces at thermal steady-state of 20-60 K. Therefore, temperature measurements reported in this study correspond to the measured steady-state rear temperatures at the center, which also coincides with the location of carbon product characterization. Because of the temperature gradient between the front and rear surfaces, the uncertainty of reported temperature measurements is increased to 60 K. A more detailed study on thermal transfer changes over time is outside the scope of this work.

4.1.3 Chemical kinetics analysis

Laser absorption spectroscopy

The full quantitative analysis using only laser absorption spectroscopy results and all the dominant species involved implements the assumption of a steady-state

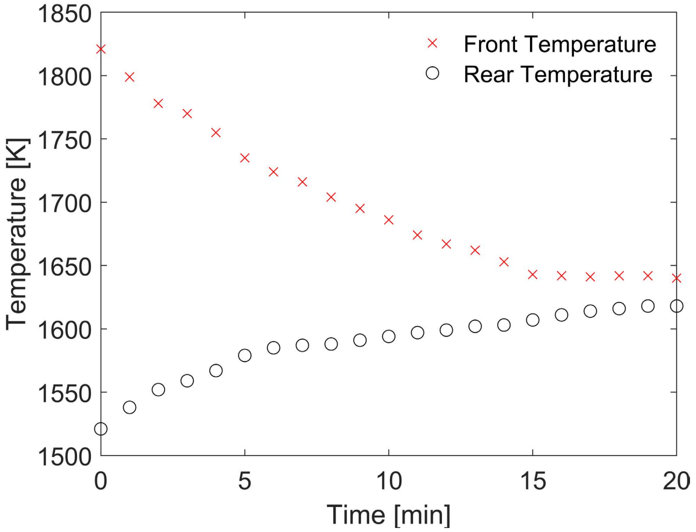

Figure 4.4: Maximum front and back temperatures measured during methane pyrolysis at solar power of 1.86 kW, methane inlet flow rate of 100 sccm, pressure of 3.33 kPa, and reaction zone thickness of 3.2 mm.

process. This assumption is due to dependency of the analysis on the total mass of carbon collected and measured through the methane decomposition process to quantify the mole fraction of C_2H_2, which is not being continuously monitored [150]. By considering only the five most dominant species in the product stream (0.1% or higher), which are H_2, CH_4, C_2H_2, C_2H_4, and C_2H_6, a list of equations is formulated for conversion and product yields quantification as described in Appendix B. In a follow-up work outside the scope of this dissertation, the capability of monitoring acetylene was further added to obtain transient conversion and yield measurements, and to have a more robust monitoring system.

Mass spectroscopy

With the product stream composition (mole fractions) fully quantified using the calibrated MS, methane conversion (X_{CH4}), hydrogen yield (Y_{H2}), and carbon yield (Y_{C}) of the process can be identified. The analysis considers only the five most dominant species in the product stream (0.1% or higher), which are H_2, CH_4, C_2H_2,

C_2H_4, and C_2H_6, and does not require the assumption of a steady-state process. By formulating a balance over the hydrogen atoms, the following relation ensues:

$$2\dot{n}_{\mathrm{CH_4,in}} = \dot{n}_{\mathrm{out}}(x_{\mathrm{H_2}} + 2x_{\mathrm{CH_4}} + x_{\mathrm{C_2H_2}} + 2x_{\mathrm{C_2H_4}} + 3x_{\mathrm{C_2H_6}}) \tag{4.4}$$

where the molar flow rate of CH_4 is quantified through $\dot{n}_{\mathrm{CH_4,in}} = \dot{V}_{\mathrm{CH_4}}\bar{\rho}_{\mathrm{CH_4}}$. $\dot{V}_{\mathrm{CH_4}}$ is the volumetric flow rate controlled via the mass flow controllers and $\bar{\rho}_{\mathrm{CH_4}}$ is the methane gas density under standard conditions. Note that "out" has been omitted from mole fractions of the product stream for brevity; no mole fractions are presented for the inlet stream because the inlet flow is pure methane. Rearranging the above, an expression to quantify the total molar flow rate out is derived as:

$$\dot{n}_{\mathrm{out}} = \frac{2\dot{n}_{\mathrm{CH_4,in}}}{x_{\mathrm{H_2}} + 2x_{\mathrm{CH_4}} + x_{\mathrm{C_2H_2}} + 2x_{\mathrm{C_2H_4}} + 3x_{\mathrm{C_2H_6}}} \tag{4.5}$$

Upon obtaining the outlet molar flow rate, methane conversion, defined as the relative difference between inlet and outlet methane flow rates, is calculated as:

$$X_{\mathrm{CH_4}} = \frac{\dot{n}_{\mathrm{CH_4,in}} - \dot{n}_{\mathrm{out}}x_{\mathrm{CH_4}}}{\dot{n}_{\mathrm{CH_4,in}}} \tag{4.6}$$

Similarly, the overall hydrogen yield, defined as the fraction of inlet hydrogen that emerges as hydrogen gas in the product stream, is quantified as:

$$Y_{\mathrm{H_2}} = \frac{\dot{n}_{\mathrm{out}}x_{\mathrm{H_2}}}{2\dot{n}_{\mathrm{CH_4,in}}} \tag{4.7}$$

Then, from a balance over carbon atoms, the rate of carbon mass deposition is:

$$\dot{m}_{\mathrm{C}} = [\dot{n}_{\mathrm{CH_4,in}} - \dot{n}_{\mathrm{out}}(x_{\mathrm{CH_4}} + 2x_{\mathrm{C_2H_2}} + 2x_{\mathrm{C_2H_4}} + 2x_{\mathrm{C_2H_6}})]M_{\mathrm{C}} \tag{4.8}$$

In a similar manner to the overall hydrogen yield, the total carbon yield is:

$$Y_{\mathrm{C}} = \frac{\dot{m}_{\mathrm{C}}}{M_{\mathrm{C}}\dot{n}_{\mathrm{CH_4,in}}} \tag{4.9}$$

4.1.4 Efficiency quantification

In this section, two approaches to efficiency quantification will be defined, where each efficiency form will provide different insights on the methane decomposition process. The first approach is a definition of the solar-to-hydrogen (STH) efficiency as [151]:

$$\eta_{\mathrm{sth}} = \frac{\dot{n}_{\mathrm{H_2,out}} HHV^{o}_{\mathrm{H_2}}}{\dot{Q}_{\mathrm{sol}}} \tag{4.10}$$

where $\dot{n}_{\mathrm{H_2,out}}$ is the hydrogen product molar flow rate and HHV is the higher heating value of hydrogen (285.8 kJ/mol) [18]. However, this STH efficiency form is generally used in solar hydrogen production from H_2O and hence it does not take into account the starting fuel (CH_4) in methane decomposition nor the carbon product. Therefore, this estimation might lead to an overestimation of the actual process efficiency. Nevertheless by taking into account this caveat, the STH efficiency can provide some insights in contrast to hydrogen production from other sources.

A different, more applicable form of efficiency for methane decomposition is provided here by the definition of solar-to-chemical (STC) efficiency as [53, 61]:

$$\eta_{\mathrm{stc}} = \frac{X_{\mathrm{CH_4}}\dot{n}_{\mathrm{CH4,in}}\left[\int_{T_{\mathrm{in}}}^{T_{\mathrm{R}}} \bar{c}_{p,\mathrm{CH4}}(T)\mathrm{d}T + \Delta H_{\mathrm{R}}(T_{\mathrm{R}})\right]}{\dot{Q}_{\mathrm{sol}}} \tag{4.11}$$

where ΔH_{R} is the reaction's molar enthalpy change at the average reaction temperature T_{R} measured on the fibrous medium, $\bar{c}_p$ is the molar heat capacity, and $X_{\mathrm{CH_4}}$ represents the degree of methane conversion. This form of efficiency assumes that ideal methane pyrolysis occurs, with no side reactions or byproducts (CH_4 converts to H_2 and C only), and it does not consider the thermal energy consumed in heating the unconverted methane feed. In quantifying the molar enthalpy change of the reaction, temperature-dependent properties of fluid [152] and solid carbon (graphite) [153] were evaluated from literature. For efficiency estimation, the solar power term $\dot{Q}_{\mathrm{sol}}$ is quantified using the exposure area of the substrate/felt in addition to the net irradiance from the HFSS as quantified in Chapter 3. For a substrate size of 68.6 mm in diameter, the net solar power is 1.86 kW under a HFSS supply current of 160 A. This compares to a gross solar power of 2.24 kW, which does not take into account optical attenuation due to the quartz window in addition to other effects.

4.1.5 Residence time and permeability

The mean residence time (or space time) of the flow is estimated based on the assumption of pure methane flow over the entirety of the reaction zone (porous carbon medium). From porosity of the fibrous medium (ψ), the mean residence time (t_{res}) is estimated using:

$$t_{\mathrm{res}} = \frac{\rho_{\mathrm{CH_4}}(T_{\mathrm{R}})\pi d_{\mathrm{R}}^2 L_{\mathrm{R}}\psi}{4\dot{m}} \tag{4.12}$$

where $\psi = 0.952$, d_{R} and L_{R} are the reaction zone diameter (6.86 cm) and thickness, $\dot{m}$ is the mass flow rate of inlet methane, and $\rho_{\mathrm{CH_4}}(T_{\mathrm{R}})$ is the density of CH_4 gas at the average reaction temperature. Certainly, gas residence times are anticipated to have a relatively wide distribution due to flow dispersion through the fibrous medium and temperature gradients within the reaction zone that can significantly affect chemical kinetics. However, detailed analysis of the residence time distribution is outside the scope of this work. Furthermore, fluid permeability (k_p) through the porous medium is estimated roughly using an expression for an incompressible isotropic fluid steady-state flow through a unidirectional fiber bed [154], which provides comparable results to other work [155]:

$$\frac{k_p}{r_\mathrm{f}} = \frac{\pi\psi(1-\sqrt{1-\psi})^2}{24(1-\psi)^{1.5}} \tag{4.13}$$

where r_f is the fiber radius within the porous medium.

4.2 Overall process performance

Methane solar decomposition through a 3.2 mm thick carbon felt is tested under a maximum central gross irradiance of 3400 suns with 99.999% pure methane inlet flowing at 100 sccm under an operating pressure of 3.33 kPa for a duration of 20 min. This irradiance corresponds to 2.24 kW gross and 1.86 kW net radiant powers, for which the current supplied to the HFSS is 160 A (see Fig. 3.11b). The steady-state temperature distribution of the carbon felt is shown in Fig. 4.5a and the carbon felt product is shown in Fig. 4.5b. Infrared temperature mapping (Fig. 4.5a) reveals a large temperature gradient in the substrate that is primarily a consequence of the Lorentzian/Gaussian light source distribution. This characteristic of the experimental setup allows considering light intensity and temperature effects on the deposition process in a single experiment. The central circular region (20 mm diameter) of the substrate produces temperatures well above 1000 K, beyond which the substrate temperatures decrease markedly with increasing radius. The local gross heat flux at the edge of this central region (r = 10 mm) is 1450 suns, and the average from the center to r = 10 mm is 2150 suns. From a practical standpoint, these levels of temperature and solar concentration, while relatively high, have been shown to be readily achievable in large-scale field demonstrations [156, 157].

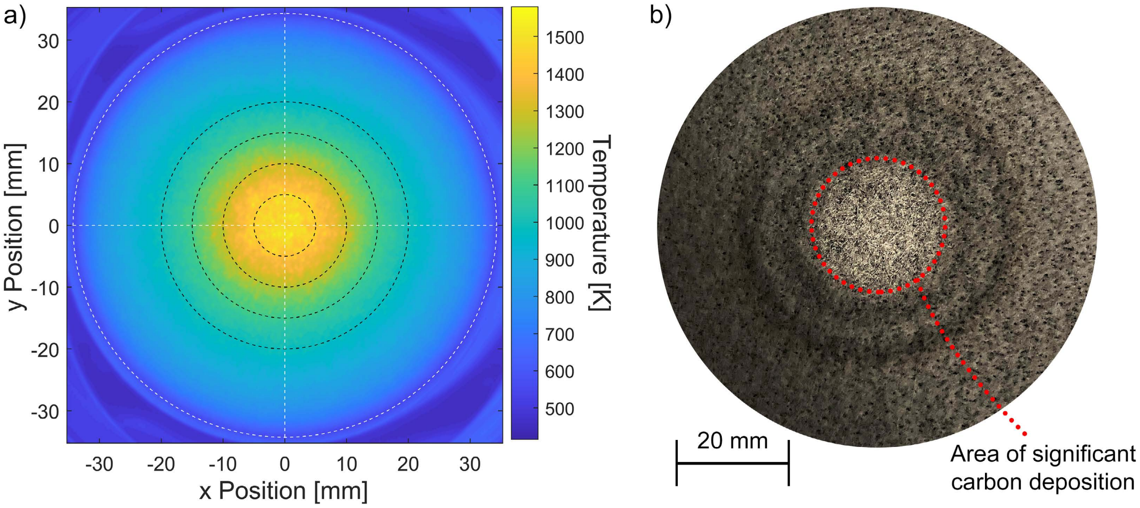

Figure 4.5: (a) Temperature profile of the carbon felt's back surface during CH_4 decomposition obtained using the IR camera (centered black rings with r = 5, 10, 15, and 20 mm illustrate distribution and angular uniformity), and (b) photograph of carbon felt with carbon deposition. CH_4 decomposition at 100 sccm flow rate, 3.33 kPa pressure, 1.86 kW net radiant power, and 20 min reaction period.

The LAS setup provides real-time product monitoring of the initial CH_4 decomposition testing. Fig. 4.6a shows time-resolved quantitative measurements of methane (CH_4), ethylene (C_2H_4), and ethane (C_2H_6) in the product gas stream. When the solar irradiance is instantaneously focused on the porous substrate and reactor initially at room temperature (at time 0), decomposition rapidly decreases methane concentration in the product stream, yielding primarily hydrogen and solid carbon deposition. From Fig. 4.6a, the transition from room temperatures to steady-state operating conditions is seen to be reached within the first minute of insolation, where methane mole fraction stabilizes at 0.16 and temperatures within the carbon felt reach semi-steady values (Fig. 4.5a). The one minute required for steady operating conditions also accounts for the residence time of the product stream from the reaction zone up until the LAS monitoring location. In contrast, the evolution of temperature under solar irradiance from room temperature is shown in Fig. 4.6b, where the process reaches steady thermal operating conditions in approximately 5 seconds. Upon methane decomposition for 20 minutes, the weight of the carbon felt increased by 0.62 g and the processed felt is shown in Fig. 4.5b with an indication of the area with significant carbon deposition. The amount of collected solid carbon on the substrate represents 58% of the available carbon in the inlet methane feed during testing.

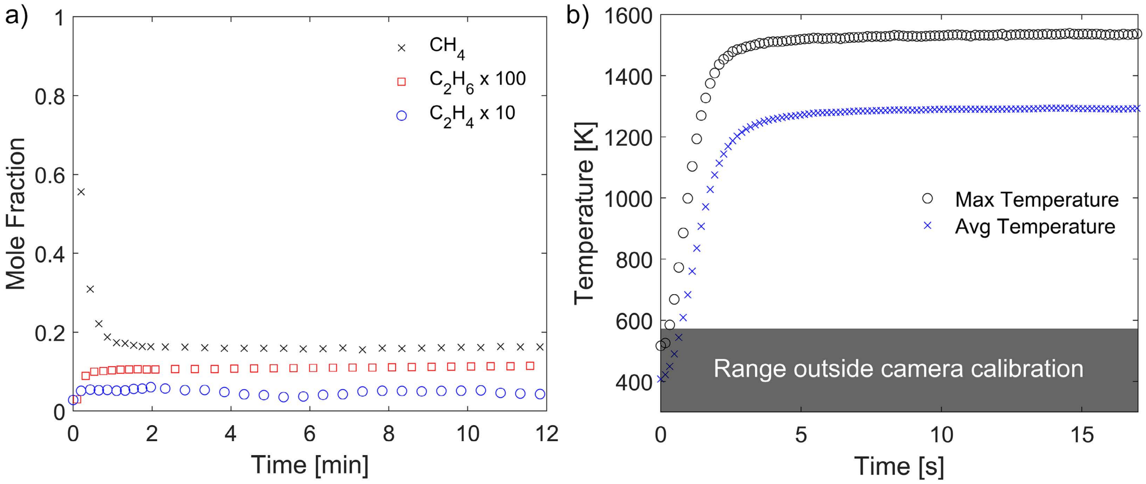

Figure 4.6: Methane pyrolysis at flow rate of 100 sccm, pressure of 3.33 kPa, solar power of 1.86 kW, and medium thickness of 3.2 mm showing (a) product mole fractions as a function of time as measured by LAS, and (b) maximum and average temperatures of the fibrous medium.

A significant challenge with many thermal energy systems, including solar-thermal fuels and electric power production, is their slow startup time response of the order of hours [158]. A slightly faster response is reported for a methane decomposition solar reactor, where it took 40 min to reach steady-state temperatures of similar magnitudes to this study [55]. Although not explicitly specified in other prior methane pyrolysis studies, the transient response period is anticipated to be longer [51]. In contrast, the process reported here shows a much faster time response of approximately 1 min to reach steady-state thermochemical conditions (see Fig. 4.6a). The fast response is primarily the result of the low thermal mass of the carbon felt, which serves as both efficient light absorber and catalytic substrate. This feature enables the opportunity for high levels of process control under realistic field insolation conditions. To highlight this attribute further, the light source was cycled in an on/off manner with a period of 2 min under constant methane flow. The resulting LAS monitoring of the methane product stream is shown in Fig. 4.7, which demonstrates the repeatability of both the fast response and return to high methane conversion levels.

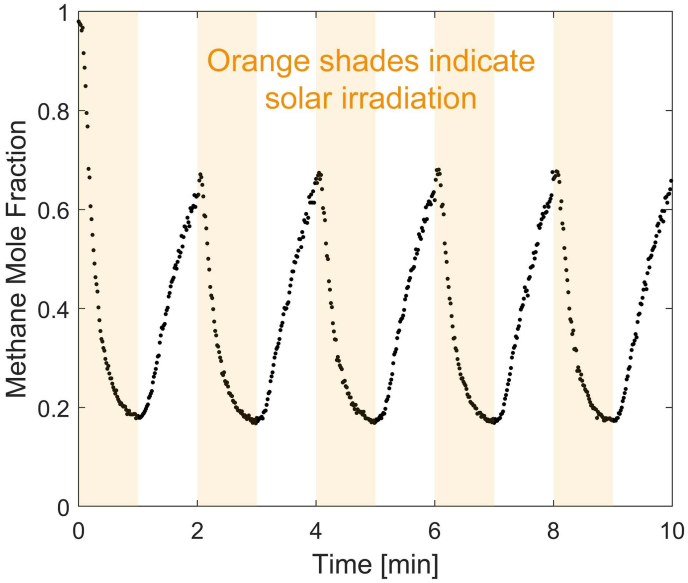

Figure 4.7: Methane product mole fraction as a function of time under HFSS solar irradiation cycling in an on/off manner at flow rate of 100 sccm, pressure of 3.33 kPa, solar power of 1.86 kW, and medium thickness of 3.2 mm.

4.3 Chemical kinetics and pyrolysis performance

To assess the overall methane-to-hydrogen conversion efficacy of the present process, the definitions of methane conversion in addition to the overall hydrogen and carbon yields (Eqs. 4.6, 4.7, and 4.9) are used. Real-time monitoring results from the calibrated MS setup are shown in Fig. 4.8 for (a) mole fractions of the five most prominent species and (b) methane-to-hydrogen performance metrics for CH_4 decomposition through the carbon felt at 100 sccm flow rate, 3.33 kPa pressure, and a total decomposition period of 20 min. Because the process reaction pathways also yield minor hydrocarbon byproducts (C_2H_2, C_2H_4, and C_2H_6), detection of these species enables a more complete understanding of the photothermal catalysis efficacy and provides for process optimization. It is clear from Fig. 4.8a that most of the methane feed is converted to hydrogen (high hydrogen selectivity), with the presence of minimal byproducts out of which C_2H_2 is the most prominent one.

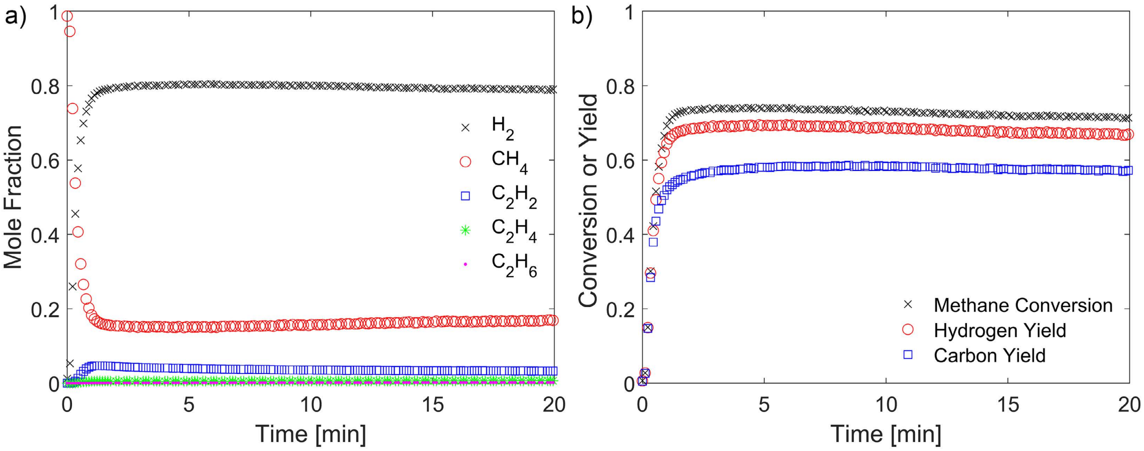

Figure 4.8: Real-time monitoring results from the calibrated mass spectrometer showing (a) mole fractions in the product stream, and (b) methane conversion and product yields for CH_4 decomposition through carbon felt at 100 sccm flow rate, 3.33 kPa pressure, 1.86 kW solar power, and 20 min reaction period.

Notably, methane conversion remains stable for 20 min during significant accumulation of solid carbon on the substrate (see Fig. 4.5b). The steady-state methane conversion, hydrogen yield, and carbon yield are 73%, 69%, and 58.3%, and the net actual carbon mass collected on the felt during the 20 min duration was 0.62 g (equivalent to carbon yield of 58%). The result of the carbon collected yield compared to that from a mass balance analysis (58% compared to 58.3%)

indicates that no or very little carbon deposition occurs outside of the carbon felt. Additionally, as a consequence of C_2H_2 formation, the hydrogen yield slightly decreases from 73% (CH_4 conversion) to 69%, while the carbon yield experiences a much greater reduction to 58.3%. This reduction is due to the four times higher carbon/hydrogen ratio in C_2H_2 as compared to CH_4. For operating conditions investigated in this initial study, process efficiencies are quantified as $\eta_{\mathrm{sth}} = 1.57\%$ and $\eta_{\mathrm{stc}} = 0.44\%$.

A distinguishing attribute of the present results is the short residence time of gases in the reaction zone that nevertheless allows high graphitic growth rates and hydrogen yields. Here, the estimated reaction residence time is 44 ms (Eq. 4.12), whereas it varied from 3 to 26 s in prior thermal CVD experiments [159]. A previous study of solar methane pyrolysis with indirect irradiation [55] at a temperature (1600 K) and residence time (70 ms) similar to the present work reported methane conversion of 72% and a substantially lower hydrogen yield of 57% due to incomplete dissociation. In this study, despite graphitic carbon growth focused at the center of the substrate, relatively high hydrogen yields are observed from the bulk flow, much of which passes through substrate regions where little carbon is captured. This observation likely results from a kinetically limited process wherein the stepwise reduction in H:C ratio via hydrogen abstraction does not reach equilibrium or solid carbon formation within the residence time. This explanation is consistent with a relatively lower carbon yield compared to hydrogen yield.

Comparison between LAS and MS results

Measurements obtained through LAS and MS for species concentration are compared in this section to further verify the accuracy of the two independent monitoring techniques. This comparison is included in Table 4.1, where CH_4, C_2H_4, and C_2H_6

are being directly monitored via both techniques. However, unlike MS, H_2 and C_2H_2 are not directly monitored in the current LAS setup but are rather estimated through balances over the carbon and hydrogen atoms. The measurements summarized in Table 4.1 are consistent, which further verify the accuracy of results reported in this work. Note that mole fractions in Table 4.1 do not add up exactly to 100% due to rounding errors.

Table 4.1: Comparison of LAS and MS measurements of species concentration for methane decomposition through carbon felt at 100 sccm flow rate, 3.33 kPa pressure, and 1.86 kW solar power.

	Mole Fraction [%]				
Technique	H_2	CH_4	C_2H_2	C_2H_4	C_2H_6
LAS	79.6	16.0	3.7	0.51	0.11
MS	80.0	15.6	3.6	0.56	0.18

4.4 Solid carbon characterization

4.4.1 Deposition rates and morphology

To quantify the carbon deposition and fiber growth rates, SEM images were obtained at radial increments of 2.5 mm starting from the center of the cylindrical felt and up to a radius of 25 mm. The most relevant raw SEM images of the processed carbon fibers are shown in Fig. 4.9 for radial locations varying from 0 to 12.5 mm.

The product stream gas-phase measurements presented earlier are consistent with post-processed SEM images of the fibers shown in Fig. 4.9. SEM images were analyzed using a post-processing software to estimate the fiber diameters at multiple locations based on the scale bar defined in each image, where a single

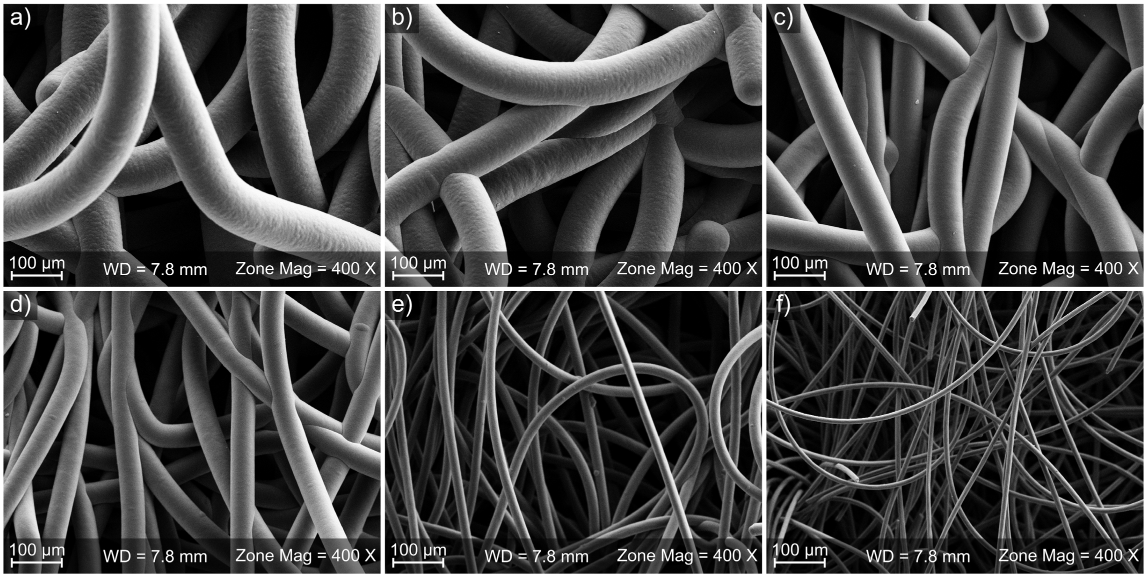

Figure 4.9: SEM images of the carbon felt after methane decomposition and carbon deposition at 100 sccm flow rate, 3.33 kPa pressure, 1.86 kW solar power, and 20 min reaction period for radial distances of (a) 0, (b) 2.5, (c) 5, (d) 7.5, (e) 10, and (f) 12.5 mm from the center and under the same magnification.

averaged fiber diameter is determined at each location with its corresponding uncertainty interval. The results are plotted in Fig. 4.10a in contrast to the original fibers diameter. Comparing the original fibers to the processed ones (Fig. 4.10a), the carbon fiber thickness at the center of the reaction zone increases significantly from 9.6 to 97 µm over the duration of 20 min only. This increase occurs around the region with a maximum temperature of $\sim$ 1500 K. The fiber diameter decreases significantly with respect to radial distance from the center due to the temperature distribution as a result of the Lorentzian/Gaussian irradiation distribution. Beyond a radial distance of approximately 25 mm, no carbon deposition took place, where the local temperature is estimated to be $\sim$ 900 K.

The original core of the fiber and the deposited carbon layers are clearly apparent in Fig. 4.10b, where the SEM image suggests a less dense and possibly microporous structure. This is further investigated and verified through N_2

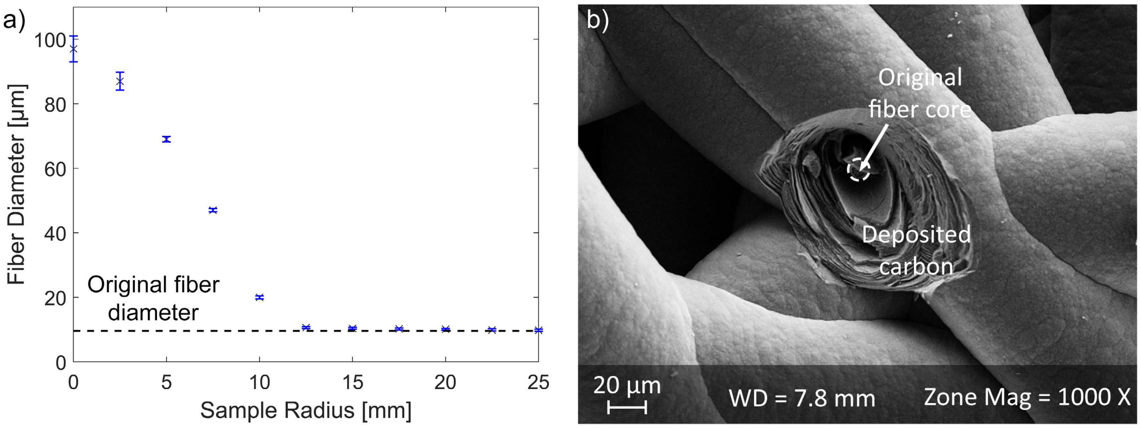

Figure 4.10: Morphology analysis on carbon felt product showing (a) fiber diameter as a function of radial distance from the center as compared to the original carbon felt diameter, and (b) SEM image at the center of the carbon felt demonstrating the nature and amount of carbon deposition. CH_4 decomposition at 100 sccm flow rate, 3.33 kPa pressure, 1.86 kW solar power, and 20 min reaction period.

adsorption and BET surface area characterization of the original carbon felt in addition to the product felt at radial ranges of 0-5 mm and 5-10 mm from the center. Samples were outgassed (as described in Chapter 3) and kept in their solid form. The BET surface characterization results are summarized in Table 4.2, with the sample mass after outgassing indicated, and the BET range used for the surface area quantification was for a relative pressure (P/P^o) of 0.1-0.3.

Table 4.2: Summary of BET results at different radial regions of the carbon felt for CH_4 decomposition at 100 sccm flow rate, 3.33 kPa pressure, 1.86 kW solar power, and 20 min reaction period.

Radius [mm]	Sample mass [mg]	BET specific surface area [m^2/g]	BET constant	Correlation coefficient
0-5	102	7.58 ± 0.09	2.07	0.997
5-10	137	3.03 ± 0.09	2.23	0.984
Original	85	1.54 ± 0.04	3.49	0.996

Although the BET correlation is below 0.999 and can be subject to slight inaccuracies, the purpose of this characterization was mostly to compare the relative surface area of the original carbon felt to that containing the carbon product through CH_4 decomposition. Through such a comparison, the nature of the carbon product deposited can be determined. For completeness, BET plots obtained for the carbon product in the central region (0-5 mm) in addition to the original carbon felt are shown in Fig. 4.11.

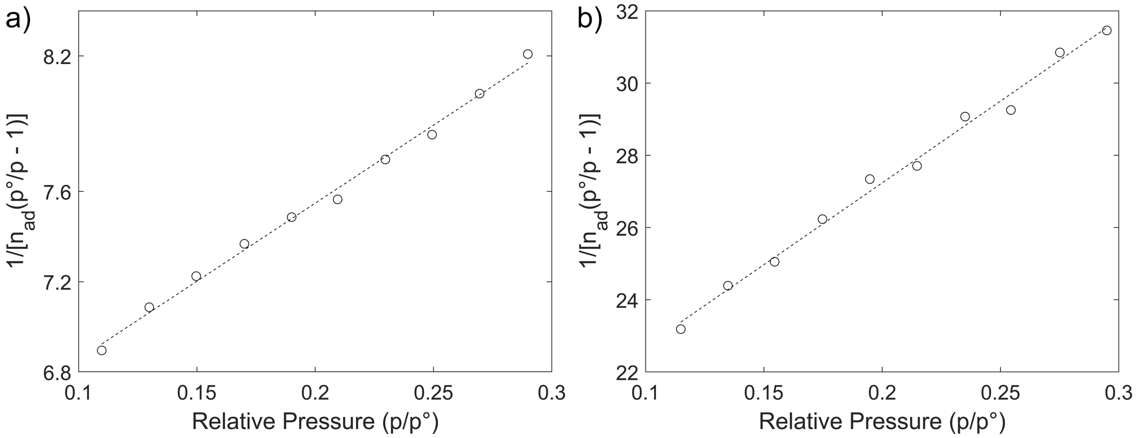

Figure 4.11: BET results for the (a) carbon product from 0-5 mm radius and (b) original carbon felt for CH_4 decomposition at 100 sccm flow rate, 3.33 kPa pressure, 1.86 kW solar power, and 20 min reaction period.

Using SEM results presented earlier, the fiber diameters were determined to be 97, 69, and 20 µm at 0, 5, and 10 mm from the center of the carbon felt product. These diameters compare to a fiber diameter of only 9.6 µm for the original carbon felt. If the carbon product was of the same density and porosity as the original felt, the specific surface area would correlate with area/volume ratio which is proportional to $1/D_{\text{fib}}$, where D_{fib} is the fiber diameter. Using the maximum and minimum diameters within each range (0-5 mm and 5-10 mm), the expected reduction in the specific surface area was determined to be approximately 7-10 times for the 0-5 mm region and 2-7 times for the 5-10 mm region. However, the specific surface area has increased instead by five and two folds, respectively. This is a clear indication that the deposited carbon product has a significantly lower density and thus is microporous in nature. The production of a microporous solid product is expected to be useful in electrochemical energy storage applications.

The growth rate of conformal *graphitic* films on the fiber substrate appears to be exceptionally high. For comparison, a recent report [160] of graphite-like films grown by chemical vapor deposition (CVD) on nickel, involving carbon dissolution in nickel followed by surface precipitation upon cooling, indicated an effective growth rate of 1 µm/hr with a maximum thickness of 500 nm. An earlier report [159] of hot-wall thermal CVD by methane pyrolysis at temperatures, pressures, and flow rates similar to those of the present study, reports a maximum graphitic mass deposition rate of 20 mg/hr on a large graphite rod substrate, which corresponds to a film growth rate of approximately 5.7 µm/hr. In contrast, the growth rate observed in the initial experiment based on the collected carbon mass is much higher. On a mass basis, deposition rate of approximately 1850 mg/hr was observed, which is 93 times higher than the maximum observed by Bammidipati et al. [159] for a system with a much larger reaction zone. In terms of film growth rates, current results indicate a radial fiber growth rate of 135 µm/hr in the center of the felt substrate, which is a value that is 25 times higher.

Comparing present growth rates to *carbon black* production via solar methane pyrolysis under a maximum irradiance of 3000 suns, the work by Pinilla et al. [36] reported carbon deposition rate on a catalyst mass basis of 2.83 mg/g_{cat} per minute. In the current initial study, the graphitic deposition rate of 28.2 mg/g_{cat} per minute determined based on a starting carbon felt mass of 1.10 g_{cat} is ten times higher. It is further emphasized that the centrally heated portion of the circular felt substrate is only approximately 10% of the felt's total area. Therefore, the high carbon deposition and hydrogen production rates in the present experiments, while already high, should be readily amenable to further increases by, for example, expanding the area of high heat flux via optical adjustments and/or decreasing the size of flow area to minimize methane bypass through the lower-temperature annulus.

The totality of the foregoing distinctions related to deposition rate, yield, and residence time suggests a strong photothermal catalytic effect from the concentrated light source that enhances chemical kinetic rates. While thermal reaction pathways of methane pyrolysis to the gas-phase precursors of solid carbon (i.e., polycyclic aromatic hydrocarbons, or PAHs) are generally well understood, the latter transition steps from PAHs to solid carbon and its various forms have been a persistent mystery [161]. Prior work on strictly thermal methane decomposition has concluded that graphitic deposition impedes the reaction on a variety of carbon catalyst types [162], and that 40-50 graphene layers on iron particles are "implicated in the deactivation of the catalyst" [163]. Conversely, the present results indicate a clear autocatalytic behavior, with continued high activity with many orders of magnitude more graphene layers ($\sim 10^5$ layers, corresponding to > 30 µm thickness). Recent insights into hot-carrier plasmonic photocatalytic decomposition of ammonia [49] may apply to the present methane decomposition, where in this case the intermediate presence of graphene-like domains could serve as plasmonic centers [50, 164]; however, further controlled studies of such behavior would be necessary to assess this hypothesis.

4.4.2 Product quality

The thickness of the conformal graphitic deposition depends strongly on radial position, as shown in Fig. 4.10a, with the majority of deposition in the hot central region ($r \leq 10$ mm). To assess the quality of the carbon product, Raman spectra of the carbon felt before and after deposition were obtained and shown in Fig. 4.12a.

The presence of a distinct 2D peak and low D/G peak ratio in the deposited carbon clearly indicates the formation of a high-quality graphitic carbon product at the center of the substrate as well as at $r = 5$ mm (refer to Chapter 3 for background). Clearly, the original carbon felt Raman spectrum lacks these desirable features. The formation of a layered graphitic structure is also apparent in the SEM image of Fig. 4.10b, which shows a fractured cross section with deposited ring-like layers surrounding the original microfiber core. Additionally, the crystalline structure of the carbon product within the central 15 mm diameter region is determined and compared to the original carbon felt, as shown by the XRD spectra in Fig. 4.12b. The average interplanar distances, d_{002}, determined from the (002) reflection position and Bragg's law (Eq. 3.8) are 3.56 and 3.42 Å for the original carbon felt and that with the carbon product. Furthermore, the average crystallite sizes along the c-axis as determined from the Scherrer equation (Eq. 3.9) are 2.07 and 9.69 nm, respectively. The average interplanar distance is a clear indication of the significant upgrade in the crystalline structure and quality of the carbon product, where the interplanar distance of a perfectly crystalline graphite is 3.35 Å [165].

The graphitic product of the solar methane decomposition process presented here is of high distinctive quality compared to those reported in literature via no or carbon-based catalysts. From the Raman results in Fig. 4.12a, the intensity ratios of the D and G Raman peaks ($I_{\mathrm{D}}/I_{\mathrm{G}}$) of the carbon product are determined to be 0.21 and 0.41 at the center and at 5 mm radius, with both locations showing distinctive 2D peaks. These compare to a $I_{\mathrm{D}}/I_{\mathrm{G}}$ ratio of approximately 1.6 as reported by Rodat et al. [59] and the absence of a 2D peak, which further demonstrates the high quality of the present graphitic product. The average inter-defect distances ($L_{\mathrm{D,Ram}}$) of the carbon product at the center and at 5 mm radius are estimated to be 26.3 and 18.9 nm (see Eq. 3.3). Additionally, given the presence of distinct XRD peaks

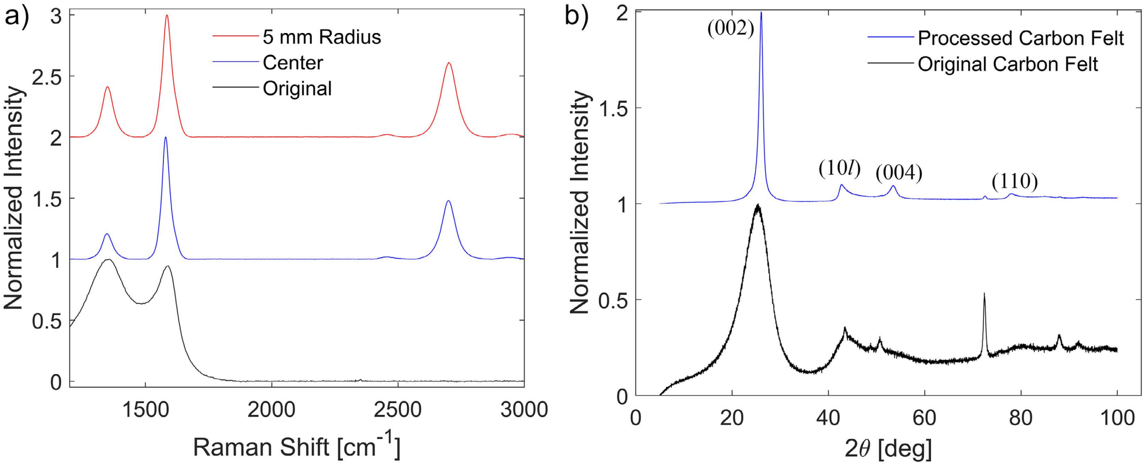

Figure 4.12: Structural analysis on carbon felt product showing (a) Raman spectra of the carbon product at the center and 5 mm radial distance as compared to the original carbon felt, and (b) XRD spectra of the carbon product at the central region as compared to the original carbon felt. CH_4 decomposition at 100 sccm flow rate, 3.33 kPa pressure, 1.86 kW solar power.

and significant change in the interplanar distance of the graphitic product (d_{002} = 3.42 Å) as compared to the original carbon felt (d_{002} = 3.56 Å), the current graphitic product is of much higher quality compared to the amorphous carbon obtained by Pinilla et al. [36] and closer to their carbon nanofibers and nanotubes (d_{002} = 3.38 Å) obtained using metallic-based special catalysts. However, many challenges exist for metallic-based catalysts, such as sintering, fast deactivation, and the need to separate the carbon product from the catalyst, for which the deterioration in carbon quality upon separation is unknown.

4.5 Other process characteristics

4.5.1 Process transient performance

To assess the CH_4 decomposition performance over time and any catalytic deactivation (if present), the process was further examined through a long-duration test lasting for 120 min under the same operating conditions of 100 sccm flow rate, 3.33 kPa pressure, and 1.86 kW solar power. The MS process monitoring results are shown in Fig. 4.13. Results indicate a relatively consistent behavior as that presented earlier initially, but methane conversion and total hydrogen yield decrease substantially beyond the initial 20 min, to reach values of 41% and 36% after 120 min. The net carbon product collected on the original felt was measured to be 2.26 g, which is two times more than the starting mass of the original carbon felt. If only the area with active carbon deposition is considered (25 mm in diameter, see Fig. 4.10a), the net carbon product collected increases to 15.5 g/g_{cat}. This compares to a net carbon production value of only 0.34 g/g_{cat} in an earlier study with a similar test duration of 120 min [36]. It is further emphasized that as a result of the present localized heated reaction region on the carbon felt, no carbon deposition occurred on the quartz window and no noticeable deposition occurred on the reactor's walls over the duration of all testing, unlike reactor clogging issues commonly reported in prior literature for long duration experiments [55, 60].

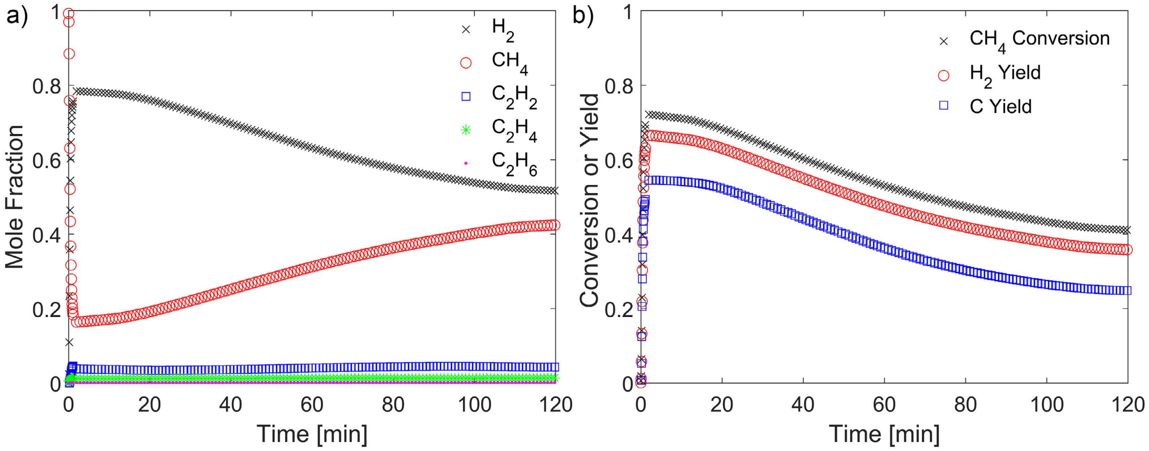

Figure 4.13: Real-time monitoring results from the calibrated mass spectrometer showing (a) mole fractions in the product stream, and (b) methane conversion and product yields for CH_4 decomposition through carbon felt at 100 sccm flow rate, 3.33 kPa pressure, 1.86 kW solar power, and 120 min reaction period.

The long-term reduction in process efficiency over the 120 min is attributed to increased flow resistance in the central region due to decreasing porosity caused by highly enlarged and coalesced microfibers, as shown in Fig. 4.14. The coalesced microfibers decrease residence time due to flow area restriction and increase flow bypass through lower-temperature annular regions. It is important to note that the issue of process efficiency reduction could be readily addressed by adopting a roll-to-roll process that exploits the carbon felt's mechanical flexibility [166], as demonstrated in Chapter 6.

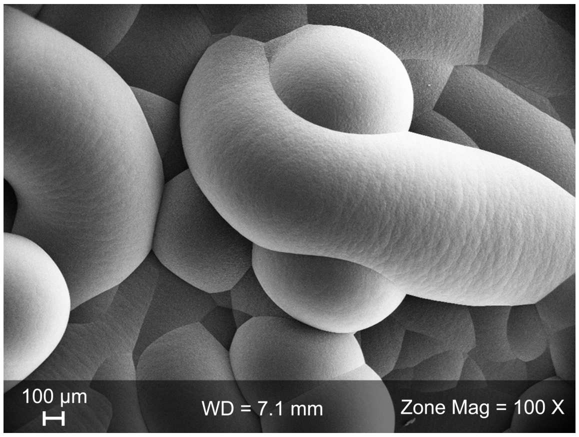

Figure 4.14: SEM image of the carbon felt's central region after CH_4 decomposition and carbon deposition at 100 sccm flow rate, 3.33 kPa pressure, 1.86 kW solar power, and 120 min reaction period.

4.5.2 Effect of process substrate

To assess the effect of the starting material (carbon felt), methane decomposition was tested using an alumina/silica wool (Morgan Advanced Materials, Cerablanket) under the same operating conditions of 100 sccm flow rate, 3.33 kPa pressure, 1.86 kW solar power, and a total decomposition duration of 20 min. The ceramic fiber wool consists of 46% alumina and 54% silica by weight. The ceramic cloth was of the same dimensions as the carbon felt (diameter of 6.86 cm and thickness of 3.2 mm);

however, the ceramic cloth's different fiber diameter and porosity could potentially contribute to differences in performance results. Despite the significantly different material used for methane decomposition, process results are very similar as shown in Fig. 4.15. The steady-state methane conversion, hydrogen yield, and carbon yield for the aforementioned conditions were estimated to be 75%, 71%, and 64%. These results demonstrate the possibility of the present methane decomposition process being expanded to other starting porous substrates to yield similar performance.

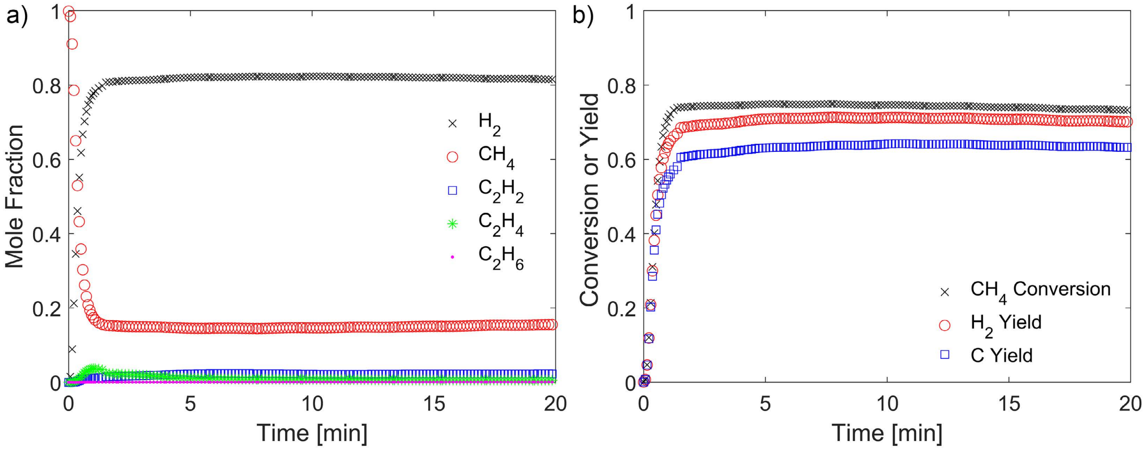

Figure 4.15: Real-time monitoring results from the calibrated mass spectrometer showing (a) mole fractions in the product stream, and (b) methane conversion and product yields for CH_4 decomposition through ceramic felt at 100 sccm flow rate, 3.33 kPa pressure, 1.86 kW solar power, and 20 min reaction period.

4.6 Conclusions

In this chapter, an initial study of methane decomposition through porous substrates (mainly carbon felts) was presented. The present process offers the following advantages: (a) all process heat derives from solar energy, and (b) the process inherently sequesters carbon into a high-value solid form. The product stream of the process was thoroughly monitored through two different techniques that reported very consistent results: (a) LAS and (b) MS. These two techniques allowed for monitoring trace products such as C_2H_4 and C_2H_6 with product mole fractions of 0.5% and 0.1%. The quantified methane conversion, hydrogen yield, and carbon yield were estimated to be 73, 69, and 58.3%, where the actual carbon collected and measured after methane decomposition agreed very well with that estimated using the theoretical carbon yield. This agreement and other observations reported in this chapter indicate that no or very little carbon deposition occurs outside of the reaction region (carbon felt). Therefore, issues of uncontrolled carbon deposition and reactor clogging were mitigated. Additionally, the carbon product of the decomposition process was thoroughly studied using SEM, Raman, XRD, and BET measurements, and it is clear that the product is of a high-quality microporous graphitic properties.

Therefore, the carbon product's high economic value may be a major driving force for solar methane decomposition to become as competitive as SMR, and with the added benefit of being green. Although SMR offers an intrinsic advantage in producing one more mole of hydrogen per reactant mole of methane molecule than pyrolysis, this benefit comes with the cost of higher heat input, $\Delta H^o_{\mathrm{SMR}} = 206$ kJ/mol [22]. Some of this extra hydrogen must be consumed for reaction heat, and using hydrogen's lower heating value of -242 kJ/mol, at least 54% of the additional hydrogen from SMR must be used for process reaction heat. Additionally, the basic SMR process (gray hydrogen) releases significant amount of greenhouse gases into the atmosphere, as reviewed in Chapter 1. Although combination of SMR with carbon capture and sequestration has been proposed (blue hydrogen) [167], the energetic and emissions benefits have recently been projected to be small, largely due to the required energy drawn from methane combustion to drive carbon capture [168].

Chapter 5:
Parametric Study of Methane Decomposition

The solar-thermal methane decomposition process, performance, and products were thoroughly presented and studied in Chapter 4 for limited experimental conditions. In this chapter, solar methane pyrolysis through fibrous carbon media is tested under different operating conditions to characterize the performance of the process and quality of products, in a manner similar to that performed in Chapter 4. Different operating conditions considered include various methane inlet flow rates (10 to 2000 sccm), solar concentrations (1 to 3.5 $\mathrm{MW/m^2}$) and powers (0.92 to 2.49 kW), pressures (1.33 to 40 kPa), and fibrous medium thicknesses (0.36 to 9.6 mm). Process conversions, yields, efficiencies, and product qualities are reported and discussed.

5.1 Methodology

Solar-thermal methane decomposition through a fibrous carbon medium is evaluated using pure methane (99.999% pure) inlet flow at various operating conditions in a parametric study. Between each experimental test, the reactor is evacuated and then purged with nitrogen for sufficient time to achieve an oxygen-free environment. Following vacuum conditions, methane flow is introduced at a fixed flow rate, and steady irradiation from the solar simulator is applied to the fibrous material at the reactor operating pressure. The effect of the initial thermal transient state of CH_4 decomposition on the carbon product quality as the reaction zone heats up is safely neglected, as the process reaches steady thermal operating conditions in approximately 5 seconds (see Fig. 4.6b). This fast transient response is a result of the localized heating of fibrous medium with a low thermal mass, and is desired for solar thermochemical applications to maximize effective use of daylight by the process. Finally, the setup is verified to be gas-tight such that the MS detects the presence of no CO_x species during CH_4 pyrolysis.

5.2 Thermal treatment

The fibrous carbon medium used in testing is initially thermally-treated under the corresponding experimental solar power for a duration of approximately 20 min, as briefly described in Chapter 4. The motivation for this thermal treatment is to remove any volatiles that might otherwise prevent measuring an accurate mass of carbon produced and captured, which is calculated based on the carbon mass before an after experimentation and is compared to the theoretically estimated carbon mass. It is possible that process temperatures might affect the quality of the carbon medium, and might in turn affect the decomposition process. To investigate the effects of this thermal treatment (if any), the fibrous medium was both treated and not treated for identical methane pyrolysis operating conditions; methane flow rate of 100 sccm, pressure of 3.33 kPa, solar power of 1.86 kW, and medium thickness of 3.2 mm. Real-time performance results comparing the effect of thermal treatment is shown in Fig. 5.1. Both results are relatively identical, where steady-state results of methane pyrolysis without (with) pretreatment are: methane conversion of 74% (73%), hydrogen yield of 70% (69%), and carbon yield of 59% (58%). Therefore, it is concluded that the pretreatment of the carbon felt has no contribution to the CH_4 decomposition process kinetics. The present measurements also illustrate the good consistency and repeatability of experimental results, as also noted at other operating conditions.

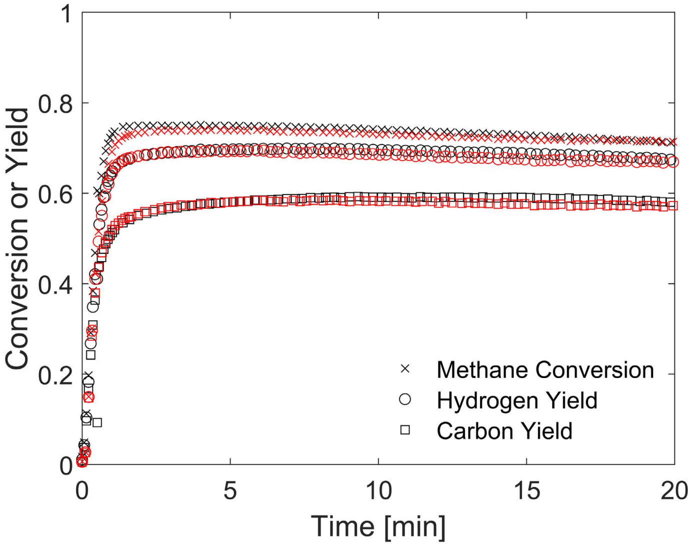

Figure 5.1: Methane conversion, hydrogen yield, and carbon yield for methane pyrolysis at flow rate of 100 sccm, solar power of 1.86 kW, pressure of 3.33 kPa, and medium thickness of 3.2 mm with thermal pretreatment (red) and without thermal pretreatment (black).

High temperatures (1500-3000 °C) often lead to graphitization of carbon, where defect concentrations in amorphous carbon decrease with increasing temperature [142, 169]. Therefore, the effect of the heat treatment process implemented here on the fibrous starting material is also assessed. The fibrous medium is thermally treated in vacuum at a solar power of 1.86 kW (corresponding to measured front maximum temperature of 1820 K) for a duration of 20 min. Fig. 5.2 shows the (a)

Raman, (b) XRD, and (c) EDS spectra of the carbon material before and after the heat treatment process.

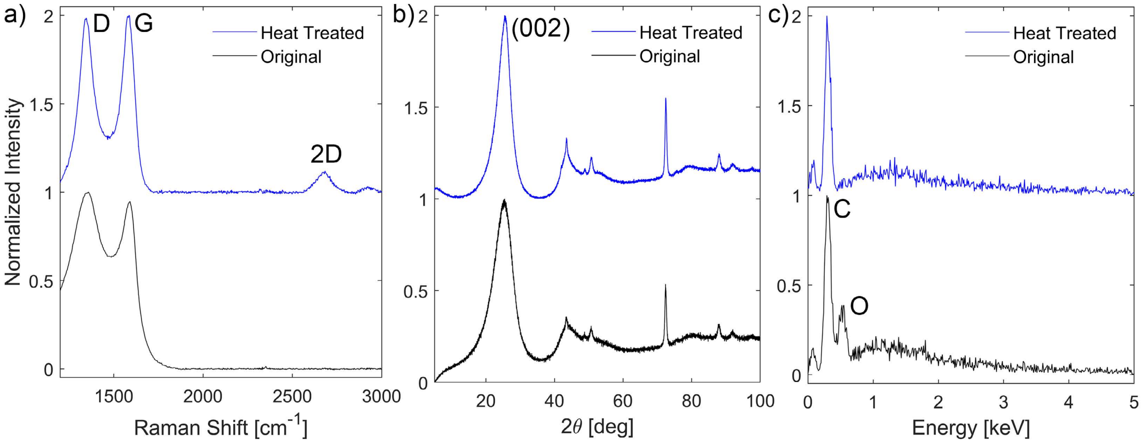

Figure 5.2: (a) Raman, (b) XRD, and (c) EDS spectra of original fibrous carbon material and thermally-treated material under vacuum at a solar power of 1.86 kW for a duration of 20 min.

Results in Fig. 5.2 indicate slight changes in the starting material's structure and quality with heat treatment. From Raman spectra (Fig. 5.2a), $I_{\mathrm{D}}/I_{\mathrm{G}}$ decreases slightly from 1.06 to 0.98, a weak 2D peak appears, and the FWHM of the D and G peaks decrease slightly upon thermal treatment. The existence of a small 2D peak indicates that a small portion of the carbon felt has undergone graphitization [142]. Such observations are consistent with the XRD spectra (Fig. 5.2b), where the FWHM of the (002) reflection decreases with a slight increase in θ_{002}. The heat treatment thus changes d_{002} from 3.56 to 3.53 Å and increases $L_{\mathrm{D,Ram}}$ from 11.7 to 12.2 nm. The enhancement observed is primarily attributed to deoxygenation and slight graphitization of the fibrous material, where the EDS spectra reveal the disappearance of the oxygen peak upon thermal treatment (Fig. 5.2c). However, this enhancement in the carbon quality is not close to that of the methane decomposition product, especially when considering the $I_{\mathrm{D}}/I_{\mathrm{G}}$ ratio which still remains high even after heat treatment ($I_{\mathrm{D}}/I_{\mathrm{G}} = 0.98$) with merged D and G peaks.

Comparing the present Raman spectra to similar spectra of untreated and graphitized CB samples at different temperatures found in literature [142], the heat-treated spectrum closely matches that reported at 1500 °C (1773 K). This observation is consistent with the maximum temperature measurement reported here. Additionally, the thermal treatment process was verified to have no detectable effect on the carbon product quality based on measurements of Raman and XRD spectra (not shown). This observation indicates that original impurities and treatment of starting material have no significant effects on the pyrolysis process.

5.3 Representative carbon product characteristics

Although representative characteristics of the carbon product were discussed in Chapter 4, they are revisited and expanded on here due to the importance of the carbon product quality in driving the cost of solar methane pyrolysis down to competitive levels. Characterization of the carbon product at a solar power of 1.86 kW, pressure of 3.33 kPa, pure CH_4 inlet flow rate of 100 sccm, and fibrous medium thickness of 3.2 mm are shown in Fig. 5.3. For these experimental conditions, residence time is estimated to be 44 ms and maximum rear temperature is measured as 1630 ± 60 K. Fig. 5.3 includes (a) Raman and XRD spectra of carbon product, (b) a SEM image of original starting material, and (c) a cross section of a representative carbon formation over an original fiber ligament. The significantly higher quality of the carbon product compared to the original and thermally treated fibrous materials is apparent (cf. Fig. 5.2). The EDS spectrum of the product is identical to that of the thermally treated material, but the Raman and XRD spectra are much more distinctive with significantly smaller FWHM for all peaks. The Raman I_D/I_G ratio decreases significantly compared to the heat-treated material from 0.98 to 0.21, corresponding to more than two-fold increase in $L_{D,Ram}$ from 12.2 to 26.4 nm and a significant reduction in defects and structural vacancies. Additionally, the presence of a strong 2D peak in the growth product corresponds to existence of long-range graphitic structures [170]. For the XRD spectra, θ_{002} noticeably increases, with a corresponding decrease in d_{002} from 3.53 to 3.42 Å. The smaller interplanar distance is a clear indication of the significantly increased crystallinity of the carbon product, where the interplanar distance of a perfectly crystalline graphite is 3.35 Å [165]. The foregoing discussion in addition to the broad and overlapping (100) and (101) XRD peaks, observed as a single peak ($10l$) in Fig. 5.3a, indicate the production of a relatively high-quality turbostratic graphite [171].

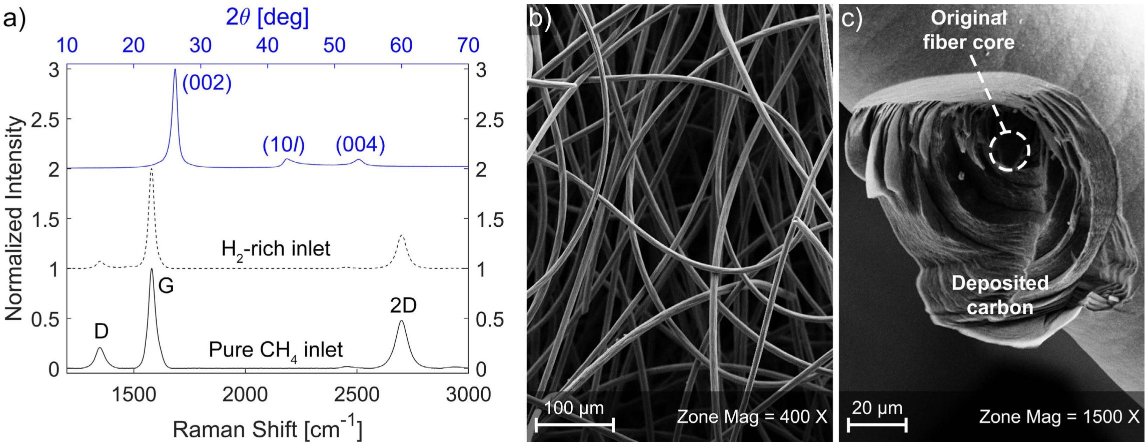

Figure 5.3: (a) Raman and XRD spectra of representative conditions of 1.86 kW solar power, 3.33 kPa pressure, 100 sccm CH_4 inlet flow rate, and 3.2 mm fibrous medium thickness. (b,c) SEM images of (b) original fibrous material and (c) representative cross-sectional cut of fibrous medium with carbon deposition.

The chemical composition of the gaseous product stream can provide insights into the carbon deposition form and quality. For the spectra shown in Fig. 5.3a, the product stream consists primarily of hydrogen in addition to lower concentrations of unconverted methane and acetylene secondary byproduct with no detectable aromatic hydrocarbons; measured outlet mole fractions are $x_{\mathrm{H_2}} = 80\%$, $x_{\mathrm{CH_4}} = 15.6\%$, $x_{\mathrm{C_2H_2}} = 3.6\%$, $x_{\mathrm{C_2H_4}} = 0.6\%$, and $x_{\mathrm{C_2H_6}} = 0.2\%$. The absence of aromatic hydrocarbons is postulated to be primarily due to the low process residence time, but may additionally be attributed to photocatalytic effects. Prior work on densification of a fibrous carbon material by chemical vapor infiltration (CVI) with methane at 1095 °C indicated that formation of high-quality textured carbon is strongly affected by the ratio of small linear hydrocarbons, primarily C_2H_2, to aromatic hydrocarbons [172]. Additionally, high hydrogen concentration inhibits the formation and growth of aromatic hydrocarbons, influencing the carbon formation chemistry and leading to higher-quality textured carbon deposition. However, more recent work on methane CVI at 1150 °C reports a contrasting observation, where significant reduction in texture quality of carbon deposition is observed under high hydrogen concentrations [173].

The latter conclusion is evaluated in the present work by pyrolyzing CH_4 under the conditions of Fig. 5.3 but with an additional H_2 inlet flow rate of 900 sccm, yielding results consistent with prior literature [172]. The Raman spectrum of the carbon product is shown as a dashed line in Fig. 5.3a, and reveals a significant increase in quality under hydrogen-rich flow when compared to pure CH_4 inlet flow. The $I_{\mathrm{D}}/I_{\mathrm{G}}$ ratio decreases from 0.21 to 0.07 and $L_{\mathrm{D,Ram}}$ increases from 26.4 to 45.7 nm. The foregoing results suggest possible contributions of the gaseous product stream on enhancing the quality of carbon product.

Producing graphitic carbon with low $I_{\mathrm{D}}/I_{\mathrm{G}}$ ratio and high deposition rate is relatively challenging. In prior solar CH_4 pyrolysis studies, the solid product is observed to mostly be CB [53, 56, 57], with high $I_{\mathrm{D}}/I_{\mathrm{G}}$ ratio and no distinct Raman 2D or XRD peaks [36, 59]. In contrast, direct solar irradiation of the carbon material in this work in addition to its relatively long residence time at high operating temperatures, as compared to flow-seeded reactors, potentially contribute towards obtaining high-quality graphitic product. Additionally with non-solar studies utilizing metal-based catalysts, high $I_\mathrm{D}/I_\mathrm{G}$ ratios have been observed for the solid product [174] even after electrochemical carbon purification [170]. $I_\mathrm{D}/I_\mathrm{G}$ ratios similar to those reported here were only observed after thermal purification and treatment at very high temperatures (2800 °C) [170].

The significant volume of graphitic carbon deposition on the present original fibrous material is illustrated in Fig. 5.3c. Comparing the product to the original fibers (Fig. 5.3b), central fibers grow in diameter from approximately 10 to 95 µm, with more space for continued growth, over a period of 20 min under 100 sccm CH_4 inlet flow rate. This growth corresponds to a maximum deposition rate of 128 µm/hr (at the center with maximum temperature) and equates to specific deposition of 90 $\mathrm{g/g_{cat}}$ and deposition rate of 4.5 $\mathrm{g/g_{cat}}$ per min by assuming that the fibrous material is a catalyst. Growth and deposition rates are further subject to significant increase with increasing flow rate, as will be demonstrated in later sections. The foregoing results compare well to those reported in literature. For solar and non-solar CH_4 pyrolysis studies, the specific carbon deposition in $\mathrm{g/g_{cat}}$ reported here falls in the high range of specialized metal-based catalysts, and at least an order of magnitude higher than that obtained with carbon-based catalysts [36, 44]. The observed deposition rate (4.5 $\mathrm{g/g_{cat}}$ per min or 128 µm/hr) is also significantly higher compared to rates of 2 to 16 $\mathrm{mg/g_{cat}}$ per min in a prior solar CH_4 pyrolysis study using different catalysts [36]. In contrast to prior work on CVI through a fibrous carbon medium [173] and chemical vapor deposition (CVD) on graphite [159] at similar temperatures and pressures, pyrolytic carbon (with $I_\mathrm{D}/I_\mathrm{G} = 1.28$) and graphitic carbon deposition rates of 0.53 µm/hr and 5.7 µm/hr were observed, respectively. These order(s) of magnitude lower graphitic deposition rates suggest a strong contribution from photocatalytic effects.

The deposition of smooth graphitic carbon layers is also apparent in the cross-sectional image shown in Fig. 5.3c, which also suggests a microporous structure that has been verified through specific surface area measurements (see Chapter 4). Additionally, the carbon purity has been characterized by elemental analysis conducted by Midwest Microlab (IN, USA) via product combustion in ultra-pure oxygen at 1263 K to determine the percentage mass composition of elemental C, H, and N. Two representative sample tests yielded the following compositions: (1) C = 99.76% and undetected H and N, and (2) C = 99.67%, H = 0.25%, and N = 0.05%. Such high-purity results are expected from well-controlled, oxygen-free CH_4 decomposition process. A parametric study is presented in the following sections to correlate carbon product form and quality with operating conditions. Tabulated summary of results obtained in this parametric study can be found in Appendix C.

5.4 Effect of flow rate

The effect of inlet methane flow rate is considered first at a solar power of 1.86 kW (corresponding maximum solar flux of 2.6 MW/m^2), pressure of 3.33 kPa, and fibrous medium thickness of 3.2 mm. Different flow rates from 10 to 2000 sccm were tested, for which rear maximum temperatures measured on the fibrous material range from 1560 to 1650 K ± 60 K. Methane conversion, hydrogen yield, and carbon yield for the different flow rates are shown in Fig. 5.4a. Process conversion and yields decrease significantly with increasing flow rates due to significant reduction in residence time; X_{CH_4} decreases from 95.5% to 22.4%, Y_{H_2} from 93.8% to 20.8%, and Y_{C} from 90.9% to

17.1% as methane flow rate increases from 10 to 2000 sccm. The flow rate conditions represent residence times within the reaction zone from 2.2 ms at 2000 sccm to 450 ms at 10 sccm (see Appendix C), with average reaction temperatures around 1440 K. The reduction in carbon yields from methane conversions as compared to hydrogen yields is primarily due to the presence of C_2H_2 secondary byproduct as a result of low residence times, especially at high flow rates. The C_2H_2 mole fraction decreases from 4.0% to 0.6% with reduction in flow rate, while mole fractions of other light hydrocarbons are significantly lower; C_2H_4 ranges from 0.6% to 0.4%, and C_2H_6 is usually below 0.1%.

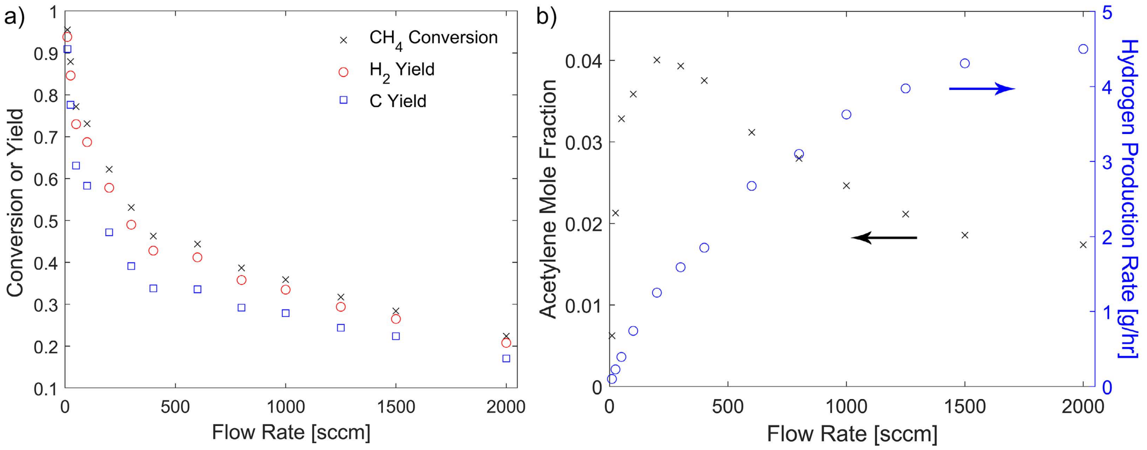

Figure 5.4: Methane decomposition at a pressure of 3.33 kPa, solar power of 1.86 kW, and medium thickness of 3.2 mm. Effect of methane inlet flow rate on (a) methane conversion, hydrogen yield, and carbon yield, and (b) acetylene byproduct concentration and hydrogen production rate.

Although reductions in conversion and yields with increasing flow rates are significant, they are not as severe as those reported for volumetric/tubular reactors with or without particle seeding. This improvement likely occurs because the porous substrate acts as an effective medium for heat transfer, allowing methane flow to reach higher temperatures under low residence times. For comparison, a prior study on methane pyrolysis in a tubular reactor at operating temperatures of

1623 K reported reductions in X_{CH_4} from 74% to 20% and Y_{H_2} from 66% to 15% under increasing methane inlet flow rate from 100 cm^3/min to 300 cm^3/min [53]. The three-fold increase in methane flow rate decreases CH_4 conversion and H_2 yield by a factor of four [53]. In contrast, the present conversion and yield results for increased methane flow rate from 100 to 300 sccm indicate reductions in X_{CH_4} from 73% to 53%, Y_{H_2} from 69% to 49%, and Y_C from 58% to 39% (see Fig. 5.4a). In this case, the three-fold flow rate increase corresponds to reductions by less than a factor of two.

Fig. 5.4a shows an initially substantial reduction in conversion and yields with increasing flow rates up to approximately 400 sccm (11 ms), after which conversion and yields continue to decrease but at a lower rate. Additionally, the gaps between conversion and yields increase due to incomplete dissociation of converted methane and the increased production of acetylene byproduct. Fig. 5.4b shows the acetylene product mole fraction and the hydrogen production rate at different flow rates. If the extent of methane decomposition remains the same (Eq. 1.4), the acetylene mole fraction in the product stream should have reduced with the decreasing methane conversion at higher flow rates. Instead, $x_{C_2H_2}$ at low flow rates increases significantly to a maximum of 3.9% at 300 sccm (15 ms) due to less complete methane dissociation. Thereafter, $x_{C_2H_2}$ continues to decrease at higher flow rates primarily due to decreased methane conversion (Fig. 5.4a). This behavior is consistent with prior observations indicating less C_2H_2 formation with increasing residence times [55], though residence times for the tests shown in Fig. 5.4 are significantly lower than those reported in prior work (see Table 1.1).

The hydrogen production rate, though approaching an asymptote around 5 g/hr at 2000 sccm, monotonically increases with methane inlet flow rate (Fig. 5.4b). This increase in H_2 production rate leads to a significant increase in the solar-to-chemical efficiency, though with lower hydrogen yield. As flow rate increases from 25 to 2000 sccm, η_{stc} increases from 0.14% to 2.84%. In contrast to other hydrogen production technologies using a common metric (solar energy consumption), these efficiencies correspond to 8130 and 413 kWh of solar power per kg of H_2. The latter value compares well to current values for solar-driven alkaline electrolysis (around 250 kWh of solar power per kg of H_2) [9, 12], and is expected to significantly improve with design and process optimization (e.g., adjusting optics to obtain more uniform and higher temperature distribution from the solar input). Importantly, the solar energy consumption metric does not account for the high-value graphitic product that is produced by the present methane pyrolysis process. For results shown in Fig. 5.4, the carbon co-product is high-quality microporous graphite as indicated by various characterization techniques that include SEM, Raman, and XRD measurements. The Raman spectra of the carbon product at different flow rates from 10 to 2000 sccm are shown in Fig. 5.5a, while SEM images of the carbon product with methane flow rates of 25 and 2000 sccm are shown in Figs. 5.5b and c.

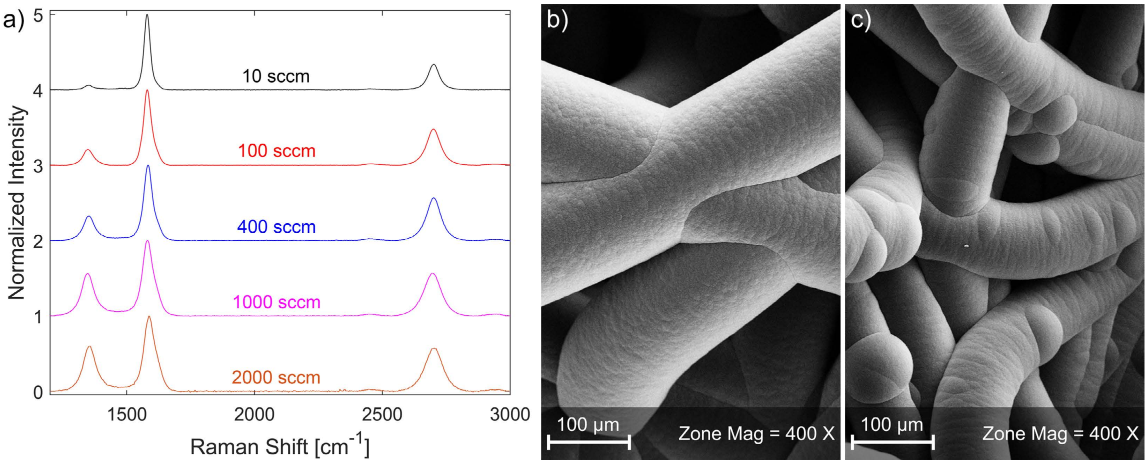

Figure 5.5: Methane pyrolysis at solar power of 1.86 kW, pressure of 3.33 kPa, and reaction zone thickness of 3.2 mm. (a) Raman spectra of carbon product at different methane inlet flow rates. (b,c) SEM images in the central region of the fibrous medium at (b) 25 sccm after 80 min and (c) 2000 sccm after 3 min.

Results in Fig. 5.5a show a dependence of the carbon product quality on methane inlet flow rate. As a general trend, the quality degrades as a result of increasing flow rate and is attributed to decreasing residence times that result in lower effective gas temperatures; increasing flow rate from 10 to 2000 sccm significantly decreases t_{res} from 445 to 2.2 ms. Even though temperatures of the porous medium decrease with increasing flow rate, such reductions are insufficient to markedly affect the carbon product's quality. The $I_{\mathrm{D}}/I_{\mathrm{G}}$ ratios at 10 and 2000 sccm are 0.06 and 0.59, which correspond to $L_{\mathrm{D,Ram}}$ of 49 and 15.7 nm, respectively. This reduction in $L_{\mathrm{D,Ram}}$ indicates a significant increase in defect concentration with increasing flow rates, and is also apparent from the SEM images in Fig. 5.5. At a low flow rate of 25 sccm, the carbon deposition within the fibrous material grows conformally over the fiber ligaments (Fig. 5.5b). However, at a significantly higher flow rate of 2000 sccm (Fig. 5.5c), rougher deposition layers with irregularities form as a result of increasing defects. These irregularities produce higher $I_{\mathrm{D}}/I_{\mathrm{G}}$ ratios at higher flow rates, but the quality of graphitic carbon product obtained at the highest flow rate is still relatively good compared to prior literature. Notably, the product quality (from $I_{\mathrm{D}}/I_{\mathrm{G}}$ ratio) degrades significantly with increasing flow rates in the lower range, whereas the quality is significantly less sensitive to flow rate in the higher flow rate range. This observation suggests that the process can be further scaled-up to higher flow rates with little further degradation in quality.

Despite the moderate reduction of the carbon product quality with increasing flow rate, the deposition rate and the solar-to-chemical efficiency significantly improve. Increasing $\dot{m}_{\mathrm{CH_4}}$ from 10 to 2000 sccm increases the measured $\dot{m}_{\mathrm{C}}$ from 0.29 to 11 g/hr and η_{stc} from 0.06% to 2.84%. Methane conversion and carbon and hydrogen production rates at the various inlet flow rates are shown in Fig. 5.6, with carbon production rates three-fold higher than those of hydrogen as expected from the global CH_4 dissociation reaction. As methane conversion significantly decreases with increasing flow rate, hydrogen concentration in the product stream and reaction residence time decrease as well. Moreover, upstream and cross-stream diffusion of hydrogen product through the fibrous material to locations with high methane concentration may be less significant as inlet flow rate increases. Therefore, with increasing carbon production rates and decreasing product quality, the optimum inlet flow rate will be the maximum that still provides the desired quality of the carbon product.

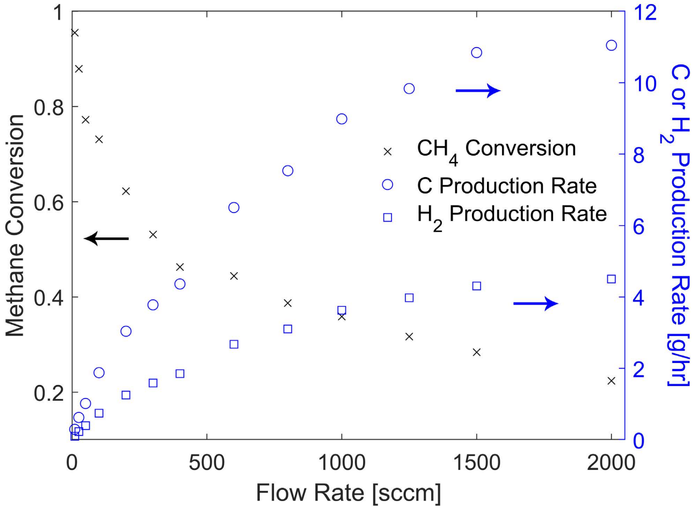

Figure 5.6: Methane conversion in addition to carbon and hydrogen production rates at various methane inlet flow rates for methane pyrolysis at solar power of 1.86 kW, pressure of 3.33 kPa, and reaction zone thickness of 3.2 mm.

5.5 Effect of solar power

CH_4 pyrolysis temperature affects the process chemical kinetics in addition to the solid carbon form and quality. Therefore, the effects of solar power input and thus temperature on the methane pyrolysis process are assessed at a CH_4 inlet flow rate of 100 sccm, pressure of 3.33 kPa, and fibrous medium thickness of 3.2 mm. Process conversion and yield results for power inputs between 0.92 to 2.49 kW (maximum solar fluxes from 1.28 to 3.48 MW/m^2) are shown in Fig. 5.7, with maximum temperatures measured at the center of the porous medium indicated and range from 1370 to 1750 K ± 60 K. However, the temperature variation on the porous medium is large due to the nature of irradiation from the solar source (Fig. 3.11), as evident from maximum and average temperatures indicated in Fig. 4.6b.

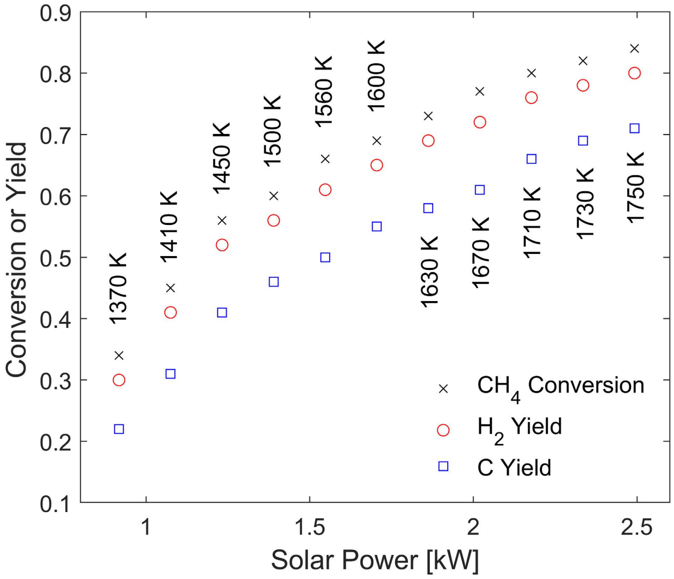

Figure 5.7: Effect of solar power (and maximum operating temperature) on methane conversion, hydrogen yield, and carbon yield at operating pressure of 3.33 kPa, methane inlet flow rate of 100 sccm, and medium thickness of 3.2 mm.

Process conversion and yields increase significantly with increasing solar power from 0.92 to 2.49 kW, with the maximum temperature increasing from 1370 to 1750 K, X_{CH_4} from 34% to 84%, Y_{H_2} from 30% to 80%, and Y_C from 22% to 71%. The methane pyrolysis process depends highly on solar power, and thus temperature, under these process conditions. However, process temperatures reported here are relatively low compared to those reported in prior literature for equivalent methane conversions (see Table 1.1), likely due to the enhanced thermal exchange from the porous medium to the gas phase. Residence times for results shown in Fig. 5.7 are relatively similar, decreasing from 55 ms at 0.92 kW to 41 ms at 2.49 kW. As for secondary byproducts, no distinct behavior is observed other than a general reduction of C_2H_2, C_2H_4, and C_2H_6 outlet mole fractions at higher solar powers. Because CH_4 conversion increases with increasing solar power, reductions in byproduct mole fractions indicate more complete dissociation of methane as expected at higher temperatures. However, complete decomposition was not observed due to short residence times (41 to 55 ms). For conditions of Fig. 5.7, $x_{\mathrm{C_2H_2}}$ ranges from 3% to 4%, $x_{\mathrm{C_2H_4}}$ from 0.5% to 1%, and $x_{\mathrm{C_2H_6}}$ from 0.1% to negligible concentrations.

For the process efficiency, η_{stc} is 0.38% at 0.92 kW and then increases to a maximum of 0.48% at 1.23 kW, after which it decreases to 0.42% at the maximum solar power of 2.49 kW. This local maximum in η_{stc} is caused by two competing phenomena, where at higher temperatures CH_4 conversion and product yields increase, as do thermal losses to the surroundings. The maximum gradient in product yields occurs at a solar power input of 1.23 kW with corresponding maximum temperature measured as 1450 K. Even though significantly higher conversion and yields are achieved at higher solar powers and temperatures, operating at solar powers higher than 1.23 kW (for the present experimental setup and conditions) is not beneficial from process efficiency perspective. However, this perspective does not account for the requirement of more CH_4 separation (and possible recycling) at lower solar powers that could potentially decrease overall process efficiencies.

Similar to the carbon co-product obtained at different flow rates, tests presented in Fig. 5.7 produce high-quality microporous graphite product. Fig. 5.8a shows the Raman spectra of the carbon product generated at different solar powers from 0.92

to 2.49 kW, with the accompanying SEM images at the bounding solar powers shown in Figs. 5.8b and c.

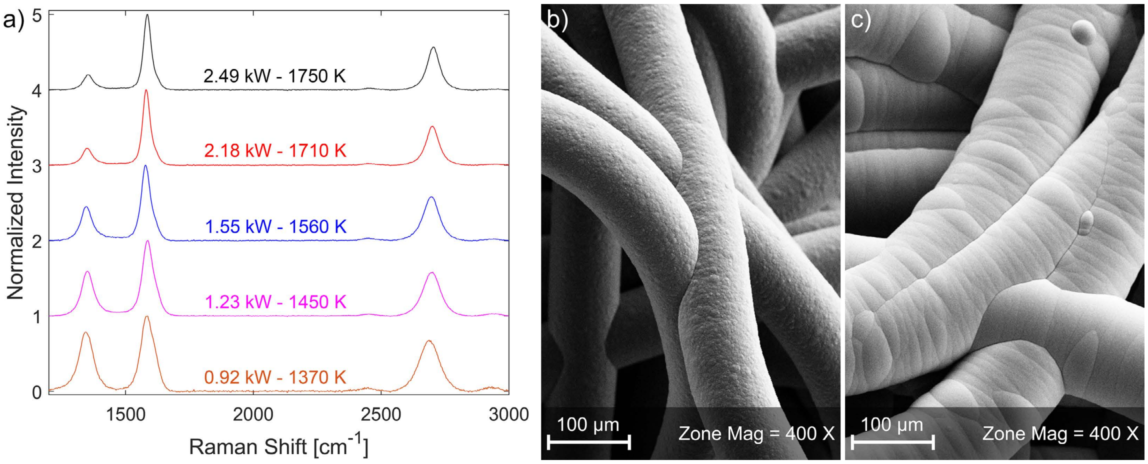

Figure 5.8: Methane pyrolysis at inlet flow rate of 100 sccm, pressure of 3.33 kPa, and reaction zone thickness of 3.2 mm. (a) Raman spectra of carbon product at different solar powers and maximum temperatures. (b,c) SEM images in the central region of the fibrous medium at (b) 2.49 kW after 20 min and (c) 0.92 kW after 30 min.

As a result of reducing the solar power input and hence maximum temperature from 1750 to 1370 K, the three dominant Raman peaks broaden, and the $I_{\mathrm{D}}/I_{\mathrm{G}}$ ratio increases from 0.20 to 0.79. This increase corresponds to reduction in $L_{\mathrm{D,Ram}}$ from 27 to 13.6 nm, which correlates well with increased defects as indicated by the formation of larger irregularities in the SEM image shown in Fig. 5.8c. Notably, the carbon product quality observed in Fig. 5.8a is insensitive or less sensitive to operating temperature beyond a certain high solar power input (1.86 kW or maximum temperature of 1630 K). In contrast to other techniques and production of various value-added carbon forms [175], the product form of the present solar pyrolysis process does not exhibit constrained maximum and minimum temperatures at which graphitic carbon forms, within the investigated temperature range and operating conditions. The quality of the graphitic carbon continues to improve with increasing temperature. However, based on the trend shown in Fig. 5.8a, CB would form if operating temperatures were reduced further.

In addition to prior observations, methane conversion and carbon yield significantly increase with solar power, as the carbon production rate under the same methane inlet flow increases from 0.7 to 2.3 g/hr with solar power from 0.92 to 2.49 kW. Similar to results of varying flow rates, the deterioration of quality with reduction in temperature can be partially attributed to lower methane conversion and hydrogen concentration in the product stream (see Fig. 5.7). However, the carbon product remains graphitic with distinct D, G, and 2D peaks even at the lowest temperature, as opposed to formation of amorphous CB product in other work at similar or higher temperatures [53, 59, 176]. This observation appears to indicate a photocatalytic contribution that favors quality of the carbon product.

5.6 Effect of pressure

The methane pyrolysis process under different operating pressures is considered next at a flow rate of 100 sccm, solar power of 1.86 kW, and porous medium thickness of 3.2 mm. Process conversion and yield results are shown in Fig. 5.9 for pressures from 1.33 to 40 kPa, for which maximum temperatures of the fibrous medium are estimated to fall within the range from 1580 to 1660 K ± 60 K. Results indicate that process kinetics improve with increasing operating pressure, as pressure increase from 1.33 to 40 kPa increases $X_{\mathrm{CH_4}}$ from 69% to 78%, $Y_{\mathrm{H_2}}$ from 64% to 73.1%, and Y_{C} from 53.3% to 63%.

The increase in conversion and yields with pressure is primarily attributed to increased gas residence time in the reaction zone, from 18 ms at 1.33 kPa to 530 ms at 40 kPa. Increased residence time enables the gas phase to reach higher

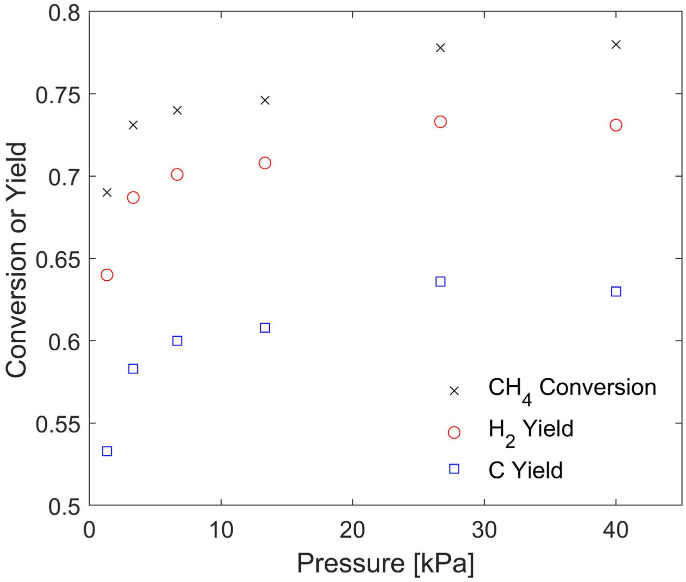

Figure 5.9: Effect of operating pressure on methane conversion, hydrogen yield, and carbon yield at methane inlet flow rate of 100 sccm, solar power of 1.86 kW, and medium thickness of 3.2 mm.

temperatures that increase methane conversion. However, this increase is significant primarily at low pressures below 6.67 kPa (t_{res} of 88 ms), above which increased pressure has a small effect on conversion and yields. This behavior is likely due to two competing phenomena that drive the overall reaction, as increased pressure (1) shifts the decomposition reaction backward per Le Chatelier's principle (decreases conversion), and (2) increases the mean residence time of the gas phase (increases conversion). Increasing residence time from 1.33 to 40 kPa increases methane conversion, yet $x_{\mathrm{C_2H_2}}$ decreases from 3.6% to 3% and $x_{\mathrm{C_2H_6}}$ decreases from 0.2% to below 0.1%. However, $x_{\mathrm{C_2H_4}}$ exhibits a local minimum of 0.4% at 13.3 kPa, whereas it is 0.9% at 1.33 kPa and 1.2% at 40 kPa. The increase in ethylene concentration at 40 kPa explains the reduction in hydrogen and carbon yields at 40 kPa compared to that at 26.7 kPa for nearly identical methane conversions (see Fig. 5.9). Finally, with increase in pressure, heavier hydrocarbons were observed in

MS measurements. This observation also supports the reduction in hydrogen and carbon yields at the highest pressure.

Despite increasing conversion and yields at higher pressures, graphitic quality of the carbon product obtained at higher pressures decreases significantly with no substantial increase in hydrogen and carbon production rates. Raman spectra of the carbon product at different operating pressures from 1.33 to 40 kPa are shown in Fig. 5.10a, and corresponding SEM images of the bounding pressure values are shown in Figs. 5.10b and c. As pressure increases, the $I_{\mathrm{D}}/I_{\mathrm{G}}$ ratio significantly increases under the same CH_4 inlet flow rate from 0.19 to 0.58. This increase correlates to a reduction in $L_{\mathrm{D,Ram}}$ from 27.7 to 15.9 nm with no significant increase in carbon production rate, with $\dot{m}_{\mathrm{C}}$ only increasing from 1.7 to 2.0 g/hr as a result of increased residence time. SEM images at the bounding pressures also illustrate a similar decrease in quality. The carbon deposition at the lowest pressure is significantly more uniform than the relatively irregular deposition at highest pressure (Figs. 5.10b and c).

The reduction in product crystallinity is attributed to the significant increase in particle collision frequency with the solid product at higher pressures as the gas concentration increases and mean free path decreases by more than one order of magnitude. Additionally, increasing pressure possibly results in formation (or increase) of trace heavier hydrocarbons that shift the carbon formation chemistry and lead to a significantly lower-quality textured carbon deposition [177]. Although higher hydrogen yields at higher pressures may contribute to increasing the quality of the carbon product as illustrated earlier (Fig. 5.3), this contribution is postulated to be very small especially as the mean free path of molecules decreases, impeding hydrogen diffusion upstream through the fibrous medium. Despite the advantage of producing significantly higher product quality at lower pressures, this

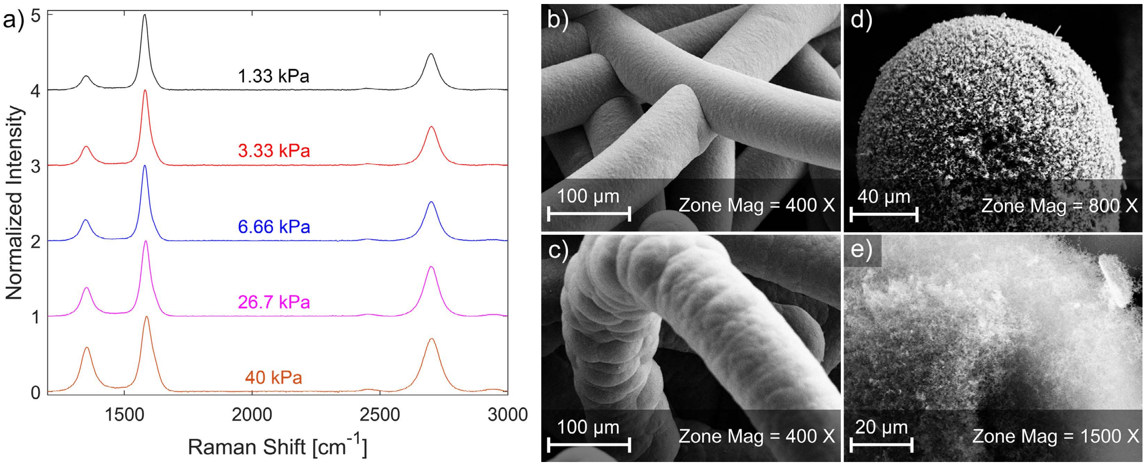

Figure 5.10: Methane pyrolysis at solar power of 1.86 kW, inlet flow rate of 100 sccm, and reaction zone thickness of 3.2 mm. (a) Raman spectra of carbon product at different operating pressures. (b,c) SEM images in the central region of the fibrous medium after 20 min at (b) 1.33 kPa and (c) 40 kPa. (d,e) SEM images of amorphous CB produced in lower temperature regions of the fibrous medium at 40 kPa.

improvement comes at the expense of higher vacuum operating costs and sealing concerns. However, the added value of the graphitic product possibly outweighs the additional costs and challenges, based on prior techno-economic analyses [12, 39].

Although carbon products from all tests presented in Fig. 5.9 are graphitic (based on Raman spectra), its form at higher pressures approaches a transition from high-quality graphite to lower quality carbon black. At the highest tested pressure of 40 kPa, amorphous CB forms and deposits in small amounts on annular regions of the fibrous material with significantly lower temperatures ($\sim$ 300 K lower than the maximum temperature). These amorphous CB nanostructures are shown in Figs. 5.10d and e, where their form is highly irregular with aggregates and filaments of various sizes. These amorphous CB nanostructures exhibit high Raman $I_{\mathrm{D}}/I_{\mathrm{G}}$ ratios with no 2D peaks (spectra not shown), which confirms the solid product's low quality. This observation warrants the investigation of the carbon product obtained at relatively high pressures further.

Therefore, CH_4 pyrolysis was conducted at various inlet flow rates from 100 to 800 sccm at an elevated pressure (13.3 kPa), relative to that in Fig. 5.4, while still operating at a solar power of 1.86 kW and fibrous medium thickness of 3.2 mm. Conversion and yield results at 3.33 kPa and 13.3 kPa for flow rates from 100 to 800 sccm are shown in Fig. 5.11.

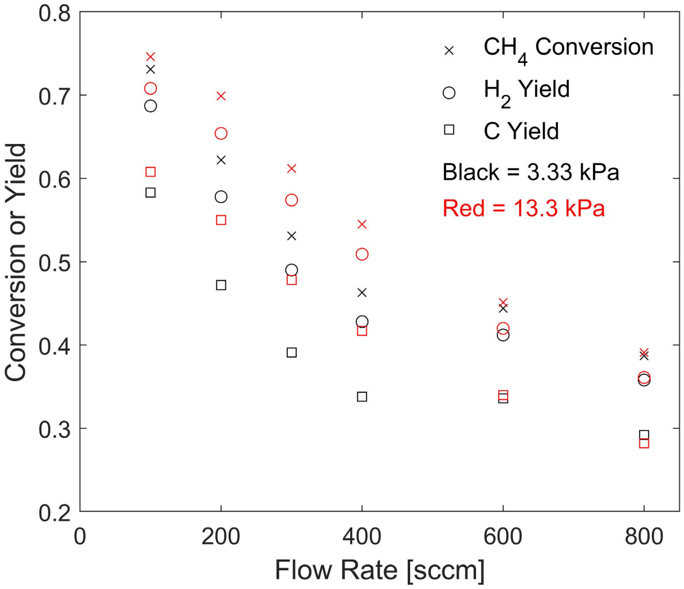

Figure 5.11: Comparison of methane conversion, hydrogen yield, and carbon yield at varying flow rates for two operating pressures (3.33 kPa and 13.3 kPa), solar power of 1.86 kW, and medium thickness of 3.2 mm.

Results shown in Fig. 5.11 for low to moderate flow rates (100 to 400 sccm) are consistent with those presented in Fig. 5.9; pressure increase enhances process conversion and yields. For example, at a flow rate of 200 sccm, a pressure increase from 3.33 to 13.3 kPa improves $X_{\mathrm{CH_4}}$ from 62.2% to 69.9%, $Y_{\mathrm{H_2}}$ from 57.8% to 65.4%, and Y_{C} from 47.2% to 55%. However, conversion and yield results do not increase with increasing pressure at higher flow rates of 600 and 800 sccm, with Fig. 5.11 indicating similar results at the latter two flow rates despite significant increases in residence times. Notably, as discussed next, the graphitic carbon product quality significantly degrades at 13.3 kPa beyond 200 sccm, where the onset of CB formation occurs near 400 sccm. This observation contrasts with prior work in which CB is noted to act as a much more effective catalyst compared to graphitic carbon [162], and graphitization usually leads to decay in catalytic activity [178]. However, in prior studies, the CB catalysts had significantly larger specific surface areas compared to graphite catalysts as well as the starting porous carbon medium and the graphitic product in the present study. Surface areas of the original medium and graphitic product were characterized using the BET method, with specific surface areas estimated as 1.5 m^2/g and 7.6 m^2/g, respectively (see Chapter 4). These surface areas are 2 to 3 orders of magnitude lower than CB catalysts tested in prior literature [162]. Based on the foregoing discussion, it is postulated that formation of CB, rather than graphitic product, negatively impacts the present methane pyrolysis process potentially due to a reduction in the product's thermocatalytic behavior. Further investigating the effect of carbon product form generated via methane pyrolysis on process kinetics through a more precise comparison is warranted.

The corresponding Raman spectra of the carbon product of experimental tests indicated in Fig. 5.11 at a pressure of 13.3 kPa are shown in Fig. 5.12a, with SEM images at the maximum tested flow rate shown in Figs. 5.12b and c. The reduction in carbon product quality and form at relatively high operating pressure is clearly apparent from results in Fig. 5.12a, which indicate a significantly higher sensitivity to inlet flow rate compared to results obtained at lower operating pressure (see Fig. 5.5a). At higher pressure and with increasing flow rates, the FWHMs of all Raman peaks increase up to the point where the D and G peaks begin to merge and the 2D peak disappears, corresponding to the absence of long-range graphitic structures. Additionally, increasing the inlet flow rate beyond 200 sccm generates amorphous CB with I_D/I_G ratios exceeding unity and leads to significant reduction in the average inter-defect distance. The highly irregular carbon aggregates and filaments are shown in Figs. 5.12b and c, and are very distinct from the smooth graphitic carbon deposition observed at lower pressure. In contrast, at a lower pressure of 3.33 kPa production of significantly higher-quality graphitic product is sustained up to flow rates of 2000 sccm (which is the system's maximum). The foregoing observations are expected to motivate further research into vacuum-aided methane pyrolysis processes for the production of high-quality carbon and hydrogen fuel, especially using concentrated solar power, where prior literature with this scope is very limited [35]. Additionally, direct solar-driven processes will potentially benefit from photocatalytic contributions in forming high-quality carbon products, as previously suggested for CNT formation [31].

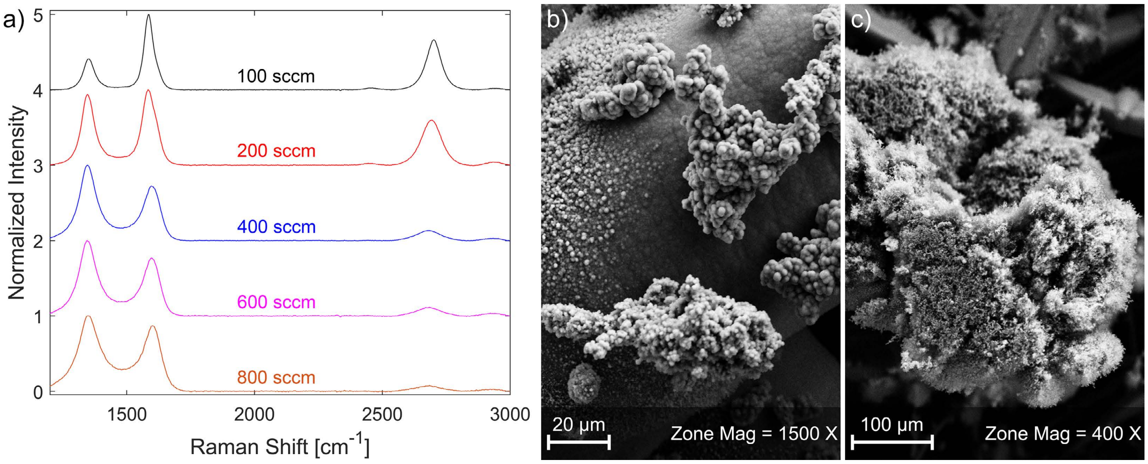

Figure 5.12: Methane pyrolysis at solar power of 1.86 kW, pressure of 13.3 kPa, and reaction zone thickness of 3.2 mm. (a) Raman spectra of carbon product at different methane inlet flow rates and a relatively elevated pressure. (b,c) SEM images of the fibrous medium at 800 sccm after 5 min.

Increased methane conversion and product yields as a result of increasing pressure and residence time decreases with the significant production of CB at flow rates of 600 and 800 sccm, as previously discussed. At a flow rate of 800 sccm and with increasing pressure, methane conversion does not increase (39% at both pressures) and carbon product formed at the higher pressure is poorly graphitized. This result contrasts with prior literature on CH_4 decomposition, which concludes that, compared to graphite, CB is a significantly more effective catalyst primarily due to its high specific surface area [162]. In contrast to prior work, the amorphous CB generated in the present study might potentially not have significantly higher surface area as compared to the more graphitic carbon, and the reduction in catalytic activity could be primarily due to less efficient thermal transfer. The formation of amorphous CB with significantly lower thermal conductivity and contact area between its grains reduces heat conduction radially and axially through the fibrous medium, correlating with decreasing temperatures measured at the rear side of the fibrous medium upon significant CB deposition at 600 and 800 sccm. This deterioration in thermal transport decreases the extent of the high-temperature region, and consequently leads to less effective dissociation of methane. Contrary to literature observations, the formation of CB instead of graphitic carbon in this work negatively impacts the decomposition process.

5.7 Effect of reaction zone size

For directly irradiated porous media, one challenge for thermochemical applications is the limited propagation of solar irradiation into the porous medium, which usually produces a temperature gradient [179]. To study this effect in combination with residence time, the thickness of the reaction zone (porous medium) was varied between 0.36 to 9.6 mm. Process conversion and yields are shown in Fig. 5.13 for methane pyrolysis at a pressure of 3.33 kPa, solar power of 1.86 kW, and methane flow rate of 100 sccm.

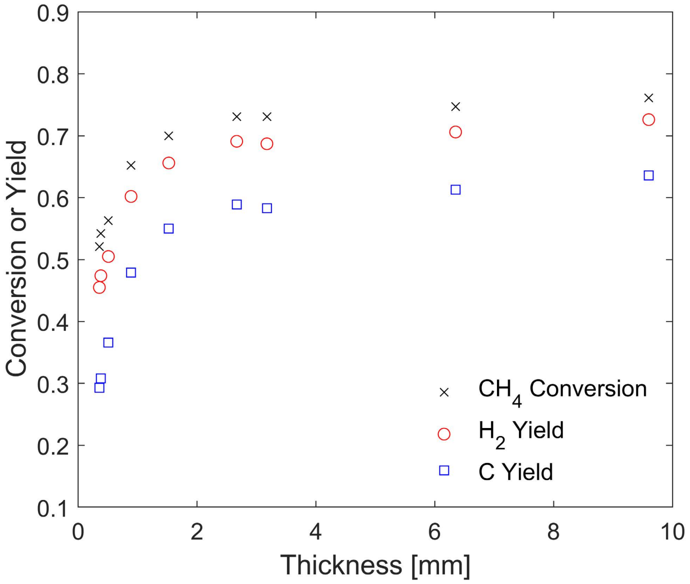

Figure 5.13: Effect of reaction zone size thickness on methane conversion, hydrogen yield, and carbon yield at operating pressure of 3.33 kPa, solar power of 1.86 kW, and methane inlet flow rate of 100 sccm.

Results indicate significant enhancement of conversion and yields for thicker substrates, and increasing the fibrous medium thickness from 0.36 to 9.6 mm increases $X_{\mathrm{CH_4}}$ from 52.1% to 76.1%, $Y_{\mathrm{H_2}}$ from 45.5% to 72.6%, and Y_{C} from 29.3% to 63.6%. This significant increase in conversion and yields is attributed to increased residence time, which varies between 4.2 ms at thickness of 0.36 mm to 133 ms at thickness of 9.6 mm. For results presented in Fig. 5.13, mole fractions of secondary byproducts, especially C_2H_2, decrease with increasing medium thickness despite significant increases in methane conversion, where $x_{\mathrm{C_2H_2}}$ decreases significantly from 6.5% to 3.1%. Other secondary byproducts exhibit general reductions, with $x_{\mathrm{C_2H_4}}$ decreasing from 1% to 0.4% and $x_{\mathrm{C_2H_6}}$ decreasing from 0.2% to below 0.1%. These results are consistent with prior literature showing that amount of C_2H_2 decreases with increasing residence times [55].

However, the significant enhancement in conversion and yields presented in Fig. 5.13 diminishes for reaction zone thicknesses larger than 2.67 mm ($t_{\mathrm{res}} = 32$

ms). This behavior is likely due to limited propagation of direct solar and thermal radiation across the porous medium that results in a significant negative temperature gradient into the substrate. Process conversion and yields at a thickness of 2.67 mm are nearly identical to those at 9.6 mm despite more than three-fold increase in thickness, and mole fractions of secondary byproducts are also low, with $x_{\mathrm{C_2H_2}} = 3.6\%$, $x_{\mathrm{C_2H_4}} = 0.5\%$, and $x_{\mathrm{C_2H_6}} < 0.1\%$. To enhance the decomposition process further and increase conversion and yields with increasing reaction zone thickness, the fibrous medium can be chosen based on an optimum configuration of porosity, fiber diameters, and fiber orientations that would result in more effective radiation propagation through the medium [180].

To observe performance of a thicker reaction zone with higher flow rate that provides a relatively higher solar-to-chemical efficiency, methane pyrolysis was tested at an operating pressure of 3.33 kPa, solar power of 1.86 kW, flow rate of 2100 sccm, and medium thickness of 6.35 mm, resulting in $X_{\mathrm{CH_4}} = 22.9\%$, $Y_{\mathrm{H_2}} = 21.5\%$, and $Y_{\mathrm{C}} = 18.4\%$. These results correspond to a solar-to-chemical efficiency of 3.05%, which can be further enhanced via design and process optimization as described earlier. Other additional experimental tests and chemical kinetics measurements are summarized in Appendix C.

As for the carbon product quality, Fig. 5.14 shows the (a) Raman spectra of the graphitic carbon generated at various thicknesses and (b) SEM image of the thinnest fibrous medium upon methane decomposition for 20 min. A correlation between the fibrous medium thickness and the $I_{\mathrm{D}}/I_{\mathrm{G}}$ ratio is observed in Fig. 5.14a, where the ratio decreases from 0.58 to 0.19 with increasing medium thickness and thus increases $L_{\mathrm{D,Ram}}$ from 15.9 to 27.7 nm. This enhancement in quality is attributed to multiple changing conditions, including increased residence time, methane conversion and hydrogen concentration, and front temperatures. As previously discussed, increasing fibrous medium thickness from 0.36 to 9.6 mm significantly increases process conversion and yields under the same methane flow rate, with a significant decrease in concentrations of secondary byproducts (mainly acetylene). The significantly higher concentration of secondary byproducts relative to hydrogen at smaller thicknesses adversely affects the carbon deposition quality.

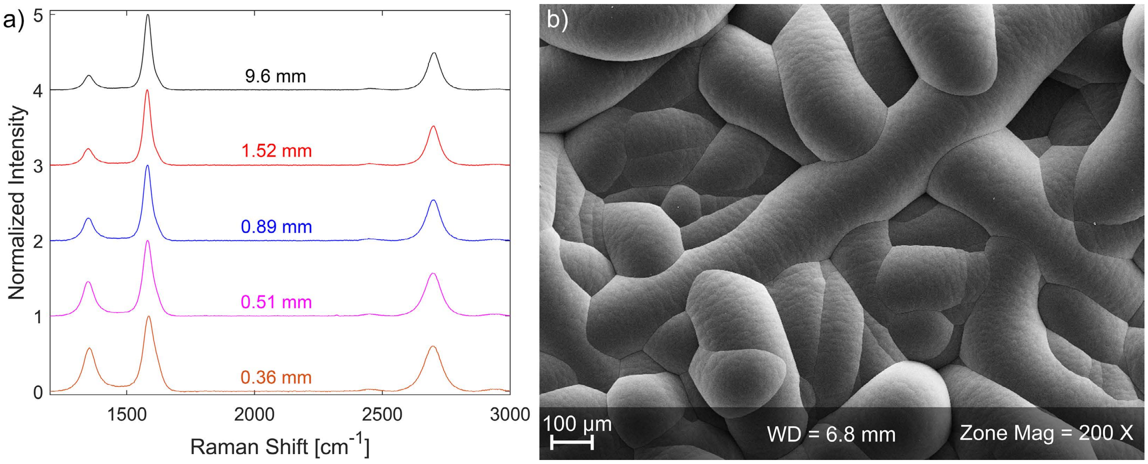

Figure 5.14: Methane pyrolysis at solar power of 1.86 kW, pressure of 3.33 kPa, and inlet flow rate of 100 sccm. (a) Raman spectra of carbon product with different reaction zone thicknesses. (b) SEM image in the central region of the fibrous medium with zone thickness of 0.36 mm after 20 min of CH_4 decomposition.

Solely investigating the effect of increased residence time with fibrous medium thickness without changing temperature is relatively challenging due to the nature of radiation propagation through the porous medium. A portion of the solar irradiation transmits through the material, and when the fibrous medium is thin ($<$ 0.89 mm), the rear surface temperature of the medium is nearly the same as the front surface. Therefore, thermal radiation losses are significantly higher, resulting in slightly lower front temperatures (as much as 100 K). As the fibrous medium thickness increases, front temperatures increase up to a certain point (observed at a thickness of 1.52 mm), above which front temperature changes are insignificant. This behavior leads to a plateauing of the enhancement of carbon quality as the reaction zone thickness extends beyond 1.52 mm, where more than six-fold increase in thickness only decreases $I_{\mathrm{D}}/I_{\mathrm{G}}$ from 0.22 to 0.19.

5.8 X-ray diffraction

XRD spectra (Fig. 5.15) of the carbon product generated in the central region of the fibrous material were measured at select operating conditions to complement Raman spectroscopy and SEM characterization results. As conditions become more favorable for the production of higher-quality graphitic product, the FWHM of the (002) peak reduces, and the peak location shifts to increasing θ_{002}, approaching that of crystalline graphite. As a result of enhancement in product quality, d_{002} significantly decreases from 3.53 Å for the thermally treated starting material to range between 3.43 and 3.40 Å, depending on pyrolysis conditions. Additionally, $L_{\mathrm{c,XRD}}$ significantly increases from 4.8 nm to range between 8.1 and 10.8 nm. However, because XRD measurements require a relatively large quantity of sample, isolating the sample to the local surface product formed at the maximum temperature was not possible. Therefore, XRD spectra and results of Fig. 5.15 have lower spatial fidelity as compared to Raman results.

Once again, all foregoing results indicate the production of high-quality turbostratic graphitic carbon product under most of the investigated operating conditions, and the present carbon product's d_{002} is similar to that of carbon nanofibers and nanotubes obtained via solar methane pyrolysis using metal-based specialized catalysts (d_{002} = 3.38 Å) [36]. Striking however is the XRD spectrum obtained at a solar power of 1.86 kW, flow rate of 800 sccm, and pressure of 13.3 kPa. The spectrum still shows a relatively crystalline product as opposed to a highly amorphous structure, as expected from CB. Deposition of higher-quality

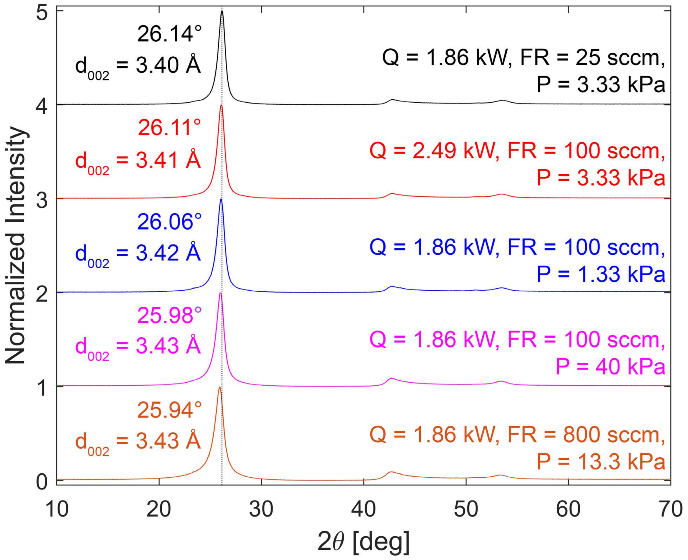

Figure 5.15: XRD spectra of the central region of carbon product generated at various process operating conditions of solar power (Q), flow rate (FR), and pressure (P), all with a reaction zone thickness of 3.2 mm.

graphitic product is postulated to occur in the initial decomposition stage, which then transitions to amorphous CB at a later stage due to reduction of front temperatures with enhancement in thermal conductivity across the fibrous medium as carbon product deposits. Therefore, regions of higher-quality product are possibly present within the sample used for the XRD measurement.

5.9 Transient performance and carbon capture

5.9.1 Transient performance

In prior thermocatalytic methane pyrolysis studies, catalysts deactivate due to carbon deposition that ultimately covers active catalytic sites. This deactivation results in significant reduction in process conversions and yields over time. Although the characteristics and mechanism involved are different, the process investigated in the present work undergoes a slightly similar reduction in transient performance. As previously discussed in Chapter 4, outlet methane mole fraction increases with decomposition time after a certain period, which decreases process conversion and yields. From Fig. 4.13, process conversion and yields gradually reduce over the 120 min decomposition duration, where $X_{\mathrm{CH_4}}$ decreases from 73% to 41.1%, $Y_{\mathrm{H_2}}$ from 67.3% to 35.8%, and Y_{C} from 55.1% to 24.8%.

Temporal results of the current solar methane decomposition process are presented for three different operating conditions in Fig. 5.16a. As shown in Fig. 5.16a, carbon yield generally undergoes three distinct regimes that extend depending on the process operating conditions: (i) relatively steady performance due to enhancement of the medium's thermocatalytic activity under carbon deposition, (ii) reduction in performance due to progressing carbon deposition that constricts and diverts flow away from the central hot region to regions of lower temperature, and (iii) final steady performance due to complete blockage of central flow that results in surface growth on the high temperature region and slight growth on lower temperature regions. Solid accumulation in the second stage leads to significant reduction in available flow area, residence time (Eq. 4.12), and permeability (Eq. 4.13) through the central region, which degrades process performance. The SEM image in Fig. 5.14b illustrates the final stage, in which complete blockage of flow occurs in the central region of the fibrous medium.

Similar observations apply to methane conversion and hydrogen yield, where the time that each stage extends for depends on process operating conditions; higher flow rate and solar power in addition to lower medium thickness results in faster progression through the regimes. The two former conditions correlate with higher carbon production and deposition rates, while the latter condition corresponds to less available volume for carbon deposition before flow blockage. For an experimental test with low inlet flow rate of 100 sccm and relatively thick medium of 3.2 mm thickness

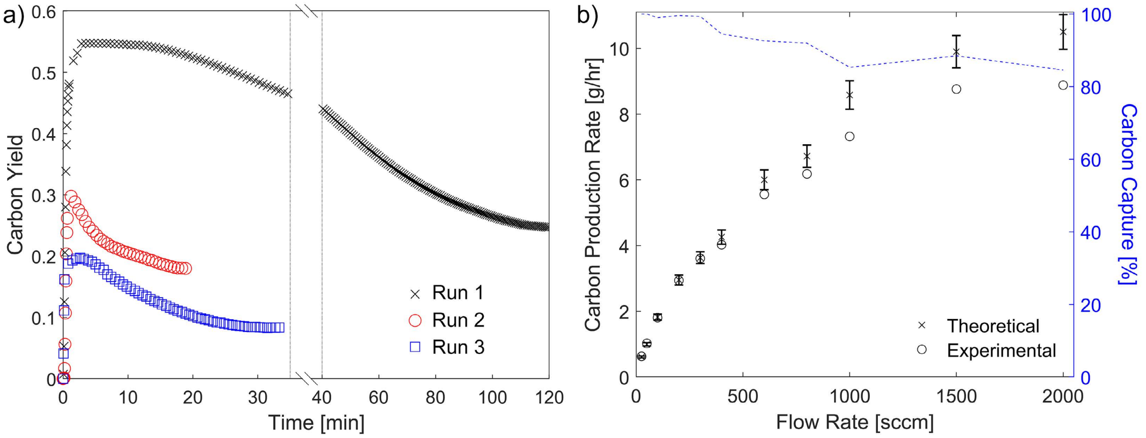

Figure 5.16: (a) Transient carbon yields at solar power of 1.86 kW and pressure of 3.33 kPa with (i) Run 1: $\dot{m}_{\mathrm{CH}_4}$ of 100 sccm and reaction zone thickness of 3.2 mm, (ii) Run 2: $\dot{m}_{\mathrm{CH}_4}$ of 100 sccm and reaction zone thickness of 0.36 mm, and (iii) Run 3: $\dot{m}_{\mathrm{CH}_4}$ of 1750 sccm and reaction zone thickness of 6.35 mm. (b) Theoretically and experimentally measured carbon deposition rates at different inlet flow rates, solar power of 1.86 kW, pressure of 3.33 kPa, and reaction zone thickness of 3.2 mm.

(Run 1 in Fig. 5.16a), Y_{C} decreases from 55% to 25% over the span of 120 min. In contrast, for a significantly thinner medium of 0.36 mm thickness (Run 2), Y_{C} decreases from 30% to 18% over only 20 min; the SEM image of the porous medium after CH_4 pyrolysis (Fig. 5.14b) clearly illustrates complete flow blockage and arrival at the final steady performance stage. Conversely, with a significantly higher flow rate of 1750 sccm and thicker medium of 6.35 mm thickness (Run 3), Y_{C} decreases from 20% to 8% over the span of 35 min.

Despite significant reductions in process conversion and product yields over time, such behavior is not attributed to catalytic deactivation mainly due to the low catalytic activity of the starting material. The original fibrous material used herein has a specific surface area of approximately 1.5 m^2/g, which is orders of magnitude lower than carbon materials typically used in prior literature with surface areas in the order of 100 to 1000 m^2/g. Therefore, the fast deactivation in catalytic activity as a result of reduction in surface area of the starting material is not applicable. Instead, the graphitic product generated has specific surface area that is greater than that of the starting material [9], possibly indicating higher catalytic activity, consistent with prior literature results. A previous study of methane pyrolysis using various carbonaceous catalysts with different properties and origins concluded that process conversions with different catalysts ultimately decline to the same steady-state performance upon carbon deposition [41]. This steady-state performance was significantly better than the initial performance using CNF catalyst due to its relatively smaller initial specific surface area, suggesting that the CH_4 pyrolysis carbon product can have superior catalytic properties and lead to a self-catalyzing process. Similar observations have been made in other prior studies [42, 181, 182], where the generated product is noted to have significant catalytic activity that aids in extending the catalytic persistence of the process. Therefore, the foregoing results and discussion indicate the presence of a self-catalyzing decomposition process.

5.9.2 Carbon capture

By concentrating solar irradiation directly onto the fibrous medium utilized here, the reaction zone and its high operating temperatures are confined to a relatively small local region. This circumstance minimizes CH_4 decomposition and carbon deposition outside of the reaction zone, leaving most of the carbon product on the central fibrous material in a readily extractable form that can be scaled-up via a roll-to-roll process [166, 183]. Such an approach would mitigate challenges related to solid carbon confinement and thermophoretic deposition on windows and reactor walls, which can lead to window cracking and tube clogging [39, 60]. To determine the efficiency at which the carbon product is captured, the theoretical average carbon deposition rate estimated using the time-average of Eq. 4.8 is compared to the experimentally determined rate based on mass gain measurements and decomposition time. Both the theoretical and experimental average deposition rates in addition to the solid carbon capture efficiency at various CH_4 inlet flow rates are shown in Fig. 5.16b.

All carbon product generated via CH_4 decomposition at inlet flow rates up to 300 sccm is measured and captured within the fibrous medium. At flow rates of 400 sccm and higher, the carbon balance does not entirely close, potentially indicating that a small portion of the solid product is carried by the flow through the fibrous network or elsewhere in the reaction chamber. The gap between experimental and theoretical deposition rates initially increases significantly with flow rate from 300 to 1000 sccm, but the carbon capture efficiency later plateaus at approximately 85% for flow rates above 1000 sccm. Solid carbon capture remains a challenge for large-scale methane pyrolysis; a prior solar decomposition study without a catalyst observed that approximately 94% of the solid carbon product deposited within the reactor and only 6% of the product was captured downstream [32]. In contrast, the fibrous carbon material in the present work acts as an effective medium in which carbon deposits and grows, and the carbon capture efficiency is anticipated to improve further with design optimization.

5.10 Conclusions

In this chapter, the solar-thermal methane decomposition process is investigated through a parametric study. Direct solar irradiation is concentrated onto a fibrous carbon medium, resulting in localized solar heated region with effective optical and thermal properties. Due to localized heating, the process reaches steady-state thermal and chemical operation from room temperature within the first minute of solar irradiation, and almost all theoretical carbon product is collected within the fibrous medium as a readily extractable high-quality graphitic product. Various process operating conditions were tested, with pure methane inlet flow rates ranging from 10 to 2000 sccm, solar powers from 0.92 to 2.49 kW, pressures from 1.33 to 40 kPa, and fibrous medium thicknesses from 0.36 to 9.6 mm. Results provide methane conversions ranging from 22% to 96%, hydrogen yields from 21% to 94%, and carbon yields from 17% to 91%, with corresponding maximum temperatures ranging from 1370 to 1750 K and mean residence times ranging from 2 to 530 ms in a potentially self-catalyzing, photocatalytic process. For the present solar pyrolysis process, hydrogen production rates and solar-to-chemical efficiencies as high as 4.88 g/hr and 3.05% are demonstrated, and are expected to significantly improve with design and process optimization.

Additionally, the solid carbon product is rigorously characterized under various testing conditions. Results of the parametric study indicate that high-quality turbostratic graphite ($> 99.65\%$ pure) is typically produced with Raman D/G peak ratios and average interplanar distances as low as 0.06 and 3.40 Å, unlike amorphous CB generally produced in prior literature with the use of no or carbonaceous catalysts. The difference in product quality compared to prior literature is potentially attributed to the contributions of (i) photocatalytic effects as a result of direct solar irradiation with high intensity, (ii) relatively long residence time in the fibrous medium at high temperatures, (iii) favorable carbon deposition at relatively low pressure, and (iv) very low trace concentrations of aromatic hydrocarbons (undetected). The quality of the carbon product formed generally degrades with increasing pressure and flow rate in addition to decreasing solar power (temperature) and fibrous medium thickness, with the quality being highly sensitive to operating pressure. To obtain continuous operation and overcome reduction in process performance with decomposition time due to flow constriction, Chapter 6 focuses on scaling-up the current pyrolysis process via a roll-to-roll configuration [166, 183]. The present solar-driven pyrolysis process provides a sustainable way of meeting the rapidly growing demands for clean hydrogen fuel and electrodes for Li-ion batteries [184].

Chapter 6: Process Scale-Up for Continuous Processing[1]

In this chapter, a scalable route to continuous solar-thermal methane pyrolysis is developed in a large-scale solar reactor [183]. The route employs a continuous roll-to-roll mode of operation to supply fresh fibrous medium after significant carbon deposition and to mitigate process performance decline with time that was presented in Chapter 5. The efficacy of the roll-to-roll approach for methane decomposition is evaluated, and a parametric variation of operating conditions is presented.

6.1 Introduction

Scaling-up solar methane decomposition processes has been an ongoing challenge due to the production of solid carbon product with a tendency to agglomerate and deposit on reactor walls [35]. Various routes for scale-up to achieve continuous processing have been considered in prior studies. Early studies focused on methane pyrolysis in large-scale volumetric/tubular solar reactors without a catalyst [55].

---

[1] All or some portions of this chapter contributed to paper by M. Abuseada and T. S. Fisher, titled Continuous solar-thermal methane pyrolysis by roll-to-roll processing, published in Energy Proceedings 25 (2022).

This type of solar reactor allows continuous processing but requires very high operating temperatures (1600-2100 K), and it suffers from high radiation losses [51] and from uncontained carbon production and deposition within the reactor that cause window obstruction or tube clogging [32]. The issue of uncontained carbon deposition eventually leads to complete tube blockage and process interruption [55]. However, a previous study [37] used a porous graphite tubular reactor with hydrogen inflow to mitigate issues related to carbon deposition and obstruction. Although this approach may be effective in reducing deposition challenges, it further increases thermal losses and leads to dilution of the primary reactant.

To enhance thermal transfer efficiencies through effective radiant absorbers, a prior study investigated the use of carbon black powder catalysts in a flow-seeded solar reactor [56]. The particles were continuously fed with the methane inlet flow and should ultimately exit the solar reactor with minimal deposition within the reactor under an appropriate flow field. However, such an approach does not utilize the powder catalysts effectively due to the low residence time of particles within the reactor. Additionally, it suffers from the need for relatively high flow rates of carrier gas to minimize carbon deposition [185], which negatively impacts process performance and may be subject to flow instabilities that lead to progressing carbon deposition and ultimately to failure. A similar approach was considered in another study using an entrained-flow reactor [53] in which carbon particles are fed through a tubular reactor from above and are collected in a filtering device as they fall by gravitational force. Although this approach allows for continuous processing, it suffers from additional thermal loads of the particles introduced into the reactor at room temperature that often do not compensate for the added benefits of increased reaction surface area [53]. Other studies have considered rotary-bed [36] and packed-bed [57, 186] reactors that use carbonaceous and/or metal-based catalysts. Despite demonstrating functional approaches for continuous injection of particles, the need for continuous solid carbon removal often results in a semi-continuous mode of operation [185]. Additional solar reactor designs for other thermochemical processes can be found in a related review paper [187].

A different approach to continuous methane pyrolysis utilizes molten metal reactors [47, 48]. The molten alloys enhance heat transfer to the CH_4 gas medium, mitigate catalyst deactivation, and enable a relatively effective and continuous carbon removal method (solid carbon particles float on top of the molten medium) [48]. However, the presence of significant metal impurities (approximately 8%) within the solid carbon product [47, 188] typically necessitates additional energy-intensive purification methods and leads to the consumption of the molten metals over time. Establishing efficient carbon extraction and continuous operation remains a challenge.

In this study, a different route to scaling up solar-thermal methane pyrolysis for continuous production is considered by implementing a roll-to-roll deposition method. Roll-to-roll has been utilized for scale-up and continuous growth of various materials, such as graphene films and membranes [189–192], graphitic petals [166], and solar cells [193]. Roll-to-roll has also been used in continuous materials processing and post-treatment [194, 195], but has not been previously considered for the production of graphite and hydrogen via methane decomposition. In this chapter, a continuous solar-thermal methane pyrolysis process utilizing a roll-to-roll mechanism and a fibrous carbon medium is presented, and the efficacy of this approach in scaling up the process and mitigating issues related to declining process performance with time [9] due to carbon deposition and accumulation is evaluated. The process is rigorously evaluated with parametric variations of operating conditions under different methane inlet flow rates (25 to 2000 sccm), solar powers (0.92 to 2.34 kW), and pressures (0.67 to 4.67 kPa).

6.2 Experimental setup and methodology

The experimental setup consists of a large-scale solar reactor, a solar simulator, roll-to-roll mechanism, and other auxiliaries. The solar reactor integrates the roll-to-roll manufacturing approach to achieve continuous processing once significant carbon deposition has accumulated within the fibrous carbon medium. This approach supplies the process with fresh fibrous medium to enable continuous operation over much longer duration, after which the roll can be replaced for a new batch of processing. The roll-to-roll approach is also amenable to further scale-up and enhancement by designing different chamber zones [192] that allow continuous feeding of the fibrous roll in and out of the solar reactor. Hence, eliminating the need for roll replacement and batch processing. Fig. 6.1 shows an overview of the roll-to-roll solar-thermal methane decomposition process and main components.

6.2.1 Large-scale solar reactor

The large-scale solar reactor, shown in Fig. 6.2, is embedded within a cart that allows ease of movement of the reactor for roll substitutions, and it provides means of accurate placement of the solar reactor under the solar simulator (see Fig. 6.1). The solar reactor consists of a large cold-wall stainless steel cylindrical chamber with an overall height of 40.6 cm and inner diameter of 30.5 cm. The chamber walls are cooled via embedded water lines, and cooling is supported using the 1.4 kW chiller introduced in Chapter 3. A 12.7 mm thick quartz that is 25.4 cm in diameter is used to seal the reacting flow while allowing direct irradiation from the solar simulator

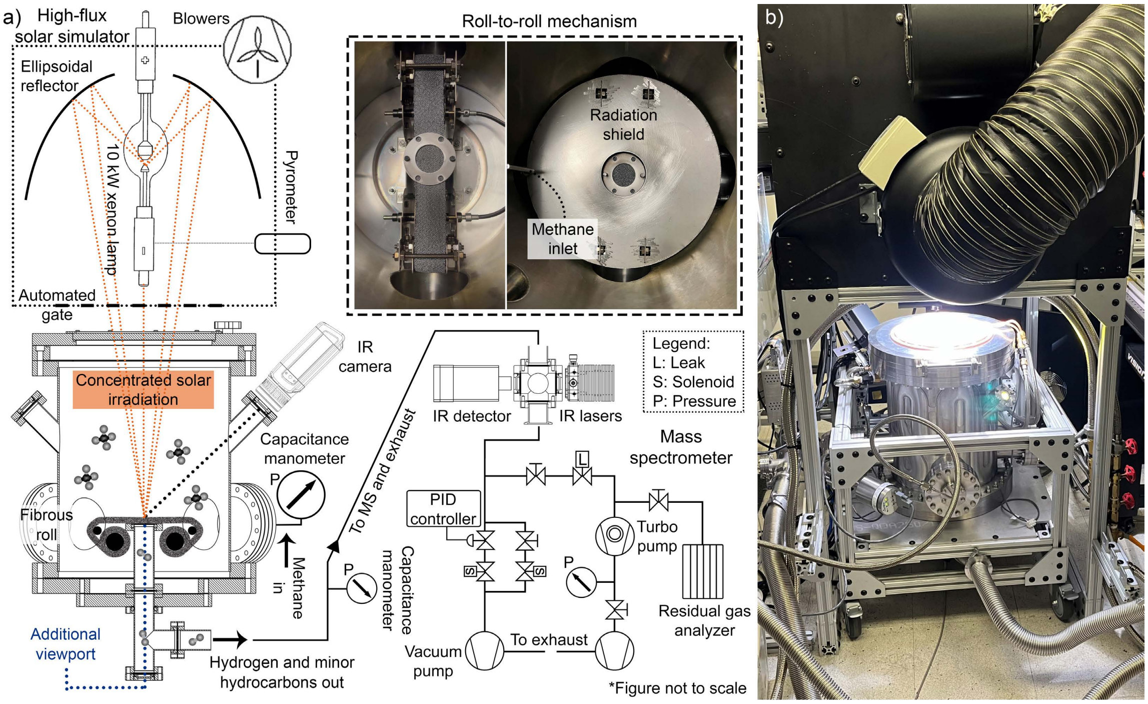

Figure 6.1: (a) Process overview of the roll-to-roll solar-thermal methane pyrolysis experimental setup. Figure inset in the top right shows photographs of the roll-to-roll mechanism and radiation shield. (b) Photograph of the roll-to-roll experimental setup.

onto the carbon fibrous roll. To maintain the thermal integrity of the quartz window and to avoid unwanted carbon deposition, the quartz window is supported by a water-cooled flange and is additionally cooled using a blower.

The solar reactor has a total of seven additional ports. Four of these ports are located at 90° angles from the reactor's focal plane (where the carbon roll is located) and interface with an upstream capacitance manometer, thermocouples, motors for the roll-to-roll mechanism, and the inlet feedstock line. Furthermore, two ports are located at a 45° angle from the focal plane to allow optical access to the top side of the roll, where the high-resolution longwave IR camera measures temperatures up to 2000 °C and monitors front side spatial temperatures. As mentioned in Chapter 4, the IR camera was calibrated to the fibrous material and viewports against a type

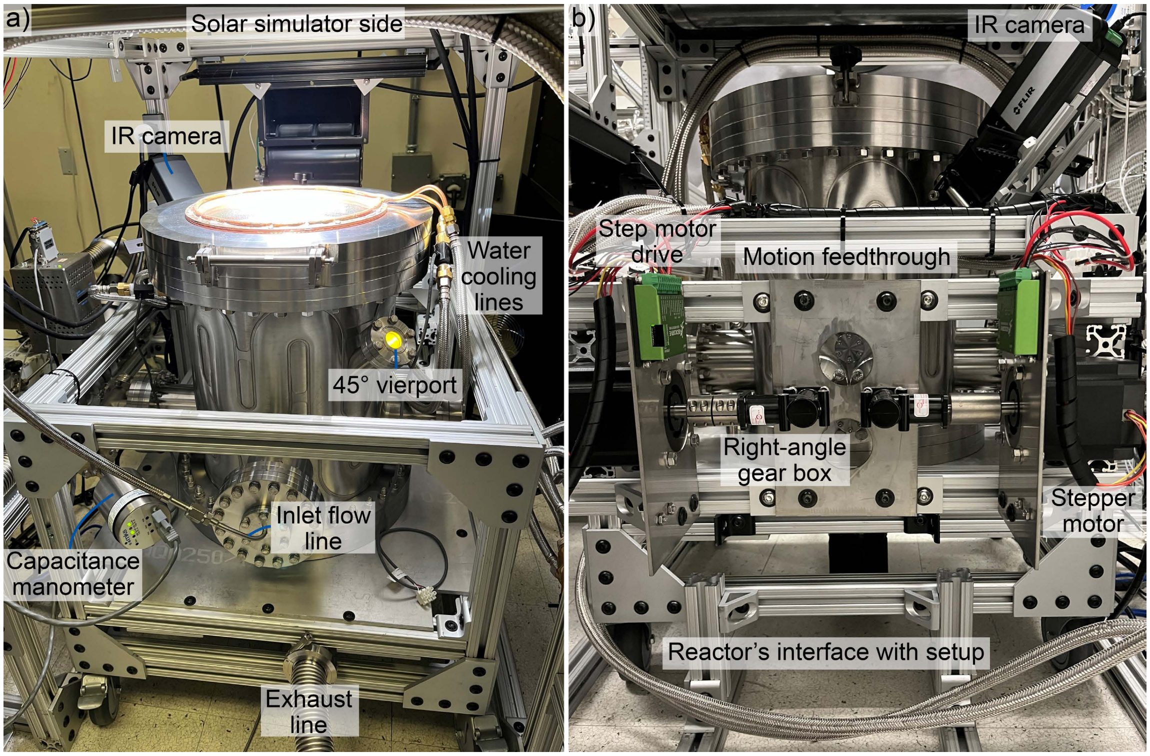

Figure 6.2: Photographs of the (a) large-scale roll-to-roll solar reactor used for continuous processing and (b) roll-to-roll auxiliaries and motion feedthroughs.

K thermocouple, leading to an apparent emissivity of 0.9 and an uncertainty of ± 30 K for temperatures reported throughout this work. The last port (3.8 cm in diameter) is located directly below the roll to serve as the reactor's exhaust and to allow monitoring the roll's temperature from the rear side, as previously shown in Fig. 4.3.

6.2.2 Solar simulator and auxiliaries

For process scale-up, the solar simulator introduced in Chapter 2 is rotated into a beam-down configuration (see Fig. 6.1) to concentrate solar irradiation into the roll-to-roll solar reactor. The characteristics of the solar simulator are identical to those presented in Chapter 2 and all dimensions were configured so that the solar simulator's focal plane coincides with the reactor's focal plane and the location of the fibrous roll. The concentrated light source brings the porous carbon roll to high temperatures locally, where pure methane (99.999% pure) enters the solar reactor and rapidly decomposes on the fibers of the carbon porous roll, depositing solid carbon and producing mainly hydrogen and unconverted methane in the product stream. The configuration of all upstream and downstream auxiliaries and instrumentation, such as mass flow controllers and valves, is the same as that presented in Chapter 3 for the small-scale solar reactor. The reactor's gaseous product stream is directed to the in situ mass spectrometer for continuous monitoring of the process performance by quantifying methane conversion and product yields using the same methodology described in Chapter 4.

The only additional auxiliaries integrated into the large-scale solar reactor consist of two motion feedthroughs to support the operation of the roll-to-roll mechanism. Fig. 6.2b shows a photograph of auxiliaries pertaining to the roll-to-roll mechanism. The two feedthroughs allow interfacing motor components outside the reactor to the roll-to-roll mechanism inside the reactor. For external components, the system consists of two stepper motors, two right-angle gear boxes, and two step motor drives, as shown in Fig. 6.2b. Auxiliary components enable automating the roll's motion in LabVIEW, which has been added to the existing VI in a separate independent loop as shown in Appendix A.

6.2.3 Roll-to-roll mechanism

The roll-to-roll mechanism, shown in Fig. 6.3, is custom built from stainless steel and allows for a roll width of 3.8 cm to be used, matching the size of the exhaust port. The processed region of the roll is always located within the focal plane of the reactor and solar simulator, where irradiation is most concentrated. One side of the mechanism is used to store the full carbon roll prior to experimentation, after which the roll moves to the other side during methane pyrolysis to allow for continuous processing in batches. Two independent stepper motors are used (see Fig. 6.2b) to drive the roll from the initially loaded side to the empty side while maintaining the roll's proper tension within the reaction region. The shafts of both roll sides are connected to the motion feedthroughs (and hence the motors) using flexible shafts. Furthermore, an annular disk with a circular aperture of 3.8 cm gently applies additional tension on the roll's reaction zone to minimize flow bypass through the exhaust line, and a stainless steel radiation shield is added to protect the roll-to-roll mechanism and its auxiliaries as shown in Fig. 6.1a. The entire roll-to-roll mechanism then bolts onto the base plate of the large-scale solar reactor, and can be removed from the reactor for loading and unloading the carbon rolls.

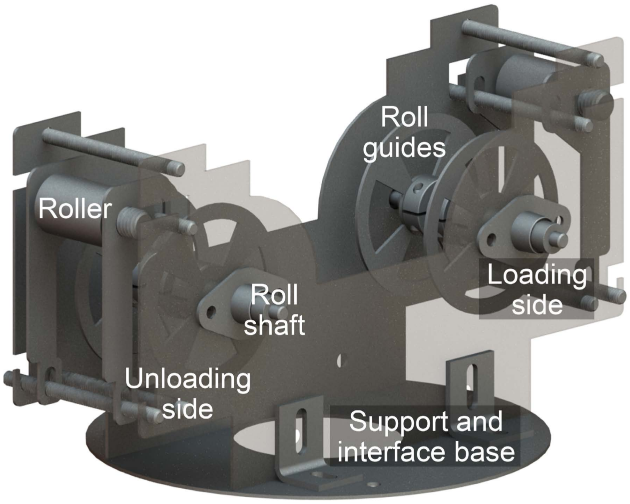

Figure 6.3: CAD model of the roll-to-roll mechanism.

6.2.4 Materials and characterization techniques

The carbon roll starting materials used in this study consist of carbon felts and cloths. The carbon felt (FuelCellEarth, C200) is comprised of nonwoven polyacrylonitrile-based carbon fibers of 9.6 µm nominal diameter with an estimated effective porosity of 0.952 and relatively low specific surface area (1.5 m^2/g) [9], identical to the C100 felt introduced in Chapter 4. In contrast, the carbon cloth (FuelCellEarth, CC6) is comprised of woven carbon fibers of 8.7 µm nominal diameter with an estimated effective porosity of 0.82. Both the carbon felt and cloth are resistant to high temperature decomposition, as concluded from mass loss measurements and a thermogravimetric analysis. For solid carbon characterization, the same equipment and techniques described in Chapter 3 were used; Scanning electron microscope (SEM) images were captured by a ZEISS Supra 40VP field emission SEM with a secondary electrons detector and energy dispersive X-ray spectroscopy (EDS) detector, Raman spectra were obtained using a 532 nm laser with a 40× achromatic objective lens and a CCD detector of a Horiba iHR 550 imaging spectrometer, and X-ray diffraction (XRD) spectra were measured by a Panalytical X'Pert Pro X-ray powder diffractometer with a Cu Kα source.

6.3 Transient process performance

6.3.1 Methane conversion and product yields

Tests were conducted at various operating conditions implementing the use of the developed roll-to-roll mechanism to investigate its efficacy for solar-thermal methane pyrolysis. The solar reactor is first evacuated while purging with nitrogen to ensure an oxygen-free environment, and the reactor is confirmed to be gas-tight. Solar irradiation then begins at vacuum condition, after which pure methane flow is introduced to the solar reactor at the tested flow rate. Gaseous product monitoring data using the in situ MS was used to determine transient methane conversion and product yields as presented in Fig. 6.4. The solar power is once again estimated, in a manner consistent with that presented in Chapter 4, by integrating the net irradiance from the HFSS over an area of 68.6 mm in diameter.

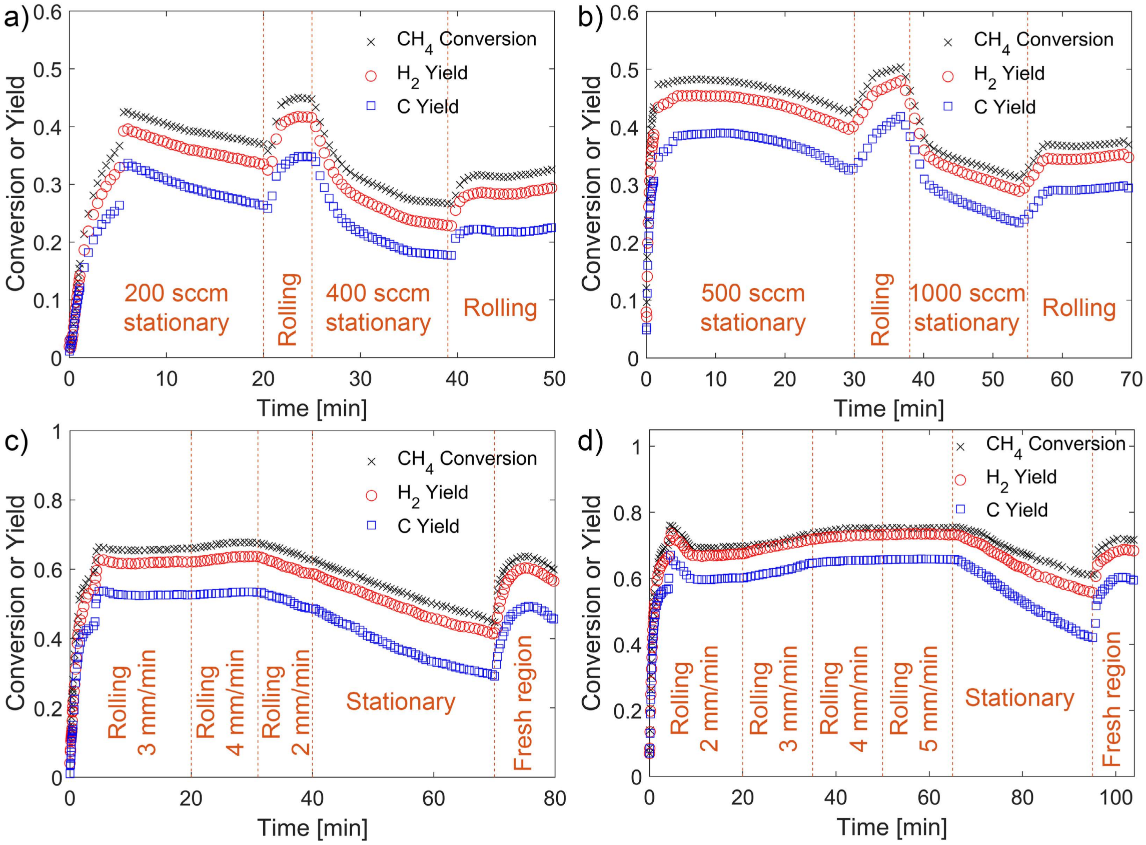

Figure 6.4: Experimental testing of roll-to-roll solar-thermal methane pyrolysis demonstrating effective operation at four operating conditions as quantified via conversion and yields. Testing at operating pressure of 3.33 kPa and (a) power of 1.86 kW and thickness of 0.89 mm (b) power of 1.86 kW and thickness of 6.35 mm (c) flow rate of 200 sccm, power of 2.34 kW, and thickness of 0.89 mm, (d) flow rate of 200 sccm, power of 2.26 kW, and thickness of 1.78 mm.

The first test (Roll 1, Fig. 6.4a) was conducted using the carbon cloth (CC6) with a thickness of 0.89 mm at operating pressure of 3.33 kPa, solar power of 1.86 kW (160 A), and with methane inlet flow rates of 200 and 400 sccm. The estimated reaction residence times through the thickness of the cloth at these flow rates are 11 and 5.9 ms, respectively, with an average temperature of 1470 ± 30 K measured on the irradiated side of the cloth. As shown in Fig. 6.4a, methane conversion and product yields decrease over time when the roll is stationary at both tested flow rates. This reduction is due to progressive deposition of graphitic carbon on the roll's fibers that leads to flow obstruction and reduced gas residence times, as discussed in Chapter 5.

However, when the carbon cloth roll is moved to a fresh region and remains rolling, methane conversion and product yields significantly increase and approach maximum values without any flow obstruction. At 200 sccm, methane conversion increases from 36% to 45% upon rolling, while it increases from 27% to 33% at 400 sccm. Similarly, hydrogen and carbon yields undergo similar enhancements, where the improvement in performance should increase with the stationary decomposition duration. However, due to the combination of flow rate, solar power, and roll thickness, methane conversions and product yields are moderate, and are expected to improve upon mitigation of issues such as flow bypass around the porous carbon roll and optimization of thermodynamic conditions.

The second test (Roll 2, Fig. 6.4b) was performed on a carbon felt (C200) with a thickness of 6.35 mm at pressure of 3.33 kPa, solar power of 1.86 kW, and inlet flow rates of 500 and 1000 sccm. The resulting average temperature of the felt under solar irradiation was 1520 ± 30 K. As a result of increased roll thickness, the performance benefits from higher flow rates due to increased reaction zone length, for which gas residence times at 500 and 1000 sccm are 36 and 18 ms. Methane conversions for the two considered flow rates had maximum values of 50% and 38%, respectively. Enhancement in process performance upon rolling the carbon felt is similar to that observed for Roll 1 (Fig. 6.4a), with 21% and 23% increases in methane conversions at 500 and 1000 sccm. However, in contrast to the thin carbon cloth, the thick felt rolls less easily and will stop rolling upon significant carbon deposition. Therefore, this type of roll was not used in further testing.

Two additional tests were conducted to assess the influence of web speed and its effect on the pyrolysis process while further demonstrating the capability of the roll-to-roll mechanism at higher solar powers. A carbon cloth (CC6) with a thickness of 0.89 mm (Roll 3, Fig. 6.4c) was tested at pressure of 3.33 kPa, solar power of 2.34 kW (190 A), and inlet flow rate of 200 sccm, with web speeds of 2, 3, and 4 mm/min. The carbon web requires rolling for a distance of 38 mm to fully replace the starting roll section, and hence the tested web speeds translate to effective decomposition periods of 19, 12.7, and 9.5 min, respectively. With continuous rolling of the fibrous carbon cloth at different web speeds, the process performance remains stable over the decomposition period.

Methane conversion as high as 68% was observed at the maximum web speed with an average temperature and gas residence time of 1580 ± 30 K and 11 ms, for which the steady-state process performance enhances with higher web speed. In contrast to changing web speed from 2 to 3 mm/min, a web speed increase from 3 to 4 mm/min resulted in relatively small enhancement in process conversion and yields. Therefore, moving the carbon cloth roll at a speed of 3 mm/min appears to be a good compromise between process performance and roll consumption. Upon stopping the roll (Fig. 6.4c - stationary), methane conversion and product yields continue to decrease with decomposition time, as expected. The process performance is restored again upon rolling to a fresh region by moving the fibrous cloth by $\sim$ 40 mm at a speed of 100 mm/min, after which methane conversion increases from 45% to 64%.

In contrast to initial testing, Roll 3 with a web speed of 4 mm/min exhibits enhancement in methane conversion up to 1.5 times higher than that of the stationary cloth. Another carbon cloth with a thickness of 1.78 mm (Roll 4, Fig. 6.4d) was tested at pressure of 3.33 kPa, solar power of 2.26 kW (185 A), and inlet flow rate of 200 sccm. Roll 4 yielded similar results to those of Roll 3, but with higher methane conversion (as high as 76%) due to the increased gas residence time (21 ms) despite the slight reduction in solar power. Hydrogen and carbon yields were significantly higher and closer to the methane conversion as a result of presence of less minor hydrocarbons (mainly C_2H_2) in the product stream due to more complete dissociation. Consistent with results of Roll 3 (Fig. 6.4c), increasing web speed from 2 to 3 mm/min results in a significant improvement in the steady-state process performance. Further increasing the speed from 3 to 4 mm/min results in relatively smaller enhancement, and increasing the web speed beyond 4 mm/min results in no improvement (see Fig. 6.4d). In contrast to Roll 2, the reduced thickness of Roll 4 enabled it to roll relatively smoothly.

6.3.2 Solid carbon product characterization

The quality of the carbon product generated during testing of the four rolls is presented in Fig. 6.5, where SEM images indicate that the graphitic carbon product conformally grows over the starting fibers. This observation is consistent with prior results presented for the small-scale solar reactor in Chapter 5. Comparing graphitic growth of the roll's fibers using SEM images, the original cloth fibers (Fig. 6.5a) undergo significant growth under short processing time. The fibers in Rolls 1, 3, and 4 (Fig. 6.5b-d) grow up to 5.5 times their initial diameters up to the point at which they coalesce. EDS spectra of the carbon product were obtained (not shown) and have revealed only single atomic carbon peaks, indicating the high purity of the carbon product as expected from prior observations and from an oxygen-free environment. In contrast to Roll 4, fibers in Roll 1 (Fig. 6.5b) exhibit more surface irregularities and slightly rougher deposition due to the non-ideal pyrolysis conditions (i.e., lower solar power and gas residence time). These minor irregularities indicate that the carbon product of Roll 1 contains more structural defects. To characterize the nature of the graphitic product further, an SEM image of a cross-sectional cut of one of the fibers of Roll 2 is shown in Fig. 6.5e, which demonstrates the significant growth of the original fibers in addition to the formation of microporous graphitic layers [9], as discussed in Chapter 4.

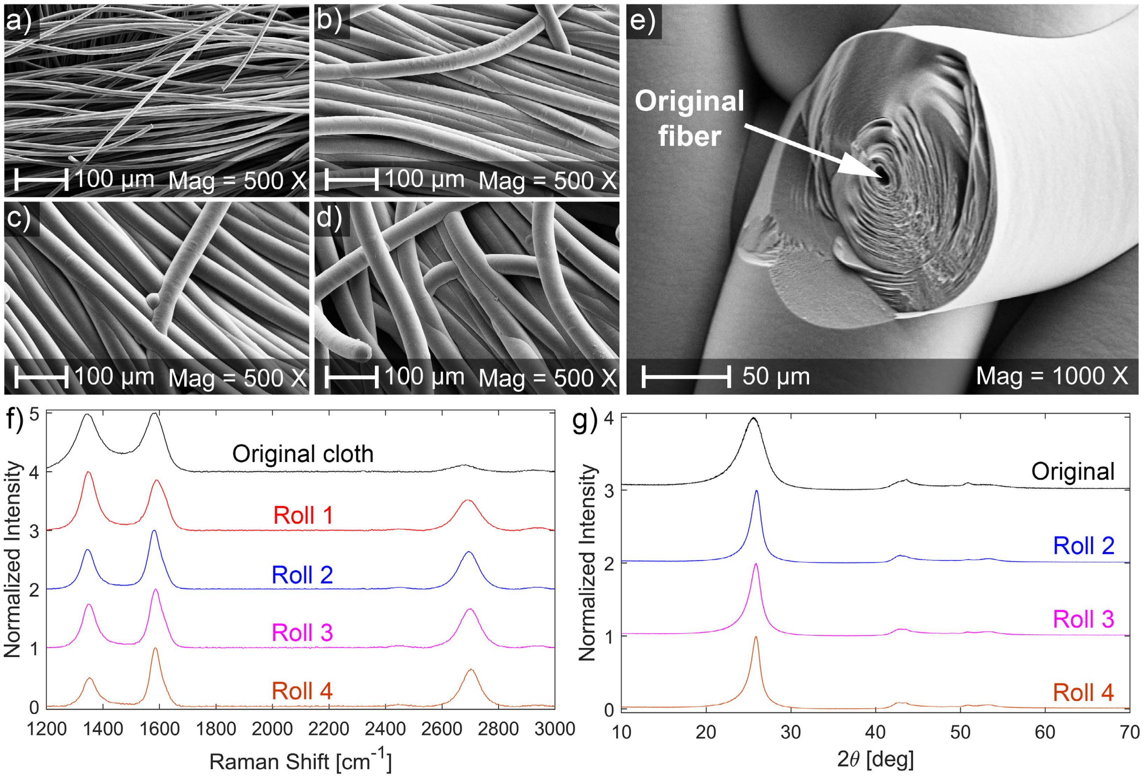

Figure 6.5: Characterization results of solid carbon product of the four different experimental roll-to-roll initial tests. SEM images for: (a) original carbon cloth/roll, (b) Roll 1, (c) Roll 3, (d) Roll 4, and (e) cross-section of Roll 2. (f) Raman and (g) XRD spectra of the roll-to-roll original carbon cloth and carbon products of different tests.

The carbon product was further characterized by obtaining Raman (Fig. 6.5f) and XRD spectra (Fig. 6.5g). Raman D, G, and 2D peaks are present for all processed samples and are distinct, indicating the production of relatively high-quality carbon product. This characteristic is in contrast to the weak/missing Raman 2D peak in the original starting material and amorphous carbon generally produced in prior literature by carbonaceous catalysts [59]. A similar observation applies to the XRD spectra, where prior literature shows missing distinct XRD peaks for the amorphous product generated [36]. Consistent with SEM images, Roll 4 produced a much higher quality carbon product compared to Roll 1, where the D/G peak ratio is 0.49 (compared to 1.16). XRD spectra also complement the Raman spectra and indicate the presence of a relatively high-quality graphitic product with a distinct and narrow (002) peak. The peak occurs at a 2θ of approximately 26.0°, which corresponds to an average interplanar distance of 0.342 nm using Bragg's law [142], compared to 0.335 nm for perfectly crystalline graphite and to 0.348 nm for the starting material. The graphitic quality of the product is expected to improve further with design and process optimizations.

6.4 Parametric study

Similar to the work presented in Chapter 5 for the small-scale solar reactor, parametric variations of flow rate, solar power, and pressure were conducted. The process performance and carbon product quality are characterized and presented in the following subsections to correlate them with different operating conditions, and to evaluate further the efficacy and integrity of the established roll-to-roll solar-thermal methane decomposition process.

6.4.1 Process performance

Effect of flow rate

The effect of inlet methane flow rate is considered first at a solar power of 2.34 kW (corresponding to maximum solar flux of 3.26 MW/m^2) and pressure of 3.33 kPa. Different flow rates from 25 to 2000 sccm were tested using two roll thicknesses of

0.89 and 1.78 mm of the fibrous carbon cloth material (CC6). For these tests, average temperatures measured on the front side of the roll after significant deposition range from 1550 to 1640 K ± 30 K. Methane conversion and product yields for the different flow rates are shown in Fig. 6.6a for 0.89 mm thick roll and in Fig. 6.6c for 1.78 mm thick roll. For the considered operating conditions, $X_{\mathrm{CH_4}}$ ranges between 87.4% and 29.5%, $Y_{\mathrm{H_2}}$ ranges between 86.1% and 26.2%, and Y_{C} ranges between 83.5% and 19.9%. Additionally, acetylene mole fractions in the outlet stream and the production rates of hydrogen and carbon are shown in Fig. 6.6b for the 0.89 mm thick roll and in Fig. 6.6d for the 1.78 mm thick roll.

Process conversion and product yields decrease significantly with increasing flow rates due to significant reductions in gas residence times. For the 0.89 mm thick roll, residence times at 25 and 1200 sccm are 11 and 0.24 ms, with methane conversion decreasing from 83.9% to 29.5%. In contrast, for the 1.78 mm thick roll gas residence times at 50 and 2000 sccm are 11 and 0.29 ms, with methane conversion decreasing from 87.4% to 33.6%. Compared to the thinner roll, higher methane conversion and product yields are achieved with the thicker roll, despite the two-fold increase in flow rate.

Reduction in methane conversion with increasing flow rates reported here, although significant, are not as large as those reported in prior literature for volumetric/tubular reactors. For example, in prior work of methane decomposition in a particle seeded tubular reactor at 1623 K [53], reduction in $X_{\mathrm{CH_4}}$ from 74% to 20% were reported with increase in methane inlet flow rate from 100 to 300 $\mathrm{cm^3/min}$. This reduction translates to decrease in methane conversion by a factor of four. Under a larger increase in flow rate from 100 to 400 sccm (four-fold increase in contrast to three-fold), $X_{\mathrm{CH_4}}$ decreases from 72% to 55% for the 0.89 mm roll and from 81% to 62% for the 1.78 mm roll. These reductions correspond

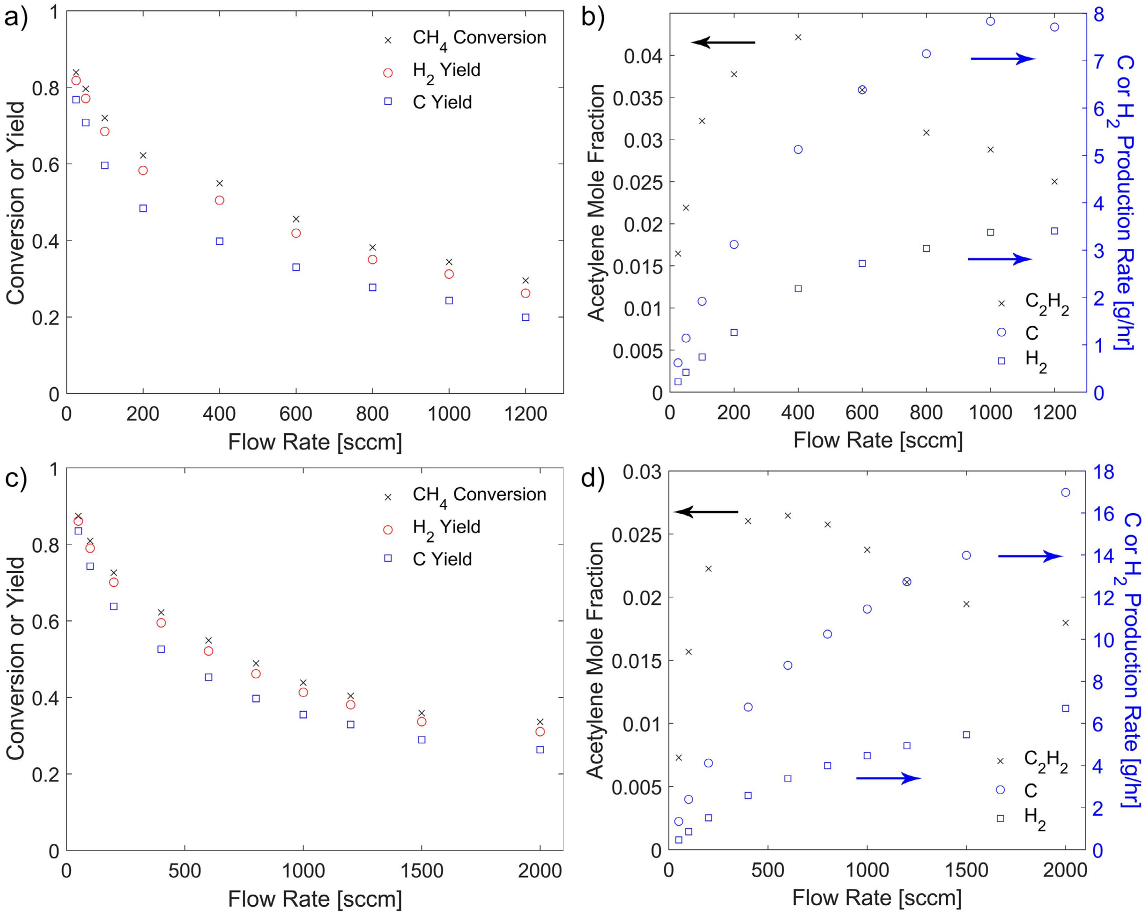

Figure 6.6: Roll-to-roll methane pyrolysis at a pressure of 3.33 kPa and solar power of 2.34 kW. (a,c) Effect of methane inlet flow flow rate on methane conversion and product yields with (a) 0.89 mm and (c) 1.78 mm thick rolls. (b,d) Effect of inlet flow rate on acetylene secondary byproduct and hydrogen and carbon production rates for (b) 0.89 mm and (d) 1.78 mm thick rolls.

to decrease in methane conversions by a factor of 1.3, which is significantly lower than that of prior work due to the fibrous medium acting as an effective medium for heat transfer under direct solar irradiation.

As flow rate increases for both rolls, the gaps between product yields and methane conversions increase due to incomplete methane dissociation, which results in more secondary byproducts (mainly acetylene). From Fig. 6.6, acetylene mole fractions as high as 4.2% were detected in the product stream for the 0.89 mm roll, while they were only as high as 2.6% for the 1.78 mm roll despite the higher methane conversions. The lower acetylene byproduct using the 1.78 mm roll is due to increased thickness of the reaction zone that provides increased gas residence times to reach a more complete reaction, consistent with prior observations [55]. If the extent of the dissociation reaction stays the same, the acetylene mole fraction should directly correlate with methane conversion. However, Fig. 6.6 shows a maximum in acetylene mole fraction around 400 sccm for both roll thicknesses. This maximum is a contribution of two competing behaviors, where increasing the flow rate decreases methane conversion but also decreases diffusion contributions and the extent at which the dissociation reaction completes. All results for the effect of flow rate thus far are consistent with prior observations made in Chapter 5 for the small-scale solar reactor.

With increasing methane inlet flow rate, production rates and process efficiencies continue to increase significantly, as shown in Fig. 6.6. One measurement that stands out in this increasing trend is that for a 0.89 mm roll at 1200 sccm, for which the carbon and hydrogen production rates are lower than that at 1000 sccm. This observation is possibly due to the very low gas residence time within the reaction zone that provides significantly less effective dissociation. Overall, the roll-to-roll solar-thermal methane decomposition process has demonstrated promising results during laboratory-scale testing, with hydrogen and carbon production rates as high as 6.7 and 17.0 g/hr and solar-to-chemical efficiencies as high as 3.75% (at 2000 sccm). These parameters are subject to further significant increases through scale-up in addition to process and optical optimizations, such as by using a secondary concentrator as presented in Chapter 7.

Effect of solar power

The effect of solar power, and thus temperature, was considered next at a flow rate of 100 sccm and pressure of 3.33 kPa. Different solar powers from 0.92 to 2.32 kW were tested using two roll thicknesses of 0.89 and 1.78 mm. Methane conversion and product yields for the different solar powers are shown in Fig. 6.7 for the two rolls, where average temperatures measured on the fibrous medium are reported and vary from 1220 to 1630 K ± 30 K. Methane conversions and product yields continue to increase significantly as a result of increasing solar powers, for which $X_{\mathrm{CH_4}}$ ranges between 8% and 81%, $Y_{\mathrm{H_2}}$ ranges between 7% and 78%, and Y_{C} ranges between 5% and 72%. For the 0.89 mm roll, acetylene mole fraction directly correlates with solar power increase from 0.92 to 2.18 kW, increasing from 0.4% to 3.1%. However, the acetylene mole fraction drops significantly to 2.5% at 2.32 kW as a result of a more complete dissociation reaction. Similar trends occur for the 1.78 mm roll, but acetylene mole fractions are generally lower (due to increased gas residence time) and the peak occurs at a significantly lower solar power of 1.55 kW with an acetylene mole fraction of 2.7%.

As solar power increases, so do the hydrogen and carbon production rates in addition to the process efficiencies. This occurs within a narrow range of gas residence times for each roll thickness, ranging from 2.8 to 3.7 ms for the 0.89 mm roll and 5.6 to 7.1 ms for the 1.78 mm roll. For the 0.89 mm roll, production rates of hydrogen and carbon increase from 0.07 and 0.17 g/hr at 0.92 kW to 0.76 and 2.03 g/hr at 2.32 kW. Similarly for the 1.78 mm roll, hydrogen and carbon production rates increase from 0.16 and 0.39 g/hr to 0.86 and 2.33 g/hr. Consistent with observations at different flow rates, a thicker roll results in significant increase in methane conversion and product yields as a result of increased gas residence times. From Fig. 6.7, the

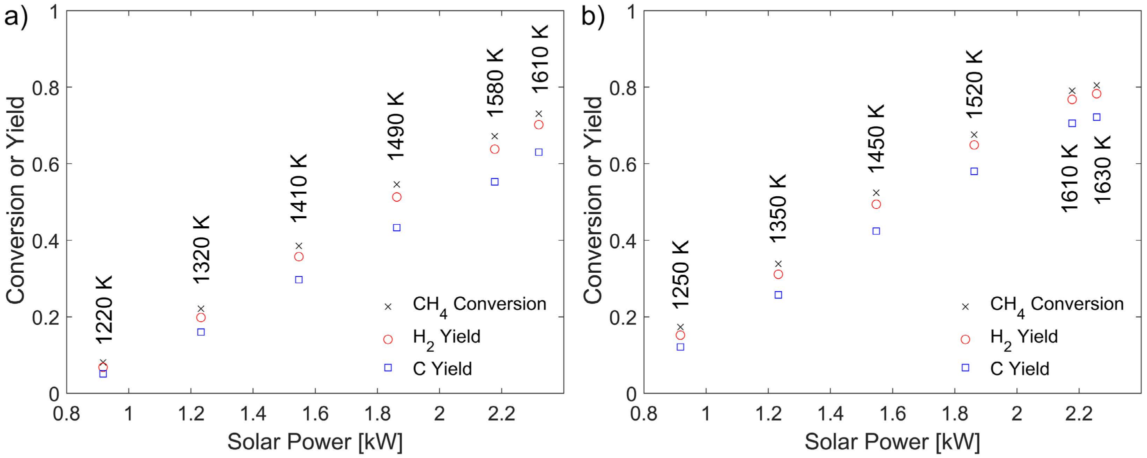

Figure 6.7: Effect of solar power on methane conversion and product yields for roll-to-roll methane decomposition at methane inlet flow rate of 100 sccm and pressure of 3.33 kPa, with (a) 0.89 mm and (b) 1.78 mm thick rolls.

combined effect of production rates and solar power may result in a local maximum in solar-to-chemical efficiencies. For the 0.89 mm roll, solar-to-chemical efficiencies continue to rise with solar power, reaching a maximum of 0.42% at 2.32 kW. In contrast, for the 1.78 mm roll η_{stc} has a maximum of 0.49% at 2.18 kW. Therefore, the optimum solar power concentration may be a compromise between the production rate and process efficiency, similar to observations discussed in Chapter 5 for the small-scale solar reactor.

Effect of pressure

The effect of pressure was then considered at a flow rate of 100 sccm, solar power of 2.34 kW, and a roll thickness of 0.89 mm. Methane decomposition at operating pressures from 0.67 to 4.67 kPa were tested, for which gas residence times ranged from 0.56 ms at 0.67 kPa to 4 ms at 4.67 kPa. Process conversion and product yields at different pressures are shown in Fig. 6.8, where average temperatures measured range between 1580 and 1650 K ± 30 K. As a result of increasing pressure from 0.67 to 4.67 kPa, X_{CH_4} increased from 60% to 71%, Y_{H_2} from 56% to 68%, and Y_{C} from

50% to 59%. The increase in methane conversion and product yields with pressure is mainly attributed to increased residence times from 0.56 to 4 ms. This increased residence time allows the gas more time to reach higher temperatures, and thus drives the dissociation reaction forward. However, the increase in performance plateaus at a pressure around 2 kPa, above which increased pressure has a negligible effect on methane conversion. Such behavior is mainly due to two competing phenomena that dictate the overall reaction extent, as decreasing pressure shifts the dissociation reaction forward (per Le Chatelier's principle) but it also decreases the gas residence time. The next section discusses the carbon product quality at different operating conditions, generally showing that quality decreases with increasing pressure.

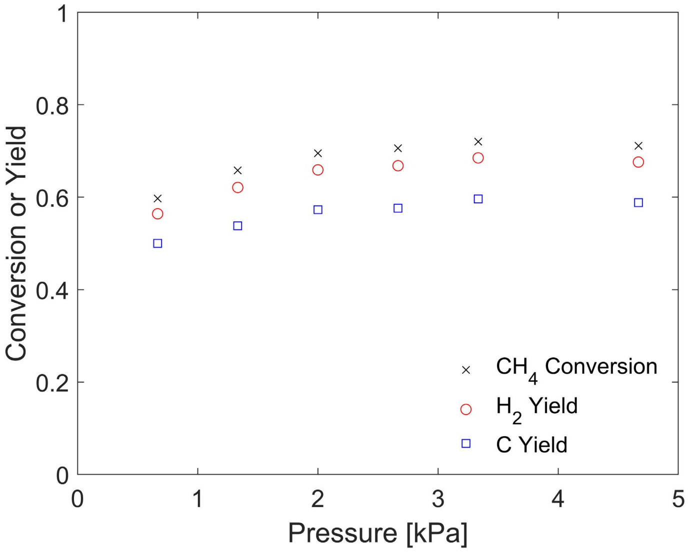

Figure 6.8: Effect of pressure on methane conversion and product yields for roll-to-roll methane pyrolysis at methane inlet flow rate of 100 sccm and solar power of 2.34 kW, with 0.89 mm thick roll.

6.4.2 Carbon product quality

The carbon product quality is affected by the process operating conditions. Raman spectra were measured at different operating conditions for both roll thicknesses and are shown in Fig. 6.9. For the 0.89 mm roll and at different solar powers, Fig. 6.9a shows a general increase in the graphitic product's quality with increased solar power, and thus temperature, as expected. At a solar power of 0.92 kW, the Raman D and G peaks begin to merge together, and the 2D peak is relatively wide and weak, indicating the presence of weak long-range graphitic structures [170]. As solar power increases to 2.18 kW, all full widths half maximum (FWHMs) of the three dominant Raman peaks decrease significantly, and the $I_{\mathrm{D}}/I_{\mathrm{G}}$ ratio of the carbon product decreases from 1.20 to 0.54. These observations correspond to a significant increase in the product crystallinity, for which the average inter-defect distance ($L_{\mathrm{D,Ram}}$) increases from 11 to 16.4 nm.

Fig. 6.9b shows Raman spectra of the carbon product acquired at different operating pressures ranging from 0.67 to 4.67 kPa at a solar power of 2.34 kW and flow rate of 100 sccm with 0.89 mm thick roll. The spectra reveal a general reduction of quality with increasing pressure, where FWHMs of the three dominant carbon peaks and the $I_{\mathrm{D}}/I_{\mathrm{G}}$ ratio increase. For a pressure change from 0.67 to 4.67 kPa, $I_{\mathrm{D}}/I_{\mathrm{G}}$ increases from 0.43 to 0.62, while $L_{\mathrm{D,Ram}}$ decreases from 18.4 to 15.3 nm with no significant increase in product yields and production rates. The increase in quality with decreasing pressure is likely a result of decreasing particle collision frequency with the solid product as the gas concentration decreases and the mean free path increases.

A higher pressure also results in more acetylene byproduct and possibly higher tendency to form trace aromatic hydrocarbons that change the carbon formation chemistry and lead to a lower-quality textured carbon deposition [177]. At a pressure of 0.67 kPa, the acetylene mole fraction in the product stream was 2.1%, while it increased significantly to 3.1% at 4.67 kPa under the same solar power and flow rate. Although lower operating pressure improves the carbon product quality, it leads

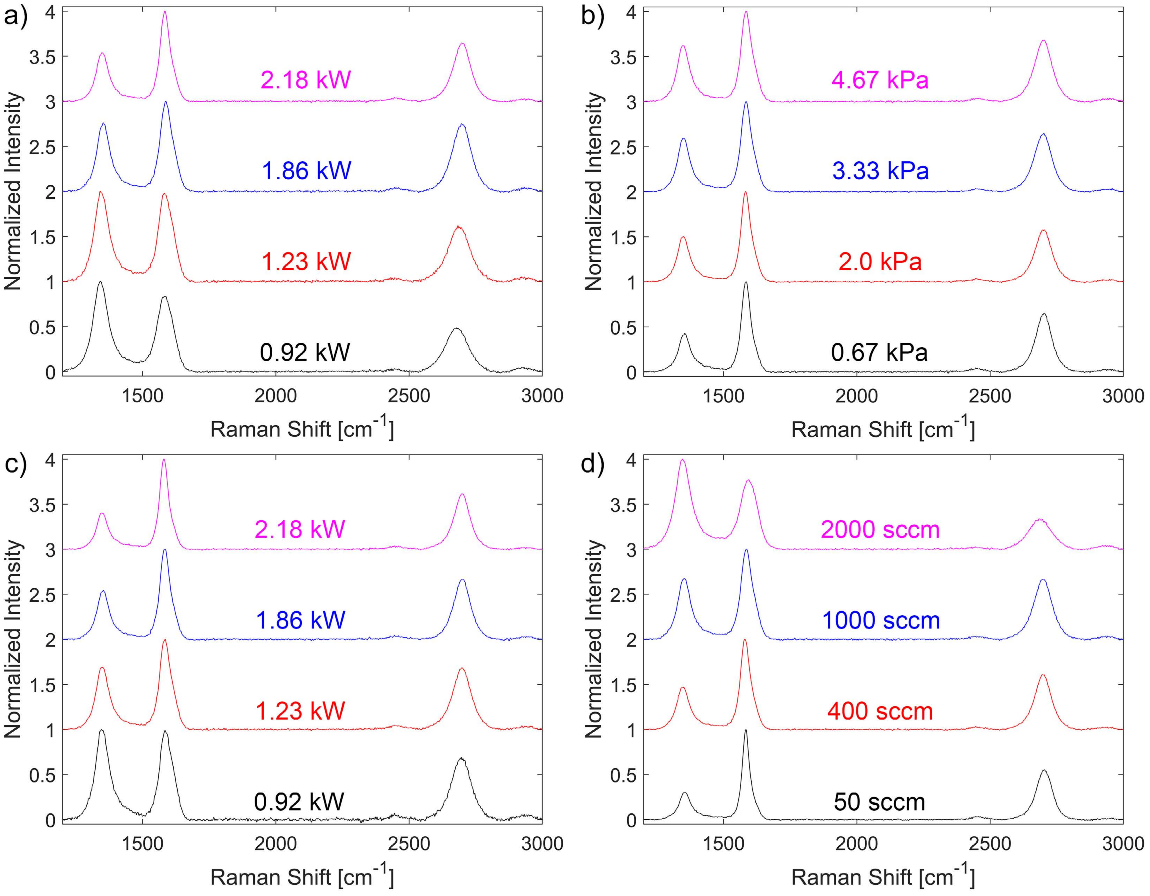

Figure 6.9: Raman spectra of carbon product at (a) different solar powers at pressure of 3.33 kPa and inlet flow rate of 100 sccm with 0.89 mm thick roll; (b) different pressures at solar power of 2.34 kW and flow rate of 100 sccm with 0.89 mm thick roll; (c) different solar powers at pressure of 3.33 kPa and inlet flow rate of 100 sccm with 1.78 mm thick roll; (d) different flow rates at solar power of 2.34 kW and pressure of 3.33 kPa with 1.78 mm thick roll.

to higher vacuum operating costs and sealing concerns. Therefore, a compromise between the two characteristics can be reached depending on the added value of the higher quality graphitic product [12].

The carbon products from the 1.78 mm thick rolls have also been characterized and are shown in Fig. 6.9 at different (c) solar powers ranging from 0.92 to 2.18 kW and (d) methane inlet flow rates ranging from 50 to 2000 sccm. In contrast to the 0.89 mm roll, Fig. 6.9c shows higher carbon product quality for the 1.78 mm roll at the same operating conditions, which is due to the two-fold increase in residence times that allow the gas to reach higher effective temperatures prior to dissociation. The general increase in carbon product quality with solar power is consistent with that shown in Fig. 6.9a, and increasing solar power from 0.92 to 2.18 kW results in a decrease in $I_{\mathrm{D}}/I_{\mathrm{G}}$ from 1.01 to 0.4 and a significant increase in $L_{\mathrm{D,Ram}}$ from 12 to 19.1 nm. Similar comparisons and observations apply to the two rolls at different methane inlet flow rates.

Raman spectra of the carbon product for the 1.78 mm roll at different flow rates are shown in Fig. 6.9d, where the carbon product quality reduces significantly with increase in flow rate. As the inlet flow rate increases from 50 to 2000 sccm, the FWHMs of all peaks increase significantly, and the $I_{\mathrm{D}}/I_{\mathrm{G}}$ increases from 0.3 to 1.3, which translates to a decrease in $L_{\mathrm{D,Ram}}$ from 22.1 to 10.6 nm. The significant reduction in carbon product quality with increasing flow rate is attributed to decreasing residence times, and hence lower effective gas temperatures; t_{res} decreases from 11 to 0.29 ms when flow rate increases from 50 to 2000 sccm. Despite the fibrous medium's temperature decreasing slightly with increasing flow rate, the temperature reduction is insufficient to affect the carbon product's quality significantly. Additionally, diffusion of the hydrogen product upstream through the reaction zone is less pronounced at higher flow rates, and such diffusion can contribute significantly to the product quality [172]. As demonstrated in Chapter 5, presence of hydrogen can improve the graphite product's quality.

6.5 Conclusions

In this chapter, the use of roll-to-roll mode of operation as a scalable route to continuous solar-thermal methane pyrolysis in a large-scale solar reactor is presented and investigated. The roll-to-roll approach for methane decomposition is observed to be effective in achieving a continuous process, during which the rolling supply of fresh fibrous medium mitigates decline in process performance with time due to significant carbon deposition. The roll-to-roll fibrous medium maintains stable and relatively high methane conversions compared to that of a stationary substrate, with enhancements in methane conversions up to 1.5 times higher. The efficacy of the roll-to-roll reactor was additionally evaluated through parametric variations of operating conditions, which include solar power, methane inlet flow rate, pressure, and roll thickness. In terms of process kinetics and performance with parametric variations, results presented in this chapter are consistent with those presented in Chapter 5.

However, the overall quality of the carbon product of the roll-to-roll reactor are generally lower than those obtained in Chapter 5 for the small-scale solar reactor. This behavior is primarily due to the reduced thickness of the fibrous medium used in a roll form, as compared to the stationary thicker felt used in Chapter 5, which results in significantly lower residence times that decrease the quality of the carbon product. However, the carbon product quality is still relatively high with distinct D, G, and 2D Raman peaks, and with D/G peak ratios as low as 0.3. The product quality can be further improved through process and optical optimizations, such as by decreasing the operating pressure further or by implementing a secondary concentrator to further increase solar concentration ratios attained within the fibrous reaction zone. The latter optimization approach is presented next in Chapter 7.

Chapter 7: Optical Optimization of the Solar Reactor

In this chapter, the in-house MCRT code developed and validated in Chapter 2 is used to optimize the optical design of the large-scale solar reactor and roll-to-roll solar-thermal methane decomposition process presented in Chapter 6. The optical optimization is achieved by using a conical secondary concentrator that further increases solar concentration ratios on the fibrous reaction zone, allowing for more effective radiative heat transfer. Dimensions of the secondary concentrator were optimized based on MCRT numerical simulations to capture the highest irradiation on the reaction zone. The enhancement in solar power concentration resulting from the secondary concentrator is evaluated, and its improvements to the solar-thermal methane decomposition process and product quality are presented.

7.1 Introduction

One of the technical challenges in solar methane pyrolysis is obtaining sufficiently high process conversion and production rates with high yields that provide high-purity products [29]. An approach to addressing this challenge is through optimized optical and thermal reactor designs that allow more efficient collection and utilization of concentrated solar power. One possible route for enhancing concentration ratios is through the use of a secondary concentrator [196]. The work in this chapter considers the implementation of a secondary solar concentrator with optimized geometry to enhance the roll-to-roll solar methane pyrolysis process presented in Chapter 6 [183].

The most common approach to optical and thermal radiation analysis is through Monte Carlo ray tracing (MCRT) because only few analytical, closed-form solutions exist. The Monte Carlo method is a broad group of stochastic techniques that utilize random numbers and statistical sampling to simulate a problem of interest. MCRT simulates radiation heat transfer by dividing a radiation source into a large number of emitted energy bundles (rays) that are then followed as they interact with different surfaces, allowing for multiple reflections and absorption(s) [103]. The manner in which rays interact with different surfaces is ensured via random numbers and proper statistical sampling with a large number of rays (order of millions or higher) required for successful convergence. A recent review on MCRT as applied to solar applications can be found in literature [104].

Prior work has used MCRT to aid in studying and optimizing different aspects of concentrated solar power applications through in-house developed algorithms or by utilizing commercial software. Open-source and commercial software include SolTrace, TracePro, CUtrace, Zemax, and Tonatiuh [197]. MCRT models can be coupled to computation fluid dynamics (CFD) models to investigate thermal transfer and optimize process design aspects, such as solar reactor geometry [198], aperture size [199], inclination angle [200], and flow configuration [201], or they can be further used to drive model-based control systems [58]. MCRT is also used to estimate and optimize the optical efficiency of solar collector systems, such as secondary concentrators or compound parabolic collectors [202]. In a recent work

[203], various optical geometries were investigated for redirecting convergent solar irradiation. Out of the four types of reflectors studied (flat, ellipsoidal, hyperboloidal, and paraboloidal), a flat reflector provided the highest system optical efficiency. While most literature utilizes the traditional MCRT method, other work has focused on advancing the method's computational efficiency for more specialized applications. In one prior work [204], a quasi-MCRT algorithm that utilizes precomputed set of random variables and more efficient sampling and processing methods was developed for a central receiver system. The proposed algorithm simulates radiative flux distribution from a heliostat field and onto a receiver more accurately and efficiently than the tradition MCRT method.

Prior studies demonstrated optimization and implementation of different secondary concentrator types, where usually a compound parabolic concentrator (CPC) is used with a heliostat field and a conical concentrator is used with a primary concentrator (parabolic/ellipsoidal concentrator). In one study [196], both the energetic and economic performances were investigated for a solar central receiver with a secondary CPC using an in-house developed MCRT model. Simulation results indicate that both of these performance metrics improve with a secondary concentrator only at relatively high operating temperatures (> 1000 K), which is the temperature range for which methane pyrolysis advances at desirable rates. In a similar study [205], MCRT aided in designing and evaluating secondary CPCs for a solar thermochemical system. In a different work on solar-thermal methane cracking in a flow-seeded reactor [56], a water-cooled, conical copper secondary concentrator was implemented into the reactor design to improve its solar absorption efficiency. The reactor's absorption efficiency was estimated to approach that of a blackbody using MCRT. In a similar study [67], a stainless steel conical secondary concentrator was designed and integrated into a directly irradiated tubular solar reactor system that drives a catalytic dry methane reforming process. The secondary concentrator's geometry was optimized using TracePro, and the optimization resulted in enhancing the concentration and uniformity from the solar source onto the catalyst bed. In contrast to prior work [56], the placement of the secondary concentrator outside of the solar reactor [67] might induce additional thermal stresses on the quartz window, which would be less desirable for point reactors (parabolic dish and central receiver systems) [10].

In this chapter, the in-house MCRT code developed and validated in Chapter 2 is used to optimize the design of a secondary concentrator that further increases solar concentration ratios attained within the fibrous reaction zone. Experiments performed utilize the large-scale roll-to-roll reactor and solar simulator in a beam-down configuration, as presented in Chapter 6. In addition to numerically simulating the enhancement in solar power resulting from the secondary concentrator using MCRT, experimental testing with and without the optimized secondary concentrator is presented to explicitly quantify the added benefit of the concentrator. Two comparative experimental sets are presented for a fibrous medium placed at the focal plane: (a) purely thermal measurements under vacuum conditions and (b) methane pyrolysis through a fibrous carbon medium following the work in previous chapters [9, 183]. Such explicit quantification, both numerically and experimentally, is observed to be missing in prior work.

7.2 Setup and secondary concentrator

The experimental setup considered here builds on the system introduced in Chapter 6, which is comprised of the high flux solar simulator in a beam-down configuration, large-scale solar reactor, roll-to-roll mechanism, and temperature and gas species monitoring systems. The system is shown in Fig. 7.1.

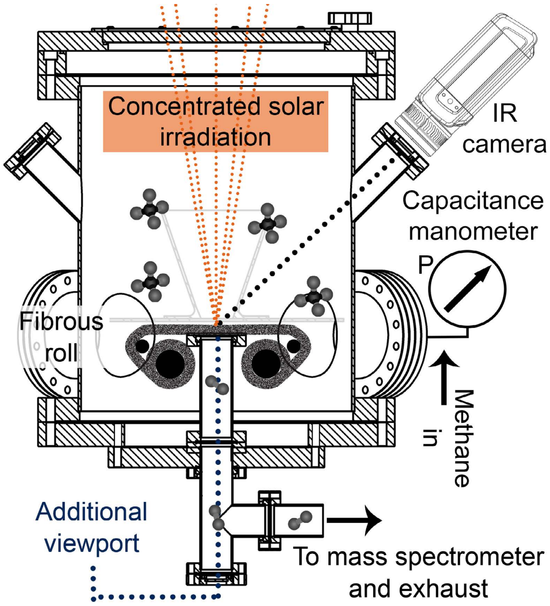

Figure 7.1: Schematic illustration of the large-scale solar methane pyrolysis experimental setup with secondary concentrator.

The thermal and optical design of the solar reactor can be further improved by implementing a secondary concentrator that aims to increase light concentration and absorption efficiency. A representative, arbitrary-sized secondary concentrator is illustrated in Fig. 7.1 in lighter color gradient, where it is supported on a radiation shield that mounts on top of the roll-to-roll mechanism (not shown) to protect reactor auxiliaries. Multiple options are available for the secondary concentrator geometry, such as conical, CPC, and ellipsoidal. Prior work [203] has shown that a conical secondary concentrator potentially provides the highest optical efficiencies for converging irradiation, and hence it is studied and implemented in the present work. The geometry of the conical secondary concentrator is then optimized such that it provides significantly higher irradiation at the fibrous medium's active deposition area, which is 3.8 cm in diameter.

7.3 Theory and methodology

7.3.1 Monte Carlo ray tracing

A MCRT in-house 3D code of the solar simulator and its methodology was previously presented [105] and validated for the solar simulator in Chapter 2 [68]. In this chapter, the ray tracing code is expanded to include the solar reactor and a secondary concentrator to enhance the capture of solar irradiation by optimizing the concentrator's geometry. The system and geometry modeled into the MCRT code are shown in Fig. 7.2, which illustrates the modeled enclosure that includes semi-transparent surfaces (quartz window), black imaginary surfaces to reduce simulation complexity, and real surfaces (concentrator, target, and reactor walls). Black imaginary surfaces are appropriate whenever irradiation intercepted by these surfaces has a negligible chance of being redirected to the target. The target in this case is the fibrous medium (reaction zone), and it is assumed to be black for the purposes of this optimization.

The MCRT model considers some assumptions that aim to reduce the simulation complexity without significantly affecting the results' accuracy. First, the model assumes the irradiation source to be gray and that all surfaces have wavelength-independent optical properties as irradiation spectral characteristics are not important at this stage. Additionally, the model assumes temperature-independent constant properties. In reality, the latter consideration might depart slightly from the assumption as the secondary concentrator and quartz window heat up over time under irradiation. Furthermore, the model assumes that air and all surfaces outside the solar reactor (except the solar simulator's ellipsoidal reflector) are non-participating, with any reflection effects

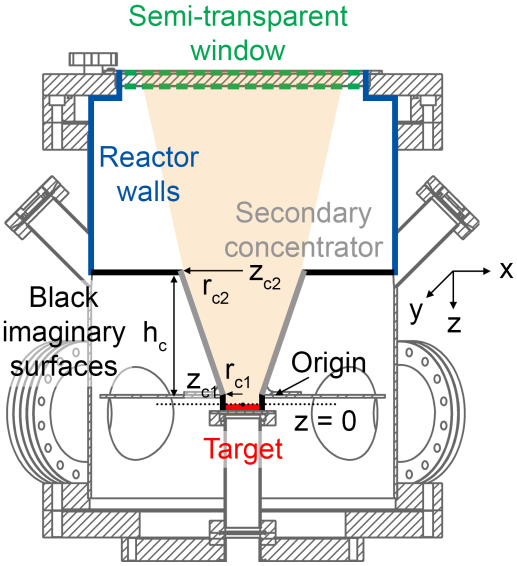

Figure 7.2: Geometry and surfaces modeled within the MCRT simulation for the secondary concentrator.

neglected. Radiation emission from reactor inner surfaces and components are also neglected because their radiation contribution is expected to be small given their significantly lower temperatures compared to that of the target. Also, gaps between the conical concentrator surfaces and reactor walls are modeled as black imaginary surfaces because almost none of the irradiation intercepted by these gaps is redirected back to the target. A MCRT simulation not implementing this idealization has more than 60% computational load, and indicates that less than 0.2% of the irradiation intercepted by the gap eventually reaches the target. Finally, the flow within the reactor (e.g., methane) is assumed to be a non-participating medium, and formation of any carbon particles upstream of the fibrous medium is assumed to be negligible.

The methodology of the MCRT code implemented in MATLAB is illustrated in Fig. 7.3, for which pseudo-random numbers ($\mathcal{R}$) are used to predict events such as reflection, absorption, direction of emission/reflection, and location of emission. The initial components of the MCRT algorithm includes initializing the simulation and modeling the solar simulator light source and its emission distribution [68]. Irradiation from the light source is divided into a large number of rays to be traced, N_{rays}, for which emission counters of the source, N_i, and absorption counters of surface j, N_j, keep track of the rays simulated. Components highlighted in orange in Fig. 7.3 consider the solar simulator, and their methodology has been outlined in prior work [105]. These components will be skipped here for brevity.

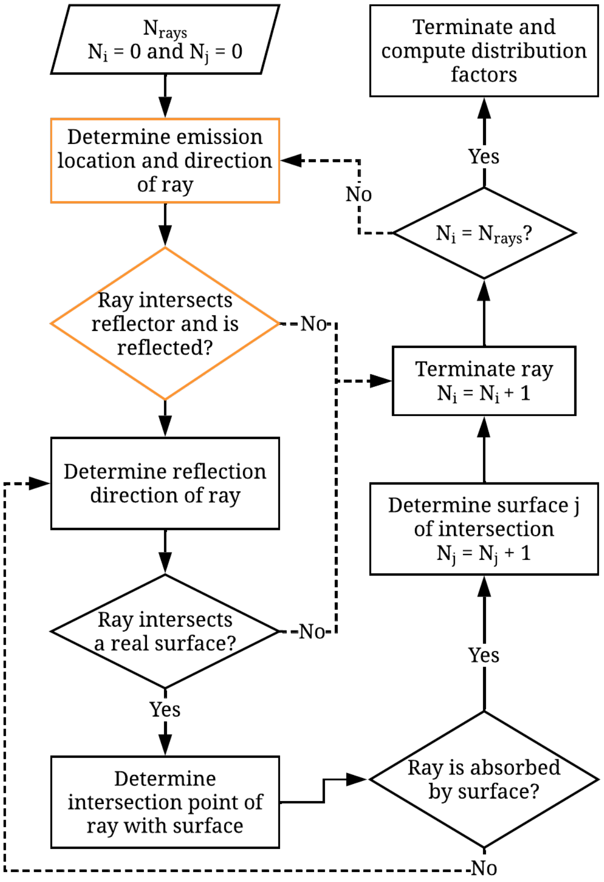

Figure 7.3: Flowchart illustration of the MCRT algorithm. Sections highlighted in orange correspond directly to the solar simulator and its modeling.

Ray tracing in Cartesian coordinates occurs through a systematic way that uses surface unit normal ($\hat{\mathbf{n}}$) and two tangential vectors ($\hat{\mathbf{t}}_1$ and $\hat{\mathbf{t}}_2$) along with emission or reflection zenith (θ) and azimuth (ϕ) angles to define the direction unit vector ($\hat{\mathbf{u}}$) and path of the ray ($\hat{\mathbf{P}}$) as:

$$\hat{\mathbf{u}} = \cos\theta\,\hat{\mathbf{n}} + \sin\theta\cos\phi\,\hat{\mathbf{t}}_{\mathbf{1}} + \sin\theta\sin\phi\,\hat{\mathbf{t}}_{\mathbf{2}} \tag{7.1}$$

$$\hat{\mathbf{P}} = \hat{\mathbf{OP}} + s\hat{\mathbf{u}} \tag{7.2}$$

where $\hat{\mathbf{OP}}$ is the ray's initial position and s defines the length of ray travel. The tangential vectors are defined such that $\hat{\mathbf{t}}_{\mathbf{1}} \cdot \hat{\mathbf{n}} = 0$ and $\hat{\mathbf{t}}_{\mathbf{2}} = \hat{\mathbf{n}} \times \hat{\mathbf{t}}_{\mathbf{1}}$. The initial position and direction of a ray upon emission are obtained from the portion of the MCRT modeling the radiation source [68], and then reflections from surfaces (if any) are treated either as fully diffuse for dull surfaces or as non-ideal specular for polished surfaces. Dull surfaces include the reactor walls and outer surfaces of the conical concentrator, with angles of reflection determined using [206]:

$$(\theta, \phi) = \left(\sin^{-1}\left(\sqrt{\mathcal{R}_\theta}\right), 2\pi\mathcal{R}_\phi\right) \tag{7.3}$$

where each angle has its own set of random numbers ($\mathcal{R}_\theta$ and $\mathcal{R}_\phi$). Reflections from coated and polished surfaces (ellipsoidal reflector and inner surfaces of conical concentrator) are treated here by modifying the law of ideal reflection through a modified surface normal ($\hat{\mathbf{n}}'$) [98]:

$$\hat{\mathbf{n}}' = \cos\theta_{\text{se}}\,\hat{\mathbf{n}} + \sin\theta_{\text{se}}\cos\phi_{\text{se}}\,\hat{\mathbf{t}}_{\mathbf{1}} + \sin\theta_{\text{se}}\sin\phi_{\text{se}}\,\hat{\mathbf{t}}_{\mathbf{2}} \tag{7.4}$$

where θ_{se} and ϕ_{se} are the zenith and azimuth angles inducing a specular reflection error to model real surfaces. For all non-ideal specular reflections, ϕ_{se} has a uniform distribution between 0 and 2π. However, the value of θ_{se} is treated as a normal distribution around zero with standard deviation of 50 mrad for the conical concentrator inner surfaces and 6.75 mrad for the ellipsoidal reflector (see Chapter 2) [68]. The reflected direction of the ray then simply implements the law of ideal reflection using the modified surface normal as:

$$\hat{\mathbf{u}}_{\mathrm{r}} = \hat{\mathbf{u}}_{\mathrm{in}} - 2\hat{\mathbf{n}}' \left(\hat{\mathbf{u}}_{\mathrm{in}} \cdot \hat{\mathbf{n}}'\right) \tag{7.5}$$

Tracing of each ray then proceeds as it interacts with different surfaces until the ray is absorbed. Once absorbed, the ray and its history are terminated, and the appropriate counters are incremented, at which the simulation proceeds with the next ray.

For the secondary concentrator, a conical shape is chosen with a surface equation as:

$$x^2 + y^2 - \frac{(z - C_{\mathrm{c1}})^2}{C_{\mathrm{c2}}^2} = 0 \quad \text{for } z_{\mathrm{c2}} \leq z \leq z_{\mathrm{c1}} \tag{7.6}$$

where C_{c1} and C_{c2} are geometrical constants, and z_{c1} and z_{c2} define the length and location of the conical concentrator. Similar equations can be constructed for flat circular plates and cylinders that occupy the rest of the enclosure in Fig. 7.2 [51]. The intersection of a ray with the different surfaces can then be determined by substituting Eq. 7.2 into each surface equation and solving for s, which needs to be a real positive number for an interaction to exist.

Optical properties of different surfaces involved in the MCRT simulation depend on material and surface finish. The reactor walls consist of dull stainless steel surfaces, with an estimated reflectivity of 0.4 and a fully diffuse reflection treatment [207]. The inner surfaces of the in-house polished stainless steel conical reflector are treated using non-ideal specular reflection, with a reflectivity value of 0.85 [207, 208]. The quartz window is assumed to have constant index of refraction of 1.45 [209] and a transmissivity value of 0.92 [127].

7.3.2 Geometry constraints and optimization

Some geometrical constraints are applied to the conical concentrator due to available space, desired concentration area, or practical limitations. First, the smaller inner radius of the conical concentrator r_{c1} is treated as fixed, with a radius of 1.9 cm being the same as the outlet flow and active reaction zone. Additionally, the secondary concentrator is kept 1 cm away from the reaction zone to avoid significant heating due to reradiation from the fibrous medium and carbon deposition during methane pyrolysis, while avoiding significant divergence of the concentrated irradiation. Therefore, z_{c1} is fixed at -1 cm, and the value for z_{c2} is driven by the desired height of the secondary concentrator (h_{c}). This height is limited by the available space within the reactor above the reaction zone, and hence $h_{\mathrm{c}} \leq 29$ cm.

The two parameters that need to be optimized for the secondary concentrator are h_{c} and r_{c2} (see Fig. 7.2). Optimization is performed by exploring the space for $3.8 \leq r_{\mathrm{c2}} \leq 10.2$ cm and $1 \leq h_{\mathrm{c}} \leq 29$ cm. The improvement in power captured by the reaction zone was estimated at each concentrator geometry, and the maximum power corresponds to the final concentrator dimensions. As optimization depended on the total power captured rather than resolving a full map, 10^7 rays were used for the analysis, which was sufficient for convergence. In contrast for determining full heat flux maps with high spatial resolution, the number of rays needed for convergence was in the order of 10^9 rays.

7.3.3 Materials and methods

Solar methane decomposition is tested in a manner similar to that presented in Chapter 6, by which the solar reactor was first evacuated and purged with nitrogen flow to obtain an oxygen-free environment. Irradiation from the solar simulator then starts at vacuum condition, after which pure methane is introduced into the solar reactor. The fibrous medium used in this chapter is a polyacrylonitrile-based carbon felt (FuelCellEarth, C100), similar to that used in Chapter 5, which has a porosity of 0.95, an average fiber diameter of 9.6 µm, and a specific surface area of 1.5 m^2/g [9]. The fibrous carbon medium remained stationary at the focal plane of the solar simulator and reactor.

For gaseous stream monitoring, the in situ calibrated MS was used to quantify mole fractions of the gaseous products and determine process conversion and product yields. For solid carbon characterization, the same equipment and techniques described in Chapter 3 were used; scanning electron microscope (SEM) images were captured by a ZEISS Supra 40VP field emission SEM with a secondary electrons detector, and Raman spectra were obtained using a 532 nm laser with a 40× achromatic objective lens and a CCD detector of a Horiba iHR 550 imaging spectrometer.

7.4 Results and discussion

7.4.1 Simulations and optimization

MCRT simulations were performed across the constrained geometry space to estimate the enhancement in power concentration. Fig. 7.4a presents a contour of percentage increase in power, relative to the case with no secondary concentrator, as a function of concentrator's height (h_c) and collection radius (r_c2). To better visualize the overall trend, plots of power enhancement for select concentrator radii as a function of height are shown in Fig. 7.4b. As demonstrated in Fig. 7.4, there exists an optimum angle for which the secondary concentrator maximizes power capture, and hence the concentrator height continues to increase with collection radius. At small collection areas, the peak in power concentration enhancement increases significantly with increasing radius because irradiation from the solar simulator is still significant at these areas. However, this increase rapidly decays beyond a radius of 5.1 cm, after which the enhancement in power collection is not very significant.

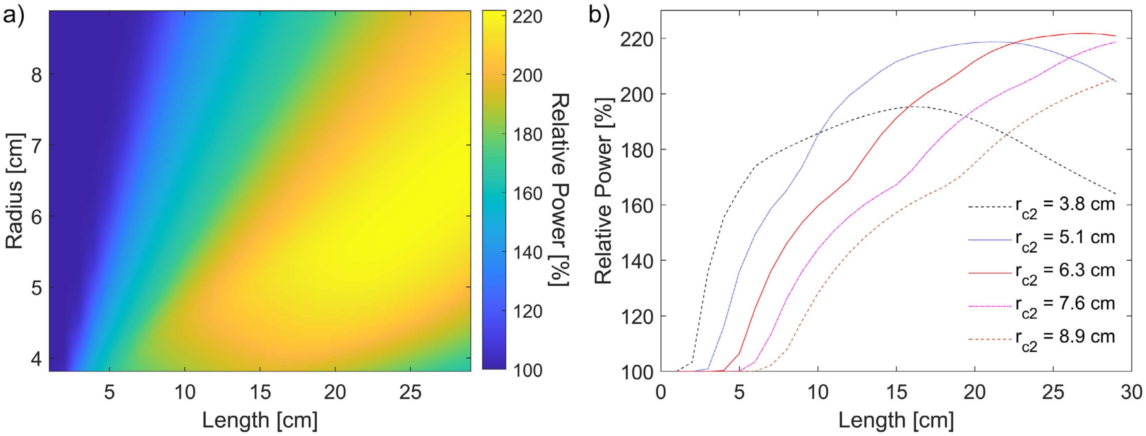

Figure 7.4: MCRT simulation results of relative power enhancement with secondary concentrator geometry showing (a) a contour map of relative power with respect to concentrator's length and radius, and (b) 2D plots of relative power variation with concentrator's length at different radii.

The power distribution from the solar simulator is also quantified through the MCRT simulation and is shown in Fig. 7.5a for the cases with no concentrator and with the optimized secondary concentrator. The optimized concentrator dimensions were chosen as $h_{\mathrm{c}} = 26.2$ cm and $r_{\mathrm{c2}} = 62.5$ mm, with an overall thickness of 3 mm. This thickness aims to provide structural integrity to the secondary concentrator to avoid failing under thermal stress and creep. From Fig. 7.5a, 24.5% of the power output from the lamp is lost within the solar simulator through absorption by its housing (i.e., not collected by the reflector), absorption by the ellipsoidal reflector, or in the form of stray light. This portion of power output from the lamp is constant for the cases with and without a secondary concentrator, and indicates that further optimization can be done on the ellipsoidal reflector's geometry. However, such a consideration is outside the scope of this work. The power absorbed by the quartz window is also almost identical for both cases, and differ very slightly due to absorbed light that is reflected from the reaction chamber. With a secondary concentrator geometry that is not optimized, this difference can be large as the concentrator may reflect back significant amount of irradiation.

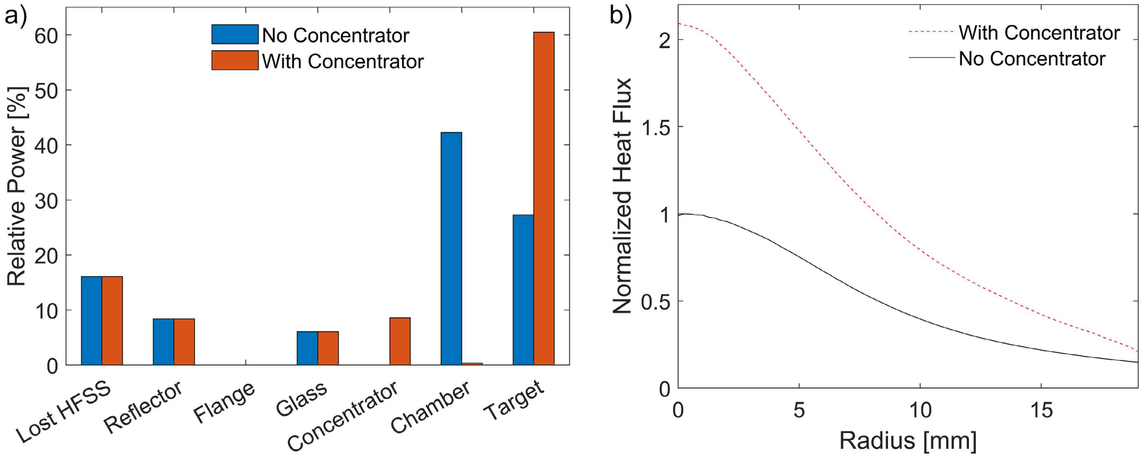

Figure 7.5: (a) Output power distribution from the solar simulator for the cases with and without a secondary concentrator. (b) 2D radially-averaged normalized heat flux distributions at the focal plane with and without secondary concentrator.

The biggest distinctions between the power distribution for the cases with and without the secondary concentrator are for the power absorbed by the reaction chamber and target (i.e., reaction zone). For the case with no secondary concentrator, most of the irradiation from the solar simulator does not reach the reaction zone, for which 42.2% is absorbed by the reaction chamber and only 27.3% ultimately intercepts the target. The secondary concentrator aims to minimize the irradiation absorbed by the reaction chamber and redistribute this power to the reaction zone. With an optimized secondary concentrator, the amount of power absorbed by the chamber drops to 0.3% and that intercepted by the target increases significantly to 60.5%, with the concentrator absorbing 8.6% of irradiation output from the solar simulator. This redistribution represents a relative power enhancement of 222% with the optimized concentrator, and is expected to significantly enhance the performance and efficiencies of the solar reactor.

The normalized heat flux distributions with and without the secondary concentrator are shown in Fig. 7.5b. Due to the linear relationship between solar simulator's current supply and output irradiation, the normalized distribution can be directly translated to a heat flux distribution based on characterization results presented in Chapter 2 [68]. As a result of adding the secondary concentrator, the heat flux distribution approximately increases linearly by two-fold in magnitude, providing more than 200% increased solar powers. However, the heat flux still resembles the original non-uniform Lorentzian/Gaussian distribution as the objective of the present optimization is to enhance the total irradiation power captured by the target. Obtaining a more uniform distribution will be at the expense of decreasing power, and is not considered in the present work.

7.4.2 Secondary concentrator design

The final design of the secondary concentrator and its configuration are shown in Fig. 7.6. The secondary concentrator is mounted on top of a radiation shield that sits on top of the roll-to-roll mechanism, with slots that provide space for thermal expansion. These slots are vital as the concentrator heats up and expands under long operations, and hence they ensure that any warping is avoided. Additionally, the concentrator has a 45° through hole with a diameter of 12.7 mm that coincides with one of the angled viewing ports of the reactor and the center of the reaction zone. This through hole allows for obtaining temperature measurements from the top side of the fibrous medium using the IR camera. A photograph of the assembled secondary concentrator system within the solar reactor is also shown in the inset of Fig. 7.6, where the angle viewports, secondary concentrator, radiation shield, and the fibrous medium can be seen.

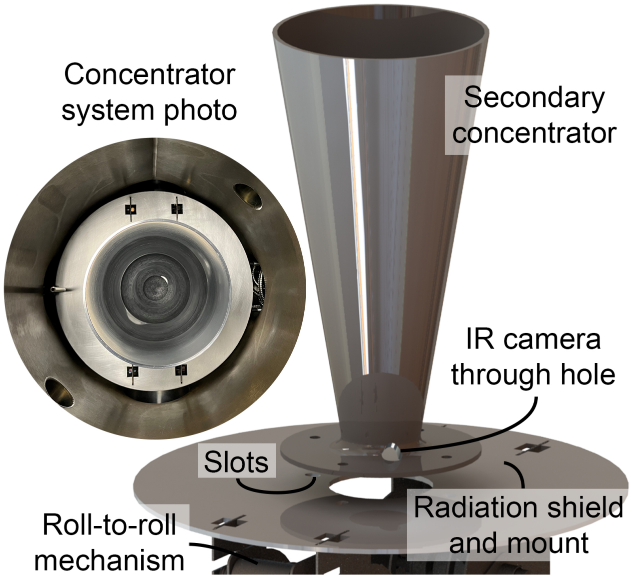

Figure 7.6: CAD model of the conical secondary concentrator and configuration. Figure inset on the left shows a photograph of the secondary concentrator system placed within the solar reactor.

7.4.3 Thermal measurements

The thermal enhancement from the secondary concentrator was first investigated under vacuum conditions. Temperature measurements from the IR camera were recorded for the front side of the fibrous material under direct irradiation from the solar simulator at different supplied currents. Maximum temperature measurements with and without the secondary concentrator are shown in Fig. 7.7a, while a representative temperature contour with the secondary concentrator at 170 A is shown in Fig. 7.7b. A significant improvement from the secondary concentrator is evident based on an increase in fibrous medium temperatures by values up to 300 K ± 40 K. The gradient of temperature with varying current using the secondary concentrator is slightly less than that without the concentrator due to the significantly higher temperatures for which radiation losses are higher (radiation losses are non-linear). Therefore, the temperature increase with the secondary concentrator reduces from 300 K at 100 A to 265 K at 170 A.

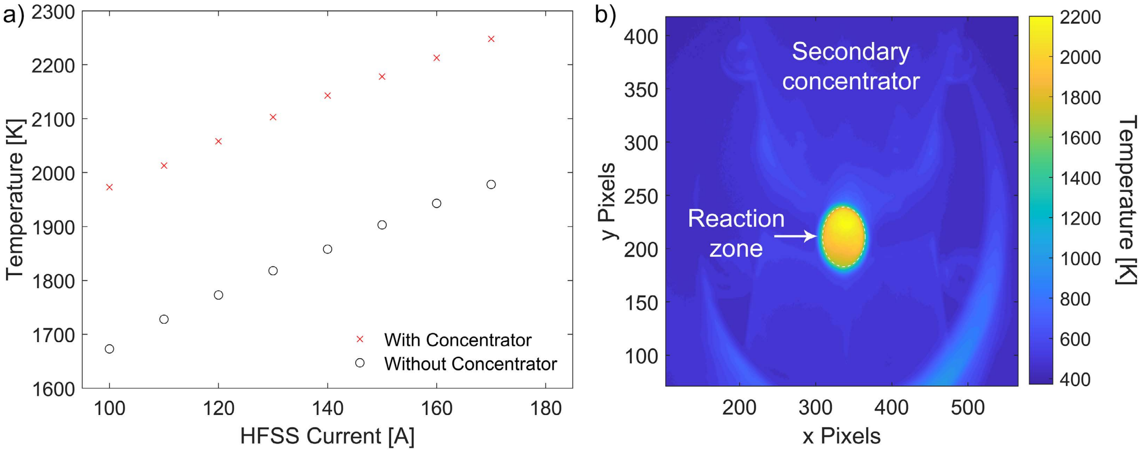

Figure 7.7: (a) Maximum temperatures with and without secondary concentrator as a function of solar simulator's current, and (b) representative temperature contour with secondary concentrator at 170 A as measured using the IR camera.

The experimentally-observed enhancement in power can be estimated by interpolating results of maximum temperatures at different operating powers without the secondary concentrator and matching those to the ones measured with the secondary concentrator. The maximum temperature with the secondary concentrator at 100 A is 1973 K, whereas the temperature without the concentrator at 170 A is 1978 K. By interpolating experimental measurements and using the characterized supply current to output power relation, the enhancement in power due to the secondary concentrator is estimated to be 218%. This value agrees well with the numerically-estimated enhancement of 222%, thus verifying numerical results and demonstrating the added benefit of the secondary concentrator.

7.4.4 Methane pyrolysis

Solar-thermal methane pyrolysis was conducted next with and without the secondary concentrator to determine the enhancement in the overall process performance under different operating conditions. Fig. 7.8 shows transient methane conversion and product yields measurements with and without the concentrator under a methane inlet flow rate of 100 sccm, solar power of 1.86 kW (HFSS current of 160 A), pressure of 3.33 kPa, and fibrous medium thickness of 3.2 mm. Methane pyrolysis begins at time zero with the introduction of solar irradiation and methane flow concurrently at vacuum conditions. From Fig. 7.8, the process reaches faster thermochemical steady-state using the secondary concentrator because of the higher methane conversion and hydrogen yields, hence increasing species molar concentrations and reaching the operating pressure faster; one methane mole dissociates into two hydrogen moles. The sudden increases in methane conversion and product yields that occur between 6 to 10 min is the result of reaching the desired operating pressure, at which the exhaust control valve opens to maintain a uniform pressure and the process progresses towards the thermochemical steady-state.

For the case in Fig. 7.8 without a secondary concentrator and at steady-state, methane conversion is 61.3%, hydrogen yield is 57.7%, and carbon yield is 48.7%. In contrast with a secondary concentrator, $X_{\mathrm{CH_4}}$ increases to 85%, $Y_{\mathrm{H_2}}$ increases to 83.5%, and Y_{C} increases to 80.2% due to higher operating temperatures that drive the decomposition reaction forward. With the secondary concentrator and relative to the case with no concentrator, hydrogen and carbon yields are much closer to methane conversion due to more complete methane dissociation and increased selectivity towards the two main products (carbon and hydrogen). Mole fractions of secondary byproducts reduce significantly despite the higher methane conversion,

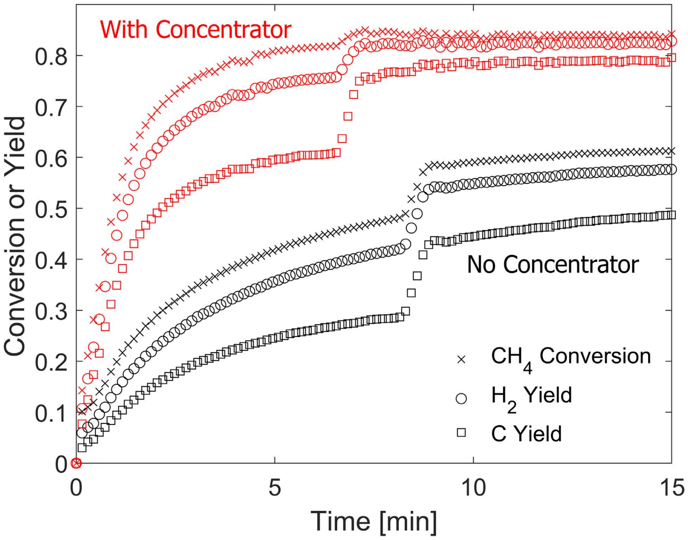

Figure 7.8: Methane conversion and product yields with and without secondary concentrator for methane pyrolysis at a flow rate of 100 sccm, solar power of 1.86 kW, pressure of 3.33 kPa, and fibrous medium thickness of 3.2 mm.

for which the mole fraction of C_2H_2 decreases from 3.4% to 1.1%, C_2H_4 decreases from 0.5% to 0.2%, and C_2H_6 remains below 0.1%. By extrapolating results of the parametric study presented in Chapter 5 at various solar powers, the power enhancement during methane pyrolysis can be roughly estimated. These results provide a relative increase in power of 198%, which is consistent with the other previously discussed evaluation methods.

Methane pyrolysis was tested at three additional operating conditions, and process conversions, product yields, and solar-to-chemical efficiencies are summarized in Table 7.1. Consistent with results from the earlier test (Exp 1), methane conversion and product yields increase significantly using the secondary concentrator, and the fraction of secondary byproducts (i.e., acetylene, ethylene, and ethane) decrease significantly. For operating conditions of Exp 2 (see Table 7.1), methane conversion increases from 78.7% without a concentrator to 93.3% with the secondary concentrator. Similar increase in performance occurs at

Exp 3 and Exp 4 operating conditions, for which methane conversions increase from 62.8% to 79.5% and from 34.6% to 47.8%, respectively. One of the important criteria for solar-thermal processes is the solar-to-chemical efficiency, which is very sensitive to methane inlet flow rate. This efficiency also improves significantly with the addition of the secondary concentrator as summarized in Table 7.1, where the solar-to-chemical efficiencies increase by 62%, 38%, 46%, and 59% at the different operating conditions. The highest estimated process efficiency is 6.5%, which occurs at the maximum tested flow rate of 2000 sccm. The process efficiency is expected to improve further at higher methane flow rates and during process scale-up and optimization.

Table 7.1: Methane pyrolysis process conversions, product yields, and solar-to-chemical efficiencies with and without the secondary concentrator at four operating conditions. Exp 1: 1.86 kW power, 100 sccm flow rate, 3.33 kPa pressure, and 3.2 mm thick medium; Exp 2: 2.26 kW, 100 sccm, 3.33 kPa, and 6.4 mm thick; Exp 3: 2.26 kW, 400 sccm, 0.67 kPa, and 6.4 mm thick; Exp 4: 2.26 kW, 2000 sccm, 3.33 kPa, and 6.4 mm thick.

	Without Concentrator				**With Concentrator**			
Parameter	Exp 1	Exp 2	Exp 3	Exp 4	Exp 1	Exp 2	Exp 3	Exp 4
$X_{\mathrm{CH_4}}$ [%]	61.3	78.7	62.8	34.6	85.0	93.3	79.5	47.8
$Y_{\mathrm{H_2}}$ [%]	57.7	76.0	59.5	32.0	83.5	92.4	77.0	45.7
Y_{C} [%]	48.7	70.2	52.5	27.3	80.1	90.6	72.0	41.9
η_{stc} [%]	0.42	0.47	1.51	4.10	0.68	0.65	2.20	6.53

7.4.5 Carbon product quality

As a result of increasing reaction zone temperatures by using the secondary concentrator, the carbon product quality enhances significantly. Fig. 7.9a shows the Raman spectra of the graphitic carbon product of Exp 1 without and with the secondary concentrator, whereas b and c show SEM images of the solid product, respectively. The carbon product for the case with no concentrator is of moderate to high graphitic quality with a Raman D/G peak ratio of 0.54. In contrast with a concentrator, the quality of the graphitic product enhances significantly, by which the D/G peak ratio reduces from 0.54 to 0.12, the FWHMs of all peaks decrease, and the D+D' peak disappears. These peak ratios correspond to more than two-fold increase in the average inter-defect distance, $L_{\mathrm{D,Ram}}$, from 16.4 to 34.9 nm, respectively, and indicate a significant upgrade in the product's quality. Such enhancement is also illustrated by the SEM images in Figs. 7.9b and c, which show a much smoother deposition of graphitic product over the original fibers while using the secondary concentrator.

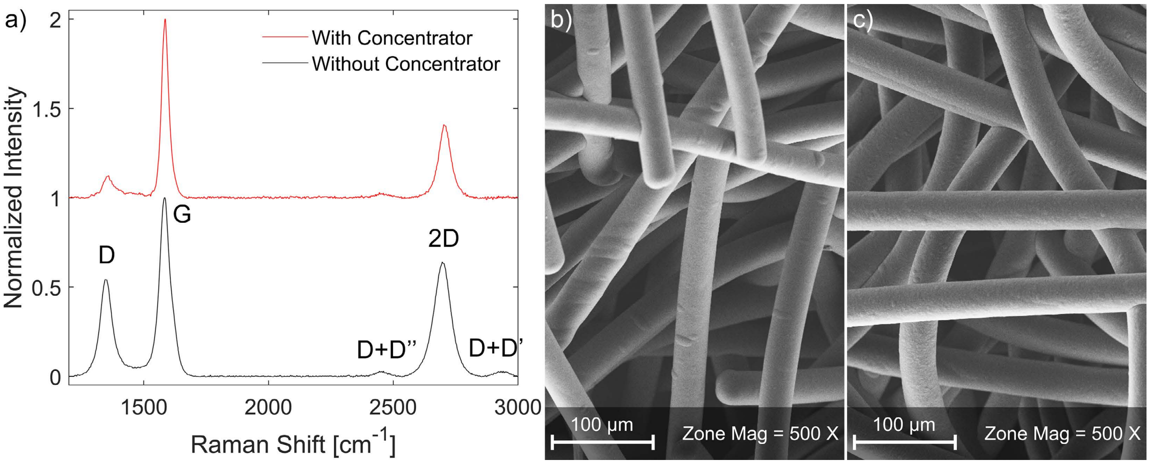

Figure 7.9: (a) Raman spectra and (b,c) SEM images of graphitic carbon product of Exp 1 (b) without and (c) with the secondary concentrator.

7.5 Conclusions

In this chapter, an in-house developed MCRT code is used to enhance the optical design of the large-scale solar reactor by using a conical secondary concentrator. The stainless steel concentrator's geometry was optimized through MCRT simulations to provide the highest solar concentration ratios and powers obtained within the fibrous reaction zone. With the optimized concentrator geometry, MCRT simulations estimated an increase in solar power intercepted on the reaction zone by 222%. To evaluate the actual enhancement in solar power concentration, various tests were performed with and without the secondary concentrator to provide a direct comparison. The first experimental measurements consisted of maximum temperatures recorded within the reaction zone, and indicated a temperature increase of more than 250 K and increase in power by 218% as a direct result of integrating the secondary concentrator. Next tests considered evaluating enhancements during methane decomposition at different operating conditions. Results indicated a significant improvement in methane conversions and product yields, and improved selectivity towards the primary products (carbon and hydrogen). Due to higher temperatures achieved within the reaction zone by using the secondary concentrator, the quality of the graphitic product improved significantly, by which the Raman D/G peak ratio decreased from 0.54 to 0.12, corresponding to more than two-fold increase in the average inter-defect distance (from 16.4 to 34.9 nm). Solar-to-chemical efficiencies also improved significantly by using the secondary concentrator, for which they increased by up to 62% and reached efficiency values as high as 6.5%. Current methodology and results demonstrate the importance of optimizing a solar reactor's optical and thermal designs, for which MCRT is a powerful tool that aids in such optimizations. Reported solar-to-chemical efficiencies are very promising, and they should drive future work into scaling-up and optimizing the present process, improving efficiencies further.

Chapter 8:
Closure

In this chapter, additional considerations and characteristics of the solar-thermal methane decomposition process are briefly discussed to complement results introduced in earlier chapters, and to provide insight into future work. These considerations include the photocatalytic contribution to the process that can help explain results presented in Chapter 5, specifically the high graphite deposition rates that are order(s) of magnitude higher than that reported in prior literature. In addition, results obtained using alternative starting materials are presented and discussed, with the possibility of using silica starting materials to produce fibrous core-shell silicon-graphite composites. This chapter concludes with opportunities for future work.

8.1 Photocatalytic contribution

Utilization of light to enhance chemical reactions through photocatalysis is usually achieved using plasmonic metal nanostructures [210–212], and it is of great interest especially for solar power applications. Photocatalytic contributions to process kinetics can aid in decreasing apparent reaction barriers or increasing reaction rates [213]. Therefore, quantifying the photocatalytic contribution (if present) to a thermochemical process is important, especially at the design stages of solar reactors. Solar reactors are classified as direct or indirect [39]. In direct solar reactors, the reacting flow and primary active materials are heated with direct solar irradiation by using transparent windows, whereas with indirect solar reactors the primary flow and materials are contained within an opaque chamber that exchanges thermal energy through reradiation [52]. Therefore, only direct solar reactors can utilize photocatalytic effects across ultraviolet (UV) wavelengths.

In this section, the photocatalytic contribution towards the reported solar-thermal methane decomposition process presented in earlier chapters is investigated [9, 150]. The process provides high graphite deposition rates that are order(s) of magnitude higher than that reported in prior literature [9]. Another prior work has suggested a photocatalytic contribution towards solar methane pyrolysis and CNT formation [31], but so far there has been no direct evidence of photocatalytic effects or attempts to quantify their contributions. Therefore, this section focuses on providing initial direct evidence of photocatalysis and, because graphite is not known to be a photocatalyst, the increase in deposition rates observed in this work is speculated to originate from the gas phase. Likely autocatalytic precursors in the present methane decomposition process are gas-phase polycyclic aromatic hydrocarbons (PAHs) [161].

8.1.1 Temperature-dependent deposition rates

Temperature-dependent deposition rates during methane pyrolysis are calculated by measuring fiber growths at different locations within the fibrous carbon medium using SEM images. Correlating diameters measured at various locations with IR camera temperature measurements can provide means to extracting reaction kinetics and forming an Arrhenius plot [214, 215] using results from a single experiment. For such an analysis, the following assumptions are considered: (1) carbon deposition and fiber growth occurs at a uniform solid density, irregardless of fiber diameter and temperature, and (2) carbon deposition rates are constant over the entire duration of methane pyrolysis. Therefore, increasing fiber volumes linearly translate to mass increases, and any changes can be averaged over the duration of the test. Based on the aforementioned assumptions and using measurements of the initial fiber radius (r_i = 9.6 µm) and fiber radii after methane pyrolysis (r_f) for some time (Δt), the fiber volumetric growths (ΔV_fib) and carbon deposition rates ($\dot{m}_\mathrm{c}$) are:

$$\frac{\Delta V_\mathrm{fib}}{L} = \pi(r_\mathrm{f}^2 - r_\mathrm{i}^2) \tag{8.1}$$

$$\frac{\dot{m}_\mathrm{c}}{L} = \dot{m}'_\mathrm{c} = \frac{\rho_\mathrm{c}\pi(r_\mathrm{f}^2 - r_\mathrm{i}^2)}{\Delta t} \tag{8.2}$$

where ρ_c is the density of the graphitic carbon product, and the deposition rate is normalized by length L. The graphite density was measured using a 10 ml pycnometer, deionized water, and 0.301 g of solid graphite product, giving graphitic carbon density of ρ_c = 1650 kg/m^3. The above parameters can instead be normalized by the initial fiber mass (m_cat) using $m_\mathrm{cat}/L = \rho_\mathrm{fib}\pi r_\mathrm{i}^2$, where ρ_fib is the density of the original PAN fibers (1840 kg/m^3) [148].

Four experiments were conducted at two different methane decomposition times (15 and 20 min) and at two different power levels (1.55 and 1.86 kW), with a pressure of 3.33 kPa, methane inlet flow rate of 100 sccm, and fibrous medium thickness of 3.2 mm. Substrate temperatures measured using the IR camera after significant carbon deposition are used to correlate radius from the center to temperature values, and a representative temperature contour is shown in Fig. 8.1a. Spatial temperatures are then related to fiber diameters measured using SEM at different radii, as shown by a representative plot for one of the tests in Fig. 8.1b.

For each SEM radial measurement, four diameter measurements were obtained from the positive and negative x and y directions, and were then averaged to reduce errors and provide an uncertainty interval.

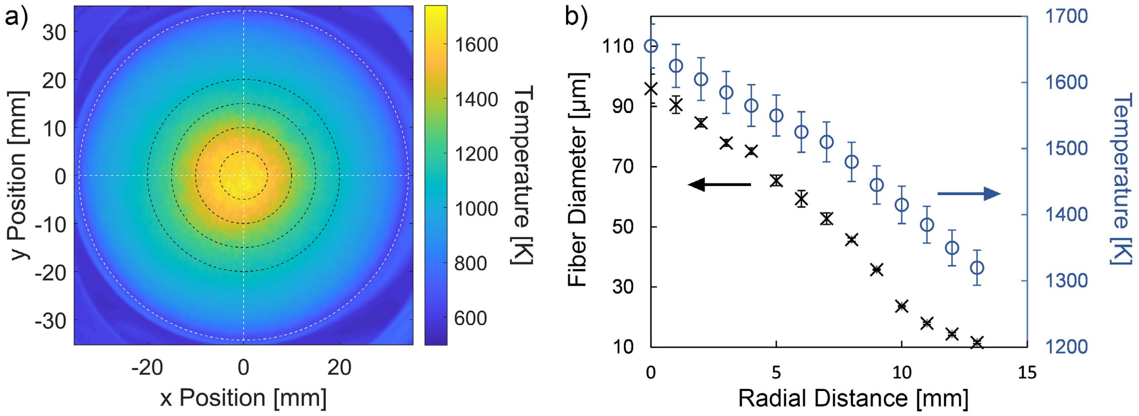

Figure 8.1: (a) IR camera temperature measurements of a representative test for methane pyrolysis at solar power of 1.86 kW, pressure of 3.33 kPa, methane inlet flow rate of 100 sccm, and fibrous medium thickness of 3.2 mm (centered black rings with $r = 5$, 10, 15, and 20 mm illustrate distribution and angular uniformity). (b) Fiber diameter measurements of a representative test using SEM images of the carbon medium after methane pyrolysis for 20 min.

Following the methodology described for Eq. 8.2, fiber diameter measurements were converted into carbon deposition rates ($\dot{m}_c$). The deposition rate directly correlates with the reaction rate ($r_{\mathrm{CH_4}}$) and reaction rate constant (k_r), and provides a basis to creating an Arrhenius plot and determining the activation energy (E_a) of the reaction. Therefore, $r_{\mathrm{CH_4}} \sim k_r = A \exp\left(-E_a/RT\right)$, where A is the pre-exponential factor and R is the universal gas constant. By taking the natural logarithm of the reaction rate, E_a can be determined through a linear fit of the data following: $\ln\left(r_{\mathrm{CH_4}}\right) = \ln\left(A'\right) - E_a/R\ (1/T)$. Normalized carbon molar deposition rates are plotted in Fig. 8.2a for the four different experimental tests against $1000/T$ to extract the apparent reaction activation energy.

Fig. 8.2a shows a nonlinear Arrhenius plot with temperature, as opposed to the linear relationship expected from the Arrhenius equation. Although the nonlinear

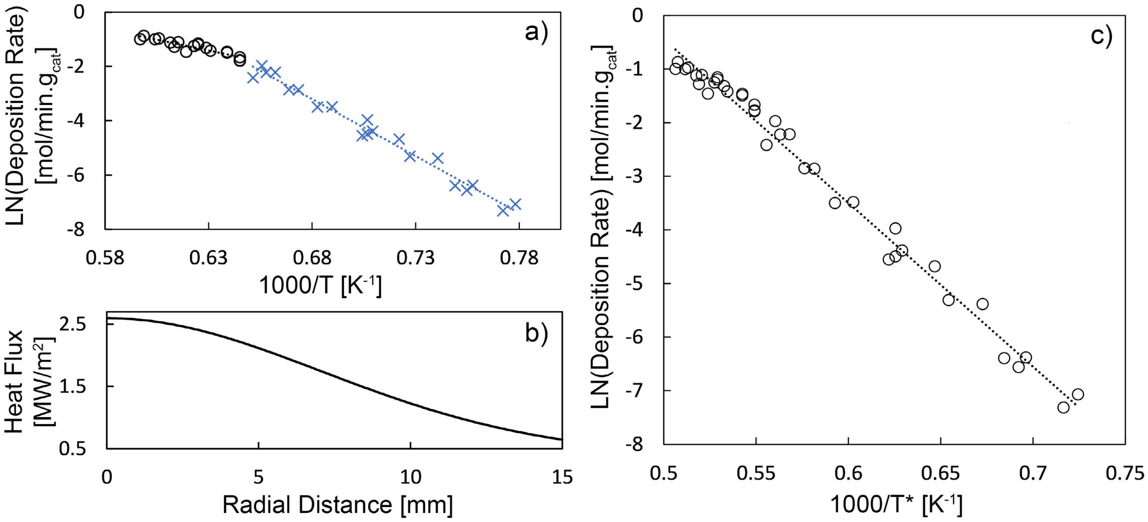

Figure 8.2: (a) Arrhenius plot of reaction kinetics raw measurements, with negative slopes of the blue and black linear fits being 41.9 and 15.9 $\times 10^3$ K, respectively. (b) Heat flux distribution along the fibrous medium's surface at a solar power of 1.86 kW. (c) Adjusted Arrhenius plot, accounting for 300 K temperature increase from solar irradiation absorbed by PAHs.

plot is continuous and smooth, it can be divided into two relatively linear regions (for demonstration purposes only) for values lower and higher than $1000/T = 0.65$, as illustrated in Fig. 8.2a. The slopes of these linear fits provide apparent activation energy values of 348 kJ/mol for the blue fit and 132 kJ/mol for the black fit. These two values are higher and slightly lower than E_a values reported in prior literature for methane pyrolysis with different carbonaceous catalysts [39, 41], potentially indicating the presence of additional unaccounted effects. A possible contribution to reaction kinetics is due to solar irradiation absorbed by PAHs present in the gas-phase, which usually constitute a small fraction of the flow (∼ 0.1%) [216–219]. PAHs generally exhibit strong absorbance to light in the UV region, which accounts for approximately 10% of the solar simulator's irradiation [68].

Given that the heat flux distribution of present testing (Fig. 8.2b) varies spatially, such variation may potentially induce the nonlinear trend shown by the

Arrhenius plot in Fig. 8.2a. To investigate this speculation further, absorption by PAHs is assumed to increase the effective reaction temperatures by magnitudes that vary linearly with the heat flux distribution, from Beer–Lambert law and plateauing specific heat capacities at high temperatures. Based on this approach, temperature measurements of the Arrhenius plot are presently incremented by an arbitrary temperature value of 300 K for a heat flux of 2.6 MW/m^2, varying linearly with heat flux. The temperature-adjusted (T*) Arrhenius plot is shown in Fig. 8.2c, exhibiting a more linear relationship with a negative slope of 30.5 × 10^3 K. This slope value provides an activation energy of 254 kJ/mol, which now lies within E_a values reported in prior literature [39, 41]. This observation possibly indicates the presence of unaccounted temperature contributions, potentially due to photocatalytic effects. Certainly, these preliminary results and observations are relatively rough and require more detailed investigation in future work to quantify the temperature increase resulting from light absorption by PAHs.

8.1.2 Direct and indirect solar irradiation

To further observe the contribution of direct solar irradiation, a test is conducted using the small-scale solar reactor through the configuration shown in Fig. 8.3a. A 1.5 mm thick graphite light shield (Fig. 8.3b) is placed 3.5 mm in front of the fibrous medium, covering the central region up to 5 mm in radius. Four 1 mm wide ligaments support the center of the light shield while minimizing conduction losses to ensure more effective radiation transfer to the fibrous medium. The dimensions of the light shield were optimized so that the shield covers the central part of the thin fibrous medium from high direct solar irradiation, while still providing significant reradiation to the medium to obtain relatively constant temperatures across covered and uncovered portions. Fig. 8.3c shows the contour of IR camera temperature measurements during methane pyrolysis at a solar power of 2.41 kW, methane inlet flow rate of 100 sccm, and pressure of 3.33 kPa while using the light blocker. Uniform temperatures around 1500 K were obtained across the central region of the medium up to a radius of 1 cm, reducing the effect of any temperature gradients between the covered and uncovered regions on fiber growths at different locations.

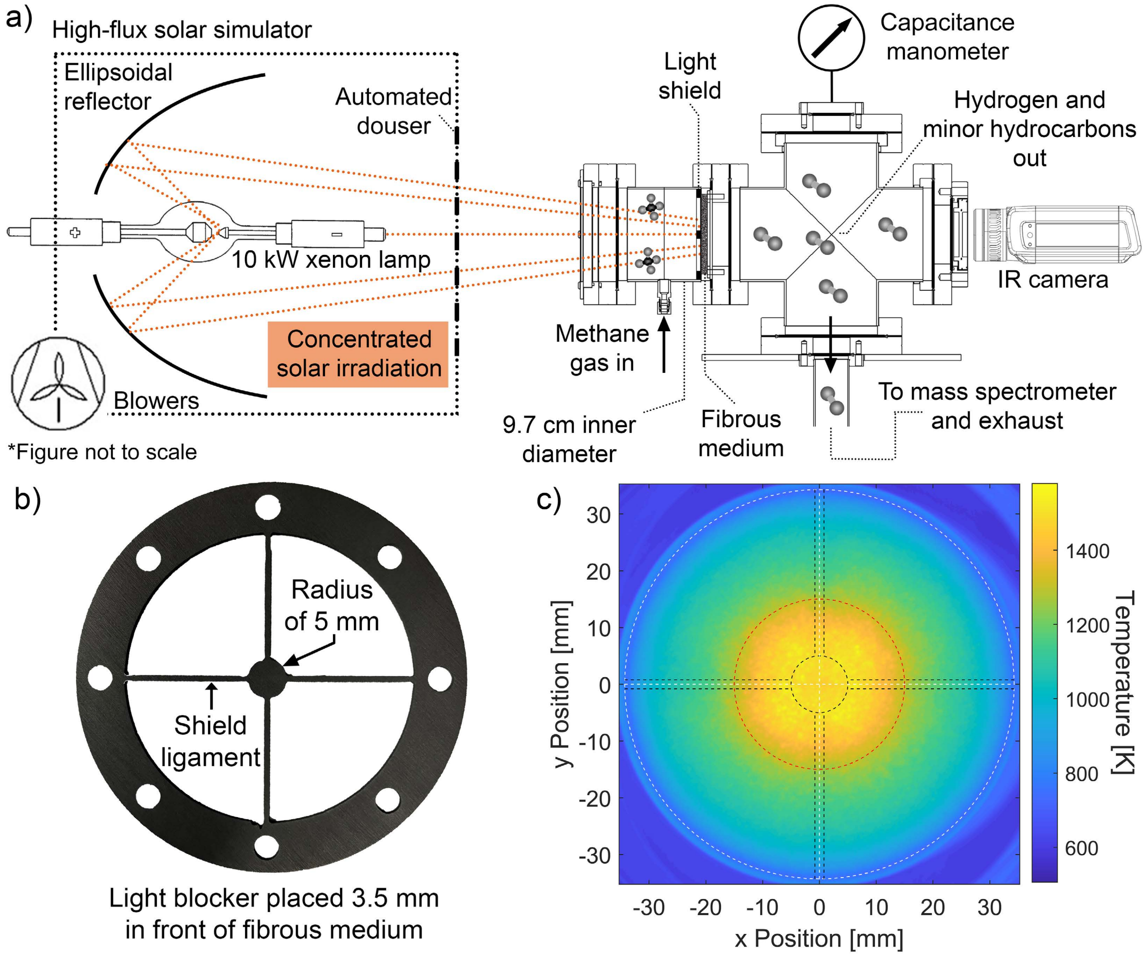

Figure 8.3: (a) Experimental setup of solar methane pyrolysis testing with direct and indirect irradiation. (b) Photograph of light shield used for direct and indirect solar irradiation. (c) Contour of IR camera temperature measurements for testing with a light shield, where black lines indicate the area covered by the light shield.

In a manner similar to obtaining chemical kinetics, SEM images of the fibrous medium were obtained at various radial locations after methane pyrolysis for 25 min, while avoiding areas covered by the light shield's ligaments. Fiber diameters of the product at different positions are shown in Fig. 8.4a, where the shaded region indicates central portion of the fibrous medium protected from direct solar irradiation. From Fig. 8.4a, the region receiving no direct solar irradiation had fiber diameters around 33 µm, remaining relatively constant for radial positions between 0 and 3.5 mm. Thereafter, fiber diameters significantly increase to 52 and 78 µm at radii of 4.5 and 5.5 mm, and the fiber diameter peaks at 6.5 mm with a diameter of 88 µm. This sudden transition in fiber growths from the region with indirect solar irradiation to the region with direct irradiation indicates a strong photocatalytic contribution to carbon deposition, for which the growth rate increases up to 8-fold. For radial locations beyond the fiber diameter's peak, growth rates gradually reduce with radial distance as a result of decreasing surface temperatures (Fig. 8.3c) and heat flux magnitudes (Fig. 8.2b). These two parameters significantly affect chemical kinetics and reaction rates, decreasing carbon deposition rates.

The significant photocatalytic contribution is further demonstrated by SEM images shown in Fig. 8.4. Fig. 8.4b shows a sample region at the light shield's edge, where roughly the upper right corner of the image was exposed to direct irradiation while the lower left corner was fully shadowed. The contrast in the size of fibers reveals the contribution of light in significantly increasing methane pyrolysis reaction rates. However, acknowledging that fibers shown in Fig. 8.4b may potentially be at slightly different effective temperatures, a single continuous graphitic fiber is tracked across the region transitioning from indirect to direct solar irradiation, as shown in Fig. 8.4c. As the temperature is relatively uniform across this region (Fig. 8.3c) and due to the high thermal conductivity of graphitic structures, a temperature gradient (if present) is not expected to cause this significant variation in growth. As shown in Fig. 8.4c, the fiber growth rate varies

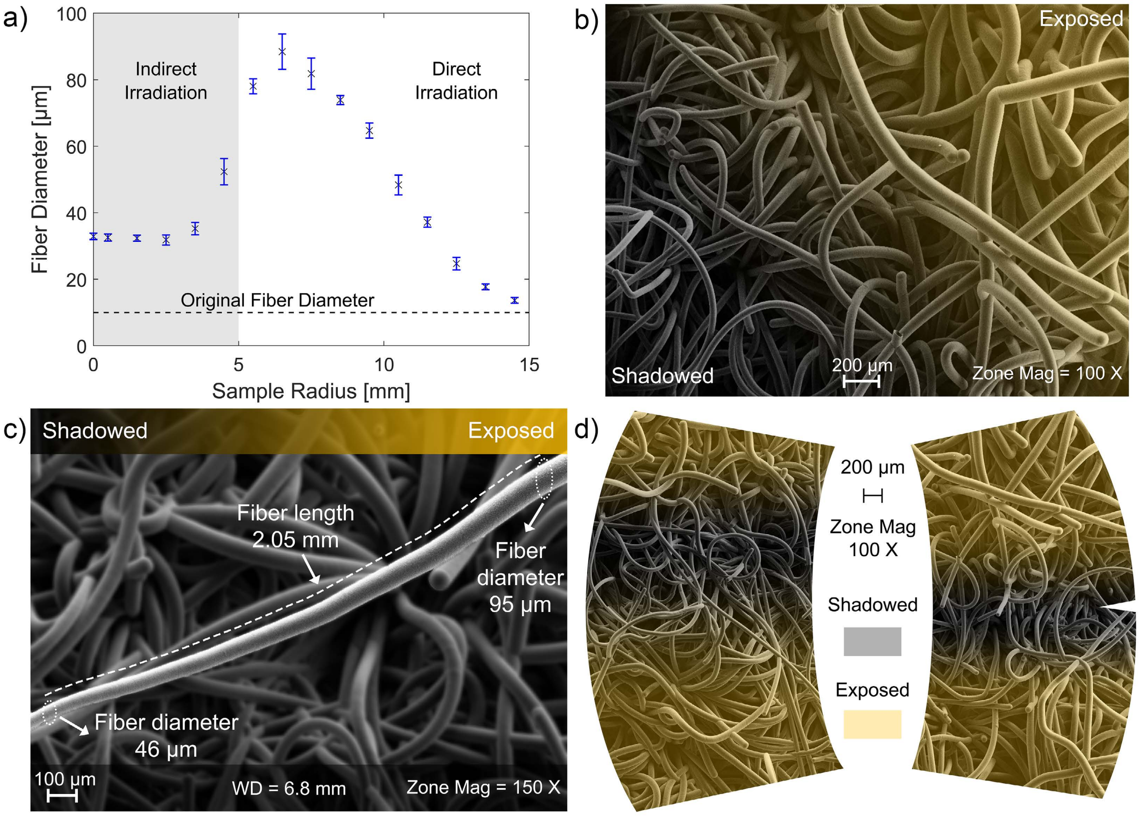

Figure 8.4: (a) Fiber diameters after methane pyrolysis with light shield for 25 min at solar power of 2.41 kW, methane inlet flow rate of 100 sccm, and pressure of 3.33 kPa. (b-d) SEM images of the carbon product demonstrating the significant fiber growths at regions receiving direct solar irradiation, showing (b) fibers at edge of the light shield, (c) a 2 mm long single fiber at the transition between indirect and direct irradiation, and (d) fibers across two light shield's ligaments.

significantly across a distance of 2 mm, where the fiber is 46 µm on one end and is 95 µm on the other end. This observation further supports a photocatalytic contribution to solar-thermal methane decomposition.

Similar observations are made over the fiber regions covered by the light shield's 1 mm thick ligaments, as shown in Fig. 8.4d for two different regions. Across these regions especially, a temperature gradient (if present) is expected to insignificantly affect carbon deposition growth rates, and the contrast in fiber growth (Fig. 8.4d) is mostly driven by photocatalytic effects. It can be postulated that the light shield and its ligaments may obstruct the flow through the covered fibrous regions, leading to lower apparent carbon deposition rates. However, given that the light shield is located 3.5 mm away from the fibrous medium's surface and that the mean free path of methane at the process operating conditions is 10 µm (orders of magnitude lower), such an effect should be insignificant. Additionally, possible added resistance due to larger fibers in the regions exposed to direct irradiation should compensate for any flow constriction caused by the light shield.

A heat transfer analysis can be performed in future work to confirm that an insignificant temperature gradient exists between regions with indirect and direct solar irradiation, especially along a single fiber (Fig. 8.4c). However, the thermal conductivity of the graphite product will need to be known for such an analysis. Therefore, in the next subsection, the effective thermal conductivity of the solid product is measured. The observations and brief discussion presented in this subsection aim to initially explain the high graphite deposition rates observed in this work, and guide future efforts investigating photocatalytic effects further.

8.1.3 Thermal conductivity

A rectangular graphite sample was prepared to measure the effective thermal conductivity of the solid product obtained from the present solar-thermal methane pyrolysis process. Methane was decomposed for 120 min through a 3.2 mm thick C100 carbon felt at a solar power of 1.86 kW, methane flow rate of 100 sccm, and pressure of 3.33 kPa. After methane decomposition, the fibers in the central region fully coalesced, providing a continuous and dense graphite product. The central region of the sample was then cut into a rectangular slab and polished using a 1200 grit sandpaper, giving a rectangular slab with a length, width, and thickness of 2.47 cm, 6.05 mm, and 0.65 mm. An SEM image of the graphite slab's surface is shown in Fig. 8.5a at a low magnification, indicating the formation of a relatively smooth and continuous surface. In contrast, Fig. 8.5b shows an image of the surface at a high magnification, indicating that original fibers and graphitic product are not aligned along the surface. The latter observation indicates that thermal conductivity along the length of the surface (characterized later) represents the effective thermal conductivity of the product, which is expected to be lower than that oriented along the length of fibers. Nevertheless, the thermal conductivity of the solid product is expected to be high due to its relatively high-quality, as presented by the Raman spectrum shown in Fig. 8.5c.

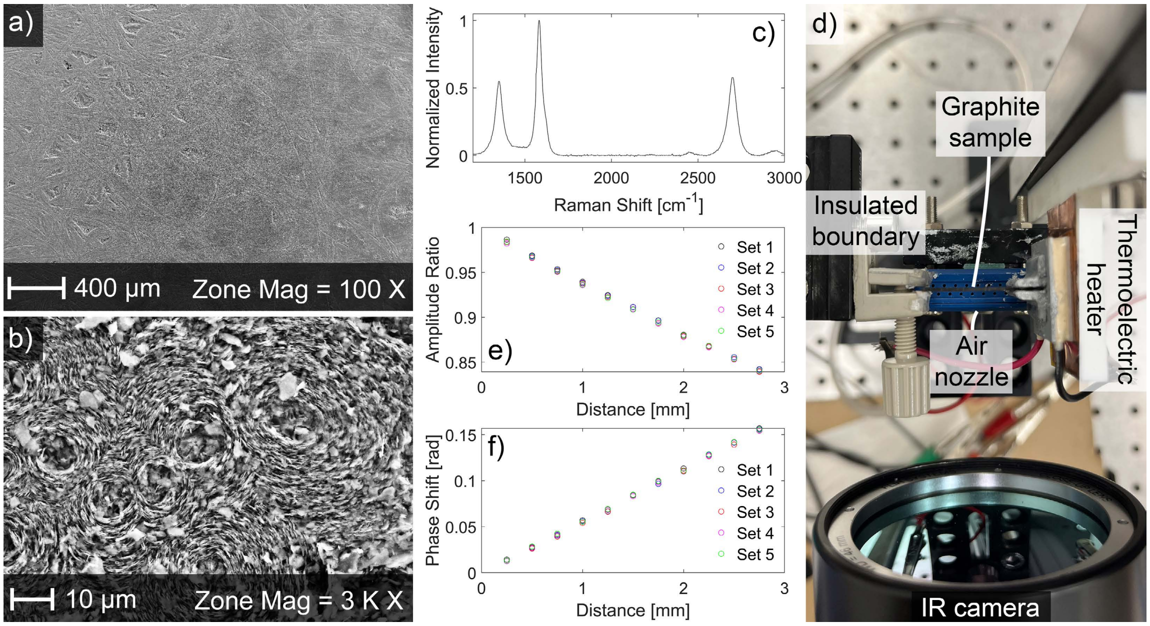

Figure 8.5: (a,b) SEM surface images and (c) Raman spectrum of the graphite product used for thermal diffusivity measurements. (d) Photograph of the experimental setup for thermal diffusivity measurements using a modified Ångström's method. (e,f) Amplitude ratio and phase shift measurements along tested graphite sample at a heating frequency of 0.1 Hz.

The thermal diffusivity of the graphite product at room temperature was measured using a modified Ångström's method and an in-house setup described in prior work [220] and shown in Fig. 8.5d. Briefly, a thermoelectric module was used to modulate temperatures sinusoidally across an edge of tested samples, where amplitude ratios and phase shifts of temperatures at different locations along the sample measured using an IR camera provide accurate estimates of the material's thermal diffusivity. The thermal diffusivity was measured at four different heating frequencies varying from 0.1 to 0.25 Hz with an increment of 0.05 Hz, and by using five sets of measurements for each heating frequency. Figs. 8.5e and f show representative plots of amplitude ratio and phase shift along the graphite sample at a heating frequency of 0.1 Hz. Results were then averaged, providing an effective thermal diffusivity of 93.5 ± 6.1 mm^2/s. By using the density of the graphite product measured using a pycnometer (1650 kg/m^3) and the specific heat capacity of graphite at room temperature (685 J/kg·K) [153], the effective thermal conductivity is determined as 106 W/m·K, which corresponds to a graphite product with a porosity of 0.27 based on graphite's theoretical density of 2260 kg/m^3. This thermal conductivity value compares well with other graphite materials [115], and can be used as the lower limit of thermal conductivity of fibers in future work.

8.2 Alternative starting materials

Alternative starting materials were used for solar-thermal methane pyrolysis to characterize process performance and solid product. These materials primarily consisted of silica, alumina, and zirconia, which are known to be resistant to high temperature conditions. Different materials tested and process performance metrics are summarized in Table 8.1, for which methane pyrolysis was conducted at a solar power of 1.86 kW, methane inlet flow rate of 100 sccm, and pressure of 3.33 kPa.

Methane conversion and product yields significantly depend on characteristics of the starting material. From Table 8.1, the highest methane conversion (77%)

Table 8.1: Results of different materials tested for solar methane pyrolysis.

Material	Thickness [mm]	Density [kg/m^3]	Supplier	X_{CH_4} [%]	Y_{H_2} [%]	Y_C [%]
C	3.2	89	FuelCellEarth (C100)	73.1	68.7	58.3
Al_2O_3/SiO_2	3.2	128	Morgan (Cerablanket)	74.6	71.1	64
Al_2O_3	3.2	140	ZIRCAR (RS-3000)	77	72.5	62.6
SiO_2	3.2	150	ZIRCAR (SB-2000)	58	51.9	38.5
ZrO_2	2.5	240	ZIRCAR (RS-Z)	76.4	73.8	70.3

was obtained with a 3.2 mm thick alumina substrate, while the lowest conversion (58%) was recorded for a 3.2 mm thick silica substrate. Certainly the constituent materials and their catalytic contributions affect process results, but these parameters are in addition to the orientation and nominal size of fibers within the porous medium. Uncoupling effects of the constituent materials and configuration of the fibrous medium was not attempted in this study, but can potentially be considered in future work. In this work, the initial primary focus was on the characteristics of the solid product and the potential of the current process for producing various carbon composites that may be of interest. Therefore, the solid products with different materials summarized in Table 8.1 were characterized using Raman spectroscopy, and the measured spectra of the carbon product are shown in Fig. 8.6a. All starting materials provided high-quality graphitic carbon products with Raman I_D/I_G ratios varying from 0.11 with a zirconia substrate to 0.47 with a silica substrate. The difference in the carbon product quality is potentially due to material's optical and thermal properties, catalytic behavior, and its crystallinity, but generally the carbon product quality can be further improved with process optimization as demonstrated in previous chapters.

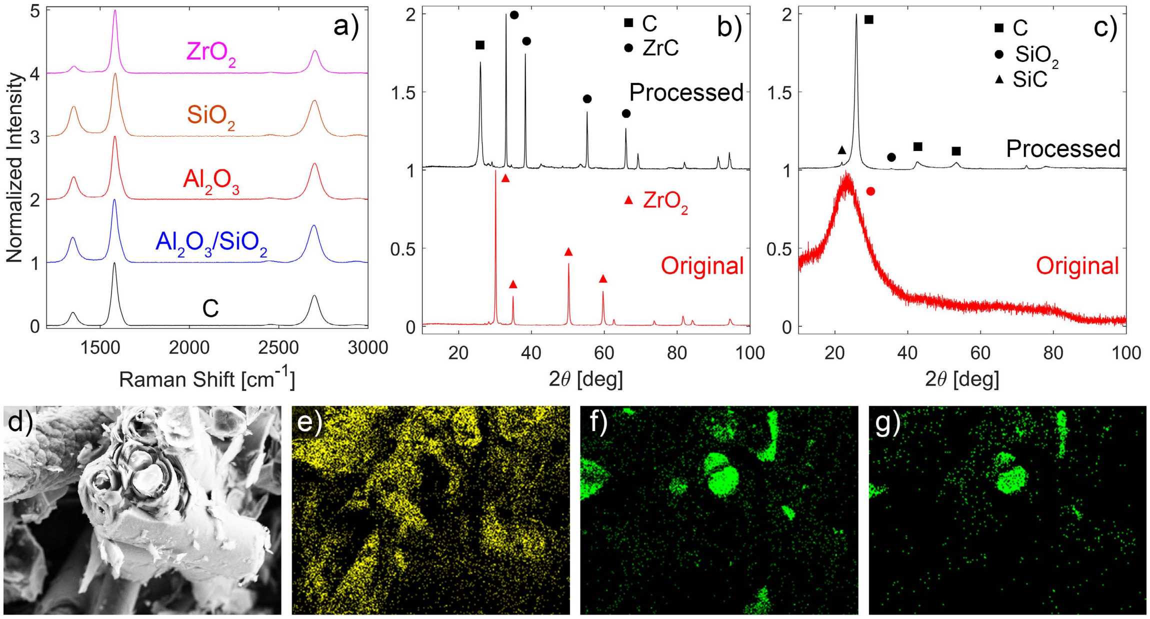

Figure 8.6: (a) Raman spectra of carbon product obtained with different starting materials after methane decomposition at a solar power of 1.86 kW, methane inlet flow rate of 100 sccm, and pressure of 3.33 kPa. (b,c) XRD spectra of starting material and solid product for (b) zirconia and (c) silica substrates. (d) SEM image and (e-g) EDS maps of the solid product with a silica substrate representing constituent (e) carbon, (f) silicon, and (g) oxygen elements.

XRD spectra of zirconia and silica starting materials and their processed solid products are shown in Figs. 8.6b and c. Consistent with prior observations, XRD spectra reveal that zirconia has a crystalline structure based on its distinct peaks, as compared to the broad peak present for the amorphous silica starting material. This difference in crystalline structure potentially causes the difference in Raman spectra shown in Fig. 8.6a. XRD spectra also reveal that upon processing, the zirconia substrate reduces and forms a carbon/zirconium carbide composite based on the presence of C and ZrC XRD peaks and absence of ZrO_2 peaks (see Fig. 8.6b) [221]. In contrast for the amorphous silica substrate, the only strong and distinct XRD peaks present are those corresponding to graphite (see Fig. 8.6c). Two additional weak peaks corresponding to crystalline SiO_2 (cristobalite) and SiC were additionally observed [222, 223], indicating the possible reduction and upgrade of the silica starting material.

An SEM image of the processed silica substrate (after grinding) and EDS maps of elemental carbon, silicon, and oxygen are shown in Figs. 8.6d-g. EDS maps reveal regions within the solid product where oxygen does not overlap with silicon, potentially suggesting partial reduction of silica into silicon. This observation is consistent with MS qualitative measurements indicating the production of H_2O, instead of H_2, during the initial stage of methane decomposition as a result of material reduction. However, the XRD spectrum of the silica processed substrate (Fig. 8.6c) does not reveal peaks corresponding to silicon, as amorphous silicon is possibly produced. The silica substrate is of interest here due to its potential in producing silicon/graphite composites through silica reduction [224, 225] and graphite deposition. This composite form has been studied in literature for Li-ion battery anodes due to the promising high capacity of silicon and the high conductivity and structural stability of graphite [226, 227]. Therefore, a fibrous core-shell silicon-graphite composite should be of great interest, as the graphite shell mitigates the issue of silicon's volume expansion upon lithiation to provide enhanced stability [228]. Initial results presented in this section are promising, and future work should focus on further confirming the reduction of silica in addition to optimizing process conditions to obtain enhanced silicon/graphite composites.

8.3 Opportunities for future work

There are many opportunities for future work, in addition to further investigating photocatalytic effects in solar-thermal methane pyrolysis and the potential for producing fibrous core-shell silicon-graphite composites. The most important scope of follow-up work consists of investigating approaches to further reduce the process operating costs. In this work, most of the focus has been on producing high-quality graphitic carbon product with high commercial value and demand in order to obtain favorable process economics and drive hydrogen production costs lower. Future work can investigate other characteristics that were not considered in this work, such as optimizing the process and carbon product for near atmospheric pressures, as operating costs and sealing concerns significantly increase when operating under vacuum conditions. A possible route to enable operating near atmospheric pressures can be achieved by using molecular-scale carbon seeds or precursors that would produce high-quality graphitic carbon product [229]. Another process aspect that is of great interest considers investigating alternative organic starting materials with significantly lower costs compared to the engineered fibrous carbon materials used throughout this study. The cost of starting materials can be significant, affecting the overall process economics.

Although solar-to-chemical efficiency values as high as 6.5% were reported in this work, there are still more significant improvements that can be incorporated. To further improve the present process performance, future thermal modeling should focus on integrating more optimized optical components that would enhance the capture of solar irradiation and provide a more uniform light distribution. The uniform distribution would be necessary to obtain consistent solid product quality. Additionally, process conversions and product yields can be further improved by investigating optimized porous media configurations that would result in more effective radiation propagation and capture. Characteristics of interest include the medium's starting porosity, fiber diameters, and fiber orientations [180]. Furthermore, future work into roll-to-roll reactor designs that provide less flow bypass should be investigated, as process efficiencies are expected to increase with less flow bypass around the fibrous roll.

Another important consideration for future work consists of translating the current technology beyond laboratory work by driving the process with real solar irradiation and by decomposing natural gas, or other renewable sources such as biogas. A possible route to solar field scale-up and implementation is illustrated in Fig. 8.7, which utilizes a parabolic dish system to provide the required solar concentrations and drive the pyrolysis reaction. Results presented throughout this work should be used to guide numerical modeling efforts on optimizing dimensions of the solar reactor and its reaction zone. The solar-to-chemical efficiency of the process is expected to significantly improve with scale-up in addition to design and process optimizations, to finally realize this process at scale and avoid the emissions of 10 kg of CO_2 per kg of H_2 and 5 kg of CO_2 per kg of graphite.

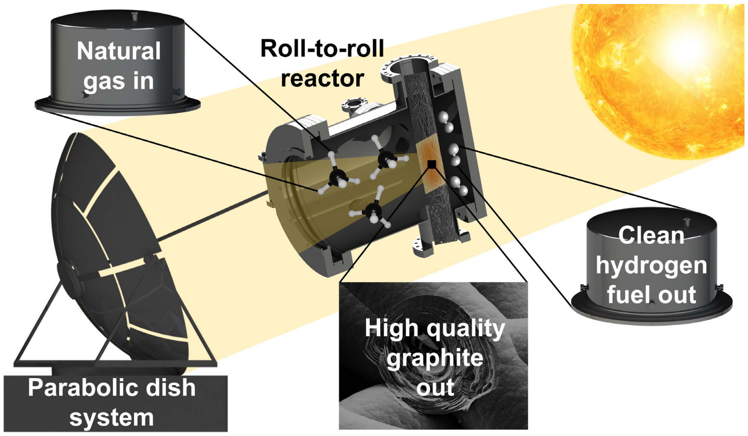

Figure 8.7: Schematic illustration of a roll-to-roll solar-thermal methane decomposition process for solar field implementation with a parabolic dish system.

Appendices

A Methane decomposition process schematics

The overall P&ID schematic of the small-scale methane decomposition experimental setup and auxiliaries is shown in Fig. A.1. The schematic illustrates how different components are integrated together, and indicates any additional instrumentation that were not discussed in the main text.

As discussed in Chapter 3, the entire experimental setup is automated via LabVIEW for data acquisition and controls. A portion of the LabVIEW front panel for the small-scale methane decomposition experimental setup is shown in Fig. A.2. Various illuminating indicators are included for ease of visualization, where the warning indicator turns on when non-urgent experimental issues arise, such as a large pressure drop between the gas manifold and downstream of the solar reactor. This large pressure drop may indicate buildup due to the start of reactor clogging (if applicable).

Additionally, a portion of the LabVIEW block diagram for the small-scale methane decomposition experimental setup is shown in Fig. A.3. The VI contains multiple safety interlocks and tripping points to maintain the integrity of operation and minimize any human errors.

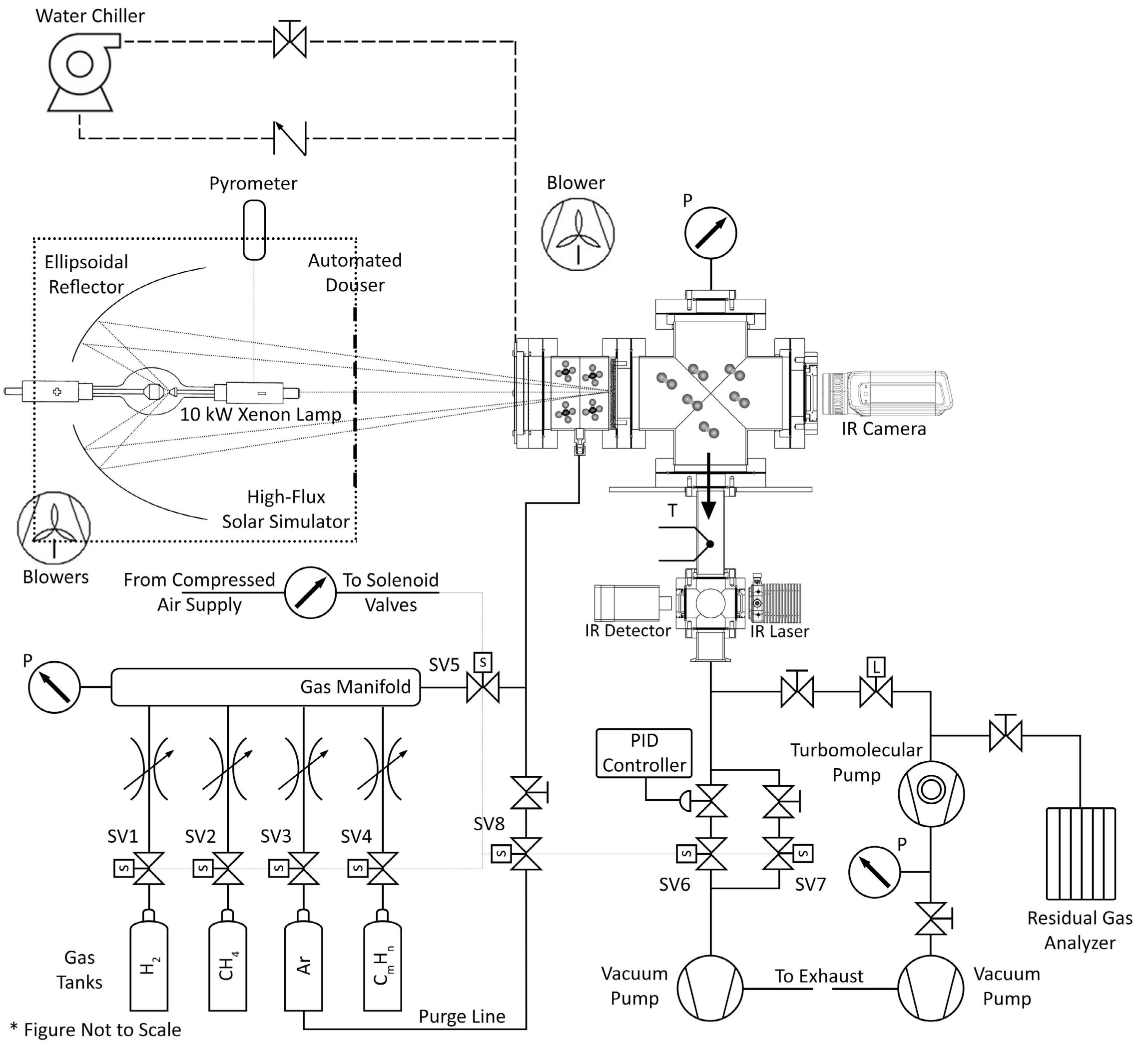

Figure A.1: An overall P&ID schematic illustration of the small-scale methane decomposition experimental setup and auxiliaries.

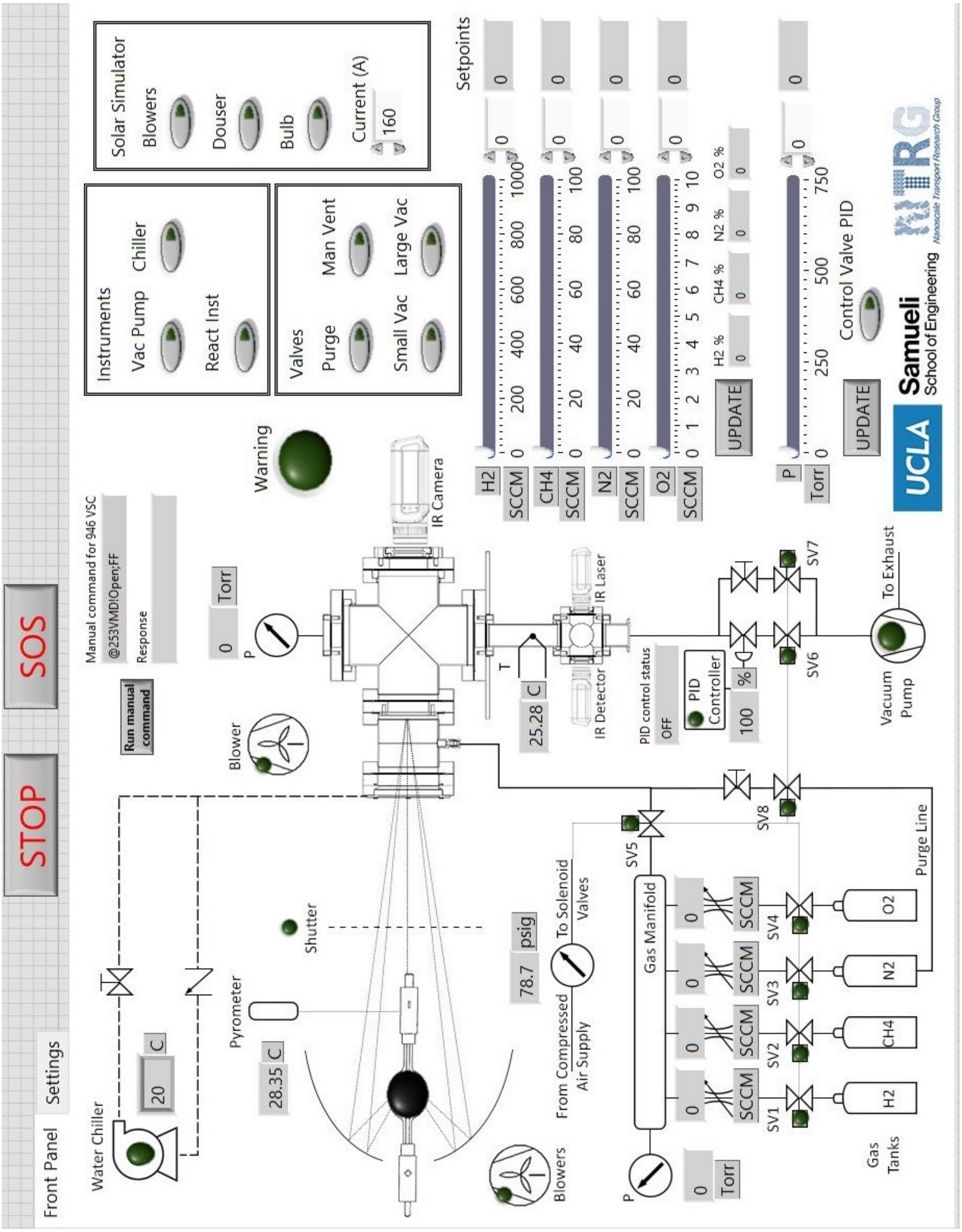

Manual command for 946 VSC: @253VMD!Open;FF

Response:

Water Chiller: 20 C

Pyrometer: 28.35 C

T: 25.28 C

P: 0 Torr

From Compressed Air Supply: 78.7 psig

Gas Manifold P: 0 Torr

H2: 0 SCCM

CH4: 0 SCCM

N2: 0 SCCM

O2: 0 SCCM

PID control status: OFF

PID Controller: 100 %

Current (A): 160

		Scale	Setpoint
H2	SCCM	0 – 1000	0
CH4	SCCM	0 – 100	0
N2	SCCM	0 – 100	0
O2	SCCM	0 – 10	0
P	Torr	0 – 750	0

H2 %: 0

CH4 %: 0

N2 %: 0

O2 %: 0

Figure A.2: LabVIEW front panel screenshot of VI created for controlling and monitoring the small-scale methane decomposition experiments.

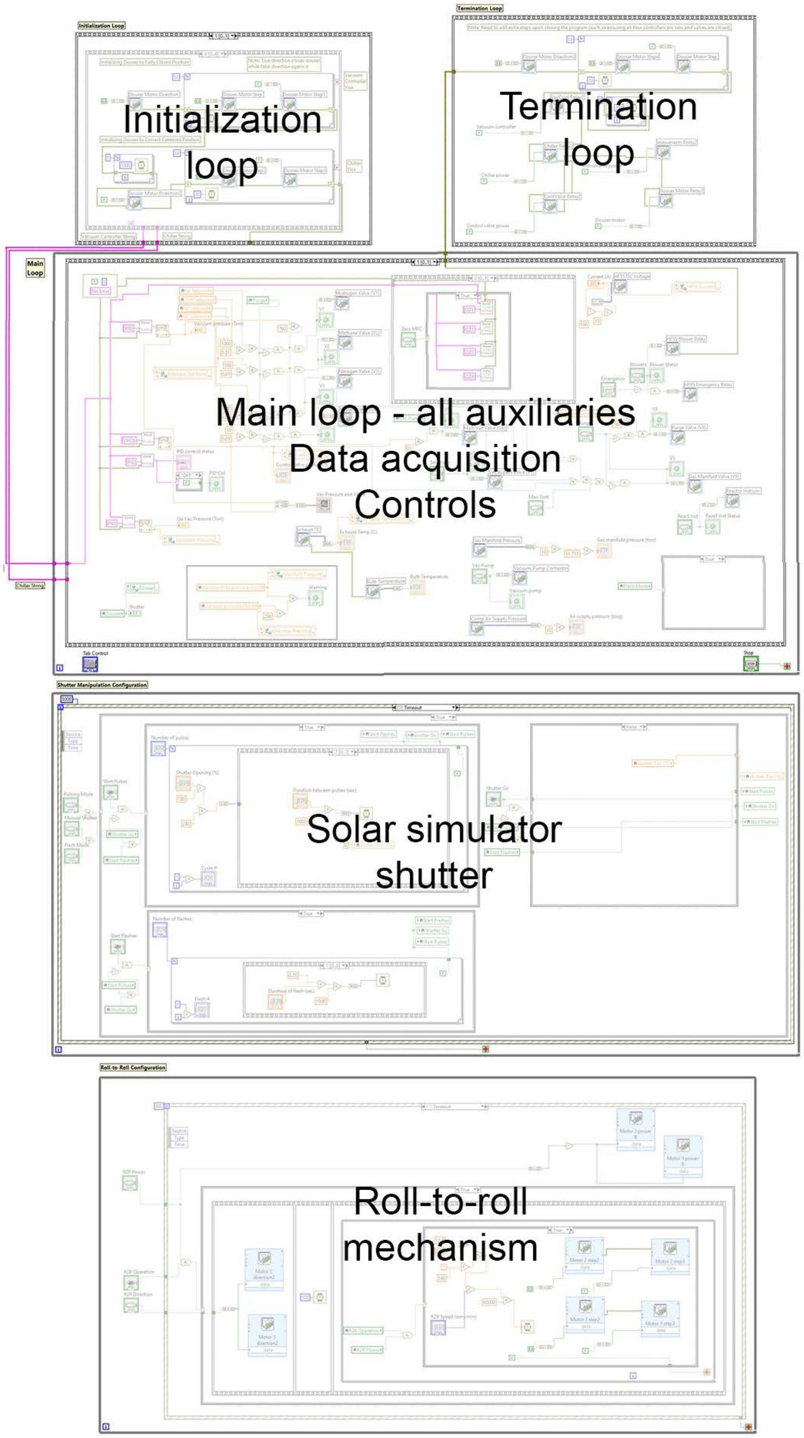

Figure A.3: LabVIEW block diagram screenshot of VI created for controlling and monitoring the methane decomposition experiments.

B LAS chemical kinetics methodology

The full quantitative analysis using only IR absorption spectroscopy results and all the dominant species involved implements the assumption of a steady state process. This is due to its dependency on the total mass of carbon collected and measured through the methane decomposition process to quantify the mole fraction of C_2H_2, which is not being continuously monitored. By considering only the five most dominant species in the product stream (0.1% or higher), which are H_2, CH_4, C_2H_2, C_2H_4, and C_2H_6, we can formulate the following list of equations for conversion and yield quantification. Starting with the basis that the mole fraction must add to unity:

$$1 = x_{\mathrm{H_2}} + x_{\mathrm{CH_4}} + x_{\mathrm{C_2H_2}} + x_{\mathrm{C_2H_4}} + x_{\mathrm{C_2H_6}} \tag{B.1}$$

Then, by formulating a balance over hydrogen atoms, we find:

$$2\dot{n}_{\mathrm{CH_4,in}} = \dot{n}_{\mathrm{out}}(x_{\mathrm{H_2}} + 2x_{\mathrm{CH_4}} + x_{\mathrm{C_2H_2}} + 2x_{\mathrm{C_2H_4}} + 3x_{\mathrm{C_2H_6}}) \tag{B.2}$$

Combining Eqs. B.1 and B.2, we can quantify the total molar flow rate out as:

$$\dot{n}_{\mathrm{out}} = \frac{2\dot{n}_{\mathrm{CH_4,in}}}{1 + x_{\mathrm{CH_4}} + x_{\mathrm{C_2H_4}} + 2x_{\mathrm{C_2H_6}}} \tag{B.3}$$

A balance over carbon atoms can also be formulated, assuming steady state conditions and that all the carbon produced is collected and measured, yielding:

$$\dot{n}_{\mathrm{CH_4,in}} = \dot{n}_{\mathrm{out}}(x_{\mathrm{CH_4}} + 2x_{\mathrm{C_2H_2}} + 2x_{\mathrm{C_2H_4}} + 2x_{\mathrm{C_2H_6}}) + \dot{m}_{\mathrm{C}}/M_{\mathrm{C}} \tag{B.4}$$

where $\dot{m}_{\mathrm{C}}$ is the carbon deposition rate as determined from the ratio of the total carbon mass measured (m_{C}) to the duration of methane decomposition (t_d). Rearranging Eq. B.4, the mole fraction of C_2H_2 can be quantified using:

$$x_{\mathrm{C_2H_2}} = \frac{1}{2\dot{n}_{\mathrm{out}}}(\dot{n}_{\mathrm{CH_4,in}} - \frac{\dot{m}_{\mathrm{C}}}{M_{\mathrm{C}}}) - 0.5x_{\mathrm{CH_4}} - x_{\mathrm{C_2H_4}} - x_{\mathrm{C_2H_6}} \tag{B.5}$$

The hydrogen mole fraction can then be easily obtained using Eq. B.1. Following that, methane conversion in addition to total hydrogen and carbon yields can be determined using Eqs. B.6, B.7, and B.8, respectively.

$$X_{\mathrm{CH_4}} = \frac{\dot{n}_{\mathrm{CH_4,in}} - \dot{n}_{\mathrm{out}}x_{\mathrm{CH_4}}}{\dot{n}_{\mathrm{CH_4,in}}} \tag{B.6}$$

$$Y_{\mathrm{H_2}} = \frac{\dot{n}_{\mathrm{out}}x_{\mathrm{H_2}}}{2\dot{n}_{\mathrm{CH_4,in}}} \tag{B.7}$$

$$Y_{\mathrm{C}} = \frac{\dot{m}_{\mathrm{C}}}{M_{\mathrm{C}}\dot{n}_{\mathrm{CH_4,in}}} \tag{B.8}$$

C Methane pyrolysis results summary

Table C.1: Results summary of the small-scale reactor parametric study. Methane pyrolysis operating conditions, chemical conversions and yields, solar-to-chemical efficiencies, carbon product deposition rates, and Raman quality. Reported values are based on initial steady-state measurements observed prior to slight reduction in performance due to significant flow constriction.

Begin of Table

$\dot{m}_{\mathrm{CH_4}}$ [sccm]	$\dot{Q}_{\mathrm{s}}$ [kW]	P [kPa]	L_{R} [mm]	t_{res} [ms]	$X_{\mathrm{CH_4}}$ [%]	$Y_{\mathrm{H_2}}$ [%]	Y_{C} [%]	$\dot{m}_{\mathrm{C}}$ [g/hr]	η_{stc} [%]	$I_{\mathrm{D}}/I_{\mathrm{G}}$
10	1.86	3.33	3.2	445	96	94	91	0.29	0.06	0.06
25	1.86	3.33	3.2	178	88	85	78	0.63	0.14	0.20
100	1.86	3.33	3.2	44	73	69	58	1.88	0.46	0.21
200	1.86	3.33	3.2	22	62	58	47	3.04	0.79	0.25
300	1.86	3.33	3.2	15	53	49	39	3.78	1.01	0.29
400	1.86	3.33	3.2	11	46	43	34	4.36	1.17	0.33
600	1.86	3.33	3.2	7.4	44	41	34	6.50	1.69	0.42
800	1.86	3.33	3.2	5.6	39	36	29	7.53	1.96	0.49
1000	1.86	3.33	3.2	4.5	36	34	28	8.98	2.28	0.56
2000	1.86	3.33	3.2	2.2	22	21	17	11.0	2.84	0.59
100	0.92	3.33	3.2	55	34	30	22	0.70	0.38	0.79
100	1.23	3.33	3.2	51	56	52	41	1.32	0.48	0.59
100	1.55	3.33	3.2	47	66	61	50	1.60	0.48	0.45
100	2.18	3.33	3.2	42	80	76	66	2.12	0.45	0.22
100	2.49	3.33	3.2	41	84	80	71	2.28	0.42	0.20
100	1.86	1.33	3.2	18	69	64	53	1.72	0.44	0.19

Continuation of Table C.1

$\dot{m}_{CH_4}$ [sccm]	$\dot{Q}_s$ [kW]	P [kPa]	L_R [mm]	t_{res} [ms]	X_{CH_4}	Y_{H_2}	Y_C	$\dot{m}_C$ [g/hr]	η_{stc} [%]	I_D/I_G
100	1.86	6.67	3.2	88	74	70	60	1.93	0.47	0.28
100	1.86	13.3	3.2	176	75	71	61	1.96	0.47	0.41
100	1.86	26.7	3.2	353	78	73	64	2.05	0.49	0.38
100	1.86	40	3.2	530	78	73	63	2.03	0.49	0.58
200	1.86	13.3	3.2	88	70	65	55	3.55	0.89	0.94
400	1.86	13.3	3.2	44	55	51	42	5.38	1.38	1.38
600	1.86	13.3	3.2	29	45	42	34	6.57	1.71	1.30
800	1.86	13.3	3.2	22	39	36	28	7.27	1.98	1.16
100	1.86	3.33	0.36	4.2	52	46	29	0.94	0.32	0.58
100	1.86	3.33	0.51	5.5	56	51	37	1.18	0.36	0.46
100	1.86	3.33	0.89	11	65	60	48	1.54	0.41	0.29
100	1.86	3.33	1.52	17	70	66	55	1.77	0.44	0.22
100	1.86	3.33	9.6	133	76	73	64	2.05	0.48	0.19

End of Table

References

[1] C. Figueres, H. J. Schellnhuber, G. Whiteman, J. Rockström, A. Hobley, and S. Rahmstorf, "Three years to safeguard our climate", Nature **546**, 593–595 (2017).

[2] International Energy Agency, *Electricity Information: Overview*, tech. rep. (IEA, Paris, 2020).

[3] International Energy Agency, *Renewables 2019*, tech. rep. (IEA, Paris, 2019).

[4] N. M. Haegel et al., "Terawatt-scale photovoltaics: Transform global energy", Science **364**, 836–838 (2019).

[5] International Energy Agency, *Data and statistics*, tech. rep. (IEA, Paris).

[6] S. Rodat, S. Abanades, H. Boujjat, and S. Chuayboon, "On the path toward day and night continuous solar high temperature thermochemical processes: A review", Renewable and Sustainable Energy Reviews **132**, 110061 (2020).

[7] H. Song, S. Luo, H. Huang, B. Deng, and J. Ye, "Solar-driven hydrogen production: Recent advances, challenges, and future perspectives", ACS Energy Letters **7**, 1043–1065 (2022).

[8] M. Fu, T. Ma, L. Wang, S. Dai, Z. Chang, H. Xu, J. Liu, and X. Li, "Hydrogen production via a novel two-step solar thermochemical cycle based on non-volatile GeO2", Solar Energy **179**, 30–36 (2019).

[9] M. Abuseada, C. Wei, R. M. Spearrin, and T. S. Fisher, “Solar–thermal production of graphitic carbon and hydrogen via methane decomposition”, Energy & Fuels **36**, 3920–3928 (2022).

[10] D. Yadav and R. Banerjee, “A review of solar thermochemical processes”, Renewable and Sustainable Energy Reviews **54**, 497–532 (2016).

[11] S. van Renssen, “The hydrogen solution?”, Nature Climate Change **10**, 799–801 (2020).

[12] S. Timmerberg, M. Kaltschmitt, and M. Finkbeiner, “Hydrogen and hydrogen-derived fuels through methane decomposition of natural gas – GHG emissions and costs”, Energy Conversion and Management: X **7**, 100043 (2020).

[13] V. Dias, M. Pochet, F. Contino, and H. Jeanmart, “Energy and cconomic costs of chemical storage”, Frontiers in Mechanical Engineering **6**, 1–17 (2020).

[14] International Energy Agency, *The future of hydrogen*, tech. rep. (IEA, Paris, 2019).

[15] J. Majewska and B. Michalkiewicz, “Production of hydrogen and carbon nanomaterials from methane using Co/ZSM-5 catalyst”, International Journal of Hydrogen Energy **41**, 8668–8678 (2016).

[16] M. Pudukudy, Z. Yaakob, and M. S. Takriff, “Methane decomposition over Pd promoted Ni/MgAl 2 O 4 catalysts for the production of COx free hydrogen and multiwalled carbon nanotubes”, Applied Surface Science **356**, 1320–1326 (2015).

[17] H. F. Abbas and W. Wan Daud, “Hydrogen production by methane decomposition: A review”, International Journal of Hydrogen Energy **35**, 1160–1190 (2010).

[18] K. K.-y. Kuo, *Principles of combustion*, 2nd Editio (John Wiley & Sons, Inc., New Jersey, 2005), pp. 45–47.

[19] P. L. Spath and M. K. Mann, *Life Cycle Assessment of Hydrogen Production via Natural Gas Steam Reforming*, tech. rep. No. NREL/TP-570-27637 (National Renewable Energy Laboratory (NREL), Golden, CO (United States), 2000), pp. 1–23.

[20] P. L. Spath and W. A. Amos, *Assessment of natural gas splitting with a concentrating solar reactor for hydrogen production*, tech. rep. (National Renewable Energy Laboratory (NREL), Golden, CO, 2002), pp. 1–27.

[21] E. J. Sheu, E. M. Mokheimer, and A. F. Ghoniem, "A review of solar methane reforming systems", International Journal of Hydrogen Energy **40**, 12929–12955 (2015).

[22] R. A. Dagle, V. Dagle, M. D. Bearden, J. D. Holladay, T. R. Krause, and S. Ahmed, *An overview of natural gas conversion technologies for Co-production of hydrogen and value-added solid carbon products*, tech. rep. (Pacific Northwest National Laboratory (PNNL), Richland, WA (United States), 2017), pp. 1–45.

[23] P. Ganguly, M. Harb, Z. Cao, L. Cavallo, A. Breen, S. Dervin, D. D. Dionysiou, and S. C. Pillai, "2D Nanomaterials for photocatalytic hydrogen production", ACS Energy Letters **4**, 1687–1709 (2019).

[24] J. Jia, L. C. Seitz, J. D. Benck, Y. Huo, Y. Chen, J. W. D. Ng, T. Bilir, J. S. Harris, and T. F. Jaramillo, "Solar water splitting by photovoltaic-electrolysis with a solar-to-hydrogen efficiency over 30%", Nature Communications **7**, 13237 (2016).

[25] W. C. Chueh, C. Falter, M. Abbott, D. Scipio, P. Furler, S. M. Haile, and A. Steinfeld, “High-flux solar-driven thermochemical dissociation of CO2 and H2O using nonstoichiometric ceria”, Science **330**, 1797–1801 (2010).

[26] S. Subramanian, Y. Song, D. Kim, and C. T. Yavuz, “Redox and nonredox CO2 utilization: Dry reforming of methane and catalytic cyclic carbonate formation”, ACS Energy Letters **5**, 1689–1700 (2020).

[27] R. K. Parsapur, S. Chatterjee, and K.-W. Huang, “The insignificant role of dry reforming of methane in CO2 emission relief”, ACS Energy Letters **5**, 2881–2885 (2020).

[28] L. Alves, V. Pereira, T. Lagarteira, and A. Mendes, “Catalytic methane decomposition to boost the energy transition: Scientific and technological advancements”, Renewable and Sustainable Energy Reviews **137**, 110465 (2021).

[29] A. Boretti, “A perspective on the production of hydrogen from solar-driven thermal decomposition of methane”, International Journal of Hydrogen Energy **46**, 34509–34514 (2021).

[30] N. Ozalp, M. Epstein, R. Davis, C. Ophoff, and I. Vinck, “A critical assessment of present hydrogen production techniques: is solar cracking a viable alternative?”, Current Opinion in Chemical Engineering **21**, 111–115 (2018).

[31] J. Yeheskel and M. Epstein, “Thermolysis of methane in a solar reactor for mass-production of hydrogen and carbon nano-materials”, Carbon **49**, 4695–4703 (2011).

[32] S. Rodat, S. Abanades, and G. Flamant, “Co-production of hydrogen and carbon black from solar thermal methane splitting in a tubular reactor prototype”, Solar Energy **85**, 645–652 (2011).

[33] J. X. Qian, T. W. Chen, L. R. Enakonda, D. B. Liu, G. Mignani, J.-M. Basset, and L. Zhou, “Methane decomposition to produce CO -free hydrogen and nano-carbon over metal catalysts: A review”, International Journal of Hydrogen Energy **45**, 7981–8001 (2020).

[34] N. Ozalp and V. Shilapuram, “Thermogravimetric analysis of carbon based catalysts on methane decomposition”, Chemical Engineering Transactions **39**, 733–738 (2014).

[35] N. Ozalp, H. Abedini, M. Abuseada, R. Davis, J. Rutten, J. Verschoren, C. Ophoff, and D. Moens, “An overview of direct carbon fuel cells and their promising potential on coupling with solar thermochemical carbon production”, Renewable and Sustainable Energy Reviews **162**, 112427 (2022).

[36] J. Pinilla, D. Torres, M. Lázaro, I. Suelves, R. Moliner, I. Cañadas, J. Rodríguez, A. Vidal, and D. Martínez, “Metallic and carbonaceous –based catalysts performance in the solar catalytic decomposition of methane for hydrogen and carbon production”, International Journal of Hydrogen Energy **37**, 9645–9655 (2012).

[37] J. K. Dahl, K. J. Buechler, R. Finley, T. Stanislaus, A. W. Weimer, A. Lewandowski, C. Bingham, A. Smeets, and A. Schneider, “Rapid solar-thermal dissociation of natural gas in an aerosol flow reactor”, Energy **29**, 715–725 (2004).

[38] J. Zhang, X. Li, H. Chen, M. Qi, G. Zhang, H. Hu, and X. Ma, "Hydrogen production by catalytic methane decomposition: Carbon materials as catalysts or catalyst supports", International Journal of Hydrogen Energy **42**, 19755–19775 (2017).

[39] M. Msheik, S. Rodat, and S. Abanades, "Methane cracking for hydrogen production: A review of catalytic and molten media pyrolysis", Energies **14**, 3107 (2021).

[40] N. Muradov, "Catalysis of methane decomposition over elemental carbon", Catalysis Communications **2**, 89–94 (2001).

[41] H. Nishii, D. Miyamoto, Y. Umeda, H. Hamaguchi, M. Suzuki, T. Tanimoto, T. Harigai, H. Takikawa, and Y. Suda, "Catalytic activity of several carbons with different structures for methane decomposition and by-produced carbons", Applied Surface Science **473**, 291–297 (2019).

[42] A. Gamal, K. Eid, M. H. El-Naas, D. Kumar, and A. Kumar, "Catalytic methane decomposition to carbon nanostructures and COx-free hydrogen: A mini-review", Nanomaterials **11**, 1226 (2021).

[43] M. Lázaro, J. Pinilla, I. Suelves, and R. Moliner, "Study of the deactivation mechanism of carbon blacks used in methane decomposition", International Journal of Hydrogen Energy **33**, 4104–4111 (2008).

[44] U. Ashik, W. Wan Daud, and H. F. Abbas, "Production of greenhouse gas free hydrogen by thermocatalytic decomposition of methane – A review", Renewable and Sustainable Energy Reviews **44**, 221–256 (2015).

[45] V. Shilapuram, N. Ozalp, M. Oschatz, L. Borchardt, and S. Kaskel, "Hydrogen production from catalytic decomposition of methane over ordered

mesoporous carbons (CMK-3) and carbide-derived carbon (DUT-19)", Carbon **67**, 377–389 (2014).

[46] N. S. N. Hasnan, S. N. Timmiati, K. L. Lim, Z. Yaakob, N. H. N. Kamaruddin, and L. P. Teh, "Recent developments in methane decomposition over heterogeneous catalysts: an overview", Materials for Renewable and Sustainable Energy **9**, 8 (2020).

[47] D. C. Upham, V. Agarwal, A. Khechfe, Z. R. Snodgrass, M. J. Gordon, H. Metiu, and E. W. McFarland, "Catalytic molten metals for the direct conversion of methane to hydrogen and separable carbon", Science **358**, 917–921 (2017).

[48] D. Paxman, S. Trottier, M. Nikoo, M. Secanell, and G. Ordorica-Garcia, "Initial experimental and theoretical investigation of solar molten media methane cracking for hydrogen production", Energy Procedia **49**, 2027–2036 (2014).

[49] L. Zhou et al., "Quantifying hot carrier and thermal contributions in plasmonic photocatalysis", Science **362**, 69–72 (2018).

[50] L. Zhou et al., "Light-driven methane dry reforming with single atomic site antenna-reactor plasmonic photocatalysts", Nature Energy **5**, 61–70 (2020).

[51] M. Abuseada and N. Ozalp, "Experimental and numerical study on a novel energy efficient variable aperture mechanism for a solar receiver", Solar Energy **197**, 396–410 (2020).

[52] G. Zsembinszki, A. Solé, C. Barreneche, C. Prieto, A. Fernández, and L. Cabeza, "Review of reactors with potential use in thermochemical energy storage in concentrated solar power plants", Energies **11**, 2358 (2018).

[53] S. Abanades, H. Kimura, and H. Otsuka, “A drop-tube particle-entrained flow solar reactor applied to thermal methane splitting for hydrogen production”, Fuel **153**, 56–66 (2015).

[54] T. Pregger, D. Graf, W. Krewitt, C. Sattler, M. Roeb, and S. Möller, “Prospects of solar thermal hydrogen production processes”, International Journal of Hydrogen Energy **34**, 4256–4267 (2009).

[55] S. Rodat, S. Abanades, J.-L. Sans, and G. Flamant, “A pilot-scale solar reactor for the production of hydrogen and carbon black from methane splitting”, International Journal of Hydrogen Energy **35**, 7748–7758 (2010).

[56] G. Maag, G. Zanganeh, and A. Steinfeld, “Solar thermal cracking of methane in a particle-flow reactor for the co-production of hydrogen and carbon”, International Journal of Hydrogen Energy **34**, 7676–7685 (2009).

[57] S. Abanades, H. Kimura, and H. Otsuka, “Hydrogen production from thermo-catalytic decomposition of methane using carbon black catalysts in an indirectly-irradiated tubular packed-bed solar reactor”, International Journal of Hydrogen Energy **39**, 18770–18783 (2014).

[58] M. Abuseada and N. Ozalp, “Experimental and numerical study on heat transfer driven dynamics and control of transient variations in a solar receiver”, Solar Energy **211**, 700–711 (2020).

[59] S. Rodat, S. Abanades, E. Grivei, G. Patrianakos, A. Zygogianni, A. G. Konstandopoulos, and G. Flamant, “Characterisation of carbon blacks produced by solar thermal dissociation of methane”, Carbon **49**, 3084–3091 (2011).

[60] A. Abánades et al., “Experimental analysis of direct thermal methane cracking”, International Journal of Hydrogen Energy **36**, 12877–12886 (2011).

[61] D. Hirsch, “Solar hydrogen production by thermal decomposition of natural gas using a vortex-flow reactor”, International Journal of Hydrogen Energy **29**, 47–55 (2004).

[62] N. Muradov, “Low to near-zero CO2 production of hydrogen from fossil fuels: Status and perspectives”, International Journal of Hydrogen Energy **42**, 14058–14088 (2017).

[63] T. Keipi, H. Tolvanen, and J. Konttinen, “Economic analysis of hydrogen production by methane thermal decomposition: Comparison to competing technologies”, Energy Conversion and Management **159**, 264–273 (2018).

[64] K. C. Mondal and S. Ramesh Chandran, “Evaluation of the economic impact of hydrogen production by methane decomposition with steam reforming of methane process”, International Journal of Hydrogen Energy **39**, 9670–9674 (2014).

[65] H. Kimura, S. Abanades, and S. Seo, “Production of C2-hydrocarbons and hydrogen from methane pyrolysis with concentrated solar energy”, in Aip conference proceedings, Vol. 2303, 1 (AIP Publishing LLC, 2020), p. 170010.

[66] X. Guo et al., “Direct, nonoxidative conversion of methane to ethylene, aromatics, and hydrogen”, Science **344**, 616–619 (2014).

[67] T. M. Abdellateif, J. Sarwar, E. C. Vagia, and K. E. Kakosimos, “Optical and experimental evaluation of a directly irradiated solar reactor for the catalytic dry reforming of methane”, Chemical Engineering Journal **452**, 139190 (2023).

[68] M. Abuseada, A. Alghfeli, and T. S. Fisher, “Indirect inverse flux mapping of a concentrated solar source using infrared imaging”, Review of Scientific Instruments **93**, 073101 (2022).

[69] B. M. Ekman, G. Brooks, and M. A. Rhamdhani, “Development of high flux solar simulators for solar thermal research”, in *Energy technology 2015*, Vol. 141 (Springer International Publishing, Cham, 2015), pp. 149–159.

[70] S. Tembhurne, F. Nandjou, and S. Haussener, “A thermally synergistic photo-electrochemical hydrogen generator operating under concentrated solar irradiation”, Nature Energy **4**, 399–407 (2019).

[71] B. Hu, B. Li, R. Zhao, and T. Yang, “Reflection-type single long-pulse solar simulator for high-efficiency crystalline silicon photovoltaic modules”, Review of Scientific Instruments **82**, 065104 (2011).

[72] J. Jin, M. Liu, P. Lin, T. Fu, Y. Hao, and H. Jin, “Ultrahigh temperature processing by concentrated solar energy with accurate temperature measurement”, Applied Thermal Engineering **150**, 1337–1344 (2019).

[73] Y. Hu, M. Abuseada, A. Alghfeli, S. Holdheim, and T. S. Fisher, “High-temperature thermal diffusivity measurements using a modified Ångström’s method with transient infrared thermography”, Journal of Heat Transfer **144**, 023502 (2022).

[74] A. Gallo, A. Marzo, E. Fuentealba, and E. Alonso, “High flux solar simulators for concentrated solar thermal research: A review”, Renewable and Sustainable Energy Reviews **77**, 1385–1402 (2017).

[75] A. Steinfeld, M. Brack, A. Meier, A. Weidenkaff, and D. Wuillemin, “A solar chemical reactor for co-production of zinc and synthesis gas”, Energy **23**, 803–814 (1998).

[76] M. Abuseada, C. Ophoff, and N. Ozalp, “Characterization of a new 10 kWe high flux solar simulator via indirect radiation mapping technique”, Journal of Solar Energy Engineering **141**, 1–14 (2019).

[77] G. Levêque, R. Bader, W. Lipiński, and S. Haussener, “Experimental and numerical characterization of a new 45 kW_el multisource high-flux solar simulator”, Optics Express **24**, A1360 (2016).

[78] R. Gill, E. Bush, P. Haueter, and P. Loutzenhiser, “Characterization of a 6 kW high-flux solar simulator with an array of xenon arc lamps capable of concentrations of nearly 5000 suns”, Review of Scientific Instruments **86**, 125107 (2015).

[79] K. R. Krueger, W. Lipiński, and J. H. Davidson, “Operational performance of the University of Minnesota 45 kWe high-flux solar simulator”, Journal of Solar Energy Engineering **135**, 044501 (2013).

[80] F. Lei, L. Freiberg, Y. Wang, I. Reddick, G. Jovanovic, A. Yokochi, and N. AuYeung, “Non-catalytic ethane cracking using concentrated solar energy”, Chemical Engineering Journal **355**, 58–64 (2019).

[81] J. Sarwar, G. Georgakis, R. LaChance, and N. Ozalp, “Description and characterization of an adjustable flux solar simulator for solar thermal, thermochemical and photovoltaic applications”, Solar Energy **100**, 179–194 (2014).

[82] M. Abuseada, “An experimental and numerical study on the heat transfer driven dynamics and control of transient variations in a solar reactor”, Masters (University of Minnesota, 2019), pp. 1–149.

[83] J. Xiao, H. Yang, X. Wei, and Z. Li, "A novel flux mapping system for high-flux solar simulators based on the indirect method", Solar Energy **179**, 89–98 (2019).

[84] P. Kuhn and A. Hunt, "A new solar simulator to study high temperature solid-state reactions with highly concentrated radiation", Solar Energy Materials **24**, 742–750 (1991).

[85] W. Wang, L. Aichmayer, J. Garrido, and B. Laumert, "Development of a Fresnel lens based high-flux solar simulator", Solar Energy **144**, 436–444 (2017).

[86] J. Garrido, L. Aichmayer, W. Wang, and B. Laumert, "Characterization of the KTH high-flux solar simulator combining three measurement methods", Energy **141**, 2091–2099 (2017).

[87] V. Pozzobon and S. Salvador, "High heat flux mapping using infrared images processed by inverse methods: An application to solar concentrating systems", Solar Energy **117**, 29–35 (2015).

[88] T.-T. Ngo, J.-H. Huang, and C.-C. Wang, "Inverse simulation and experimental verification of temperature-dependent thermophysical properties", International Communications in Heat and Mass Transfer **71**, 137–147 (2016).

[89] O. M. Alifanov, "Solution of an inverse problem of heat conduction by iteration methods", Journal of Engineering Physics **26**, 471–476 (1974).

[90] O. M. Alifanov and Y. V. Egorov, "Algorithms and results of solving the inverse heat-conduction boundary problem in a two-dimensional formulation", Journal of Engineering Physics **48**, 489–496 (1985).

[91] J. Su and A. J. Silva Neto, “Two-dimensional inverse heat conduction problem of source strength estimation in cylindrical rods”, Applied Mathematical Modelling **25**, 861–872 (2001).

[92] S. Kim, M. C. Kim, and K. Y. Kim, “An integral approach to the inverse estimation of temperature-dependent thermal conductivity without internal measurements”, International Communications in Heat and Mass Transfer **29**, 107–113 (2002).

[93] S. Kim, M. C. Kim, and K. Y. Kim, “Non-iterative estimation of temperature-dependent thermal conductivity without internal measurements”, International Journal of Heat and Mass Transfer **46**, 1801–1810 (2003).

[94] C.-L. Chang and M. Chang, “Non-iteration estimation of thermal conductivity using finite volume method”, International Communications in Heat and Mass Transfer **33**, 1013–1020 (2006).

[95] H. Li, J. Lei, and Q. Liu, “An inversion approach for the inverse heat conduction problems”, International Journal of Heat and Mass Transfer **55**, 4442–4452 (2012).

[96] M. Singhal, S. Singh, R. K. Singla, K. Goyal, and D. Jain, “Experimental and computational inverse thermal analysis of transient, non-linear heat flux in circular pin fin with temperature-dependent thermal properties”, Applied Thermal Engineering **168**, 114721 (2020).

[97] N. P. Singh and K. Reddy, “Inverse heat transfer technique for estimation of focal flux distribution for a concentrating photovoltaic (CPV) square solar parabola dish collector”, Renewable Energy **145**, 2783–2795 (2020).

[98] K. R. Krueger, "Design and characterization of a concentrating solar simulator", PhD (University of Minnesota, Minneapolis, MN, 2012), pp. 1–151.

[99] D. Learn, P. Forbes, and C. Sambuco, "Photosafety assessment", A Comprehensive Guide to Toxicology in Nonclinical Drug Development, 585–614 (2017).

[100] J. Ballestrín, S. Ulmer, A. Morales, A. Barnes, L. Langley, and M. Rodriguez, "Systematic error in the measurement of very high solar irradiance", Solar Energy Materials and Solar Cells **80**, 375–381 (2003).

[101] J. A. Nelder and R. Mead, "A simplex method for function minimization", The Computer Journal **7**, 308–313 (1965).

[102] F. Gao and L. Han, "Implementing the Nelder-Mead simplex algorithm with adaptive parameters", Computational Optimization and Applications **51**, 259–277 (2012).

[103] J. R. Howell, "The Monte Carlo method in radiative heat transfer", Journal of Heat Transfer **120**, 547–560 (1998).

[104] J. Delatorre et al., "Monte Carlo advances and concentrated solar applications", Solar Energy **103**, 653–681 (2014).

[105] M. Abuseada and N. Ozalp, "Numerical Characterization of a High Flux Solar Simulator Using Forward and Inverse Methods", Journal of Heat Transfer **142**, 022105 (2020).

[106] M. Vauhkonen, T. Tarvainen, and T. Lähivaara, "Inverse Problems", in *Mathematical modelling* (Springer, 2016), pp. 207–227.

[107] R. C. Aster, B. Borchers, and C. H. Thurber, *Parameter estimation and inverse problems*, 3rd Editio (Elsevier, 2018), pp. 1–209.

[108] S. Dai, Z. Chang, T. Ma, L. Wang, and X. Li, “Experimental study on flux mapping for a novel 84 kWe high flux solar simulator”, Applied Thermal Engineering **162**, 114319 (2019).

[109] F. Gomez-Garcia, S. Santiago, S. Luque, M. Romero, and J. Gonzalez-Aguilar, “A new laboratory-scale experimental facility for detailed aerothermal characterizations of volumetric absorbers”, in Aip conference proceedings, Vol. 1734, 1 (AIP Publishing LLC, 2016), p. 030018.

[110] J. Xiao, X. Wei, R. N. Gilaber, Y. Zhang, and Z. Li, “Design and characterization of a high-flux non-coaxial concentrating solar simulator”, Applied Thermal Engineering **145**, 201–211 (2018).

[111] T. S. Fisher, “Carrier Scattering and Transmission”, in *Thermal energy at the nanoscale* (WORLD SCIENTIFIC, 2013), pp. 113–156.

[112] S. Bapat and H. Nickel, “Thermal conductivity and electrical resistivity of poco grade AXF-Q1 graphite to 3300° K”, Carbon **11**, 323–327 (1973).

[113] C. Kittel, *Introduction to solid state physics*, 8th (Wiley, 2004), pp. 155–157.

[114] T. Pavlov, L. Vlahovic, D. Staicu, R. Konings, M. Wenman, P. Van Uffelen, and R. Grimes, “A new numerical method and modified apparatus for the simultaneous evaluation of thermo-physical properties above 1500 K: A case study on isostatically pressed graphite”, Thermochimica Acta **652**, 39–52 (2017).

[115] Entegris, *Properties and characteristics of graphite*, 2013.

[116] G. Autio and E. Scala, "The normal spectral emissivity of isotropic and anisotropic materials", Carbon **4**, 13–28 (1966).

[117] J. D. Plunkett and W. D. Kingery, "The spectral and integrated emissivity of carbon and graphite", in *Carbon* (Pergamon, 1960), pp. 457–472.

[118] R. J. Champetier, *Basal plane emittance of pyrolytic graphite at elevated temperatures*, tech. rep. (Aerospace Corp, 1967).

[119] R. J. Thorn and O. C. Simpson, "Spectral emissivities of graphite and carbon", Journal of Applied Physics **24**, 633–639 (1953).

[120] G. L. Abbott, N. J. Alvares, and W. P. J., *Total normal and total hemispherical emittance of polished metals*, tech. rep. (Naval Radiological Defense Lab, 1961).

[121] M. F. Modest, *Radiative Heat Transfer*, 3rd (Elsevier, 2013), pp. 73–82.

[122] A. B. Djurišić and E. H. Li, "Optical properties of graphite", Journal of Applied Physics **85**, 7404–7410 (1999).

[123] H. R. Philipp, "Infrared optical properties of graphite", Physical Review B **16**, 2896–2900 (1977).

[124] I. Gurwich and M. Spector, "The thermal lens effect on laser heating of a metal nano-sphere particle immersed in oil", Journal of Quantitative Spectroscopy and Radiative Transfer **252**, 107066 (2020).

[125] H. Golnabi, "Diffuse reflectance measurements from different surfaces", Journal of Sciences Islamic Republic of Iran **12**, 359–364 (2001).

[126] B. van Ginneken, M. Stavridi, and J. J. Koenderink, "Diffuse and specular reflectance from rough surfaces", Applied Optics **37**, 130–139 (1998).

[127] E. C. Beder, C. D. Bass, and W. L. Shackleford, “Transmissivity and absorption of fused quartz between 0.22 μ and 3.5 μ from room temperature to 1500°C”, Applied Optics **10**, 2263–2268 (1971).

[128] S. Madhavan, J. J. Qu, and X. Hao, “Saharan dust detection using multi-sensor satellite measurements”, Heliyon **3**, e00241 (2017).

[129] C. Wei, K. K. Schwarm, D. I. Pineda, and R. M. Spearrin, “Deep neural network inversion for 3D laser absorption imaging of methane in reacting flows”, Optics Letters **45**, 2447 (2020).

[130] K. K. Schwarm, C. Wei, D. I. Pineda, and R. Mitchell Spearrin, “Time-resolved laser absorption imaging of ethane at 2 kHz in unsteady partially premixed flames”, Applied Optics **58**, 5656 (2019).

[131] C. S. Goldenstein, R. Spearrin, J. B. Jeffries, and R. K. Hanson, “Infrared laser-absorption sensing for combustion gases”, Progress in Energy and Combustion Science **60**, 132–176 (2017).

[132] J. J. Harrison, N. D. Allen, and P. F. Bernath, “Infrared absorption cross sections for ethane (C2H6) in the 3μm region”, Journal of Quantitative Spectroscopy and Radiative Transfer **111**, 357–363 (2010).

[133] P. L. Urban, “Quantitative mass spectrometry: an overview”, Philosophical Transactions of the Royal Society A: Mathematical, Physical and Engineering Sciences **374**, 20150382 (2016).

[134] G. Loos, A. Van Schepdael, and D. Cabooter, “Quantitative mass spectrometry methods for pharmaceutical analysis”, Philosophical Transactions of the Royal Society A: Mathematical, Physical and Engineering Sciences **374**, 20150366 (2016).

[135] T. M. Annesley, “Ion Suppression in Mass Spectrometry”, Clinical Chemistry **49**, 1041–1044 (2003).

[136] P. Traldi, F. Magno, I. Lavagnini, and R. Seraglia, *Quantitative applications of mass spectrometry* (John Wiley & Sons, 2006).

[137] NIST Mass Spectrometry Data Center, W. E. Wallace, and Director, “Mass Spectra”, in *Nist standard reference database number 69*, edited by P. Linstrom and W. Mallard (National Institute of Standards and Technology, Gaithersburg MD, 20899, 2011) Chap. NIST Chemi.

[138] Z. Xu, Z. He, Y. Song, X. Fu, M. Rommel, X. Luo, A. Hartmaier, J. Zhang, and F. Fang, “Topic review: Application of Raman spectroscopy characterization in micro/nano-machining”, Micromachines **9**, 361 (2018).

[139] A. C. Ferrari and D. M. Basko, “Raman spectroscopy as a versatile tool for studying the properties of graphene”, Nature Nanotechnology **8**, 235–246 (2013).

[140] A. C. Ferrari, “Raman spectroscopy of graphene and graphite: Disorder, electron–phonon coupling, doping and nonadiabatic effects”, Solid State Communications **143**, 47–57 (2007).

[141] R. Vidano and D. B. Fischbach, “New lines in the Raman spectra of carbons and graphite”, Journal of the American Ceramic Society **61**, 13–17 (1978).

[142] M. Pawlyta, J.-N. Rouzaud, and S. Duber, “Raman microspectroscopy characterization of carbon blacks: Spectral analysis and structural information”, Carbon **84**, 479–490 (2015).

[143] F. Tuinstra and J. L. Koenig, “Raman spectrum of graphite”, The Journal of Chemical Physics **53**, 1126–1130 (1970).

[144] A. C. Ferrari and J. Robertson, “Interpretation of Raman spectra of disordered and amorphous carbon”, Physical Review B **61**, 14095–14107 (2000).

[145] A. Merlen, J. G. Buijnsters, and C. Pardanaud, “Raman spectroscopy characterization of carbon materials: From graphene to all-carbon heterostructures”, All-carbon Composites and Hybrids, 317–346 (2021).

[146] A. C. Ferrari, S. E. Rodil, and J. Robertson, “Interpretation of infrared and Raman spectra of amorphous carbon nitrides”, Physical Review B **67**, 155306 (2003).

[147] S. Brunauer, P. H. Emmett, and E. Teller, “Adsorption of gases in multimolecular layers”, Journal of the American Chemical Society **60**, 309–319 (1938).

[148] P. V. Gulgunje, B. A. Newcomb, K. Gupta, H. G. Chae, T. K. Tsotsis, and S. Kumar, “Low-density and high-modulus carbon fibers from polyacrylonitrile with honeycomb structure”, Carbon **95**, 710–714 (2015).

[149] M. Balat-Pichelin, J. Robert, and J. Sans, “Emissivity measurements on carbon–carbon composites at high temperature under high vacuum”, Applied Surface Science **253**, 778–783 (2006).

[150] C. Wei, M. Abuseada, B. Jeevaretanam, T. S. Fisher, and R. M. Spearrin, “Concentrated solar-thermal methane pyrolysis in a porous substrate: Yield analysis via infrared laser absorption”, Proceedings of the Combustion Institute, `10.1016/j.proci.2022.07.007` (2022).

[151] R. Bader, L. J. Venstrom, J. H. Davidson, and W. Lipiński, “Thermodynamic analysis of isothermal redox cycling of ceria for solar fuel production”, Energy & Fuels **27**, 5533–5544 (2013).

[152] I. H. Bell, J. Wronski, S. Quoilin, and V. Lemort, “Pure and pseudo-pure fluid thermophysical property evaluation and the open-source thermophysical property library CoolProp”, Industrial & Engineering Chemistry Research **53**, 2498–2508 (2014).

[153] A. Butland and R. Maddison, “The specific heat of graphite: An evaluation of measurements”, Journal of Nuclear Materials **49**, 45–56 (1973).

[154] J. Van der Westhuizen and J. Prieur Du Plessis, “An attempt to quantify fibre bed permeability utilizing the phase average Navier-Stokes equation”, Composites Part A: Applied Science and Manufacturing **27**, 263–269 (1996).

[155] P. Soltani, M. S. Johari, and M. Zarrebini, “Effect of 3D fiber orientation on permeability of realistic fibrous porous networks”, Powder Technology **254**, 44–56 (2014).

[156] R. Buck, J. F. Muir, and R. E. Hogan, “Carbon dioxide reforming of methane in a solar volumetric receiver/reactor: the CAESAR project”, Solar Energy Materials **24**, 449–463 (1991).

[157] M. Roeb and H. Müller-Steinhagen, “Concentrating on solar electricity and fuels”, Science **329**, 773–774 (2010).

[158] S. Stoft, *Power system economics: Designing market for power* (Wiley-IEEE Press, 2002), p. 292.

[159] S. Bammidipati, G. D. Stewart, J. R. Elliott, S. A. Gokoglu, and M. J. Purdy, “Chemical vapor deposition of carbon on graphite by methane pyrolysis”, AIChE Journal **42**, 3123–3132 (1996).

[160] Y. Zhang et al., “Chemical vapor deposition growth and characterization of graphite-like film”, Materials Research Express **7**, 015609 (2020).

[161] K. O. Johansson, M. P. Head-Gordon, P. E. Schrader, K. R. Wilson, and H. A. Michelsen, "Resonance-stabilized hydrocarbon-radical chain reactions may explain soot inception and growth", Science **361**, 997–1000 (2018).

[162] N. Muradov, F. Smith, and A. T-Raissi, "Catalytic activity of carbons for methane decomposition reaction", Catalysis Today **102-103**, 225–233 (2005).

[163] N. Muradov, F. Smith, C. Huang, and A. T-Raissi, "Autothermal catalytic pyrolysis of methane as a new route to hydrogen production with reduced CO2 emissions", Catalysis Today **116**, 281–288 (2006).

[164] M. B. Lundeberg et al., "Tuning quantum nonlocal effects in graphene plasmonics", Science **357**, 187–191 (2017).

[165] C. Barnakov, G. Khokhlova, A. Popova, S. Sozinov, and Z. Ismagilov, "XRD characterization of the structure of graphites and carbon materials obtained by the low-temperature graphitization of coal tar pitch", Eurasian Chemico-Technological Journal **17**, 87 (2015).

[166] K. R. Saviers, M. A. Alrefae, and T. S. Fisher, "Roll-to-roll production of graphitic petals on carbon fiber tow", Advanced Engineering Materials **20**, 1800004 (2018).

[167] E. J. Kim et al., "Cooperative carbon capture and steam regeneration with tetraamine-appended metal–organic frameworks", Science **369**, 392–396 (2020).

[168] R. W. Howarth and M. Z. Jacobson, "How green is blue hydrogen?", Energy Science & Engineering **9**, 1676–1687 (2021).

[169] T. Ungár, J. Gubicza, G. Ribárik, C. Pantea, and T. Zerda, "Microstructure of carbon blacks determined by X-ray diffraction profile analysis", Carbon **40**, 929–937 (2002).

[170] Y. Pan et al., “Graphitic carbon from catalytic methane decomposition as efficient conductive additives for zinc-carbon batteries”, Carbon **192**, 84–92 (2022).

[171] S.-M. Lee, S.-H. Lee, and J.-S. Roh, “Analysis of activation process of carbon black based on structural parameters obtained by XRD analysis”, Crystals **11**, 153 (2021).

[172] W. Zhang, Z. Hu, and K. Hüttinger, “Chemical vapor infiltration of carbon fiber felt: optimization of densification and carbon microstructure”, Carbon **40**, 2529–2545 (2002).

[173] B. Ren, S. Zhang, L. He, and S. Gu, “Effect of oxygen and hydrogen on microstructure of pyrolytic carbon deposited from thermal decomposition of methane and ethanol”, Journal of Solid State Chemistry **261**, 86–91 (2018).

[174] X. Guo, G. Zhi, Y. Wang, G. Jin, and X. Guo, “Bundle-like carbon nanofibers grown from methane decomposition”, Carbon **50**, 321–322 (2012).

[175] T. Keipi, K. E. Tolvanen, H. Tolvanen, and J. Konttinen, “Thermo-catalytic decomposition of methane: The effect of reaction parameters on process design and the utilization possibilities of the produced carbon”, Energy Conversion and Management **126**, 923–934 (2016).

[176] Y. Kameya and K. Hanamura, “Kinetic and Raman spectroscopic study on catalytic characteristics of carbon blacks in methane decomposition”, Chemical Engineering Journal **173**, 627–635 (2011).

[177] G. Dong and K. Hüttinger, “Consideration of reaction mechanisms leading to pyrolytic carbon of different textures”, Carbon **40**, 2515–2528 (2002).

[178] S. Y. Lee, B. H. Ryu, G. Y. Han, T. J. Lee, and K. J. Yoon, "Catalytic characteristics of specialty carbon blacks in decomposition of methane for hydrogen production", Carbon **46**, 1978–1986 (2008).

[179] A. Lidor, T. Fend, M. Roeb, and C. Sattler, "Parametric investigation of a volumetric solar receiver-reactor", Solar Energy **204**, 256–269 (2020).

[180] S. Lee, "Effect of fiber orientation on thermal radiation in fibrous media", International Journal of Heat and Mass Transfer **32**, 311–319 (1989).

[181] E. K. Lee, S. Y. Lee, G. Y. Han, B. K. Lee, T.-J. Lee, J. H. Jun, and K. J. Yoon, "Catalytic decomposition of methane over carbon blacks for CO2-free hydrogen production", Carbon **42**, 2641–2648 (2004).

[182] J. Pinilla, I. Suelves, M. Lázaro, and R. Moliner, "Kinetic study of the thermal decomposition of methane using carbonaceous catalysts", Chemical Engineering Journal **138**, 301–306 (2008).

[183] M. Abuseada and T. S. Fisher, "Continuous solar-thermal methane pyrolysis by roll-to-roll processing", Energy Proceedings **25**, 1151 (2022).

[184] J. F. Peters and M. Weil, "A critical assessment of the resource depletion potential of current and future lithium-ion batteries", Resources **5**, `10.3390/resources5040046` (2016).

[185] S. Abanades and L. André, "Design and demonstration of a high temperature solar-heated rotary tube reactor for continuous particles calcination", Applied Energy **212**, 1310–1320 (2018).

[186] H. F. Abbas and W. W. Daud, "Hydrogen production by thermocatalytic decomposition of methane using a fixed bed activated carbon in a pilot scale unit: Apparent kinetic, deactivation and diffusional limitation studies", International Journal of Hydrogen Energy **35**, 12268–12276 (2010).

[187] E. Koepf, I. Alxneit, C. Wieckert, and A. Meier, "A review of high temperature solar driven reactor technology: 25 years of experience in research and development at the Paul Scherrer Institute", Applied Energy **188**, 620–651 (2017).

[188] D. Kang, N. Rahimi, M. J. Gordon, H. Metiu, and E. W. McFarland, "Catalytic methane pyrolysis in molten MnCl2-KCl", Applied Catalysis B: Environmental **254**, 659–666 (2019).

[189] S. Bae et al., "Roll-to-roll production of 30-inch graphene films for transparent electrodes", Nature Nanotechnology **5**, 574–578 (2010).

[190] S. Naghdi, K. Y. Rhee, and S. J. Park, "A catalytic, catalyst-free, and roll-to-roll production of graphene via chemical vapor deposition: Low temperature growth", Carbon **127**, 1–12 (2018).

[191] M. A. Alrefae, A. Kumar, P. Pandita, A. Candadai, I. Bilionis, and T. S. Fisher, "Process optimization of graphene growth in a roll-to-roll plasma CVD system", AIP Advances **7**, 115102 (2017).

[192] P. R. Kidambi, D. D. Mariappan, N. T. Dee, A. Vyatskikh, S. Zhang, R. Karnik, and A. J. Hart, "A scalable route to nanoporous large-area atomically thin graphene membranes by roll-to-roll chemical vapor deposition and polymer support casting", ACS Applied Materials & Interfaces **10**, 10369–10378 (2018).

[193] B. Martin, D. Amos, E. Brehob, M. F. A. M. van Hest, and T. Druffel, "Techno-economic analysis of roll-to-roll production of perovskite modules using radiation thermal processes", Applied Energy **307**, 118200 (2022).

[194] N. Palavesam, S. Marin, D. Hemmetzberger, C. Landesberger, K. Bock, and C. Kutter, "Roll-to-roll processing of film substrates for hybrid integrated flexible electronics", Flexible and Printed Electronics **3**, 014002 (2018).

[195] T. Choi, S. J. Kim, S. Park, T. Y. Hwang, Y. Jeon, and B. H. Hong, "Roll-to-roll continuous patterning and transfer of graphene via dispersive adhesion", Nanoscale **7**, 7138–7142 (2015).

[196] L. Li, B. Wang, J. Pye, and W. Lipiński, "Temperature-based optical design, optimization and economics of solar polar-field central receiver systems with an optional compound parabolic concentrator", Solar Energy **206**, 1018–1032 (2020).

[197] T. Osório et al., "Ray-tracing software comparison for linear focusing solar collectors", AIP Conference Proceedings **1734**, 20017 (2016).

[198] H. Zhang and J. D. Smith, "Investigating influences of geometric factors on a solar thermochemical reactor for two-step carbon dioxide splitting via CFD models", Solar Energy **188**, 935–950 (2019).

[199] H. Kim and J. Kim, "Numerical study on optics and heat transfer of solar reactor for methane thermal decomposition", Energies **14**, 6451 (2021).

[200] K. Craig, M. Slootweg, W. Le Roux, T. Wolff, and J. Meyer, "Using CFD and ray tracing to estimate the heat losses of a tubular cavity dish receiver for different inclination angles", Solar Energy **211**, 1137–1158 (2020).

[201] C. Ophoff, M. Abuseada, N. Ozalp, and D. Moens, "Systematic approach for design optimization of a 3 kW solar cavity receiver via multiphysics analysis", Solar Energy **206**, 420–435 (2020).

[202] R. Acosta-Herazo, P. J. Valadés-Pelayo, M. A. Mueses, M. H. Pinzón-Cárdenas, C. Arancibia-Bulnes, and F. Machuca-Martínez, "An optical and energy absorption analysis of the solar compound parabolic collector photoreactor (CPCP): The impact of the radiation distribution on its optimization", Chemical Engineering Journal **395**, 125065 (2020).

[203] L. Li, B. Wang, R. Bader, J. Zapata, and W. Lipiński, "Reflective optics for redirecting convergent radiative beams in concentrating solar applications", Solar Energy **191**, 707–718 (2019).

[204] X. Duan, C. He, X. Lin, Y. Zhao, and J. Feng, "Quasi-Monte Carlo ray tracing algorithm for radiative flux distribution simulation", Solar Energy **211**, 167–182 (2020).

[205] L. Li, S. Yang, B. Wang, J. Pye, and W. Lipiński, "Optical analysis of a solar thermochemical system with a rotating tower reflector and a receiver–reactor array", Optics Express **28**, 19429 (2020).

[206] J. R. Mahan, *Radiation heat transfer: A statistical approach* (Wiley, New York, 2002), pp. 185–370.

[207] Y. Namba and H. Tsuwa, "Surface properties of polished stainless steel", CIRP Annals **29**, 409–412 (1980).

[208] L. S. Andrade, S. C. Xavier, R. C. Rocha-Filho, N. Bocchi, and S. R. Biaggio, "Electropolishing of AISI-304 stainless steel using an oxidizing solution originally used for electrochemical coloration", Electrochimica Acta **50**, 2623–2627 (2005).

[209] W. S. Rodney and R. J. Spindler, "Index of refraction of fused quartz glass for ultraviolet, visible, and infrared wavelengths", Journal of the Optical Society of America **44**, 677–679 (1954).

[210] J.-H. Zhang, M.-J. Wei, Z.-W. Wei, M. Pan, and C.-Y. Su, “Ultrathin graphitic carbon nitride nanosheets for photocatalytic hydrogen evolution”, ACS Applied Nano Materials **3**, 1010–1018 (2020).

[211] Y. He, Y. Liu, C. Li, X.-B. Chen, Z. Shi, and S. Feng, “Origin of the photocatalytic activity of crystalline Pphase structures”, ACS Applied Energy Materials **5**, 8923–8929 (2022).

[212] D. A. Panayotov, A. I. Frenkel, and J. R. Morris, “Catalysis and photocatalysis by nanoscale Au/TiO2: Perspectives for renewable energy”, ACS Energy Letters **2**, 1223–1231 (2017).

[213] M. Lou et al., “Direct H2S decomposition by plasmonic photocatalysis: Efficient remediation plus sustainable hydrogen production”, ACS Energy Letters **7**, 3666–3674 (2022).

[214] H. B. Palmer and T. J. Hirt, “The activation energy for the pyrolysis of methane”, The Journal of Physical Chemistry **67**, 709–711 (1963).

[215] H. Palmer, “An analysis of carbon deposition kinetics in isothermal flow systems”, Carbon **1**, 55–64 (1963).

[216] K. Norinaga, V. M. Janardhanan, and O. Deutschmann, “Detailed chemical kinetic modeling of pyrolysis of ethylene, acetylene, and propylene at 1073-1373 K with a plug-flow reactor model”, International Journal of Chemical Kinetics **40**, 199–208 (2008).

[217] K. Norinaga, O. Deutschmann, N. Saegusa, and J.-i. Hayashi, “Analysis of pyrolysis products from light hydrocarbons and kinetic modeling for growth of polycyclic aromatic hydrocarbons with detailed chemistry”, Journal of Analytical and Applied Pyrolysis **86**, 148–160 (2009).

[218] T. Bensabath, H. Monnier, and P.-A. Glaude, “Detailed kinetic modeling of the formation of toxic polycyclic aromatic hydrocarbons (PAHs) coming from pyrolysis in low-pressure gas carburizing conditions”, Journal of Analytical and Applied Pyrolysis **122**, 342–354 (2016).

[219] T. Bensabath, M. D. Le, H. Monnier, and P.-A. Glaude, “Polycyclic aromatic hydrocarbon (PAH) formation during acetylene pyrolysis in tubular reactor under low pressure carburizing conditions”, Chemical Engineering Science **202**, 84–94 (2019).

[220] Y. Hu and T. S. Fisher, “Accurate thermal diffusivity measurements using a modified Ångström’s method with Bayesian statistics”, Journal of Heat Transfer **142**, 1–9 (2020).

[221] M. Mahdavi, M. Ramazani, and Z. Darvishi, “Synthesis and characterization of zirconium carbide nanorods at low temperature”, International Journal of Refractory Metals and Hard Materials **56**, 59–62 (2016).

[222] A. Ortiz, F. Sánchez-Bajo, F. Cumbrera, and F. Guiberteau, “X-ray powder diffraction analysis of a silicon carbide-based ceramic”, Materials Letters **49**, 137–145 (2001).

[223] S.-H. Xue, H. Xie, H. Ping, Q.-C. Li, B.-L. Su, and Z.-Y. Fu, “Induced transformation of amorphous silica to cristobalite on bacterial surfaces”, RSC Advances **5**, 71844–71848 (2015).

[224] J. G. Lee, P. D. Miller, and I. B. Cutler, “Carbothermal Reduction of Silica”, in *Reactivity of solids* (Springer US, Boston, MA, 1977), pp. 707–711.

[225] M. Nagamori, I. Malinsky, and A. Claveau, “Thermodynamics of the Si-C-O system for the production of silicon carbide and metallic silicon”, Metallurgical Transactions B **17**, 503–514 (1986).

[226] Q. Xu et al., “Silicon/graphite composite anode with constrained swelling and a stable solid electrolyte interphase enabled by spent graphite”, Green Chemistry **23**, 4531–4539 (2021).

[227] P. Li, J.-Y. Hwang, and Y.-K. Sun, “Nano/microstructured silicon–graphite composite anode for high-energy-density Li-ion battery”, ACS Nano **13**, 2624–2633 (2019).

[228] E. Moyassari, T. Roth, S. Kücher, C.-C. Chang, S.-C. Hou, F. B. Spingler, and A. Jossen, “The Role of Silicon in Silicon-Graphite Composite Electrodes Regarding Specific Capacity, Cycle Stability, and Expansion”, Journal of The Electrochemical Society **169**, 010504 (2022).

[229] A. J. Way, R. M. Jacobberger, N. P. Guisinger, V. Saraswat, X. Zheng, A. Suresh, J. H. Dwyer, P. Gopalan, and M. S. Arnold, “Graphene nanoribbons initiated from molecularly derived seeds”, Nature Communications **13**, 2992 (2022).